Exploring the Regulation of Myofilament Function in the Heart using Experimental and Computational Approaches



Milda Folkmanaite

St Hilda's College

University of Oxford

A thesis submitted for the degree of

Doctor of Philosophy

Trinity 2024

Abstract

Precise spatio-temporal control of 3',5'-cyclic adenosine monophosphate (cAMP) and protein kinase A (PKA) is essential for normal cardiac function. Dysregulation of cAMP-dependent, PKA-mediated phosphorylation of myofilament proteins, such as troponin I (TNI) and myosin binding protein C (MYBPC), contributes to cardiac pathologies like heart failure. Current therapies, such as beta-blockers and phosphodiesterase (PDE) inhibitors, often lack specificity and have adverse effects. There is a gap in understanding the spatial and temporal dynamics of cAMP signalling within cardiomyocytes. Specifically, the regulation of the myofilament by multiple distinct nanodomains has not been investigated. Similarly, the impact of PKA phase separation on myofilament function is unknown. The goal of this thesis is to address this knowledge gap.

Computational modelling and experimental techniques were used to investigate the regulation of myofilament function. A new human-induced pluripotent stem cell-derived cardiomyocyte (hiPSC-CM) *in silico* electromechanical model was developed to simulate contraction and electrical activity. cAMP and PKA signalling at the myofilament were investigated using expansion microscopy and FRET cAMP sensors targeted to the myofilament proteins, including a newly developed Myomesin-CUTie sensor. The role of PKA condensation was studied using specific disruption methods.

It was found that myofilament proteins are regulated by distinct cAMP signalling domains where cAMP kinetics in response to β adrenergic activation and PDE involvement are different between the MYBPC and TNI sites. PDE4 was found to regulate cAMP at TNI but not the MYBPC site. PKA RIα and RIIβ were found to undergo condensation in cardiomyocytes. Disruption of these condensates did not affect cAMP compartmentalisation at the myofilament but reduced cytosolic cAMP increase following adrenergic stimulation. An increase in PKA RIα condensates was observed in hypertrophic cells, suggesting a potential role in cardiac disease.

Altogether, the study advances understanding of cAMP-PKA signalling at the myofilament, identifying distinct cAMP nanodomains and elucidating the role of PKA phase separation in modulating the adrenergic response. These findings provide insights into cardiac cell physiology and have implications for the development of more targeted therapies for cardiac dysfunction. The computational models offer a platform for investigating drug effects on cardiac function aiding cardiovascular drug development.

Declaration

I declare that this thesis is my own work, except when stated otherwise. The contents of this work are original and have not been submitted for consideration for another degree or qualification.

Acknowledgements

I would like to acknowledge the people who were instrumental in making this thesis possible. This work would not have been achieved without the support of my supervisors. I want to thank Manuela Zaccolo for advising and guiding me through every step of the project. Her unwavering support in all of my endeavours, applications, and personal development has been invaluable. Her mentorship has allowed me to grow as a person first, and as a scientist second, teaching me critical thinking, insight, and leadership. The time I've spent in the lab has been an incredibly rewarding experience, and I am extremely grateful for the stimulating conversations, her patience in listening to my experimental suggestions, however implausible, and my far-fetched ideas. I am also thankful for the many opportunities I had to learn and share my work, from visits to UCSD and the University of Sheffield, to scientific training courses, teaching experiences, and conferences. Her enthusiasm and encouragement have been a source of motivation to me, pushing me, and the project, forwards.

I am truly grateful to my supervisors Blanca Rodriguez and Xin Zhou for guiding me through my computational work. Their expertise helped me form a new approach to scientific problems and learn to apply computational solutions to physiological questions. I am thankful for the opportunities I had to learn more, especially during the conference in Oxford and the summer school at the Simula Institute and UCSD. It has been a privilege to feel like a part of both the Rodriguez and Zaccolo groups.

I want to thank all the current and past members of both groups for their support over the years. Special thanks to Alex, Andreas, Anna, Inky, Emily, Ester, Rahul, and Yvette for their support, teaching, patience, and friendship. Working with them has been incredibly rewarding, especially Anna and Ester, who made me feel that I was not pursuing my DPhil alone but rather that we were all working on our DPhils together. Many thanks to everyone in the Computational Cardiovascular Science team for insightful conversations, great times in Gandia, and useful advice on the project. I would also like to thank Prof. Hulley for her consistently positive attitude and delightful conversations at College, which always left me feeling uplifted and inspired.

I would like to express my deepest gratitude to the British Heart Foundation and Willson and Olegario Philanthropy for funding my studentship. I am incredibly

fortunate to have been given this opportunity. I also thank St Hilda's College for their travel grants. Many thanks to my graduate tutors and fellow students in the BHF programme, who have made my DPhil journey both possible and enjoyable.

I would like to thank all of my friends from St Hilda's, Oxford (especially The Oxford Scientist), my undergraduate years, and home for being there when I needed it most. Thanks to Justas for the support.

I would also like to thank my family. I am immensely grateful to my parents, Ruta and Tomas, and my sister Rugile for their love, understanding, and help. Completing my DPhil would have been incredibly difficult without them.

Contents

List of Figures **xiii**

List of Tables **xv**

List of Abbreviations **xvii**

1 Introduction **1**

1.1 Cardiac structure and function 1

1.1.1 Structure of the cardiomyocyte 2

1.1.2 Electrophysiology of a cardiomyocyte 8

1.1.3 The mechanism of cardiac muscle contraction 9

1.2 Cardiac cell contraction regulation: cAMP and PKA 12

1.2.1 cAMP signalling 12

1.2.2 cAMP-dependent PKA signalling 21

1.2.3 cAMP-PKA signalling compartments at the myofilament . . 28

1.2.4 Challenges in studying cAMP-PKA signalling compartmentalisation 32

1.2.5 Liquid-liquid phase separation of PKA 38

1.3 Myofilament signalling in health and disease 40

1.4 Model systems in cardiac cell signalling research 42

1.4.1 Researching cardiovascular signalling using animal models . 42

1.4.2 Advantages and limitations of hiPSC-CM cardiovascular studies 45

1.4.3 Computer modelling and simulation for studying myofilament function 47

1.5 Thesis Aims 52

2 Methods **55**

2.1 Experimental Materials and Methods 55

2.1.1 Reagents 55

2.1.2 HEK293T and hiPSC-CM culture 56

2.1.3 Primary Rat Ventricular Cardiomyocyte Isolation and Culture 56

2.1.4 Plasmids 58

2.1.5 Transfection and Infection 58

2.1.6 In vitro hypertrophy and cell size measurements 59
2.1.7 Fluorescence Resonance Energy Transfer (FRET) 59
2.1.8 Immunofluorescence 60
2.1.9 Western blotting and co-immunoprecipitation 61
2.1.10 Data and Statistical Analysis 63

3 cAMP signalling domains at the myofilament 65
3.1 Introduction 65
3.2 Methods 69
3.2.1 FRET biosensors 69
3.2.2 Expansion Microscopy 70
3.3 Results 71
3.3.1 Phosphorylation patterns across the sarcomere 71
3.3.2 Development and characterisation of the myofilament FRET sensors 76
3.3.3 Investigation of cAMP signalling from Z to M line 79
3.3.4 PDE signalling across the sarcomere in NRVMs 81
3.3.5 Characterisation of the PDE involved in the regulation of cAMP signal at the sarcomere 83
3.3.6 PDE signalling and adrenergic stimulation 86
3.3.7 PDE4 at the sarcomere 89
3.3.8 PDE4 and TNI interaction 92
3.3.9 PDE4 signalling sequestration at the myofilament: role of PKA and AKAPs 94
3.4 Discussion 98
3.4.1 Limitations 103
3.5 Conclusions 104

4 PKA condensation and control of cAMP signalling at the myofilament 105
4.1 Introduction 105
4.1.1 cAMP buffering by PKA condensation 105
4.1.2 Challenges in studying protein LLPS 108
4.1.3 Open questions in PKA condensation research 109
4.2 Methods 112
4.2.1 Cell culture 112
4.2.2 Plasmids, FRET biosensors, and imaging 112
4.2.3 PKA condensation modulating agents 112
4.2.4 PKA puncta counting methods 113
4.2.5 PDE activity assay 113

4.2.6 *In silico* protein disorder predictions . . . 113
4.2.7 PKA condensation *in vitro* . . . 114
4.2.8 Statistical analysis . . . 114
4.3 Results . . . 115
4.3.1 PKA condensation in HEK293T cells . . . 115
4.3.2 PKA puncta are dynamic . . . 116
4.3.3 PKA condensates as cAMP buffers . . . 120
4.3.4 1,6-HEX affects PDE activity *in vitro* . . . 123
4.3.5 Manipulation of PKA-AKAP interaction affects PKA phase separation . . . 125
4.3.6 PKA condenses in cardiomyocytes . . . 132
4.3.7 PKA puncta are dynamic in cardiomyocytes . . . 132
4.3.8 PKA condensation does not impact cAMP compartmetalisation and cAMP signalling at the myofilament . . . 135
4.3.9 PKA condensation enables adrenergic signal transduction in the cytosol of NRVMs . . . 138
4.3.10 PKA condensation effects on the ACs and PDEs in NRVM . 141
4.3.11 Attenuated cAMP signal after the disruption of PKA condensation involves PDE8 activation . . . 142
4.3.12 PKA condensation in hypertrophic cardiomyocytes . . . 147
4.3.13 Technical considerations when measuring cAMP signalling . 150
4.4 Discussion . . . 155
4.4.1 Limitations . . . 159
4.5 Conclusions . . . 159

5 In silico human induced pluripotent stem cell derived cardiomyocyte electromechanical modelling 161
5.1 Introduction . . . 161
5.2 Methods . . . 162
5.2.1 hiPSC-CM electro-mechanical model coupling and calibration 162
5.2.2 hiPSC-CM electromechanical model calibration and experimental evaluation . . . 170
5.2.3 Simulation protocols . . . 177
5.3 Results . . . 177
5.3.1 Experimental evaluation of the hiPSC-CM electromechanical model . . . 177
5.3.2 Comparison of hiPSC-CM and human adult cardiomyocytes 181
5.4 Discussion . . . 184
5.4.1 Limitations . . . 185
5.5 Conclusions . . . 186

6 Investigating the mechanisms regulating contraction with hiPSC-CM electromechanical modelling and simulation 187
6.1 Introduction . . . 187
6.2 Methods . . . 188
6.2.1 *In silico* drug assay design . . . 189
6.2.2 Experimental data for the evaluation of the *in silico* drug trials 190
6.2.3 Simulation protocols . . . 191
6.3 Results . . . 192
6.3.1 Simulation of drug-induced inotropic effects agree with experimental hiPSC-CM data . . . 192
6.3.2 Comparison of simulated drug-induced inotropic effects with clinical and adult cell experimental data . . . 193
6.3.3 Comparing experimental and simulated drug inotropic effects in paced hiPSC-CMs . . . 196
6.3.4 Inotropic drug effects are affected by the hiPSC-CM cell pacing mode . . . 197
6.4 Discussion . . . 203
6.4.1 Limitations . . . 206
6.5 Conclusions . . . 206

7 Discussion 209

8 Conclusions 215

Appendices

A Appendix 219
A.1 cAMP signalling at the myofilament . . . 219
A.2 PKA phase separation . . . 220
A.2.1 Endogenous PKA RIα phase separation . . . 220
A.2.2 PDE8 localises at the membrane in HEK293T cells . . . 220

B Appendix 223
B.1 IC50 and Hill coefficients for *in silico* drug trials . . . 223
B.2 Simulations of cell activity following duloxetine application in paced cells . . . 238

Bibliography 239

List of Figures

1.1 Sarcomere structure and function. 4
1.2 Different cAMP nanodomains execute βAR signalling in cardiomyocytes. 14
1.3 PDEs have a conserved catalytic domain with pronounced differences in their N terminus responsible for distinct sub-cellular localisation. 16
1.4 Schematic representation of PKA RIα and RIIβ domains. 23
1.5 cAMP signalling domains at the myofilament. 26
1.6 A schematic outlining the spacing in the sarcomere. 29
1.7 A schematic outlining the positioning of TNI and MYBPC at the sarcomere. 31

2.1 Schematic representation of different types of FRET biosensors used. 60

3.1 Calcium gradients across the sarcomere. 66
3.2 Expansion microscopy enables visualisation of the spatial distribution of phosphorylated troponin I across the sarcomere in ARVMs. . . . 72
3.3 Quantification of phospho-troponin I distribution in ARVM samples. 75
3.4 Characterisation of the FRET sensors. 78
3.5 cAMP response following stimulation with ISO differs between TNI, MYBPC, and MYOM sites at the myofilament. 80
3.6 cAMP signalling across the sarcomere. 82
3.7 PDE contribution to determining cAMP levels at the myofilament in basal conditions. 85
3.8 PDE signalling and adrenergic stimulation. 88
3.9 PDE4 signalling differs between TNI and MYBPC domains. 91
3.10 PDE4 expression and interactions in hiPSC-CMs. 93
3.11 cAMP regulation at the myofilament in health and disease. 96

4.1 Schematic representation of PKA RIα biomolecular condensates. . 107
4.2 Appearance of puncta-like PKA structures in HEK293T cells. . . . 116
4.3 PKA puncta are dynamic in HEK293T cells. 119
4.4 cAMP is sequestered inside the RI condensates. 122
4.5 1,6-HEX inhibits PDE activity *in vitro*. 124

4.6 Investigation of LLPS of other proteins in cAMP signalling cascade. 126
4.7 RIα phase separates *in vitro*. 129
4.8 PKA-AKAP interactions control PKA LLPS. 131
4.9 Representative images of PKA localisation in cardiomyocytes. . . . 133
4.10 PKA puncta in NRVMs are dynamic. 134
4.11 HT31 and 1,6-HEX treatment does not affect the adrenergic cAMP signal in the compartments at SR, plasmalemma, and myofilament. 137
4.12 HT31 and 1,6-HEX diminishes adrenergic cAMP signal in the NRVM cytosol. 140
4.13 PKA condensation disruption affects ACs and PDE activity. 142
4.14 PDE8 is activated in cells with HT31. 145
4.15 PDE8 localisation in NRVM. 147
4.16 PKA RIα condensation is increased in hypertorphy. 149
4.17 Technical considerations for studying PKA condensation disruption effects with FRET sensors. 153

5.1 Schematic representation of hiPSC-CM electromechanical model (iCEM). 164
5.2 Experimental evaluation of the electromechanical hiPSC-CM model. 179
5.3 The differences between hiPSC-CM electromechanical (iCEM) and adult contractility (Land), and adult electrophysiology (ToR-ORd-Land) models. 182

6.1 Simulation of calcium transients and active tension changes induced by 7 reference compounds in group 1 are in a qualitative agreement with experimental data. 193
6.2 Comparison of the simulated inotropic effects from the electromechanical model with experimental and clinical data from various cell types. 195
6.3 Comparison of experimental and simulation calcium data. 198
6.4 Paliperidone effects on AT and CaT are dependent on pacing. . . . 199
6.5 Paliperidone-induced changes are dependent on the cell beating rate. 201
6.6 The effects of paliperidone are beating rate-dependent. 202

A.1 Secondary antibody staining control. 219
A.2 HEK293T-RI cells transfected with FlouSTEP sensors. 220
A.3 HEK293T cells expressing PDE8-RFP and PKA RIα-GFP. 221

B.1 Duloxetine, a serotonin-norepinephrine reuptake inhibitor, is predicted to induce a negative inotropic effect. 238
B.2 Simulations predict duloxetine and paliperidone effects on hiPSC-CM AP, CaT, and active tension at 20^{o}C in paced cells (0.5Hz). 238

List of Tables

1.1 cAMP-degrading, heart-expressed PDE signalling specificity arises from their intrinsic differences in kinetics and substrate specificity. . 18
1.2 Different components of published cardiomyocyte electromechanical models. 51

2.1 The list of plasmids used. 58
2.2 The list of FRET biosensors used. 61
2.3 The list of the antibodies used. 62

5.1 Model parameters fitted in the calibration process. 169
5.2 The summary of the experimental data used for model calibration. . 172
5.3 The summary of the experimental data used for model validation. . 174
5.4 Active tension, calcium transient, and action potential biomarker values simulated using hiPSC-CM electromechanical and other models. 180

B.1 IC50 and Hill coefficient (h) values used as inputs for the in silico drug trials. 224

List of Abbreviations

AC . . . . . adenylyl cyclase

ADP . . . . . adenosine diphosphate

AKAP . . . . . A kinase anchoring protein

AMP . . . . . adenosine monophosphate

AP . . . . . action potential

APD . . . . . action potential duration

ARVM . . . . adult rat ventricular myocyte

AT . . . . . active tension

ATP . . . . . adenosine triphosphate

β**AR** . . . . . beta adrenergic receptor

C . . . . . PKA catalytic subunit

cAMP . . . . . cyclic adenosine 3,5-monophosphate

CaT . . . . . calcium transient

cGMP . . . . . cyclic guanosine 3,5-monophosphate

CNB . . . . . cyclic nucleotide binding

CNGC . . . . . cyclic nucleotide-gated channels

D/D . . . . . dimerisation docking domain

DCM . . . . . dilated cardiomyopathy

DRX . . . . . disordered relaxed state

EFTPCmax . maximal effective free therapeutic concentration

EPAC . . . . . exchange protein-activated by cAMP

ExM . . . . . expansion microscopy

FRAP . . . . . fluorescence recovery after photobleaching

FRET . . . . . Fluorescence resonance energy transfer

GPCR . . . . . G-protein coupled receptor

HEX 1,6-hexanediol

HF . . . . . heart failure

HFpEF . . . . heart failure with preserved ejection fraction

HFrEF . . . . . heart failure with reduced ejection fraction

hiPSC-CM . . human induced pluripotent stem cell derived cardiomyocyte

IBMX 3-isobutyl-1-methylxanthine

IC50 . . . . . inhibitory concentration 50%

IDR . . . . . intrinsically disrodered region

INaL . . . . . 'late' sodium current

iCEM . . . . . integrated Cardiomyocyte Electromechanical Model

IS . . . . . inhibitory sequence

ISO . . . . . isoproterenol

LLPS . . . . . liquid-liquid phase separation

LTCC . . . . . L-type calcium channels

MYBPC . . . cardiac myosin-binding protein C

MYOM . . . . myomesin

NRVM . . . . neonatal rat ventricular myocyte

PDE . . . . . phosphodieasterase

PKA . . . . . protein kinase A

PKD . . . . . protein kinase D

PKG . . . . . protein kinase G

PL . . . . . plasmalemma

POPDC . . . . Popeye domain-containing proteins

PP . . . . . phosphatase

PTM . . . . . post-translational modification

R . . . . . PKA regulatory subunit

RNP . . . . . ribonucleoprotein particles

RT . . . . . room temperature

RT50 . . . . . time to 50% relaxation

RyR . . . . . ryanodine receptor

SERCA . . . . sarcoplasmic reticulum ATPase

SG . . . . . stress granule

SR . . . . . sarcomplasmic reticulum

SRX . . . . . super-relaxed state

TNC . . . . . cardiac troponin C

TNI . . . . . cardiac troponin I

TNT . . . . . cardiac troponin T

TP . . . . . time to peak active tension

1 Introduction

1.1 Cardiac structure and function

The heart is responsible for pumping blood, enabling its circulation throughout the body, delivering oxygen and nutrients to tissues while removing waste products. The heart is divided into four chambers: two atria and two ventricles. The right atrium receives deoxygenated blood from the body and pumps it into the right ventricle, which then sends the blood to the lungs. The left atrium receives oxygenated blood from the lungs and pumps it into the left ventricle, which then sends the oxygenated blood to the systemic circulation via the aorta.

The heart functions as a coordinated pump. Its contraction and relaxation is regulated by a conduction system permitting electrical signal transmission throughout the heart. This system consists of the sinoatrial node, atrioventricular node, bundle of His, and Purkinje fibers. The sinoatrial node acts as the natural pacemaker initiating electrical impulses that cause the atria to contract. The electrical signal then travels to the atrioventricular node, from where it is transmitted through the bundle of His and Purkinje fibers, leading to the synchronized contraction of the ventricles. This carefully orchestrated sequence ensures efficient blood flow and cardiac output.

The heart is composed of three primary layers: the endocardium (innermost layer), myocardium (middle layer), and epicardium (outermost layer). The myocar-

dium consists primarily of cardiomyocytes and is responsible for the heart's contraction. Surrounding the myocardium is the epicardium which is continuous with the pericardium, a protective sac that encloses the heart.

1.1.1 Structure of the cardiomyocyte

The cardiac myocardium is highly organized and composed of various cell types, including cardiomyocytes, fibroblasts, and smooth muscle cells. Cardiomyocytes are characterised by a distinct cellular structure, typically containing one or multiple nuclei, and are encapsulated by a cell membrane known as the sarcolemma. The sarcolemma forms invaginations called T-tubules that facilitate the rapid propagation of electrical signals deep within the cell.

Cardiomyocytes are densely packed with mitochondria, accounting for about 30-40% of the volume in adult cardiac cells, which supply adenosine triphosphate (ATP), necessary for contraction [1]. The sarcoplasmic reticulum (SR) surrounds the contractile structures within the cell, playing a crucial role in calcium storage and regulation, essential for cardiomyocyte function.

Cardiomyocytes contain myofibrils that make up about 40% of the cell volume [2]. Myofibrils are insoluble protein filament bundles that contain cardiac muscle contraction machinery. Each myofibril exhibits a characteristic striated appearance due to its banding pattern, visible under a light microscope as alternating light and dark transverse bands.

The sarcomere, approximately 1.6–2.0 µm in length, is the functional unit of myofibril, responsible for generating forces in the myocardium [2]. Besides proteins actin, myosin, and titin, which make up the thin, thick, and elastic filament system, respectively, more than 200 proteins populate the cardiac sarcomere and are continuously and dynamically assembled, modified, and degraded to maintain and adapt the contractile properties of the cardiomyocyte (Fig. 1.1) [3]. The sarcomere is thought to have a rigid composition where myosin, which forms thick filaments with globular heads, can bind to actin, which forms thin filaments. Myosin and actin filaments are anchored to the Z-disc at the borders of each sarcomere. The

largest protein in human proteome, titin, spans the whole sarcomere, stabilising the contractile apparatus and contributing to the elasticity of the cardiac muscle.

The structural properties of sarcomeric proteins and their arrangement are central to cardiac contraction. Sarcomeres are connected to sarcolemma by T-tubules which speed up the rate of depolarization within the sarcomere. Universally, a mature cardiac sarcomere is a regular hexagonal lattice of thin filaments attached to the Z-disk and thick filaments interconnected in the middle of the sarcomere via the M-band [4]. Sarcomeres are connected to each other in series at the Z-disk and arranged in parallel to form bundles of myofibrils about 1 µm in diameter. Sliding of thick and thin filaments relative to each other results in muscle contraction. Different regions within the sarcomere can be identified:

- A bands (or anisotropic bands): dark bands containing the thick filament.
- I bands (or isotropic bands): light bands containing the thin filament. The thin filament lies between the two thick filaments.
- Z line: area where two thin filaments connect and transverse the I bands.
- M line: contains protein myomesin and marks the centre of the sarcomere.
- H zone: area between the M line and Z disc containing myosin (thick filament) only.
- C zone: region of the A band containing myosin binding protein C (MYBPC) between the edge of I band and H zone.

The thick filament in cardiac muscle primarily consists of myosin. Myosin is a part of a larger superfamily that includes 18 classes of myosin motors. In the heart, the class II myosins, MYH6 and MYH7, known as cardiac myosin heavy chain isoforms, are crucial. Despite being 93% identical, these isoforms exhibit distinct functional properties; MYH6 has higher ATPase activity, whereas MYH7 generates greater force [6]. Three-dimensional studies have revealed that two myosin heads can pack together to form an interacting-heads motif. This configuration

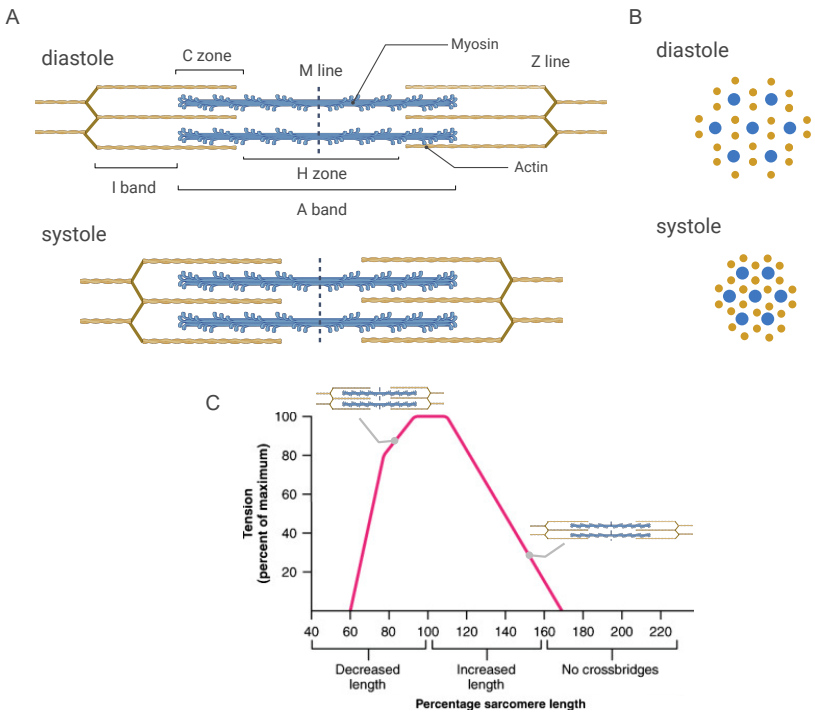


Figure 1.1: Sarcomere structure and function. **A.** Schematic of a sarcomere in diastole (top) and systole (bottom). The sarcomere consists of proteins lined out from Z line to M line, including actin (gold) and myosin (blue). Sarcomere length changes during contraction. **B.** Cross-sectional view of the sarcomere in diastole (top) and systole (bottom). **C.** Length-tension relation (Frank-Starling Law) in the sarcomere. Adapted from Rowen at al. (2020) [5] (CC BY 4.0).

is typically observed in relaxed muscles and is conserved across various species and muscle types. In this relaxed state, myosin can adopt two conformations: disordered relaxation (DRX), where one myosin head is folded, and super relaxation (SRX), where both heads are folded back along the thick-filament backbone [7]. The latter state conserves energy by keeping myosin heads inactive unless needed for increased mechanical action.

Central to the regulation of myosin activity within the sarcomere is cardiac myosin-binding protein C (MYBPC), a sarcomeric 140 kDa protein encoded by the *MYBPC3* gene. Positioned in the C-zone of each half A band, MYBPC features eight immunoglobulin-like domains and three fibronectin type-III domains, extending from the N-terminus to the C10 domain [8]. Its interaction with both myosin and titin helps maintain sarcomeric structure and regulates cardiac contraction

and relaxation. The N-terminal domain, particularly the C0–C2 domains, play a pivotal role in modulating the activity of the thick filament proteins, influencing myosin head movement and force generation. MYBPC phosphorylation by PKA can shift myosin heads from the SRX to the more active DRX state, enhancing the potential for force production [9].

Furthermore, MYBPC also interacts with the thin filament, particularly actin, through its N-terminal domain. This interaction can activate the thin filament, similar to the effects of increased calcium levels or strong myosin cross-bridge binding, leading to enhanced muscle contraction [10]. Interestingly, electron microscopy studies have shown that the N-terminus of MYBPC can shift the position of tropomyosin to the 'open' state, facilitating increased activation of the thin filament even at low calcium levels [10]. MYBPC can directly interact with cardiac troponin I (TNI) *in vitro*, in a phosphorylation- and calcium-dependent manner [11].

The thin filament consists of a double-stranded helix of actin (F-actin), two tropomyosin strands, and the three troponin subunits: troponin T (TNT), TNI, and troponin C (TNC). These components form the calcium-regulatory complex essential for muscle contraction. Tropomyosin strands provide stability, flexibility, and cooperativity as they lie within the grooves of actin.

The complexity of troponin was unraveled in the late 1960s when it was first fractionated into distinct proteins, leading to the identification of its subunits [12]. The devised nomenclature was based on the functional properties exhibited by these identified subunits. Subunit which inhibited activity of the Mg^{2+}-dependent actomyosin ATPase in the absence of calcium was named 'I' for inhibitory. TNI, approximately 24 kDa protein, by inhibiting the ATPase, prevents actin-myosin interactions and cross-bridge formation when calcium is low. TNT, about 37 kDa, binds to tropomyosin (hence named 'T') and serves as a mechanical link between tropomyosin and the troponin complex. TNC, approximately 20 kDa, is the calcium-binding subunit (and so, named 'C') that regulates the activation of the thin filament.

Given the large amount of cell volume occupied by myofilaments, it is important to note that TNC acts as a calcium buffer. About 99% of the cytoplasmic calcium

in cardiac myocytes is bound to buffers [13]. In fact, TNC, with a concentration of around 70 µM in the cardiomyocyte cytoplasm, buffers the majority of calcium in cardiac cells [13]. It is estimated that myofilaments alone can bind >90% of the total calcium and TNC buffering capacity is significantly greater than that of SR calcium ATPase (SERCA) and calmodulin [13]. TNC has different calcium binding sites: lower-affinity and high-affinity sites that can also bind Mg^{2+}. Despite TNC being an important calcium buffer at low calcium concentrations, when calcium increases to micromolar concentrations, different calcium buffers dominate [14].

Both TNI and TNT have specific cardiac and skeletal isoforms, while they share a common isoform of TNC found in slow-twitch skeletal muscle (ssTNC). In the adult heart, cardiac TNI and cardiac TNT are expressed along with c/ssTNC [15]. Certain TNI and TNT isoforms, referred to as foetal isoforms, are down-regulated postnatally but can be re-expressed under pathological conditions.

TNI is critical in regulating myofilament activation and inactivation. It has two actin-interacting sites: the inhibitory region and an additional actin-tropomyosin binding site. The inhibitory region is highly conserved across species and rich in basic amino acids. Upon calcium binding to TNC, TNI shifts to allow the hydrophobic patch of the N-terminal region of TNC's to become exposed, facilitating the removal of TNI's inhibitory arm from the actin-tropomyosin interface, thereby exposing myosin binding sites on actin [15]. This interaction is crucial for force development in cardiac muscle, and even minor amino acid changes can impair function. The regulation of this mechanism is further fine-tuned by post-translational modifications (PTMs) such as phosphorylation.

Another protein within the sarcomere fine-tuned by PTMs is titin, spanning from the Z line to the M line. It provides a structural and scaffolding function, among others. Titin is essential for passive tension generation and acts as a molecular spring [16]. The titin region located in the I-band is extensible and consists of immunoglobulin-like domains arranged in tandem, the PEVK sequence (rich in proline, glutamate, valine, and lysine residues), and the N2B element. Each functions as a distinct spring element in series [16].

Finally, within the sarcomere, a large number of accessory proteins provide structural, mechanical, signalling, and transport functions, primarily localising to the Z line and M band (region that encompasses the M line). These proteins dynamically respond to intra- and extra-cellular signals, indicating a specialised location-dependent role. Z-disk proteins include α-actinin, which cross-links anti-parallel actin filaments, filamin C, titin muscle LIM protein, telethonin, myopalladin, nebulette, nexilin, desmin, obscurin, alpha-beta crystallin, myotilin, alpha-actinin associated LIM protein (ALP), Z-band Alternative Spliced PDZ motif (ZASP), and filamin-, α-actinin-, and telethonin-binding protein of the Z-disk (FATZ) [17].

The M band, previously understood through low-resolution models, has emerged as a complex compartment involved in signalling and possibly triggering mechano-sensitive responses. It maintains the transverse hexagonal lattice of myosin filaments and supports the centering and alignment of the A band during muscle contraction and relaxation. This is achieved through a dense network of specialised proteins comparable in complexity and functionality to those of the Z line [17]. Proteins like obscurin, small ankyrin-1, and telethonin localise in both, the Z-disc and M-band [18].

Electron micrographs have detailed the architecture of the M-band, displaying vertical, electron-dense lines known as M-lines. Five major M-lines can be resolved in striated muscle with a central to the sarcomere M1 line and two consecutive lines on each side at 22 nm intervals, known as M4/M4' and M6/M6' lines. Myomesin-1 and the muscle isoform of creatine kinase localise mainly on the M4/M4' lines. Myomesin-2 is more pronounced on the M1 line in fast skeletal and cardiac muscles [18].

Despite its fundamental role, the M-band is the least studied part of the sarcomere. The M-lines are mainly containing the ubiquitously expressed proteins, myomesin-1, the muscle isoform of creatine kinase, and the C-terminal part of titin [18]. The N-terminal domain of myomesin-1 binds to myosin via an interaction that is not yet completely understood. However, it appears to be essential for keeping the thick filaments in functioning properly.

1.1.2 Electrophysiology of a cardiomyocyte

Cardiac contraction is initiated by an electrical signal generated in the sinoatrial node. Sinoatrial cells have an intrinsic pacemaker ability, allowing them to spontaneously depolarise and generate action potentials. An action potential is a rapid, transient change in the electrical potential across the cell membrane of excitable cells. The resting membrane potential of sinoatrial nodal cells is typically around -60 mV [19], primarily determined by the ratio of intracellular-to-extracellular potassium (K^+) as described by the Nernst equation:

$$E_{\text{ion}} = \frac{RT}{zF} \ln \left(\frac{[\text{A}]_{\text{out}}}{[\text{A}]_{\text{in}}} \right)$$

where E_{ion} is the equilibrium potential for the ion, R is the universal gas constant, T is the temperature in Kelvin, z is the valence (charge) of the ion, F is the Faraday constant, and $[\text{A}]_{\text{out}}$ and $[\text{A}]_{\text{in}}$ are the concentrations of the ion A outside and inside the cell, respectively.

This process of action potential generation and propagation can be further understood through the Hodgkin-Huxley model. It describes the membrane potential accounting for the contributions of three ion channels. The basic form of the Hodgkin-Huxley equation for membrane potential is

$$C_m \frac{dV}{dt} = I_{Na} + I_K + I_{leak}$$

where C_m is the membrane capacitance, I_{Na}, and I_K, are the ionic currents through the respective channels, and I_{leak} represents the leakage current. This model provides a quantitative description of how action potentials are initiated and how they propagate through the cardiac tissue. Hodgkin–Huxley descriptions of ion channels are widely used to model ion channels in the heart and further extensions of the model have been developed [20].

The membrane potential at any given time is influenced by the relative concentrations of ions inside and outside the cell, as well as the membrane's permeability to these ions. In sinoatrial cells, a small, slow inward Na^+ current, known as the

funny current (I_f), plays a crucial role in pacemaker activity. Unlike typical sodium channels, these I_f channels are unique in that they open during hyperpolarisation rather than depolarisation, contributing to the gradual depolarisation that eventually leads to the threshold for firing an action potential.

Voltage-gated calcium (Ca^{2+}) channels are involved in the upstroke of the action potential in sinoatrial node cells. In non-pacemaker atrial myocytes, this Ca^{2+} influx directly initiates contraction. Following the upstroke, L-type (long-lasting) Ca^{2+} channels close, and voltage-gated K^+ channels open, leading to membrane repolarisation. This hyperpolarisation triggers the reopening of I_f channels, starting the process again.

The action potential generated in the sinoatrial node is propagated throughout the heart. Unlike pacemaker cells, ventricular myocytes have a stable resting membrane potential. They rely on the arrival of an action potential to initiate depolarisation. In ventricular myocytes, the action potential begins with the rapid opening of voltage-gated sodium (Na^+) channels, leading to a quick depolarisation. This is followed by the opening of L-type Ca^{2+} channels, which sustain the depolarisation and initiate contraction. As the Na^+ and Ca^{2+} channels close, voltage-gated K^+ channels open, repolarising the membrane and returning it to its resting potential.

A key feature of ventricular myocytes is the refractory period, during which they cannot initiate another action potential due to the inactivation of Na^+ channels. This refractory period is significantly longer in ventricular myocytes than in skeletal muscle cells, preventing tetanic contractions and ensuring that the ventricles have time to relax and fill with blood before the next contraction.

1.1.3 The mechanism of cardiac muscle contraction

The sarcomere, composed of myosin thick filaments and actin thin filaments, enables cardiac muscle contraction. According to the sliding filament model [21], myosin heads attach to actin, forming cross-bridges that enable the sliding of filaments,

leading to sarcomere shortening and contraction (Fig. 1.1). At the functional level, the myosin head interacts directly with two adjacent actin monomers.

In the relaxed state, tropomyosin blocks the myosin-binding sites on actin filaments, preventing cross-bridge formation. When Ca^{2+} binds to troponin C (TNC), it induces a conformational change in the troponin complex, causing tropomyosin to shift and expose the myosin-binding sites, allowing myosin heads to interact with actin. This process initiates the chemomechanical cycle of actomyosin interactions, powered by ATP hydrolysis. ATP binds to the myosin head in its relaxed state, priming it into a high-energy conformation. The hydrolysis of ATP releases adenosine diphosphate (ADP) and inorganic phosphate, which triggers a strong binding of the myosin head to actin. This binding drives the power stroke, where a conformational change causes the myosin neck region to bend, pulling the actin filament towards the center of the sarcomere. The cycle resets when a new ATP molecule binds to myosin, causing it to detach from actin and return to its resting state. Together, these events illustrate excitation-contraction coupling, where an action potential triggers calcium entry into the sarcoplasm, initiating the biochemical and mechanical processes leading to contraction.

The contraction process is initiated by an action potential that triggers the opening of L-type Ca^{2+} channels (LTCC) in the T-tubules, invaginations of the sarcolemma that penetrate deep into the cell. The resulting influx of Ca^{2+} into the sarcoplasm triggers further Ca^{2+} release from the SR via ryanodine receptors (RyR), a process known as calcium-induced calcium release. The significant elevation in intracellular Ca^{2+} concentration allows Ca^{2+} to bind to TNC, reducing the affinity of TNI for actin and exposing myosin-binding sites on the actin filaments, driving contraction.

The development of contraction force in cardiac muscle is dependent on intracellular calcium levels in a non-linear, dynamic manner, largely due to the cooperative behaviour of the myofilaments [22]. Even small changes in intracellular calcium can lead to significant changes in force, a relationship well-captured by the steep

force-calcium dependence observed in cardiac muscle cells. This relationship is commonly described using the Hill equation:

$$F = \frac{1}{1 + 10^{n_H \cdot (\mathrm{pCa}_{50} - \mathrm{pCa})}}$$

where F represents the developed force, pCa is $-\log_{10}[\mathrm{Ca}^{2+}]$, the negative logarithm of the free calcium concentration, and pCa_{50} represents the pCa value at which half-maximal force is produced. n_H is the Hill coefficient indicating the steepness of the curve where the high values of n indicate significant myofilament cooperativity [23]. The calcium sensitivity of the myofilaments, represented by $[\mathrm{Ca}^{2+}_{50}]$, can be modulated by several factors, including muscle stretch, β adrenergic receptor (βAR) signalling, drugs, and mutations associated with cardiac diseases [24].

Relaxation occurs when intracellular calcium decreases, leading to the dissociation of Ca^{2+} from troponin. Tropomyosin subsequently returns to its position over the myosin-binding sites on actin, preventing further cross-bridge cycling. This calcium reduction is achieved through reuptake into the SR via SERCA, extrusion across the sarcolemma through the $\mathrm{Na}^{+}/\mathrm{Ca}^{2+}$ exchanger and Ca^{2+} ATPase, and uptake by mitochondria via the Ca^{2+} uniporter.

The heart can dynamically adjust its function in response to changes in cardiac filling. As venous return increases, the ventricles dilate, stretching the myocardium, which responds by enhancing both contractility and stroke volume. This relationship between the length of cardiac fibers and the force of contraction is crucial for regulating cardiac output. The optimal development of active tension occurs near the resting sarcomere length of approximately 2 µm and varies depending on the length-tension relationship (Fig. 1.1). Increased diastolic filling leads to an increase in sarcomere length, enhancing the tension-generating capacity as more myosin heads bind to actin. Other elements might also contribute to this phenomenon, known as Frank-Starling law, as forces generated by titin may influence the affinity of calcium ions to the negatively charged myofilaments, further affecting contraction [25].

1.2 Cardiac cell contraction regulation: cAMP and PKA

The sympathetic nervous system regulates heart function, particularly during the response to stress or exercise. This regulation is mediated through the activation of β adrenergic receptors (βARs), leading to an increase in intracellular 3,5-cyclic adenosine monophosphate (cAMP). cAMP, in turn, activates protein kinase A (PKA), which phosphorylates a wide range of different proteins in the cell thereby modulating cellular processes including cardiac muscle contraction and relaxation.

cAMP-PKA signalling is vital for fine-tuning heart function through post-translational modifications (PTMs) such as phosphorylation. cAMP signalling plays a crucial role in the coordination of cardiac muscle function through its regulation of the myofilament protein activity, calcium handling, metabolism, gene expression, and other functions of the cell. PKA-mediated phosphorylation of key myofilament proteins, including TNI and MYBPC, adjusts the calcium sensitivity of troponin while enhancing MYBPC activity, thus accelerating cross-bridge kinetics.

1.2.1 cAMP signalling

cAMP, a ubiquitous second messenger produced in response to the βAR signalling, modulates cardiac contraction and relaxation, as well as multiple other biological responses such as gene expression and regulation of metabolic pathways. cAMP can act through different effector proteins: PKA, exchange protein-activated by cAMP (EPAC), cyclic nucleotide-gated channels (CNGC), and Popeye domain-containing (POPDC) proteins.

cAMP is a second messenger synthetised by adenylyl cyclases (AC) that can be activated in response to stimulation of G protein-coupled receptors (GPCRs) coupled to the AC-stimulating G protein Gs. Gi-coupled GPCRs, on the other hand, activate the inhibitory G protein Gi that inhibits AC activity.

cAMP activates PKA, which modulates contractility by phosphorylating several proteins. PKA phosphorylation of Rad, a monomeric G-protein near LTCC, increases the open probability of LTCC channels, while phosphorylation of RyR

enhances RyR channel activity, both leading to increased cytosolic calcium levels [26]. Together, this generates a positive inotropic response. cAMP also mediates a lusitropic response through PKA phosphorylation of phospholamban and TNI [27].

PDEs, the cAMP-degrading enzymes, play a key role in the control of cAMP. PDEs degrade cAMP to adenosine monophosphate (5-AMP). PDEs belong to a superfamily of enzymes including 11 families (PDE1–11) and over 100 estimated isoforms. Different PDE isoforms have distinct localisation, allosteric modulation, substrate specificity (for cAMP and/or cyclic guanosine monophosphate (cGMP)), and enzymatic kinetics [27].

cAMP compartmentalisation

To enable hormonal specificity, cAMP signals and the activity of its effectors are compartmentalised in the cell (Fig. 1.2). The spatial and temporal regulation of cAMP signalling was first hypothesised when it was observed that stimulation of GPCR with isoproterenol (ISO), a βAR activator, or with prostaglandin induces different effects despite generating similar levels of cAMP: βAR stimulation promotes cardiac inotropy and lusitropy while activation of the prostaglandin receptor does not [28]. This hormonal specificity was shown to rely on βAR stimulation predominantly activating a subset of type II isoforms of PKA, while prostaglandin primarily activates type I PKA [29].

The heart expresses different types of βAR, including β1, β2, and β3AR, each inducing distinct effects. For instance, activation of β1AR, a predominant isoform in the heart, increases heart rate and cardiac contractility, but chronic stimulation can lead to cardiac remodelling and heart failure (HF). β2AR signalling also regulates heart rate and contractility, can activate non-classical signalling pathways, and its effects are more localised than β1, with activation being cardioprotective [30]. β3AR receptors appear to mediate negative inotropic effects in mice cardiomyocytes [31].

Multiple factors contribute to signal compartmentalisation. For example, activation of β1ARs, but not β2ARs, leads to phosphorylation of phospholamban [32]. This can be attributed to differential localisation of the receptors, as β2ARs

localise predominantly to the T tubules, whereas β1ARs can be found across the entire cell membrane. signalling through distinct AC isoforms also elicits specific effects, likely due to differential localisation of AC isoforms.

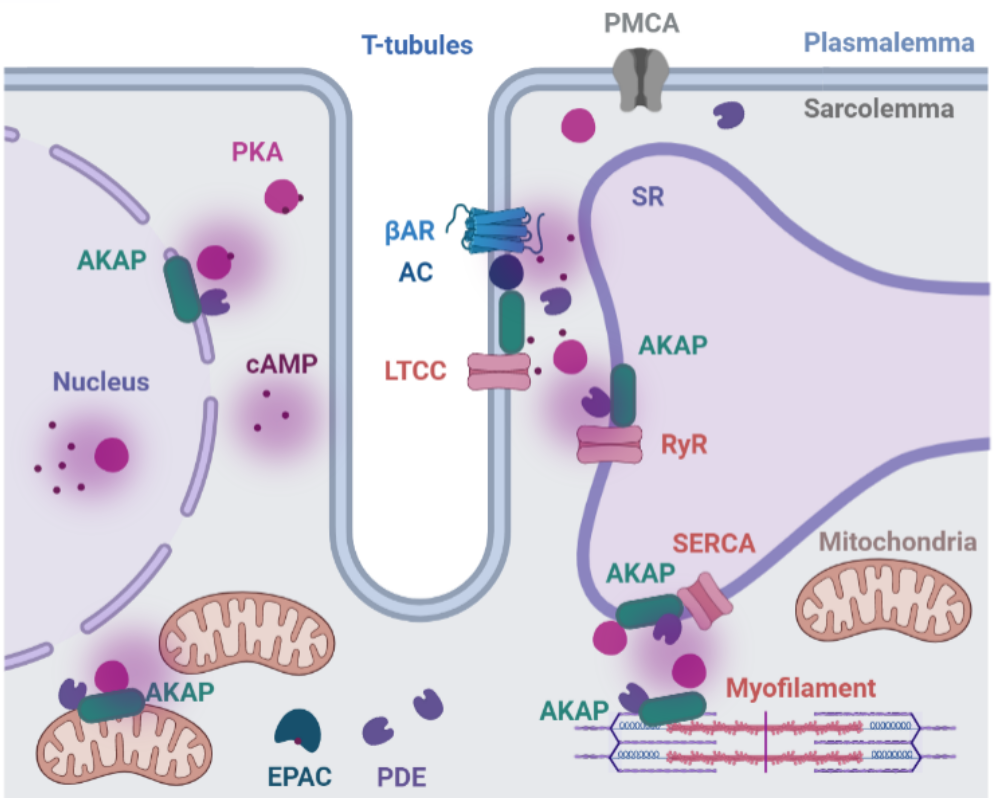


Figure 1.2: Different cAMP nanodomains execute βAR signalling in cardiomyocytes. The presence of multiple cAMP signalling components helps ensure that the correct cellular effects are achieved upon βAR activation. In the schematic, PMCA refers to plasma membrane calcium ATPase, and other abbreviations have been defined before. Adapted from Folkmanaite and Zaccolo (2023) [33].

A significant advancement in understanding cAMP regulation in the heart has been facilitated by fluorescence energy transfer (FRET)-based biosensors. These sensors, when targeted to subcellular sites and used to acquire real-time data in living cells with high spatiotemporal resolution, have allowed for direct observation of cAMP compartmentation and detailed analysis of signal regulation. Targeted FRET sensors have highlighted the role of PDEs in creating distinct subcellular cAMP signalling domains. For instance, cAMP FRET sensors targeted to various subcellular locations revealed that cAMP levels following βAR stimulation are significantly lower at the myofilament compared to other sites such as the SR

and the plasmalemma [34]. Interestingly, these local signalling differences were abolished after PDE inhibition, underscoring the importance of PDE in controlling local cAMP signals.

FRET sensors have been crucial in determining the size of cAMP signalling domains generated by different PDEs. By introducing a linker of varying length between the sensor and the catalytic domain of PDEs, it was shown that different PDEs form cAMP domains of varying sizes. For instance, the catalytic domain of PDE2A3 enzymes created a 30 nm nanodomain with low cAMP, while the catalytic domain of PDE4A1 generated a domain less than 10 nm in diameter [35]. A recent study employed a similar approach to demonstrate that activation of glucagone-like peptide 1 (GLP-1) receptors generates a high cAMP pool extending up to 60 nm in diameter around the receptor [36]. Such spatially restricted cAMP generation upon GPCR stimulation allows for precise activation of downstream pathways and signalling cascades specifically associated with that receptor, thus avoiding cross-activation. Similar nanometre-sized domains were observed at various subcellular sites, including the myofilament, SR, and sarcolemma [37].

PDE-mediated cAMP signalling control

Besides different distribution of GPCRs and ACs, PDEs are thought to be important players in cAMP signal regulation and compartmentalisation. There are clear differences in PDE expression in tissues, substrate specificity, and subcellular localisation. These PDE signatures are important as there appears to be little overlap between the PDE-governed cAMP nanodomains [38, 39]. However, multiple PDEs can act within the same subcellular compartment, perhaps functioning as a multi-layered cAMP degradation mechanism to finely regulate cAMP levels [40, 41]. cAMP-selective PDEs are 4, 7, and 8, and PDEs 1, 2, 3, 10, and 11 have dual specificity. PDEs 1–5 and 8–10 are expressed in the heart (Table 1.1). All PDEs contain a relatively conserved catalytic domain and a highly variable N-terminal domain which usually determines regulation and localisation of the enzyme (Fig. 1.3). Cyclic nucleotides or PDE inhibitors bind the catalytic site [27].

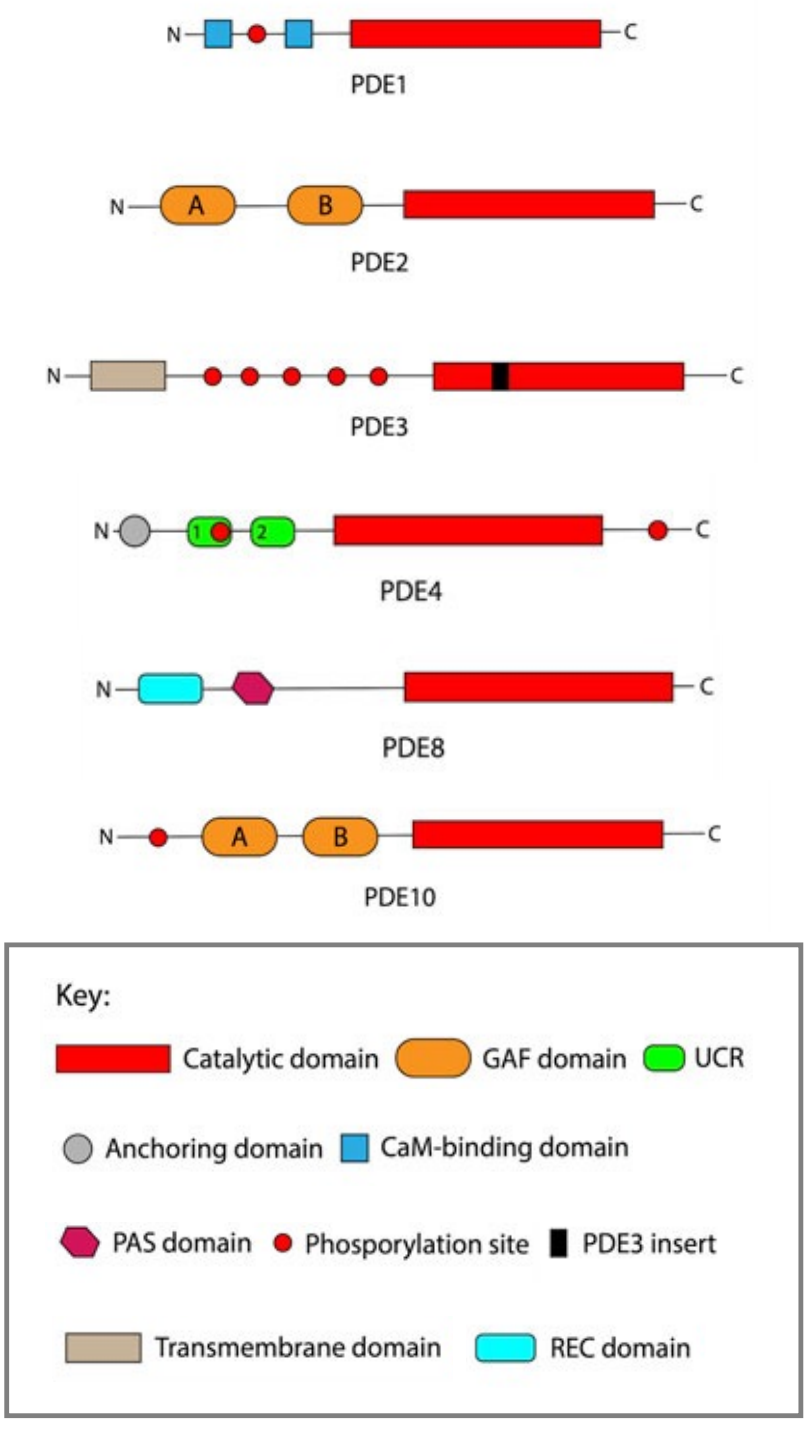


Figure 1.3: PDEs have a conserved catalytic domain with pronounced differences in their N terminus responsible for distinct sub-cellular localisation. Adapted from Bondarev at al. (2022) [42] (CC BY 4.0).

In human hearts, PDE3 and PDE2 appear to be predominant isoforms whereas PDE4-mediated hydrolysis accounts for the majority of the total PDE activity in rat cardiomyoctes [43]. However, the experiments used to determine the contributions of different PDEs measure PDE activity either by the inhibition with 3-isobutyl-1-methylxanthine (IBMX), a pan-PDE (excluding PDE8 and PDE9) inhibitor, or by inhibiting PDEs 1-4 [43]. Therefore, the contribution of PDE8-mediated cAMP hydrolysis remains currently not well established.

Investigations on the role of PDEs on cAMP signalling in the heart suggest that PDE control might not be static, but rather change depending on activation of different signalling pathways. For example, it appears that PDE4 inhibition does not influence TNI phosphorylation in resting rat cardiac myocytes, while PDE4 is reportedly the main PDE that regulates cAMP levels at the TNI cAMP nanodomain upon βAR stimulation [44]. It is unclear, however, if these results translate to human as PDE4 expression is significantly lower in human than in rodent hearts [45].

PDE4 is a cAMP-selective PDE with a low Km (1.2–10 µM). It comprises a family of 20 isoforms encoded by PDE4A, B, C, and D genes, of which all, except PDE4C, are found in the heart [46]. When comparing PDE4 activity between rodent and human hearts, many similarities were found, including a rather similar activity [43]. However, due to higher non-PDE4 activities in human heart, PDE4 is responsible for only 10% of the total cAMP-PDE activity in failing human heart and 50% in normal and failing rat heart [27]. A study on ventricular trabeculae from human failing hearts from patients treated with beta-blocker, carvedilol, showed that inhibiting PDE4 did not affect βAR mediated contractility, while inhibition of PDE3 did [47].

In reports on human, porcine, and rodent cardiac ventricle, βAR-mediated contractility was not enhanced by inhibiting PDE4 alone, despite increased levels of cAMP. Rather, simultaneous inhibition of both PDE3 and PDE4 was needed to obtain an increased contractility, both in normal and failing hearts [27]. Although multiple PDEs can work in synergy, they usually still have well-defined domains, and multiple PDEs can work in synergy in a particular domain [41]. Using *in silico* modelling, Zhao et al. (2015) showed that after ISO stimulation, PDE4 was the most

active phosphodiesterase, while the activities of PDE2 and PDE3 increased to a lesser extent [48]. Inhibition of PDE2 led to an increase in PDE4 activity, and similarly, PDE4 inhibition induced an increase in PDE2 activity, highlighting how PDEs can work in synergy [48]. The model is based on adult rat ventricular myocyte data, and validated against data from mouse, rat, rabbit, and human cardiomyocytes.

Table 1.1: cAMP-degrading, heart-expressed PDE signalling specificity arises from their intrinsic differences in kinetics and substrate specificity. The Km and Vmax values provided are for cAMP.

PDE	**Km, µM**	**Vmax, µmol/min/mg**	**Substrate**	**Ref**
PDE1	72.7-124	10-450	cAMP and cGMP	[49, 50]
PDE2	10-30	20.5	cAMP and cGMP	[51, 52]
PDE3	0.16	6.1	cAMP and cGMP	[53]
PDE4	1.2–10	8.8-37	cAMP	[43]
PDE8	0.04-1.8	6.1	cAMP	[54, 55]
PDE10	0.26-56	0.507	cAMP and cGMP	[56]

PDE8 is a cAMP-selective phosphodiesterase and has two isoforms: PDE8A and PDE8B [54]. PDE8A has a high affinity for cAMP with a Km of 0.04 to 0.15 µM, 40–100 times lower than that of PDE4. It is likely that PDE8 functions at lower cAMP concentrations than PDE4 and may thus be involved in the control of intracellular cAMP concentrations at basal levels and in the immediate response to acute increases of cAMP in specific cell regions [54]. The regulatory domain comprises a REC domain (similar to the "receiver" domains of bacterial two-component signalling systems) and a PAS domain (Period, Arnt, and Sim), however, little is known about the function of these regulatory domains [27]. PAS domain found in other proteins is known to be involved in sensing cellular environment changes. For example, in aryl hydrocarbon receptor, PAS domain mediates response to environmental cues enabling cardiac stress response [57]. In the hERG channel, PAS domain plays a critical role in modulating the gating and stabilising the open state of the channel [58]. The PAS domain in hypoxia-inducible factors

(HIFs) is key for oxygen sensing where during hypoxia, it stabilises HIF-1α and activate genes that promote angiogenesis, metabolic adaptation, and survival in low oxygen conditions [59].

PDE8 is expressed in cardiomyocytes, but its function is not completely understood. One study shows that PDE8A knock down cardiomyocytes have larger calcium transients, increased LTCC current, and increased cardiomyocyte contractility upon βAR activation [60]. Since PDE8 is not sensitive to the commonly used pan-PDE inhibitor IBMX, the results of these studies should be interpreted with consideration of the potentially undetected effects of PDE8.

The dual-substrate PDEs also have important roles in modulating contractility. The PDE1 family includes the isozymes PDE1A, PDE1B, and PDE1C [49]. These are calcium/calmodulin-dependent enzymes that can be phosphorylated by PKA. PDE1A and PDE1B catalyse cGMP degradation with higher Km than for cAMP, while PDE1C has equal affinity. Among the three isoforms, PDE1A and PDE1C are found in the heart. However, PDE1C is the predominant isoform in human heart and specifically localises to the M and Z lines in cardiomyocytes, while PDE1A is the predominant isoform in mice and rats [27, 50]. Inhibition of PDE1 in rabbit and dog hearts was shown to induce a positive inotropic and chronotropic effects through PDE1C activity over a soluble AC-cAMP nanodomain that regulates LTCC current via PKA. No changes in SERCA current, phosphorylation of phospholamban, TNI, and MYBPC were observed [61].

PDE2 is a dual substrate PDE with similar high Vmax and high Km for both cAMP and cGMP [51, 52]. PDE2A has three splice variants: PDE2A1 localised to the cytosol, PDE2A2, localised to the mitochondria, and PDE2A3, localised to the cell membrane [51]. In rat and mouse cardiomyocytes PDE2 contributes to a low fraction of the total cellular cAMP-PDE activity, while in humans with HF, it contributes to around 25% of the total cAMP-PDE activity [43]. Some studies found that upon PDE2 inhibition, there was an increase in LTCC currents and contractility, but others failed to replicate the findings [27].

PDE3 is another dual substrate PDE with two isoforms, PDE3A and PDE3B. PDE3 hydrolyzes both cAMP and cGMP with similar high affinities, while the Vmax is more than 10-fold higher for cAMP [53]. Hence, when cGMP binds, it is hydrolysed slowly and this inhibits cAMP degradation. PDE3B is localised to T-tubule membranes while PDE3A is mainly found in SR membranes [53]. The latter forms a complex with SERCA, phospholamban, and when PKA phosphorylates PDE3, cAMP hydrolysis is increased therein. Consequently, PDE3A1 regulates the cAMP-mediated control of Ca^{2+} re-uptake in the SR. PDE3 is the most abundant PDE degrading cAMP in human hearts [43].

Recently published PDE2A2 and PDE3 interactome and phosphoproteome data reveal distinct features of PDE signalling signalosomes [39]. Besides mapping cAMP domains goverened by the aforementioned PDEs, the authors show that PDE3A2 isoform operates in a nuclear nanodomain that involves SMAD family member 4 (SMAD4) and histone deacetylase 1 (HDAC-1). Inhibition of PDE3 results in increased HDAC-1 phosphorylation, leading to inhibition of its deacetylase activity, derepression of gene transcription, and cardiac myocyte hypertrophic growth. Using targeted FRET-based biosensors in rat cardiomyocytes, PDE3 subcellular activity was found to prevail around cAMP nanodomains defined by a PKA RI-targeted biosensor and regulate signalling in caveolin-enriched compartments such as T-tubules [62].

PDE10 and its role in the heart was only recently explored by Chen et al. (2020), where they showed upregulation of PDE10 in failing hearts and beneficial effects of PDE10 inhibition against hypertrophy and fibrosis [63]. It is not yet clear whether it directly regulates cardiac contractility.

Generally, considering that basal cAMP concentrations are around 1 µM and cGMP concentrations around 10 nM, PDE3 in non-stimulated conditions would mainly hydrolyse cAMP. Together with PDE3, also PDE4 has been shown to constrain basal cAMP levels. However, the affinity of PDE4 for cAMP is more than 10-fold lower than PDE3 and also above the basal cAMP levels. Moreover, PDE2 has even lower affinity for cAMP and, under normal conditions, should not

regulate cAMP at basal levels unless its (over-)abundance would be sufficient to compensate for this low affinity. However, inhibition of PDE2 was found to increase cell shortening at basal conditions in rats [64].

1.2.2 cAMP-dependent PKA signalling

cAMP activates PKA, a ubiquitously expressed kinase known to phosphorylate numerous targets in cells. The PKA holoenzyme is a heterotetramer consisting of two catalytic (C) subunits bound to a dimer of regulatory (R) subunits. The enzyme remains inactive when the cAMP-sensing R dimer binds to the C subunits. There are multiple genes for PKA subunits: three for the C subunits (Cα, Cβ, and Cγ) and four for the R subunits, divided into two classes, RI (RIα, RIβ) and RII (RIIα, RIIβ) [65].

Traditionally, PKA activation has been described by a binary model in which the binding of cAMP to the R subunits releases the C subunits, allowing them to phosphorylate target proteins freely within the cell. However, recent studies have challenged this model, revealing that even after activation, some C subunits remain tethered to the holoenzyme complex. This tethering suggests that PKA-mediated phosphorylation may occur within a highly localised nano-compartment, approximately 15–25 nm in size, rather than being diffusely distributed throughout the cytoplasm [66]. This nano-compartmentalization could have significant implications for the specificity and efficiency of PKA signalling, as it allows for precise control over which substrates are phosphorylated in response to cAMP.

However, multiple studies challenge this view [67]. An alternative explanation for C subunit compartmentalisation is the rapid recapture of freed C subunits by available R subunits. This fast recapture is supported by the significantly higher concentrations of R subunits compared to C subunits. For instance, in HEK293T cells, the concentrations of RI and RII are approximately three and seven times greater, respectively, than the concentration of C subunits [68]. In rat tissues, the average ratio of R to C subunits was approximately 17-fold, with a ratio of around 6.4 to 1 specifically in heart tissue. Notably, RI subunits outnumbered RII subunits in the rat heart by approximately twofold [68]. C subunit diffusion

rate is also regulated by membrane insertion of myristylated C subunits [69]. C subunit exists in equilibrium between 'myr-in' and 'myr-out' states, and myrtisilation controls PKA association to membranes where membrane binding motif of the myristoylated C-subunit of PKA steers the enzyme toward lipids independent of its regulatory subunit, providing an additional mechanism to localise the enzyme near membrane-bound substrates [70].

Experimental evidence suggests that, at least in the cytosol, PKA phosphorylation can be effectively achieved as C subunits diffuse only a very short distance from RII [68]. Moreover, rapid fluctuations in local cAMP concentrations, facilitated by the co-localisation of PKA with ACs and PDEs, further support the quick release and rebinding of C subunits to R subunits. This interaction is strengthened by the anchoring of PDE4 and PDE8 to A kinase anchoring proteins (AKAPs) [71, 72], and direct coupling between PKA and PDEs has been observed [73, 74]. However, it remains to be determined how anchored PKA complexes are spatially oriented in relation to their interaction partners, such as PDEs and receptors, to fully understand the dynamics of PKA signalling.

Which target is phosphorylated by PKA on activation is determined, at least in part, by the cAMP-sensing R subunits, which associate with both A-kinase anchoring proteins, AKAPs, and C subunits, facilitating spatially restricted substrate phosphorylation. The four R subunits are functionally distinct. RIα and RIIα are ubiquitously expressed, whereas RIβ and RIIβ exhibit more tissue-specific expression patterns, with RIIβ highly expressed in the heart [75].

A significant difference between RI and RII isoforms is the auto-phosphorylation capability of the inhibitor site (IS) in RII subunits, influencing RII interaction and signal amplification (Fig. 1.4) [65]. Additionally, type I PKA complexes require two magnesium ions and ATP to form the holoenzyme complex, whereas type II PKA can form a high-affinity complex without these nucleotides [76].

PKA R subunits have a conserved domain organization, starting at the N-terminus with the dimerisation and docking (D/D) domain [77]. This D/D domain is crucial for the assembly of the R subunit dimer and essential for AKAP binding.

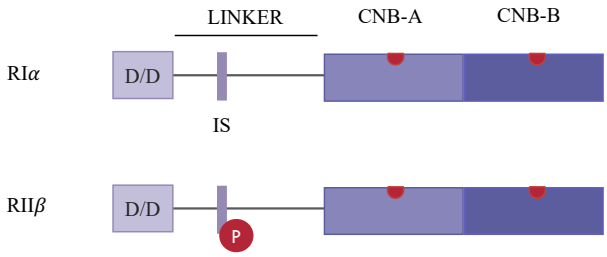


Figure 1.4: Schematic representation of PKA RIα and RIIβ domains.

The approximately 50-residue D/D segments form an anti-parallel X-type helical bundle, generating a hydrophobic surface for AKAP docking [76]. The flexible linker between the D/D domain and the C-terminal cAMP-binding domains includes the IS, containing five residues of the PKA substrate recognition sequence, which act as a pseudo-substrate by binding to the active site of the C subunits. Notably, RI lacks the IS phosphorylation motif present in RII [76].

The 20-residue linker between the IS and cAMP-binding domains is only partially ordered in the free R subunit and becomes fully ordered in the presence of the C subunit. Following the flexible linker region, two cyclic-nucleotide binding domains, A and B (CNBA and CNBB), are located on the C-terminal side. Each of these domains contains a docking site for cAMP. Conformational changes upon cAMP binding result in the disassembly of the PKA holoenzyme with the R subunits remain dimerised [76].

Cardiac myocytes express all four types of PKA isozymes. PKA isoforms exhibit different subcellular localisations, with RII associating with the particulate fraction of cell lysates and RI being primarily cytosolic [29]. Although previously thought to be not anchored, the majority of PKA RI was shown to be also associated with AKAPs, similarly to RII [29]. PKA RI tetramers are activated at lower cAMP concentrations than RII *in vitro*, and RI is more readily dissociated by cAMP than RII [78]. Previous studies have shown that cAMP produced at the plasma membrane by ACs can activate high-threshold AKAP-bound PKAs without activating low-threshold cytosolic PKA activity en route, underscoring the distinct

biological roles of PKA RI and RII [29]. However, the mechanism underlying this selective activation remains incompletely understood.

FRET experiments have demonstrated that cAMP levels rise selectively in the AKAP-PKA RI and RII compartments in a stimulus-specific manner, leading to the phosphorylation of distinct subsets of downstream PKA targets [29]. The generation of distinct cAMP pools within cells allows for the selective activation of subsets of individual PKA isoforms, which is crucial for modulating specific physiological functions. This specificity also presents opportunities for developing strategies for selective pharmacological intervention.

Additional signalling specificity and compartmentalisation are provided by the affinity of PKA for the phosphosite in the target proteins. Numerous proteins are only phosphorylated when cAMP and PKA activity are at their maximum level, while other proteins are phosphorylated even when cAMP levels and PKA activity are low. Analysis of the sequences surrounding the PKA-dependent phosphosites suggests that phosphorylation thresholds are set, at least in part, by the affinity of PKA for each site [79]. Besides different target affinities of PKA, AKAPs are important for controlling PKA phosphorylation, as discussed bellow.

Signal compartmentalisation through AKAPs

PDEs, by degrading cAMP, help create distinct cAMP signalling pools. AKAPs form PKA signalling pools by anchoring PKA to specific cellular targets. Different types of PKA are anchored to distinct PKA-anchoring proteins. The selective activation of restricted subsets of anchored PKA is achieved through the generation of subcellular cAMP gradients, which result in the phosphorylation of protein targets. Several studies further support the importance of spatial confinement in achieving hormonal signalling specificity and the precise execution of cellular functions.

AKAPs constitute a diverse family of more than 40 scaffolding proteins that localise PKA to specific intracellular domains. A key feature of AKAPs is their PKA-binding domain, an amphipathic α-helix of 14–18 amino acids, which interacts with the four-helix bundle formed by the D/D domains of PKA R subunit dimers

[80]. In addition to this PKA-binding domain, AKAPs have targeting domains that anchor them to distinct subcellular locations. As signalling hubs, AKAPs bind not only PKA but also GPCRs, ACs, EPAC, PDEs, phosphatases (PPs), and other kinases such as protein kinase G (PKG) and protein kinase C (PKC). Based on their specificity for different PKA R subunit isoforms, AKAPs are classified into three types: RI-specific, RII-specific, or dual-specific [81].

AKAPs ensure signalling specificity by anchoring PKA and other signalling components to target sites. For instance, specific AKAP-AC interactions promote cAMP generation and PKA signalling, whereas AKAP interactions with other ACs inhibit cyclase activity [82]. Overall, specific protein–protein interactions involving pathway components, combined with mechanisms of restricted diffusion and cAMP buffering, contribute to the formation of local cAMP gradients and signal compartmentalisation in cardiomyocytes, and other cell types [37].

The molecular basis for the isoform specificity of AKAPs arises from differences in the surface charge distribution of R isoforms. While RIIα has a predominantly hydrophobic interaction surface, RIα contains additional acidic and basic residues at the AKAP interaction site [83].

Given the role of AKAPs in the precise localisation of PKA, this spatial regulation is particularly important in the context of cardiac myofilament function. Myofilament AKAPs include TNT (dual specificity), myomegalin (also known as PDE4DIP, dual specificity), and ZASP (RII-specific) (Fig. 1.5). Mutations such as A123T in PDE4DIP are associated with early-onset atrial fibrillation and slow cardiac conduction, leading to heart block that often necessitates pacemakers. These effects are thought to result from impaired compartmentalisation of PKA and PDE4D. In turn, that leads to increased cAMP near the β2AR site and decreased PKA phosphorylation of desmin [84]. The TNT R173W mutation results in impaired cardiomyocyte contractility due to disrupted interactions between troponin and tropomyosin, and reduced PKA binding to sarcomere domains, causing TNI hypophosphorylation in dilated cardiomyopathy (DCM) [85].

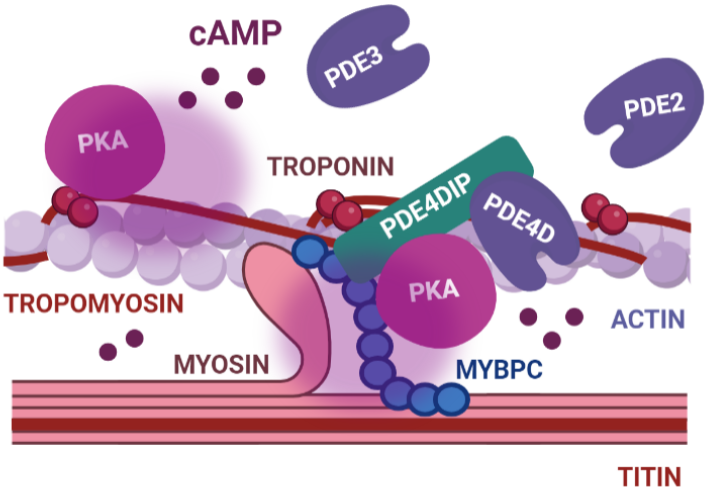


Figure 1.5: cAMP signalling domains at the myofilament. Nanodomains include PKA anchored by the AKAPs TNT and PDE4DIP. cAMP signalling at the myofilament is controlled by PDE4, PDE3, and PDE2. Adapted from Folkmanaite and Zaccolo (2023) [33].

Peptides derived from the PKA-AKAP binding sequence have been developed to study PKA-AKAP interactions. HT31, a 24-amino acid peptide based on the sequence of AKAP-Lbc, binds RII and disrupts both RI and RII AKAP complexes in cells and animal experiments [86, 87]. HT31 binds RII by interacting diagonally over one face of the D/D dimer, creating a solvent-excluded interaction site. The interaction of R-binding peptides with the D/D domain is mediated by aliphatic residues on one side of the peptide's α-helix, forming a hydrophobic ridge. This helix docks into a complementary hydrophobic groove formed by side chains from the N-terminal helices of both protomers of the RIIα D/D [88]. The RIAD peptide was designed to be RI-specific by incorporating amino acids that sterically interfere with RII binding, while the core binding region fits both RI and RII D/D domains [89]. The SUPER-AKAP-IS peptide is RII-specific due to an aliphatic residue that does not fit into the first core binding pocket of RIα [90].

Interfering with AKAP–PKA interactions in cardiac myocytes or in hearts *in vivo* using HT31 abolishes the phosphorylation of TNI, RyR, and MYBPC while still increasing the rate and amplitude of cell shortening and relaxation compared to control cells upon βAR stimulation. This demonstrates that anchored

PKA specifically regulates phosphorylation events, highlighting the importance of compartmentalised PKA signalling in the heart [91, 92].

Dephosphorylation by phosphatases

Phosphatases (PPs) terminate the PKA signal by de-phosphorylating various targets. The three main protein phosphatase families are categorized based on the amino acid sites they target for dephosphorylation: tyrosine, serine-threonine, and dual-specificity phosphatases [93]. In the heart, serine-threonine phosphatases account for 90% of dephosphorylation events [93]. This family includes the PP1, PP2A, and PP2B holoenzymes, all of which are implicated in HF and arrhythmias.

The PP1 holoenzyme, expressed ubiquitously in most cell types including atrial myocytes, consists of regulatory subunits that form a complex with the PP1 catalytic subunits. These regulatory subunits determine the subcellular localisation and substrate specificity of the holoenzyme [94]. In cardiomyocytes, PP1-interacting subunits can localise the enzyme to the nucleus, plasma membrane, or near actin.

PP2B, also known as calcineurin, is a calcium-dependent phosphatase. In adult cardiomyocytes, PP2B is predominantly localised to the T-tubules, where it contributes to plasma membrane depolarisation [95]. In contrast, neonatal mice exhibit a more homogeneous distribution of PP2B activity throughout cardiomyocytes. Overall, PP2B is typically tethered near sites of calcium release [95].

The PP2A holoenzyme exhibits distinct expression and localisation patterns in different chambers of the human heart. The catalytic and scaffolding subunits are more highly expressed in the right atria and ventricle compared to the left atria and ventricle [96]. At the cellular level, these subunits are broadly distributed throughout ventricular myocytes, present in both the cytosol and nucleus [96]. PP2A plays a crucial role in regulating and localising cardiac ion channels, transporters, and regulatory molecules that are essential for cardiac contractility and relaxation.

In the heart, PP1, PP2A, and PP2B constitute the majority of protein phosphatase activity. Each of these phosphatases has unique subcellular localisations and binding partners within cardiomyocytes. For instance, B56α, a PP2A regulatory

subunit expressed in the heart, interacts with Ankyrin-B and is localised to the M-lines in neonatal rat ventricular myocytes (NRVMs). It co-localises with the Nav1.5 channel at the intercalated discs, controlling the "late" sodium current (INaL) [93, 97]. Additionally, B56α targets PP2A to dephosphorylate components of the contractile machinery, including MYBPC and TNI [98].

Phosphatases are often considered undruggable due to the challenge of achieving inhibitor selectivity due to their highly conserved active sites. Additionally, the positively charged active sites prefer negatively charged molecules, which typically lack cell permeability. Although recent research has highlighted novel approaches to understanding PP signalling [99], much remains unknown, especially in the context of cardiac research. Future work, particularly in defining new therapeutic avenues, should focus on understanding how local PP subunits are modulated through both transcriptional and post-translational mechanisms.

For example, literature indicates that phenotypes associated with the loss of PP2A scaffolding subunits in cells and animals differ from those associated with the reduction or loss of PP2A regulatory subunits. Interestingly, the loss of PP2A regulatory subunits may paradoxically increase PP2A activity [100]. Given that each holoenzyme may consist of various splice forms and subunit compositions, significant complexity in unraveling these signalling pathways can be anticipated.

1.2.3 cAMP-PKA signalling compartments at the myofilament

Upon βAR stimulation, PKA phosphorylates TNI at serines 23 and 24 (Fig. 1.5). This phosphorylation decreases myofilament calcium sensitivity shifting the force–pCa relationship rightward, promoting faster muscle relaxation and an increased rate of crossbridge cycling. Additionally, it results in an increase in peak force generated during contraction (positive inotropy) [101]. Although positive inotropic effects might seem counterintuitive, they likely result from the PKA phosphorylation-induced increase in crossbridge cycling rate and shortening velocity [101]. Therefore, PKA-mediated TNI phosphorylation contributes to both the

enhancement of systolic function and relaxation during βAR-stimulation, resulting in increased positive inotropy and lusitropy under conditions of increased cardiac demand [101]. The entire troponin complex plays a critical role in this regulation, with TNT even serving as an AKAP, anchoring PKA to the troponin complex and enhancing the specificity and efficiency of the phosphorylation process.

Troponin complexes, located on the actin filament, repeat every 7 actin monomers, which corresponds to around 36.5-38.5 nm alongside actin under relaxed conditions. Axial thick filament repeats of myosin heads and MYBPC occur around every 43 nm. The difference in periodicities between actin binding sites (35.55 nm) and myosin crowns (42.9 nm) creates a range of longitudinal spacings between myosin heads and actin binding sites, and this range of spacings is strongly modulated by the extensibility of myofilaments (Fig. 1.6).

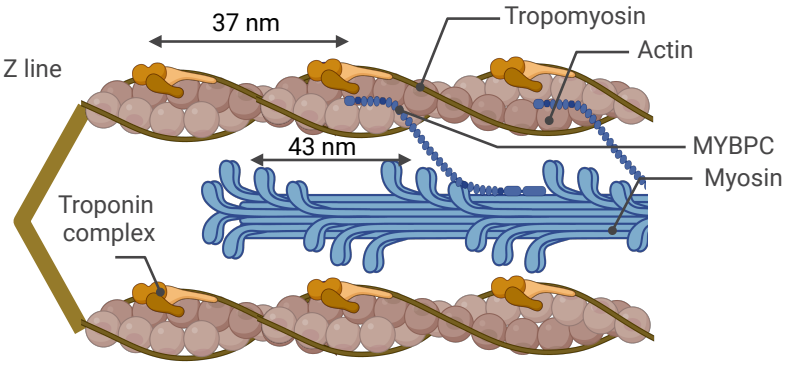


Figure 1.6: A schematic outlining the spacing in the sarcomere.

Interestingly, the increase in cAMP levels following βAR activation is significantly lower near TNI compared to other cellular compartments, such as the cytosol or other signalling hubs like AKAP18δ [34]. This differential distribution of cAMP underscores the role of various PDEs in creating distinct cAMP micro-environments at the myofilament. The primary PDEs involved in this regulation are PDE4 and PDE3, with PDE2 playing a lesser role in rat hearts. These enzymes are crucial in maintaining localised cAMP levels post-βAR stimulation, which directly affects the phosphorylation state of myofilament proteins. Intriguingly, the inhibition of

PDE4 in the absence of βAR stimulation does not alter sarcomere function or TNI phosphorylation, suggesting a stimulus-dependent activation of PDE4 [44].

Another PKA phosphorylation site is found at MYBPC on the thick filament. MYBPC is phosphorylated at up to four sites and its phosphorylation is down-regulated in failing human hearts [91]. Inhibition of PDE2, PDE3, or PDE4 increases MYBPC phosphorylation [91]. Phosphorylation of MYBPC increases the availability of myosin heads for interaction with actin and therefore enhances contraction [102]. MYBPC is known to be phosphorylated at physiological baseline [103], and de-phosphorylation of MYBPC leads to reduced contractility of the heart and the development of hypertrophy [103, 104].

Recently published phosphoproteome data indicates that phosphorylation of both TNI and MYBPC is upregulated after PDE3 inhibition with cilostamide in NRVM. MYBPC but not TNI phosphorylation is upregulated after PDE2 inhibition with BAY-60-7550 [39]. Other proteins, such as titin and PDE4, can also be phosphorylated by PKA, and titin's phosphorylation was found to increase following inhibition of both PDE2 and PDE3.

For a typical myofibril of 1.2 µm in diameter, the estimated number of thick myosin filaments from structural data is around 500–650. A myofibril runs the entire length of the muscle fiber and consists of a large number of sarcomeres in series. In a half-sarcomere, each half myosin filament with around 150 myosin molecules faces six actin filaments; each actin filament has from 360 to 440 myosin binding sites, depending on the actin filament length, arranged in a double-stranded helix. The maximum overlap region is defined by the number of myosin crowns where 50 crowns interact with around 512 active actin sites [105]. The actin filament length as well as the number of actin monomers may vary. The length of a myosin filament is around 1.58 µm, having 50 crowns, i.e., 150 myosin molecules per half-thick filament, with a crown spacing of 14.3 nm. This number of crowns and spacing provide maximum overlap with thin filament of around 0.7 µm.

Lattice spacing, which is the radial spacing between its contractile filaments, increases as muscle shortens. The skeletal muscle force–pCa simulations performed

at sarcomere lenghts of 2.5 and 2.0 µm resulted in inter-filament lattice spacing at 37.36 and 41.77 nm, respectively. However, lattice volumes in cardiac muscle are not constant and need to be independently measured. Depending on the protocols used for measuring (trypsin treated muscles, compression with 2.5% dextran), cardiac cell lattice spacing can vary from 35 to 47 nm for sarcomeres of length between 2.3 and 1.9 µm.

Taking the positioning of myofilament proteins into account, these are the estimated distances between the PKA-phosphorylatable proteins TNI and MYBPC (Fig. 1.7):

- TNI (S23/24) to MYBPC (S273, S282, S302, S307; (C0-C1 domain)): around 10-15 nm
- TNI (S23/24) to MYBPC C10 domain: around 35-47 nm

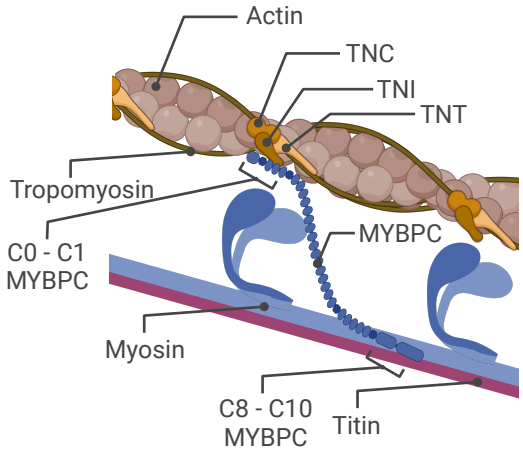


Figure 1.7: A schematic outlining the positioning of TNI and MYBPC at the sarcomere.

Given the small distance between the PKA phosphorylation sites of TNI and MYBPC, it could be that TNI and MYBPC phosphorylation is synchronised *i.e.* occurs at the same time and may be carried out by the same PKA enzyme activated by the same pool of cAMP. Sevriera et al. (2023) discuss the effects of de-coupling of TNI and MYBPC phosphorylation coordination highlighting the pathological effects that occur when the coordination is disrupted [11]. Specifically, their

findings indicate that when MYBPC is dephosphorylated, the bisphosphorylation of TNI increases calcium sensitivity and decreases cooperativity, particularly at long sarcomere lengths. This decoupling can lead to deleterious effects in physiological settings, as it may impair the heart's ability to properly regulate contraction in response to changing calcium levels. It remains to be seen if and what kind of role cAMP plays in maintaining TNI-MYBPC phosphorylation coordination. Elucidating the precise spatio-temporal regulation of myofilament protein activity is crucial for improving our understanding of cardiac cell physiology, the mechanisms underlying disease onset and progression, and for identifying new targets for drug development.

1.2.4 Challenges in studying cAMP-PKA signalling compartmentalisation

For the cell to be able to manage locally controlled cAMP-PKA nanodomains, the production, degradation, and propagation of cAMP and PKA signal must be precisely regulated. How this is executed remains to be fully elucidated. Estimates of intracellular cAMP diffusion coefficient range from 10 to 780 $\mu m^2/s$, depending on cell type and experimental conditions [35, 106]. In NRVMs, the diffusion was determined to be around 32 $\mu m^2/s$ [107].

Using experimentally established values, computational diffusion models indicate that PDEs alone cannot explain cAMP compartmentation as PDEs have relatively low catalytic rates that seem inadequate to effectively restrict the highly diffusible cAMP [106]. Even when taking into account that the activation threshold of PKA *in vivo* may be more than 20 fold higher than previously established *in vitro* [108], the activity of the PDEs alone would still appear inadequate to create functionally meaningful cAMP gradients that can selectively activate only a subset of anchored PKA. This view could change if the PDE enzyme kinetics in the cell were also significantly different from those measured *in vitro*, as described for PKA. However, this remains to be established.

Signalling and interaction between the elements in the cAMP-PKA cascade are important to consider. PKA has been shown to interact with PDEs *in silico* and

mediate the active hydrolysis of cAMP bound to PKA RIα, thereby enhancing PKA enzymatic activity [74]. According to this model, the PDE8-RIα complex forms through peripheral contacts, with the central ligand cementing this ternary interaction. Enhanced catalysis is based on the active translocation of cAMP from its binding site on RI to the catalytic site on PDE8 through direct 'channeling'. Thus, unbound cAMP maintains the PDE8-RIα complex while being hydrolysed, amplifying PKA activity by cAMP-mediated sequestration of the R-subunit by PDEs [74]. This regulatory mode explains the paradox of cAMP signal amplification by accelerated PDE-mediated cAMP turnover. Conversely, it could be argued that the cAMP signal would be reduced if PDE-mediated cAMP turnover were slower.

Altogether, this enhanced activity of the PDE8-RIα complex facilitates robust desensitisation, allowing the cell to respond to dynamic levels of cAMP rather than steady-state levels. When researching cAMP signalling pathways, the interactions between AKAP-PKA and PKA-PDE must be taken into account.

Mathematical models that integrate our current knowledge on PDE activity suggest that these enzymes could generate gradients of cAMP if the diffusion coefficient of the second messenger were significantly reduced. Factors that could slow down cAMP diffusion in the cell include physical barriers and cAMP buffering. The expression of cAMP-binding proteins has traditionally been thought to be limited, making cAMP buffering an unlikely mechanism to influence cAMP dynamics. However, a significant molar excess of PKA regulatory subunit compared to catalytic subunits has been reported, which could potentially provide substantial cAMP buffering [68].

If indeed that is the case and PKA, along with other cAMP binding proteins such as EPAC, CNGC, and POPDC acts as a cAMP buffer, then such buffer capacity could be approximated. In cardiac cells, with estimated 1 µM cAMP concentration, there are approximately 9 million cAMP molecules assuming 15 pL cardiac cell volume [109]. In skeletal muscle, the estimated concentration of PKA is 0.23 µM which corresponds to roughly 2 million PKA molecules. Given that each PKA molecule can bind up to four cAMP molecules, almost all cAMP could

theoretically be bound to PKA, leaving around 1 million cAMP molecules unbound, potentially available to bind to other proteins like EPAC.

This scenario aligns with previous findings by Bock et al. (2020), which showed that at low cAMP concentrations, a fluorescent cAMP analogue is almost immobile within the cell, with its diffusivity increasing significantly to 10–100 $\mu m^2/s$ when the concentration increases 100-fold in HEK293T cells [35]. This suggests that at basal cAMP levels, most cAMP might be bound to PKA, leading to reduced diffusion rates. Consequently, this would imply that under basal conditions, nearly all PKA regulatory subunits are saturated with cAMP, resulting in the activation of catalytic subunits.

However, if cAMP is predominantly bound under basal conditions, this raises a critical point: given the constant adrenergic tone in the heart, there may be limited or no additional binding sites available for cAMP under stimulated conditions when cAMP levels increase. In such a scenario, a significant portion of cAMP would remain unbound, and cAMP compartmentalisation would need to be tightly regulated by PDEs to prevent uncontrolled activation of downstream signalling pathways.

Mathematical modelling approaches for cAMP compartmentalisation indicate that cAMP is likely not able to freely diffuse in the cells [110]. A lack of diffusion at low cAMP concentrations suggests that a number of cellular cAMP binding sites exist that may enable the formation of cAMP nanodomains. Hydrolysis of cAMP by PDEs, together with intracellular cAMP buffering, could explain how cAMP signalling is compartmentalised in cells, although further investigations are warranted to determine the amount of non-PDE based buffering needed for the cell to be able to maintain cAMP nanodomains.

LLPS: from compartmentalising molecules to optimising biochemical reactions

A novel mechanism for how cAMP buffering could be executed in the cell has been recently reported by Zhang et al. (2020) [111]. The study shows that PKA regulatory subunits type I α (RIα) undergoes liquid–liquid phase separation

(LLPS) in the cytosol to form biomolecular condensates in various cell types, including cardiomyocytes.

LLPS is a biochemical process in cells that can drive proteins, RNA, and other molecules to concentrate into droplets. These droplets do not have a lipid membrane but rather exist as distinct organelles relative to the surrounding environment, and act as biochemical reaction chambers. Multiple LLPS functions in biology have been suggested ranging from molecular sequestration to reaction optimisation. In recent years, significant progress has been made in the study of LLPS, especially in the neurodegenerative diseases and cancer [112].

The first notable characterisation of LLPS in biology was P granules which were found to undergo LLPS in *Caenorhabditis elegans* [113]. LLPS droplets, or membrane-less organelles, form via weak multivalent interactions in the cytoplasm and nucleoplasm constituting a distinct membrane-free compartment. The droplets formed by LLPS exhibit two physical characteristics: they are spherical in cells and *in vitro*, and can undergo fusion, where several droplets merge together to form a larger droplet. These characteristics are essential for distinguishing puncta-like structures formed via LLPS from other structures such as aggregates.

Although the majority of LLPS research in biology is focused on *in vitro* studies, phase separation has been observed *in vivo* where local signal enhancement of P bodies was observed in the germ cells of *C. elegans*, indicating that the P bodies underwent local coagulation, similar to droplets observed under a microscope [113]. Under pathological conditions, various proteins can aggregate through LLPS, which hinders normal cellular function and accelerates the development of diseases. For example, TDP-43 and FUS were found to accumulate in the degenerative motor neurons of amyotrophic lateral sclerosis (ALS) patients through LLPS [112].

In recent years, studies have found that ribonucleoprotein particles (RNP) are formed via LLPS. RNPs are divided into nuclear granules, such as Cajal bodies and nucleoli, and cytoplasmic granules, such as stress granules (SGs) and P-bodies. Because RNPs are rich in RNA and proteins, RNA–protein and protein–protein interactions occur in these structures. In the cardiovascular system, RNPs can reach

the sites of myofibril synthesis in cardiomyocytes through microtubule transport to mediate cardiac hypertrophy [114].

The assembly of membrane-less organelles by LLPS is a dynamic process that relies on the weak interactions between its components. This effect is often provided by specific regions between molecules, including the intrinsically disordered regions (IDR), hydrophobic amino acid regions, charged regions, etc. The assembly starts by forming an unstable core through weak interactions and then recruiting proteins to stabilize the core [115]. In neurons, this process relies on cytoskeletal proteins and molecular motors.

The LLPS is affected by many external factors, such as light intensity, temperature, salt concentration, ATP concentration, PTMs, and chaperone proteins. Changing the concentrations of salt ions in solution is a widely studied method to induce LLPS. This is because salt ions change weak interactions between molecules, affecting the occurrence of phase separation. Moreover, ATP plays a critical role in LLPS by promoting the assembly of phase-separated droplets. It is considered a key driving force for phase separation and may also help prevent IDRs from aggregating into amyloid fibers.

PTMs have been shown to both, promote and inhibit LLPS by changing IDR's charge distributions and hydrophobic properties. PTMs allow cells to dynamically regulate the assembly and disassembly of membraneless organelles in response to various stimuli, ensuring proper cellular function and stress response. Molecular chaperones are also important factors in regulating phase separation. High levels of the chaperone heat shock protein 70 (HSP70) and 27 and were found in SOD1-positive SGs, and HSP70 was able to prevent the formation of abnormal SGs [116]. This may be related to the fact that molecular chaperones bind to disordered regions of proteins, reducing the weak interaction between proteins.

A recent phosphoproteomics dataset published by our lab indicated that HSPA4, HSPA8, Hsp90AA1, and eIF4EBP1 are proteins regulated by PDE3A [39]. Hsp90AA1, encoding the human stress-inducible 90-kDa heat shock protein alpha (Hsp90A), is involved in the formation of RNP granules and plays a critical role in the

dynamics and stability of these phase-separated structures. HSPB6 (HSP20) is known to interact with PKA and PDE4, forming a crucial complex for controlling cardiac contraction. Under basal conditions, this interaction keeps HSPB6 in a hypophosphorylated state [117]. Upon prolonged βAR stimulation, as seen in the failing heart, the pool of PDE4 tethered to HSPB6 becomes overwhelmed, leading to a local increase in cAMP, PKA activation, and phosphorylation of HSPB6 on Ser16. HSPB2, which has been extensively described in the context of LLPS, has also been shown to interact with HSPB6.

PKA and other kinases play important roles in the formation and turnover of SGs and P-bodies. These kinases appear to sense the presence of SGs and become active, regulating the kinetics of SG assembly and disassembly through phosphorylation of SG-associated factors. In *Saccharomyces cerevisiae*, isoforms 2 and 3 of the PKA C subunit, known as Tpk2 and Tpk3, localise to P-bodies during the stationary phase and under stress conditions [118]. Other SG components have been found to include eukaryotic translation initiation factor 2 subunit alpha (eIF2), ras GTPase-activating protein-binding protein 1 (G3BP1), T-cell intracellular antigen-1 (TIA-1), polyadenylate-binding protein 1 (PABP1), ataxin-2, fragile X mental retardation protein (FMRP), and tristetraprolin (TTP) [119].

Interestingly, there appears to be an overlap between the SG, P-body, and PKA interactomes. Based on STRING interactome database, PKA RIα is known to interact with DEAD-box helicases (DDX42 and DDX5), DnaJ heat shock protein family (Hsp40) members (DNAJB6, DNAJC28), eukaryotic translation initiation factors (eIF4B, eIF1A), and heat shock proteins (Hsp90AA1, HSPA5, HSPA8, HSPA9, HSPB1) [120]. DEAD-box ATPases are global regulators of phase-separated organelles, and Hsp40 proteins phase separate to chaperone the assembly and maintenance of membraneless organelles [119]. SGs include a number of different eukaryotic translation initiation factors [119].

Taking all this together, it is possible that PKA condensation enables the stress response in cardiomyocytes instead of, or together with, cAMP buffering. The specific function of PKA condensation in the heart remains to be established. Further

research is needed to clarify the role of PKA condensation in cardiac physiology and its potential implications for cardiac health. At present, exploring the biological function of LLPS is a critical task, and the definition of its physiological function and its significance in diseases is required. Recent studies have shown a close relationship between dilated cardiomyopathy (DCM) and protein LLPS, where the phase separation phenomenon, caused by abnormal RNP particle accumulation in DCM due to RBM20 mutation, plays a key role [121].

Understanding the interactions between PKA and other proteins that undergo LLPS within these condensates could provide valuable insights into the regulation of cellular stress responses and the maintenance of cellular homeostasis. Further research is needed to elucidate the specific roles of PKA in these processes and their implications for human health.

1.2.5 Liquid-liquid phase separation of PKA

The study by Zhang et al. (2020) illustrates how PKA phase separation contributes to cAMP regulation by creating membraneless organelles filled with cAMP and the PKA RIα subunit. RIα condensates appear to contain cAMP at a concentration that is higher than cAMP concentration in the bulk cytosol. Fluorescence recovery after photobleaching (FRAP) experiments performed using fluorescent cAMP show a slower fluorescence recovery within RIα condensates versus cAMP in the surrounding cytosol, with the diffusivity being around 0.004 $\mu m^2/s$ for cAMP in the droplets and more than 100 $\mu m^2/s$ for the regions outside the droplets. Based on these observations the authors conclude that RIα condensates might be able to act as a buffer for cAMP. RIα condensates appear to encompass also C subunits, providing a model for how cAMP, and C subunits, can be entrapped locally thus contributing to local regulation of signalling. D/D domain and linker domain have been found to be essential for enabling PKA LLPS.

Most importantly, Zhang et al. (2020) suggests that PKA LLPS is essential for PDE activity and the ability of PDEs to compartmentalise cAMP in nanodomains. This is inferred from the experiment where the cAMP was measured using a FRET

sensor recording cAMP levels in the space immediately surrounding PDE4D2. Normally, stimulation with forskolin, AC activator, induces a small increase in cAMP at PDE4D2 site due to PDE-mediated cAMP degradation. After LLPS disruption with 2.5% 1,6-hexanediol, LLPS disrupting agent, forskolin induced much greater cAMP signal around PDE4D2. The authors argue that this suggests that disrupting RIα condensates leads to decreased cAMP buffering and inability of the PDE to provide effective cAMP compartmentalisation.

These exciting new findings prompt further questions regarding what the impact of the RIα condensates might be on cell function. Other biomolecular condensates are known to be important for promoting enzymatic reaction optimizations, but it is currently unknown if and how LLPS affects PKA activity. Computational approaches integrating cAMP diffusion and PKA measurements with PKA LLPS could help elucidate the required ratios of diffuse to condensed PKA for buffering to occur.

Other cAMP-binding proteins, in principle, could provide a similar cAMP buffering mechanism, if they were able to phase-separate. Indeed, a recently published study suggests that cAMP can act through EPAC1 to trigger LLPS and form nuclear condensates [122]. EPAC1 seems to be able to form condensates *in vitro* and in cells, and the concentration of the protein required for condensation *in vitro* is reduced upon cAMP addition.

The suggestion that cAMP can directly modulate the dynamics of biomolecular condensates including PKA RIα and EPAC1 is interesting as this would provide a mechanism for regulation of protein phase separation by an endogenous messenger in response to extracellular ligands. It remains unclear if cAMP diffusion coefficient inside the nuclear EPAC1 condensates is reduced in a similar way as reported for RIα puncta. If confirmed, the ability of cAMP to directly regulate the dynamics of phase separation would provide another important mechanism to achieve compartmentalised signalling in basal and stress conditions. Further investigations of the functional impact of PKA phase separation will hopefully help elucidate its physiological roles.

1.3 Myofilament signalling in health and disease

Disruption of cAMP-dependent regulation of myofilament function is associated with multiple cardiovascular disorders. Reduced phosphorylation of TNI and MYBPC has been reported in human and experimental HF samples, despite total PKA activity following cAMP stimulation being comparable between failing and non-failing human hearts [123]. In some animal models, the phosphorylation of TNI appears to be increased rather than decreased [124]. However, in rat hearts, the cAMP signal triggered by βAR stimulation was found to be significantly reduced at the myofilament but preserved at the SR and in the cytosol [34]. In hypertrophic rabbit myocytes, PKA signalling at the myofilaments was reportedly upregulated inducing contractile dysfunction due to a redistribution of PDEs [125].

Myofilament proteins regulated by cAMP via PKA are hypo-phosphorylated in human HF and cardiomyopathies, in line with findings demonstrating that, despite maintained cAMP levels at the cytosol, cAMP signals triggered by βAR stimulation are significantly reduced at the myofilament [34, 104]. Interestingly, the main PDEs known to regulate cAMP at the myofilament are under-expressed in failing hearts, although changes in their spatial (re)distribution have not been extensively explored [126].

It is likely that, in the failing myocyte, rather than just downregulation or inactivation, PDEs, PKA, and possibly AKAPs, may undergo a reorganisation and redistribution. This may result in hypo- or hyper-phosphorylation of TNI and MYBPC, potentially specific to diseases of different aetiologies and possibly to different stages of disease [125].

Currently, there are no therapeutic agents that aim to modulate PKA activity at the myofilament, or the myofilament-associated interactions with AKAPs or PDEs. Cardiovascular disease continues to exert a substantial burden on the healthcare system. Gaining a better understanding of the local cAMP signalling organization could be key in developing precise and effective therapies. As evidenced by previous studies using PDE inhibitors, targeting global intracellular cAMP

signals rarely provides the desired effects, highlighting the importance of more precise therapeutic interventions.

Despite exciting new developments in the field, multiple questions remain open. PDE inhibitors, for instance, often lack specificity, leading to off-target effects and unwanted side effects such as nausea, headaches, and hypotension [46]. Furthermore, these inhibitors can lead to compensatory mechanisms within the cell, reducing their long-term efficacy. Widely prescribed beta-blockers also have their limitations. They can cause adverse effects such as fatigue, bradycardia, and worsening of symptoms in some HF patients due to their broad mechanism of action. Currently prescribed treatments for HF such as beta-blockers help reduce heart rate and mitigate some symptoms of HF, but they do not correct the underlying signalling defects [127].

Clearly, a better understanding of the system is needed, and more targeted approaches are essential. Additionally, understanding how LLPS impacts myofilament function could open new avenues for drug development, offering more precise modulation of intracellular signalling pathways.

Another underinvestigated area is the direct effect of drugs on the myofilament and force generation. It is crucial to understand signalling mechanisms, comorbidities, and how drugs might act under different physiological conditions, such as varying heart rates. Drug repurposing by exploring the mechanisms of non-cardiac drugs on myofilament signalling presents an interesting avenue for novel therapies.

Importantly, the integration of cAMP domain knowledge utilising computational tools could provide a holistic understanding of cAMP signalling effects in the heart, enabling the simulation of potential therapeutic approaches and mechanistic investigations of pathogenic alterations in diseases. The development of new computational and experimental techniques and interventions might help further expand the understanding of signalling organisation with high spatial and temporal precision [110]. Shifting the focus of investigations from global to domain-specific cAMP signalling might help discover alterations in cAMP signalling present in cardiac diseases which remain to be identified.

In silico drug testing, using computational models, offers a promising approach to understanding and manipulating these intricate signalling pathways. Recent advances in computational biology have enabled the creation of sophisticated models that simulate the dynamic behaviour of biochemical networks within cardiac myocytes. Although these models incorporate detailed information about protein interactions, enzyme kinetics, and cellular compartmentalisation, a unifying model which would allow to simulate drug effects on cAMP signalling and myofilament function is still missing.

In the future, a newly developed *in silico* model might be able to predict how potential pharmacological agents might influence the phosphorylation states of key myofilament proteins, such as TNI and MYBPC, under various pathological conditions. By simulating different scenarios, these models might be able to identify which compounds are likely to restore normal phosphorylation patterns and improve cardiac function. This approach would not only accelerate the drug discovery process but also reduce the reliance on animal models, offering a more ethical and cost-effective alternative.

1.4 Model systems in cardiac cell signalling research

Having described the physiological setting of this thesis, I now briefly discuss the background of methods used.

1.4.1 Researching cardiovascular signalling using animal models

Rat cardiomyocytes are a widely used model for studying cardiac cell signalling. Cardiomyocyte extraction process involves mincing the tissue from the ventricles of neonatal rat hearts, digesting the extracellular matrix with collagenase, and purifying the resultant cell mixture [128]. Isolated and cultured neonatal myocytes are used

to investigate various aspects of cardiac signalling, including cAMP signalling, PKA-mediated phosphorylation, regulation of myofilament proteins, and contraction mechanisms, including hypertrophic conditions [34, 39].

NRVMs as a model offer multiple advantages due to the straightforward preparation of the cells. Unlike *ex vivo* hearts, which are viable for only a few hours, cell cultures remain viable for several days. This extended viability allows the study myocytes over time. Furthermore, cultured monolayers are thin and can be plated in a manner that prevents tissue-scale effects, facilitating investigations of single-cell signalling. This approach minimizes the influence of paracrine signalling, thus reducing confounding variables and providing clearer insights into intracellular signalling mechanisms.

The advantages of using cell cultures come with a trade-off in terms of direct physiological relevance. Due to a wide range of possible perturbations (such as varying fibroblast-to-cardiomyocyte ratios and different plating conditions), non-physiological combinations can be created, and many physiological parameters are omitted, including spatial gradients of expression of proteins [129].

There are also substantial differences between the adult (ARVM) and neonatal rat myocytes including the abundance and distribution of their T tubules. Additionally, myofilament protein expression ratios and isoforms are different as well. For example, during maturation, there is the isoform switching of myosin heavy chains (MHCs), TNI (from the slow skeletal variant to the cardiac variant), and TNT [130].

PTMs play an important role in development as well. MYBPC and TNI phosphorylation levels were decreased in NRVMs compared to adult hearts [131]. This could play an important role in maturation. There is also evidence that at low agonist concentrations, βAR stimulation contributes to the positive inotropic response by increasing cAMP and increasing the amplitude of the twitch contraction force in neonatal, but not adult, myocytes [132].

One of the major advantages of using NRVMs is the capacity to study cardiac hypertrophic responses using compounds that mimic disease states, such as adrenergic stimulation. Various compounds and growth factors have been demonstrated to

induce pathological cardiomyocyte hypertrophy in NRVMs, including phenylephrine, norepinephrine, angiotensin II, endothelin-1, and others [133]. For instance, cardiac myocytes can increase in both volume and cell surface area by up to 150% within 48 hours of treatment with phenylephrine [134].

ARVMs provide a useful model for research, avoiding issues associated with NRVMs, such as immaturity. However, ARVM isolation is technically challenging. While their mature sarcomeric structure is advantageous for contractility studies, they require transfection with viral vectors, which can be costly and sometimes unavailable [133]. Additionally, they can only be maintained in culture for a short period after isolation.

A significant limitation of both ARVMs and NRVMs is their differences compared to human cells and human hearts. For instance, the human heart beats on average 60–70 times per minute at rest, while rat hearts beat at 260–450 times per minute [135]. Differences at the level of action potentials, myofilaments, isoforms of contractile proteins, and their corresponding phosphorylation status have also been reported [136].

There is a variation in protein expression levels between species. For example, mRNA expression levels of PDEs 4A, 4B, 4C, and 4D are significantly higher in rats than in humans across several tissues [137]. Studies have reported considerable similarities between rodents and humans in terms of PDE4 activity, including comparable expression levels, the presence of the same PDE4 subtypes and splicing variants, and the anchoring of PDE4 to similar subcellular compartments and signalling complexes. Additionally, both species exhibit downregulation of PDE4 activity and protein in HF [43]. Human hearts also possess a five-fold higher amount of non-PDE4 activity compared to rodents. It is known that PDE1, PDE2, and PDE3 activity is considerably greater in human cells than in rat cells [138]. Differences in PDE8 activity have not been measured.

These findings suggest that PDE4s play a similar role in the local regulation of cAMP signalling in both rodent and human hearts. However, the inhibition of PDE4 produces ‘global’ effects on cAMP signalling exclusively in rodent hearts,

as PDE4 constitutes a large fraction of the total cardiac PDE activity in rodents but not in humans [137]. This disparity may explain the distinct pharmacological effects of PDE4 inhibition observed in rodent versus human hearts.

1.4.2 Advantages and limitations of hiPSC-CM cardiovascular studies

One of the major challenges for pharmaceutical development is establishing *in vitro* assays using human cells to test potential pharmaceutical compounds for cardiotoxicity in a high-throughput manner. For these assays, it is crucial that the cardiac cells closely resemble adult human cells, as the mechanisms for cardiac repolarisation after contraction can vary significantly between species and different maturity levels [139]. Human induced pluripotent stem cell-derived cardiomyocytes (hiPSC-CMs), especially those derived from patients with genetic diseases, are increasingly regarded as invaluable tools for disease modelling and drug-screening assays [133]. hiPSC-CMs derived from patients with a genetic disease are particularly valuable because they capture the precise genetic mutation and background of the individual from whom they are derived. Consequently, the use of hiPSC-CMs could pave the way for personalised cardiomyocyte therapeutics in a manner that no other cell model has achieved.

Achieving consistent and reliably mature hiPSC-CM cells remains challenging despite the availability of various cell differentiation protocols. Growth-factor dependent methods for cardiomyocyte differentiation have been developed [140], but their reliance on recombinant growth factors introduces significant variability, technical difficulty, and increased costs. Alternatively, cost-saving protocols that use small molecules show great promise and may significantly reduce the expense of these cultures [141]. Despite advancements in cardiomyocyte differentiation from stem cells, further improvements in the efficiency of proliferation and differentiation are still needed.

Various methods have been employed to enhance hiPSC-CM maturation [142]. Metabolic maturation techniques have been shown to improve the properties of

hiPSC-CMs. Feyen et al. (2020) developed a metabolic maturation medium that included a mixture of fatty acids along with low concentrations of glucose and calcium [143]. This medium led to improved structural, electrophysiological, and functional characteristics of hiPSC-CMs. Building on this, Knight et al. (2021) combined the use of maturation medium with micropatterned surfaces to produce structurally and functionally matured hiPSC-CMs [144]. This combinatorial approach was particularly effective in modelling the hypertrophic phenotype in Danon disease, which was difficult to achieve before.

Bioengineering approaches have also been proven useful. They rely on mimicking the physiological environment of the human heart. One such approach involves the creation of 3D cardiac tissues using hiPSC-derived CMs and non-myocytes embedded in scaffolds and extracellular matrix components. Mannhardt et al. (2016) developed engineered heart tissues (EHTs) by embedding hPSC-CMs into fibrin hydrogels [145]. These tissues were attached to flexible silicone posts, enabling detailed contraction analysis. Cardiomyocytes differentiated using bioengineering approaches tend to display structural and contractile maturation similar to native human heart tissue, including a higher number of mitochondria and an increased reliance on oxidative phosphorylation over anaerobic glycolysis [146]. The inclusion of non-myocytes further facilitated extracellular matrix remodelling, tissue compaction, and significantly enhanced contractile performance [147].

Even though hiPSC-CMs remain the best models for human cardiomyocytes, the mechanisms and pathways involved in their differentiation are not fully understood, and there are numerous conflicting reports regarding the purity and maturity of these cells. Most current studies investigate hiPSC-CMs within the first 2–3 weeks after differentiation, during which these cardiomyocyte cells exhibit an immature, embryonic-like phenotype [148]. More recent studies aiming to produce more mature cardiomyocytes have examined cells 12–15 weeks after the initiation of differentiation. These cells display more rectangular architecture, the presence of mature Z-, A-, H-, and I-bands, and more parallel-oriented myofibril arrays [149]. By combining longer differentiation procedures with nanopatterned surfaces, researchers have

reduced the fragility of hiPSC-derived myofibrils, enabling measurements similar to those conducted in ARVMs [150].

Thus, while hiPSCs provide a valuable *in vitro* model for analysing cardiotoxicity for future therapeutics, their immaturity at shorter time points and the extended duration required to achieve phenotypically mature cardiomyocytes make them less ideal for applications requiring fully differentiated myocytes. Other model systems, such as ARVMs and NRVMs discussed earlier, are easier to establish, cost-effective, and exhibit relatively low variability.

Similar to NRVMs, hiPSC-CMs are largely immature, lacking T-tubules and exhibiting high expression levels of immature sarcomeric protein isoforms [151]. However, since they are human cells, their expression profiles for other proteins, such as PDEs, could be expected to be more similar to those of human cells compared to NRVMs. Advancing our understanding of the intracellular signalling processes in hiPSC-CMs and their responses to pharmacological agents may facilitate the differentiation of hiPSC-CMs into more mature phenotypes. This progress could enable experiments with human adult-like cardiomyocytes *in vitro*, providing a more accurate model for studying cardiac physiology and disease.

1.4.3 Computer modelling and simulation for studying myofilament function

The extensive data collected from cardiac cells has enabled researchers to reverse-engineer mechanisms and develop computer models of cardiac cells and the heart. These models can simulate a wide range of spatial scales, from whole 3D organs to subcellular processes [152, 153]. Computer models at the tissue and organ levels have been used to understand cellular signalling mechanisms and to study the effects of pharmaceutical interventions and drug therapies [154].

Computer modelling offers several benefits [155]. First, it allows for the simplification of complex biological systems by focusing on the key mechanisms driving a particular phenomenon. This approach reduces the influence of less critical components, which can obscure the primary factors involved in biological

systems. By simplifying, models can help to highlight the main components without being distracted by the myriad of smaller, potentially less relevant factors. Second, this simplification allows for the exploration of a wide range of parameters and conditions, which may not be feasible using experimental animal model-based approaches. While computer simulations may not provide definitive answers, they can significantly narrow the scope of necessary experiments, saving both time and resources. Third, computer models provide perfect control and observability, offering superior insights into system behaviour that experimental setups cannot match. However, it is important to note that regardless of the scale, computational models are simplifications of experimentally obtained data, which can be an inherent limitation.

Relevant to this study are single-cell models focused on cellular physiology and myofilament signalling which can be extended to tissue and 3D simulations [156]. The first electrophysiology model of this type was the Noble model [157], but the Luo-Rudy guinea pig model (1991) [158] has become a particularly prominent precursor to many contemporary models. In these models, most ionic currents are described using equations dependent on ionic concentrations, kinetic changes, or membrane potential, as outlined in Section 1.1.2. An alternative approach, employed in several currents within the Rudy family of models, is the use of Markov models to represent ion channels. This approach allows for the representation of various open and closed states of the channel and their transitions, providing greater flexibility at the cost of increased computational complexity [159].

Today, numerous cardiac cell models exist, each tailored to different cell types and species. Each model has its strengths and limitations, and the choice of model should be guided by the specific research question. There are three well-known hiPSC-CM *in silico* models, all parameterised using stem cell-derived cardiomyocyte data: the Paci [160], Koivumäki [161], and Kernik models [162]. These models are all single-cell models, with similar formulations for certain ionic currents. Notably, the Kernik and Koivumäki models use Markov formulations for Ca^{2+} release from the SR [163]. This approach captures the stochastic nature of channel opening

and closing [164]. Paci model employs a Hodgkin-Huxley formulation for the same process [163]. This approach uses a set of differential equations to describe the overall ionic currents based on empirical variables for channel activation and inactivation [165, 166]. Although the three models provide qualitatively consistent results in drug activity simulations, they exhibit varying susceptibilities to drug-induced pro-arrhythmic events [163]. The performance and characteristics of these models have been compared and characterised previously [163].

The regulation of myofilament function has also been explored using experimental and computational tools, and multiple mathematical models describing myofilament mechanics exist. The development of novel computer models describing cardiac mechanics has provided useful insights into cardiac physiology [167]. The first models describing myofilament dynamics were generated by Hill (1938) and Huxley (1957) [165, 166].

In the Huxley model, muscle tension is generated by crossbridges based on protein dynamics. This model recapitulated Hill's force-velocity relationship by modelling only two crossbridge states, attached and detached. The relative position of the actin-binding site to the equilibrium position of the nearest crossbridge was the key factor influencing the rate constants for crossbridges attachment and detachment. The force of an attached crossbridge was assumed to be a linear function of the distortion from the equilibrium position. Despite the very simplistic representation, modified versions of this two-state crossbridge model continue to be used. The sliding myofilament theory is described in the section 1.1.3.

Recent advancements in the field have resulted in a variety of models with different levels of complexity (Table 1.2). Among these is the human adult cardiomyocyte contraction model developed by Land et al. (2017) [168]. This model accurately reproduces contraction and passive viscoelasticity in human myocytes, incorporating key elements such as TNC and tropomyosin kinetics, a three-state crossbridge model accounting for crossbridge distortion, and the cellular viscoelastic response. Each component was parameterised using a comprehensive

set of experimental data that characterises the passive tension and active contractile properties of skinned human cardiac myocytes at physiological body temperature.

For active tension, the model employs a straightforward approach to cooperative activation, where thin filament kinetics are governed by the interactions between calcium ions, TNC, and tropomyosin, which regulate the availability of myosin binding sites on actin. Overall, this model provides a detailed yet computationally efficient representation of active contraction in human cardiomyocyte, aligning its complexity with the available experimental data. For these reasons, this model was selected for the computational studies conducted in this thesis. The specific cellular models utilised in this thesis are discussed in detail in Chapter 5.

For translation to humans, hiPSC-CMs electromechanical models are considered promising for experimentally validating simulation results, due to the broader availability of hiPSC-CMs compared to human primary cardiac myocytes [169]. By bridging *in silico* investigations of myofilament regulation with the utilities offered by hiPSC-CMs, an *in vitro-in silico* framework can be established. This framework facilitates quick, inexpensive, and experimentally validated insights into the regulation of myofilament function. The integration of *in silico* tools enables the evaluation of experiments and the investigation of specific simulation scenarios, a method that has been applied in both academic and industry settings [170, 171].

HiPSC-CMs are extensively used for *in vitro* studies, ranging from drug toxicity testing to patient-specific disease modelling. *In silico* hiPSC-CM studies have been instrumental in enhancing our understanding of hiPSC-CM pharmacological and physiological properties, aiding in the translation of data to adult cells [160]. However, most existing electrophysiological computer models of hiPSC-CMs lack a force generation mechanism, which is crucial for studies focused on contractility. which is crucial for studies focused on contractility. The absence of biophysical models of hiPSC-CM electromechanics that can accurately simulate the effects of drugs on both electrophysiology and contraction represents a significant gap in the field, particularly for research questions that necessitate an integrated analysis of electrical activity and mechanical function.

Table 1.2: Different components of published cardiomyocyte electromechanical models.

Model	TPN	MYBPC	cAMP/ PKA	Cell type	Ref
Rice	+	-	-	Rabbit, rat	[172]
Campbell 2010	+	-	-	Rabbit, rat	[173]
Land 2017	+	-	-	Human	[168]
Land 2012	+	-	-	Mouse	[174]
Wang-Campbell 2010	+	+	-	Mouse	[175]
Mijailovich 2017	-	-	-	Human	[176]
Campbell 2018	+	+	-	Rabbit, rat	[167]
Balakina-Vikulova	+	-	-	Human	[177]
Lyon-Dupuis	+	-	+	Human	[178, 179]
Mijailovich 2021	+	some parameters related to MYBPC	-	Rat	[180]
Forouzandehmehr-Paci-Rice 2021	+	-	-	hiPSC-CM, rabbit	[169]

By integrating *in silico* tools with *in vitro* models like hiPSC-CMs, researchers can gain detailed insights into cellular processes, explore various parameters, and develop more effective therapies. Comprehensive hiPSC-CM models are useful for understanding hiPSC-CM physiology and signalling mechanisms. The models can also simulate drug responses and pathological signalling; for example, a recent hiPSC-CM electromechanical model based on contractile rabbit data and hiPSC-CM electrophysiology has proven effective in investigating hypertrophic cardiomyopathy and drug response dynamics [169].

In silico hiPSC-CM studies also enhance our understanding of myofilament signalling in human cardiomyocytes, allowing for experimental validation of model predictions using the same cell types. This integration creates a robust *in vitro-in silico* framework, providing valuable insights into cardiomyocyte signalling mechanisms.

1.5 Thesis Aims

Properly executed cardiac contraction and relaxation are essential for maintaining the normal function of the heart. Heart's contraction is driven by a finely tuned sequence of electrical and mechanical events, including the propagation of action potentials, calcium influx, and the activation of myofilament proteins within cardiomyocytes. During systole, calcium ions bind to troponin leading to muscle contraction. During diastole, calcium ions are actively removed from the cytoplasm, and the heart muscle returns to its resting state. The ability of the heart to modulate its contractility and relaxation in response to varying physiological demands, such as exercise or stress, is critical for maintaining adequate blood flow and ensuring tissue oxygenation.

Sympathetic stimulation and catecholamine release, prompted under stress conditions (e.g., during physical strain), modulate cardiac activity. These effects are mediated by signalling pathways involving the regulation of myofilament function by cyclic cAMP and PKA. The cAMP signalling pathway plays a crucial role in regulating cardiac myofilament function. cAMP acts as a second messenger, mediating the effects of catecholamines by activating PKA. cAMP signal is terminated by the PDE-mediated hydrolysis. Upon activation, PKA phosphorylates key myofilament proteins which in turn allows for faster relaxation and increased cross-bridge cycling rate. This precise regulation is vital for adapting cardiac output to meet the physiological demands placed on the heart.

However, when these regulatory mechanisms are disrupted, it can lead to cardiac pathologies such as HF and diastolic dysfunction. HF and diastolic dysfunction are leading contributors to cardiovascular mortality and morbidity, with HF affecting over 26 million people worldwide and diastolic dysfunction being prevalent in more than 50% of HF cases [181]. Alterations in myofilament signalling and cAMP/PKA pathway dysregulation are implicated in these conditions, underscoring the importance of understanding these mechanisms in both health and disease.

Current therapeutics, such as beta-blockers and PDE inhibitors, aim to modulate these pathways but often lack specificity and can have undesirable side effects [34].

Beta-blockers, for instance, blunt sympathetic stimulation but do not selectively target subcellular cAMP domains leading to a range of systemic effects [182]. Phosphodiesterase inhibitors like milrinone increase cAMP levels but can cause arrhythmias and increased mortality in chronic HF patients, highlighting the need for more targeted therapeutic approaches [183].

There is a significant gap in knowledge regarding the specific mechanisms by which cAMP, PDEs, and PKA regulate myofilament function, particularly the spatial and temporal dynamics of cAMP signalling within cardiomyocytes. The existence and functional relevance of cAMP nanodomains within myofilaments, and how these are modulated by specific PDE isoforms, remain poorly understood. Additionally, the role of cAMP buffering, potentially mediated through PKA phase separation, in the regulation of myofilament signalling and its impact on cardiac contractility is not characterised [111]. Finally, understanding the processes of the myofilament function regulation is particularly challenging in experimental systems, where multiple overlapping pathways complicate the isolation of specific mechanisms. This limitation hinders the ability to accurately characterise how cardiac contractility is modulated. To address these challenges, this study introduces a computational modelling platform that integrates myofilament contraction dynamics. This platform complements experimental findings and provides a tool for investigating the regulatory mechanisms of myofilament function.

Addressing the previously outlined gaps and understanding how the regulation of myofilament function is achieved in cardiomyocytes is the primary aim of this thesis. In greater detail, the aims are:

1. To assess cAMP signalling at the myofilament by testing the following hypotheses: a) cAMP forms spatio-temporal gradients across the sarcomere from the Z to M line, and b) TNI, MYBPC, and M line proteins define distinct cAMP nanodomains that independently regulate cAMP-PKA signalling at the myofilament, facilitated by differential PDE activity at the different locations.

2. To characterise the impact of PKA phase separation on myofilament cAMP signalling by testing the hypothesis that PKA LLPS contributes to cAMP compartmentalisation at the myofilament.

3. To develop and validate an *in silico* platform that integrates and extends experimental findings.

After giving an overview of general methodology in Chapter 2, Chapters 3-5 describe how thesis aims are met. Studies related to aim 1 are detailed in Chapter 3; for aim 2 in Chapter 4; and for aim 3 in Chapter 5 and 6. The discussion of the findings is provided in Chapter 7.

2
Methods

This section includes the details of the methodology used in the project including the experimental reagents and protocols.

2.1 Experimental Materials and Methods

2.1.1 Reagents

Cilostamide, forskolin, 3-isobutyl-1-methylxanthine (IBMX), isoproterenol, prostaglandin E2 (PGE2), 1,6-hexanediol (HEX), 2,5-hexanediol and norepinephrine were from Sigma-Aldrich; myristoylated PKA inhibitor was from Calbiochem; BAY 60-7550 (BAY) was from Cayman Chemicals. SNAP was from Abcam and BAY 41-2272 was from Torcis Biosciences. Rolipram and Duloxetine were from Thermo Fisher Scientific. H89 was from Calbiochem, PDE8 inhibitor PF-04957325 was from MedChem Express, and semaglutide was from Cambridge Bioscience.

Collagenase A was from Roche; pancreatin was from Sigma; laminin (mouse) was from BD Biosciences; PBS, DMEM high glucose, MEM199, horse serum, newborn calf serum, penicillin/streptomycin (10000 units of penicillin [base] and 10000 µg of streptomycin [base]/mL), and L-glutamine were from Invitrogen. Transfection reagents included transfectin (BioRad) and Polyjet (Signagen).

2.1.2 HEK293T and hiPSC-CM culture

The HEK293T cell line was cultured in Dulbecco's modified Eagle medium (DMEM, Gibco) containing 1 g/L glucose, supplemented with 10% fetal bovine serum (FBS, Sigma) and 1% penicillin–streptomycin (Pen-Strep, Sigma-Aldrich). Cells were kept in a 37°C humidified incubator with 5% CO2.

Human induced pluripotent stem cells (hiPSCs) were cultured and differentiated initially with the assistance of Dr Koschinski. HiPSCs used (M180 line, from human adult myoblasts from healthy individuals) [184] were cultured in mTeSR Plus medium (Stemcell Technologies) on Matrigel (8 µg/cm^2; Corning)-coated surfaces as described previously [39]. Cells were passaged twice a week using DPBS (Gibco) for rinsing and accutase (Sigma-Aldrich) for dissociation. The ROCK (Rho Kinase) inhibitor (StemMACS Y27632, 10 µmol/L; Miltenyi Biotech) was added for the first 24 hours after seeding.

Differentiation into cardiomyocytes was induced in monolayer culture, as described previously [39]. Differentiated human induced pluripotent stem cell-derived cardiac myocytes (hiPSC-CM) were maintained in RPMI 1640 medium with Glutamax and 25 mM HEPES (Gibco) with B27 supplement (Gibco). hiPSC derived cardiomyocytes (hiPSC-CM) were used for calcium imaging experiments.

2.1.3 Primary Rat Ventricular Cardiomyocyte Isolation and Culture

All animal procedures conform to the guidelines from Directive 2010/63/EU on the protection of animals used for scientific purposes. Adult rat ventricular myocytes (ARVMs) from female Sprague-Dawley rats were isolated by Dr Chao as described previously [39]. For viral infection, isolated ARVMs were plated on dishes pre-coated with 1 µg/cm^2 laminin in culture medium (MEM 199, 5% FBS, 5 mmol/L creatine, 2 mmol/L L-carnitine, 5 mmol/L taurine, 0.1× insulin-transferrin-selenium-X, 2 mmol/L L-glutamine, 100 units/mL penicillin, and 100 µg/mL streptomycin).

Neonatal rat ventricular myocytes (NRVMs) from 2-days-old Sprague-Dawley pups were isolated as previously described [39]. Briefly, neonatal rats were decapitated using sterile scissors, and the chest was opened along the sternum. The hearts were extracted from the body and transferred immediately into the ADS buffer (1.2 mM NaCl, 0.05 mM KCl, 0.18 HEPES, 0.008 mM NaH_2PO_4, 0.06 mM glucose, 0.004 mM $MgSO_4$) on ice. Large vessels and atria were removed, and the ventricles were rinsed in the ADS buffer to remove blood. The hearts were transferred to the 60 mm dish with ADS and cut in small pieces. Tissue pieces were transferred into 5 mL of collagenase solution (0.2 mg/mL pancreatin (Sigma-Aldrich), 207 U/mL collagenase (Roche) in ADS buffer). The solution with the heart tissue was incubated under continuous agitation at 37°C for 5 min. The supernatant was discarded. Serial digestions were then performed where cardiac tissue pieces were incubated in 9 ml of collagenase solution for 20 min under continuous agitation at 37°C. After each digestion step, the cell suspension was collected and placed in 2 ml of newborn calf serum (NCS), and centrifuged at 1250 rpm for 5 minutes. The pellet was resuspended in 2 ml of NCS and kept at 37°C in the incubator.

After all digestions, the cell-suspensions in NCS were pooled and centrifuged again for 5 minutes at 1250 rpm. The pellet was then resuspended in M1 medium (4.5 g D-glucose/L DMEM (Invitrogen) with 17% M199 (Invitrogen), 10% horse serum, 5% NCS, 2 mmol/L L-glutamine, 100 units/mL penicillin and 100 µg/mL streptomycin). The cells were pre-plated in 100 mm dishes for 2 hours. After pre-plating, the cardiomyocyte-enriched fraction was removed by taking up the medium from the dishes. The remaining attached cells were labelled as non-myocytes.

For viral transduction and/or plasmid transfection, cardiomyocytes were seeded on laminin-coated 35 mm diameter coverslips with 12 mm diameter rings, as described before [185], in M1 medium, at 20-60,000 density. After 18 hours, the medium was changed to M2 medium (4.5 g/L D-glucose DMEM (Invitrogen) with 17% M199 (Invitrogen), 5% horse serum, 0.5% NCS, 2 mmol/L L-glutamine, 100 units/mL penicillin, and 100 µg/mL streptomycin), and the cells were allowed to adjust for 2 hours in a 37°C humidified incubator with 5% CO_2 before viral transduction.

2.1.4 Plasmids

A list of all the plasmid constructs used throughout this work are outlined in the Table 2.1. All previously unpublished and newly generated constructs were verified by sequencing.

Table 2.1: The list of plasmids used.

Name	Tag	Reference
PKA RIα	RFP	[29]
PKA RIα	GFP	[29]
PKA RIα dl	CFP	[186]
PKA RIIβ	RFP	[29]
PKA Cat	Venus	[186]
HT31		[186]
HT31P		[186]
RIAD		[29]
SUPER-AKAP-IS		[29]
PKI		[187]
FluoSTEP-AKAR	GFP1-10, RFP	[111]
FluoSTEP-ICUE	GFP1-10, RFP	[111]
MYOM-CUTie	CFP, YFP	
PDE4D9	VSV	[188]
PDE4B1	VSV	[188]
PDE4D9	GFP	[189]
PDE4D4	GFP	[189]
PDE4A4	GFP	[190]
Ezrin	GFP	[29]
AKAP79	RFP	[29]

2.1.5 Transfection and Infection

HEK293T cells used in the experiments were transfected with PolyJet transfection reagent according to the manufacturer's instructions (Signagen). Briefly, 1-2.0 µg of plasmid DNA was resuspended in 200 µL of transfection buffer, vortexed, and incubated for 5 min at room temperature (RT). The transfection reagent was added at a ratio 1:2 reagent to DNA. The solution was mixed and incubated for 10 min at RT before being added to the cells seeded on 35 mm glass coverslips.

Primary cardiomyocytes were transfected with DNA using Transfectin reagent (Bio-Rad) following the manufacturer's instructions, similar to the procedure

described above. Cells were used for imaging after 24-48h of transfection. Where indicated, the cells were infected with adenoviral vectors and used for imaging 18-48h after infection.

2.1.6 In vitro hypertrophy and cell size measurements

To induce hypertrophy, NRVM cells were treated with norepinephrine (10 µmol/L, Sigma-Aldrich) for 48h before cell size determination [39]. For determining cell size, cells were imaged in bright-field mode on an Olympus IX71 inverted microscope, equipped with Olympus 40× UPlanFLN and 60× PlanApoN oil immersion objectives (NA 1.3 and 1.42, respectively) using MetaFluor 7.1 (Molecular Devices). Cell surface area was calculated with ImageJ by selecting the cell area as a region of interest and by analysing the number of pixels within the region of interest.

2.1.7 Fluorescence Resonance Energy Transfer (FRET)

FRET biosensors used throughout this work are listed in the Table 2.2. General structure of FRET biosensor is outlined in the Figure 2.1.

FRET imaging experiments were performed 24-48h after infection or transfection. Cells were pre-incubated for 10 min at RT in a modified Ringer solution (125 mM NaCl, 5 mM KCl, 1 mM Na_3PO_4, 1 mM $MgSO_4$, 20 mM HEPES, 5.5 mM glucose, 1 mM $CaCl_2$, pH 7.4) before starting the experiment. For the FRET experiments, cells were imaged on an inverted microscope (Olympus IX71) using a PlanApoN, 40X, NA 1.42 oil immersion objective (Olympus, UK). The microscope was equipped with a CoolSNAP HQ2 CCD camera (Photometrics) and a DV2 beam-splitter (MAG Biosystems, Photometrics). The FRET filters used were: CFP excitation filter ET436/20x, dichroic mirror 455DCLP, GFP excitation 480/30 (all from Chroma Technology) in the microscope filter cube; dichroic mirror 505dcxr, YFP emission filter 535/30 nm, CFP emission filter 480/30 nm (Chroma Technology) in the beam splitter, GFP emission filter 535/45 nm, RFP emmission filter 653/95.

Images were acquired using Metafluor 7.1 software (Molecular Devices). FRET changes were measured as changes in the background-subtracted fluorescence

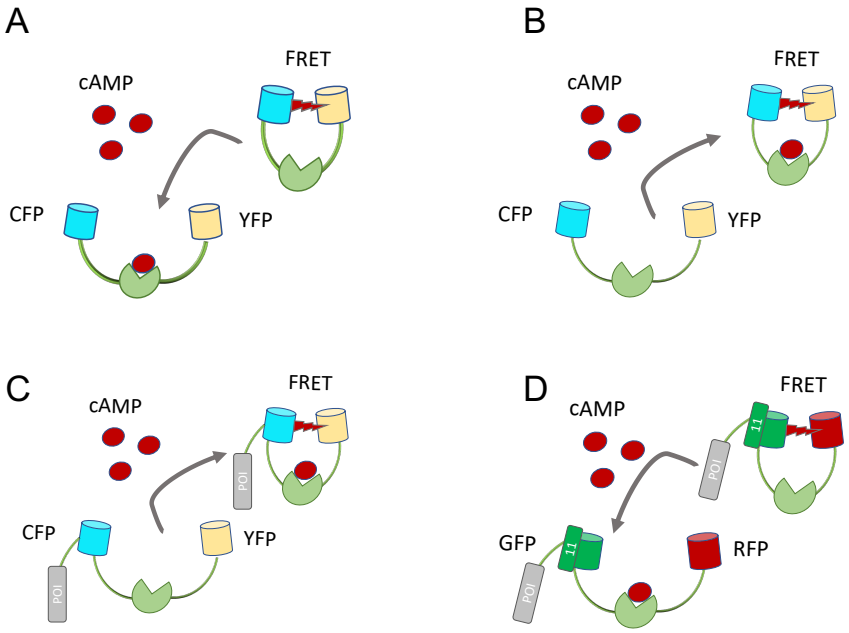


Figure 2.1: Schematic representation of different types of FRET biosensors used. Here POI - protein of interest. **A.** Loss of FRET sensor, including EPAC-SH187. **B.** Gain of FRET sensor, including CUTie cytosolic sensor. **C.** Gain of FRET targeted sensor including AKAP79 CUTie sensor. **D.** Loss of FRET sensor where donor, GFP, has to be reconstituted by binding GFP11 connected to a target. These type of sensors include FluoSTEP sensors.

emission ratio upon excitation and expressed as R/R0, where R is the ratio at any given time t and R0 is the initial ratio at time = 0 s. FRET time courses were normalized to R0 since it allows an easy comparison between different FRET curves. Quantification of these curves was performed by normalizing to the FRET value acquired after sensor saturation (achieved with 25 µM forskolin and 100 µM IBMX application) and shown as a percentage of saturation. Analysis was performed using Excel (Microsoft), MATLAB (MathWorks), and Prism (GraphPad).

2.1.8 Immunofluorescence

For immunofluorescence experiments, HEK293T, NRVM, or ARVM cells were fixed with 4% paraformaldehyde (Thermo Scientific) in PBS for 10 min, washed with PBS, permeabilised with 0.1% Triton X100 (Thermo Scientific) for 5 min, and washed with PBS again. Non-specific labelling was blocked with a 30 min incubation at RT with 1% bovine serum albumnin (BSA) (fraction V, Roche), 22.52 mg/mL glycine

Table 2.2: The list of FRET biosensors used. Here: AdV: adenoviral, SR: sarcoplasmic reticulum, PKA: protein kinase A.

Name	Fluorophores	Vector	Localisation	Gain or loss of FRET	Type	Reference
Cytosolic CUTie	CFP-YFP	AdV	cytosolic	Gain	cAMP	[34]
AKAP18δ CUTie	CFP-YFP	AdV	SR	Gain	cAMP	[34]
AKAP79 CUTie	CFP-YFP	AdV	membrane	Gain	cAMP	[34]
TPNI CUTie	CFP-YFP	AdV	myofilament	Gain	cAMP	[34]
MYBPC CUTie	CFP-YFP	AdV	myofilament	Gain	cAMP	[34]
MYOM CUTie	CFP-YFP	Plasmid and AdV	myofilament	Gain	cAMP	
EPAC-SH-187	CFP-YFP	AdV	cytosolic	Loss	cAMP	[191]
FluoSTEP-AKAR	GFP-RFP	Plasmid	cytosolic	Gain	PKA activity	[111]
FluoSTEP-ICUE	GFP-RFP	Plasmid	cytosolic	Loss	cAMP	[111]

(Thermo Scientific), and 0.1% Tween20 (Thermo Scientific) in PBS. All antibodies were diluted in the same solution. Primary antibodies were incubated for 1h at RT, followed by three washes with PBS. The samples were then incubated with secondary antibodies for 1h at RT, followed by washes with PBS. Coverslips were then either mounted using mounting media with DAPI (Ibidi) and sealed with nail varnish, or kept in PBS for further processing (for expansion microscopy, as detailed in Chapter 3). Antibody information and dilutions are indicated in the Table 2.3.

Immunofluorescence imaging was performed using a confocal laser scanning microscope at 60X, water immersion objective (TCS SP5 II; Leica, Germany). Images were acquired using NDP software (Hamamatsu) and processed using ImageJ.

2.1.9 Western blotting and co-immunoprecipitation

Western blotting and co-immunoprecipitation experiments were performed as described before [39]. For co-immunoprecipitations, where indicated, cells were transfected with PDE8A-RFP, PDE4D9-VSV, or PDE4B1-VSV plasmids. The cells

Table 2.3: The list of the antibodies used.

Type	Target	Species	Company	Dilution
Primary	Troponin	goat	Thermo Fisher Scientific	1:100
Primary	MYBPC	mouse	Abcam	1:200
Primary	α-actinin	mouse	Abcam	1:300
Primary	Phosphorylated troponin	rabbit	Abcam	1:100
Secondary	Alexa 488	anti-mouse	Thermo Fisher Scientific	1:300
Secondary	Alexa 568	anti-mouse	Thermo Fisher Scientific	1:300
Secondary	Alexa 488	anti-goat	Thermo Fisher Scientific	1:300
Secondary	Alexa 568	anti-goat	Thermo Fisher Scientific	1:300
Secondary	Alexa 488	anti-rabbit	Thermo Fisher Scientific	1:300
Secondary	Alexa 568	anti-rabbit	Thermo Fisher Scientific	1:300
Secondary	ATTO 647N	anti-rabbit	Sigma-Aldrich	1:300

(HEK293T, NRVMs, or hiPSC-CMs) were harvested, and lysates were prepared using an IP buffer (50 mM HEPES pH 7.4, 150 mM NaCl, 2 mM EDTA, 10% glycerol, 0.5% Triton-X-100 or 50 mM Tris pH7.4, 150 mM NaCl, 1 mM EDTA, and 1% nonyl phenoxypolyethoxylethanol), supplemented with PhosSTOP phosphatase inhibitor cocktail (Roche) and complete protease inhibitor cocktail (Roche). Protein concentrations were determined using the Bradford assay (Bio-Rad).

For co-immunoprecipitation, lysates were incubated overnight at 4°C with anti-TNI or anti-RFP antibodies and protein A sepharose beads (Sigma-Aldrich) or protein A agarose (Thermo Scientific) beads for 6 to 8 hours at 4°C. Bound proteins were eluted in 25 µL of SDS-loading buffer (Life Technologies) and released from the beads at 95°C for 5 minutes.

For western blotting, 10 to 30 µg of protein per sample was resolved on 4% to 12% Bis-Tris polyacrylamide gels (Invitrogen) and transferred to nitrocellulose membranes using the XCell II Blot Module (Thermo Fisher Scientific). To prevent nonspecific binding of the primary antibody, membranes were blocked in 5% milk

(Millipore) or phosphoblocker (Cell Biolabs) made in TBST for 1h at RT. Incubation with the primary antibodies (1:2000) was performed at 4°C overnight with gentle agitation. Horseradish peroxidase–conjugated secondary antibodies were used at a dilution of 1:5000. The amount of peroxidase activity remaining on the membrane after washes with TBST was determined using X-Ray Film (GE Healthcare), in combination with Clarity ECL developing solution (Bio-Rad) or Supersignal West Atto (Thermo Scientific). Chemiluminescent signal was detected using a ChemiDoc XRS+ (Bio-Rad) imaging system.

2.1.10 Data and Statistical Analysis

Data were analysed using Fiji (ImageJ) for image processing, Prism (GraphPad) for statistical analyses, Excel for FRET data collection, and MATLAB (Mathworks) for FRET data analysis.

Unless indicated otherwise in the figure legends, data presented on the graphs are visualised as means ± standard deviation (SD) for normally distributed data. For non-normally distributed data, results are presented as medians ± SD. Sample size (n) is specified in the figure legends. All data presented in the figures were obtained from at least three separate NRVM isolations to ensure reproducibility and mitigate batch effects. The number (N) of NRVM or ARVM isolations used for the experiments are indicated in the figure descriptions. For analyses of HEK293T data, all the data was acquired is from at least two different passages. For analyses of hiPSC-CM data, all the data acquired was from individual cells (n), 2 separate differentiations. Simulations with hiPSC-CM computational model serve as data augmentation tool. Error bars and shaded areas in graphs represent SD, unless otherwise specified in the figure legends.

For FRET data analysis, each data point represents observations from individual cells or specific subcellular structures, as specified in the figure legends. Observations from different cells were considered independent, supported by pilot experiments where identical stimuli elicited distinct responses in adjacent cells, validating the independence of observations.

Statistical analyses began with data collection and plotting. Normality was assessed using the Shapiro-Wilk test, suitable for small samples (<50 samples). Data were considered normally distributed if the p-value was greater than 0.05, indicating that the null hypothesis of normal distribution could not be rejected. For very small samples (less than 8), data were not assumed to be normally distributed regardless of Shapiro-Wilk test results. Homoscedasticity among groups was evaluated using the F-test and by visual inspection of data spread.

If data were normally distributed and variances were equal, a t-test was used to determine significant differences between groups. Paired t-tests were applied to data collected over time from the same cell or subcellular region. For comparisons involving more than two groups, analysis of variance (ANOVA) was conducted with a Bonferroni correction for multiple comparisons. Welch's correction was applied if variances were unequal.

For non-normally distributed data, the Mann-Whitney U test was used for two-group comparisons, and the Wilcoxon signed- rank test for paired comparisons. For multiple group comparisons, the Kruskal-Wallis test was used with Dunn's correction for multiple comparisons.

Where data distribution was analysed using regression models, the goodness of fit was assessed by RMSE and adjusted R-squared values, both reported in the figure legends. Where data correlation was assessed, Spearman's correlation coefficient (R-squared) values were reported. Where applicable, a chi-square (chi-sq) test of independence was performed to examine the relations between variables.

In the figures, p-values less than 0.05 were considered statistically significant and denoted with *, $p<0.01$ with **, and $p<0.001$ with ***. Groups not found to be significantly different were labeled as 'ns'.

3

cAMP signalling domains at the myofilament

3.1 Introduction

Cardiac myofilaments enable the heart's contraction and relaxation. Contraction is initiated by an action potential signal leading to the opening of calcium channels. The influx of calcium into the sarcoplasm, amplified by calcium-induced calcium release, elevates intracellular calcium levels.

Calcium binds to troponin C (TNC) which reduces the affinity of troponin I (TNI) for actin, thereby exposing myosin-binding sites. Myosin heads can now attach to actin and form a cross-bridge [21]. Once the cross-bridge is formed, the actin and myosin filaments slide past each other, shortening the sarcomere and resulting in muscle contraction. In addition to troponins, other regulatory proteins such as myosin binding protein C (MYBPC) are essential for enabling cardiac contraction and relaxation.

Calcium homeostasis is essential for proper cardiac contraction. In 2015, Previs et al. described the calcium gradients within the sarcomere (Fig. 3.1) [192]. During cardiac cycle, calcium is released from the T tubules that run along Z lines at the ends of the sarcomere and diffuses towards the center to fully activate the contractile proteins. The resulting spatial and temporal free calcium gradient

would be expected to lead to a nonuniform activation of cross-bridge formation. The study demonstrated that MYBPC, through its positioning on the myosin thick filaments, corrects this non-uniformity in calcium activation by sensitising the contractile apparatus to calcium in a manner that precisely counterbalances the calcium gradient.

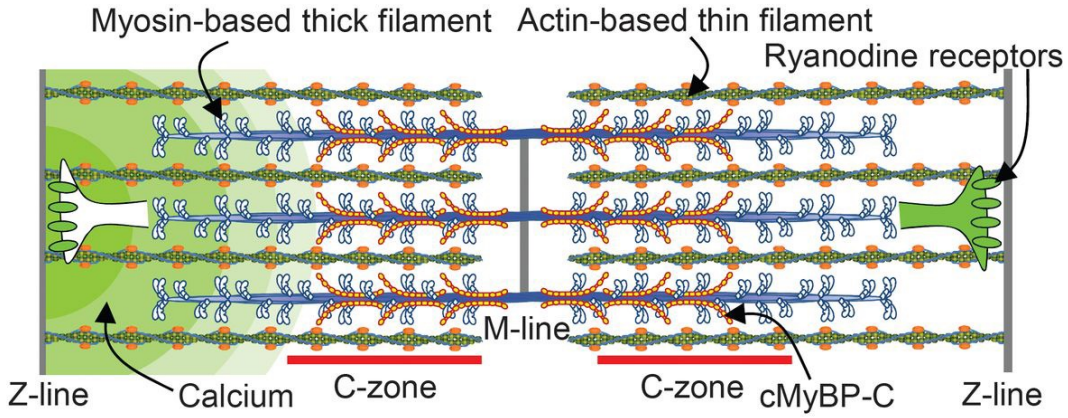


Figure 3.1: Calcium gradients across the sarcomere. Adapted from Previs et al. (2015) [192] (CC BY 4.0).

In addition to calcium, myofilament proteins and cardiac contraction are regulated by post-translational modifications. For example, cAMP-activated protein kinase A (PKA)-mediated phosphorylation of proteins such as TNI and MYBPC adjusts the calcium sensitivity of the myofilament thereby accelerating cross-bridge kinetics.

It is clear that, like calcium, cAMP signalling plays a crucial role in coordinating cardiac muscle function by regulating myofilament protein activity. Currently, it is unknown whether gradients of cAMP similar to those reported for calcium occur across the sarcomere, though it is plausible given that cAMP is thought to be predominantly generated by membrane-bound adenylyl cyclases (AC) activation of receptors localised on the membrane of T-tubules that run along Z lines.

cAMP-PKA signals are compartmentalised in the cells. Several factors are essential for enabling this compartmentalisation, including phosphodiesterases (PDEs) and PKA anchoring proteins (AKAPs). cAMP compartmentalisation has

been shown to be implicated in controlling cardiac calcium signalling, receptor function, cell cycle, and contraction [186].

cAMP-PKA compartmentalisation occurs at the myofilament and is essential for physiological cardiac cell contraction. Upon beta-adrenergic receptor (βAR) stimulation, the increase in cAMP levels is significantly lower near TNI compared to cytosol, plasma membrane, or the sarcoplasmic reticulum (SR) [34]. Furthermore, inhibition of PDEs, which abolishes this compartmentalisation and results in a homogeneous increase in cAMP throughout the cardiomyocyte, leads to a reduced contractile response to adrenergic stimulation. This finding illustrates that distinct cAMP signals with different amplitude occurring simultaneously across the cardiomyocyte are necessary to achieve maximal contraction efficiency.

This differential distribution of cAMP pools likely underscores the role of various PDEs in creating distinct cAMP microenvironments within the cell. The primary PDEs involved in this regulation at the myofilament are PDE4 and PDE3, with PDE2 playing a lesser role in rat hearts. Interestingly, the inhibition of PDE4 in the absence of βAR stimulation does not alter sarcomere function or TNI phosphorylation [44], suggesting a stimulus-dependent recruitment of PDE4 to the myofilament, or enhancement of its activity.

Upon βAR stimulation, PKA phosphorylates TNI at serines 23 and 24. This phosphorylation decreases myofilament calcium sensitivity, promoting faster muscle relaxation, increased rate of cross-bridge cycling, and an increase in peak force (positive inotropy) [101]. The entire troponin complex plays a critical role, with TNT serving as an AKAP [193], anchoring PKA to the troponin complex and enhancing the specificity and efficiency of the phosphorylation process. Both MYBPC and TNI interact with myomegalin (also called PDE4DIP), an AKAP involved in the control of MYBPC and TNI phosphorylation [84].

MYBPC is phosphorylated at up to four sites by various kinases, including PKA. PDEs play a crucial role in reducing cAMP levels in the proximity of MYBPC, and inhibition of PDE2, PDE3, or PDE4 increases MYBPC phosphorylation [91]. Phosphorylation of MYBPC increases the availability of myosin heads for

interaction with actin, thereby enhancing contraction [102]. MYBPC is known to be phosphorylated in the absence of hormonal stimulation [103], and dephosphorylation of MYBPC leads to reduced contractility of the heart and the development of hypertrophy [103, 104].

Under βAR stimulation, inhibition of PDE4 and PDE3 leads to enhanced phosphorylation of both, TNI and MYBPC. PDE2 inhibition also enhances MYBPC phosphorylation but that is not the case for TNI [44]. However, in the absence of βAR activation, PDE4 inhibition does not affect sarcomere shortening or TNI phosphorylation. In the absence of βAR activation, TNI phosphorylation is enhanced by PDE3 and PDE2 inhibition, and MYBPC phosphorylation is enhanced by PDE4, PDE3, and PDE2 inhibition [44].

cAMP signalling at the myofilament level could be highly localised, creating discrete nanodomains that specifically influence proteins like TNI and MYBPC, thereby enabling finely tuned contraction regulation. First, the distance between TNI and MYBPC (10-15 nm, Fig. 1.6) may be sufficient to form and maintain distinct, non-overlapping nanometer-sized cAMP domains. Second, from a physiological perspective, this separation would be functional, as TNI and MYBPC appear to have opposing effects: TNI phosphorylation enhances relaxation, reducing myofilament sensitivity to calcium, whereas MYBPC phosphorylation promotes contraction by modulating the interaction between myosin and actin [101, 194].

This would imply a different distribution of cAMP across the sarcomere compared to that outlined by Previs et al. (2015) for calcium. On the other hand, the small distances between the PKA phosphorylation sites of TNI and MYBPC, which range between 10 to 15 nm depending on sarcomere length and cell preparation, suggest that their phosphorylation might be carried out by the same PKA subset, occurring simultaneously and in the same location without distinct cAMP-PKA signalling signatures between these sites [11].

Understanding the precise spatio-temporal regulation of myofilament proteins is crucial for advancing our knowledge of heart cell physiology, the onset and progression of cardiac pathologies, and for identifying new drug targets.

Disruptions in cAMP-dependent regulation of myofilament function are linked to various cardiovascular disorders. In both human and experimental heart failure (HF) samples, a reduction in the phosphorylation of TNI and MYBPC has been observed, despite comparable overall PKA activity levels following cAMP stimulation between failing and non-failing hearts [91]. In hypertrophic cardiomyocytes, despite maintained cytosolic cAMP levels, cAMP signals triggered by βAR stimulation are significantly reduced at the myofilament [34], aligning with the observed hypo-phosphorylation of TNI and MYBPC. The primary PDEs regulating cAMP at the myofilament are under-expressed in failing hearts [91], highlighting the need for further investigation into myofilament-associated PDEs. Currently, no pharmacological agents specifically target PDE-myofilament or PKA-myofilament interactions.

Understanding how cAMP is regulated at the myofilament is particularly relevant for treating heart failure with preserved ejection fraction (HFpEF), which involves impaired myocardial relaxation. While beta-blockers are effective in heart failure with reduced ejection fraction (HFrEF), they are not beneficial in HFpEF, possibly because further reduction in TNI phosphorylation exacerbates the functional deficit [195, 196]. Identifying new precision medicine approaches could lead to much needed better therapies.

This chapter aims to elucidate cAMP signalling patterns at the myofilament, with a particular focus on TNI and MYBPC, proteins phosphorylated by cAMP-activated PKA and implicated in major cardiac pathologies. The primary hypothesis tested is that cAMP forms spatio-temporal gradients across the sarcomere from the Z to M line, similar to those of calcium.

3.2 Methods

3.2.1 FRET biosensors

To enable cAMP recordings at the M line, a novel FRET sensor targeted to myomesin was developed (MYOM-CUTie). The sensor was developed by cloning myomesin insert coding for 2 and 3 protein domains into the NheII site located 5' to the

CUTie sensor. The resulting sensor was sequenced to confirm the correct insertion. Sensor was characterised in cells as detailed in the Results.

3.2.2 Expansion Microscopy

Adult rat ventricular myocytes (ARVMs) were prepared, fixed, and immunostained as described in General Methods, Chapter 2. Immunostained samples were expanded to enable visualisation of fine elements in the subcellular space. Expansion microscopy (ExM) was performed on fixed and stained cell samples according to the proExM protocol for 4× expansion [197]. The protocol allows for direct anchoring of fluorescent molecules into the gel by addition of acryloyl groups. The protocol has been optimised by Dr Sheard [198]. Briefly, the cells after staining were incubated in 0.1 mg/mL anchoring reagent acryloyl-X (AcX, Thermo Scientific) in PBS overnight. Next day, samples were washed in PBS three times immediately prior to gelation.

Samples were incubated in gel monomer solution containing 8.6% sodium acrylate (Sigma-Aldrich) (w/v); 2.5% acrylamide (Sigma-Aldrich) (w/v); 0.15%, N,N-methylenebisacrylamide (Sigma-Aldrich) (w/v); 11.7% NaCl (w/v); and PBS; 0.1% for 30 min at 4°C. Gelation was carried out by forming a sealed chamber, comprising of two coverslips spaced apart by spacers. These glass spacers were created by cutting coverslips into rectangular strips with the rationale that these strips would allow to form a rigid chamber between the coverslip and parafilm coated glass slide without compressing the gel during the gelation step.

In order to polymerise the gel the coverslip with cells was incubated at 37°C for 2h in a humidified chamber in a polymer solution containing monomer solution with the addition of 0.1% amonium persulfate (APS, Sigma-Aldrich) which initiated the polymerisation, and 0.1% N,N,N,N-Tetramethylethylenediamine (TMED, Sigma-Aldrich). After the incubation, the gelation was complete.

Then, gels were removed from the parafilm-coated slide chambers with an insertion of a razor blade between the coverslip with cells and the spacer. The gel was cut into an asymmetrical shape to enable tracking which side of the gel has the fluorescent sample. The dimensions of the gel were measured to obtain the

pre-expansion size. Gels were then placed into a 35 mm diameter dishes to undergo digestion in a solution containing Proteinase K (New England Biolabs) (0.2 mg/mL, 8 units/mL) in digestion buffer (50 mM Tris pH 8.0; 1 mM EDTA; 0.5% Triton X-100; 0.8 M guanidine hydrochloride (Sigma-Aldrich); ddH20) overnight at RT on a shaker.

Next day the digested gels were placed into foil-wrapped P100 dishes. Expansion of the gel was carried out by multiple repeated washes every 30 min in fresh ddH2O for around 5 times, until there was no further change in the gel size. After expansion, gels were measured to calculate their expansion factor, which varied between 4-4.1 times. Parts of gels were selected for imaging fitting them into 35 mm Ibidi dishes. The gels were oriented so that the fluorescent sample was on the bottom surface.

For Airyscan imaging, an inverted LSM880 with Airyscan was used, with a Plan-Aprochromat 63 × 1.4 NA objective (working distance: 0.19 mm), 405 nm, 488 nm and 561 nm DPSS lasers. Pixel sampling was set to 40 nm/pixel Airyscan, at 0.7–1 Airy Units. Airyscan data were subjected to pixel reassignment and linear Wiener deconvolution via the Zen software. The true spatial scale of the images was calculated by multiplying the pixel sampling by the linear expansion factor of the given gel. Results were analysed using ImageJ and thresholded and/or segmented to select different parts of sarcomere. Thresholding involved setting the same image intensity ranges for all images, ranging from 0 to 310 intensity values so that the images acquired could be easily compared with one another.

3.3 Results

3.3.1 Phosphorylation patterns across the sarcomere

If there is a gradient of cAMP across the sarcomere, one would expect to find a gradient of TNI phosphorylation upon the activation of βAR. To assess this, an expansion microscopy technique was employed to visualise the spatial distribution of phospho-troponin I (TNI) on application of isoproterenol (ISO).

Immunostained ARVM samples were expanded. The localisation of the staining was recorded (Fig. 3.2 A) with no staining observed using secondary antibody only (Fig. A.1). To quantify phosphorylation levels, phospho-TNI images were

analysed using pseudocolour to visualise the intensity of phospho-TNI labelling. Expansion microscopy enabled the clear delineation of sarcomeric structures such as Z and M lines (Fig. 3.2 B, C). The staining was performed using phospho-troponin I antibodies detecting S22 and S23 phosphosites (Abcam, monoclonal, S22 + S23, ab251031).

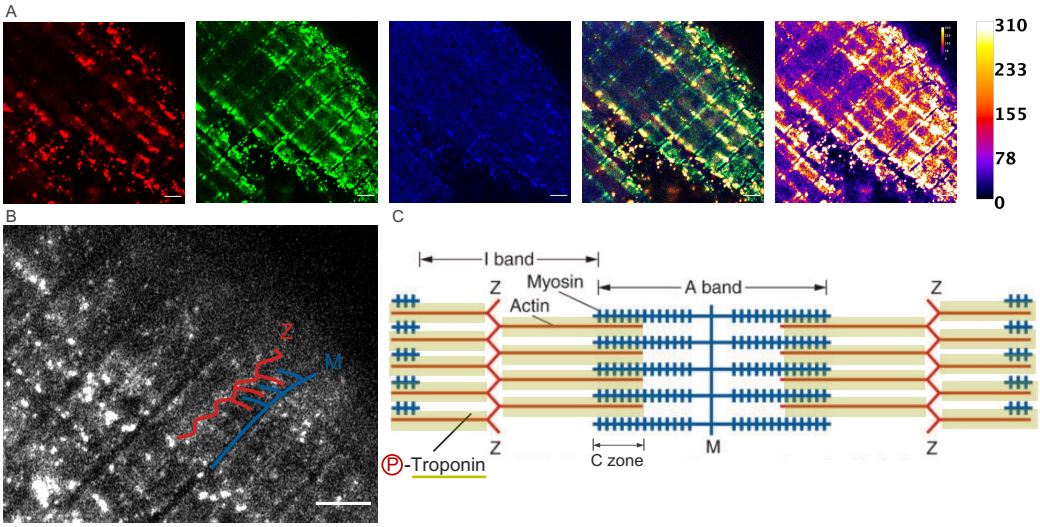


Figure 3.2: Expansion microscopy enables visualisation of the spatial distribution of phosphorylated troponin I across the sarcomere in ARVMs. Scale bar: 1.25 μm. Here the staining was performed using phospho-troponin I antibodies (Abcam, monoclonal, S22 + S23, ab251031). **A.** Staining of ARVM samples treated with 25 μM forskolin (FSK) and 100 μM IBMX. From left to right: total troponin I, phospho-troponin I, phalloidin staining for actin, overlay of the three stains, and pseudocolour visualisation of phospho-troponin I. The calibration bar for the pseudo-colour ranges from 0 to 310 intensity values. **B.** Expanded samples allow identification of fine structures within the sarcomere. Here: red line denotes the Z line, the blue line denotes the M line, red horizontal lines denote the thin filaments attached to the Z line, and blue horizontal lines denote thick filaments attached to the M line. Phospho-troponin I staining. **C.** Schematic representation of the sarcomere with the colours of the Z and M lines, as well as thin and thick filaments corresponding to the colours used in panel B. 'P-Troponin refers to phospho-troponin localisation across the sarcomere.

Next, ARVM samples treated with 5 nM isoproterenol (ISO), a βAR activator, for 1, 5, and 10 min, as well as untreated controls and cells treated with 25 µM FSK and 100 µM IBMX, were expanded and imaged. Different levels of phospho-TNI staining were observed (Fig. 3.3 A). First, the phospho-TNI signal in non-treated controls was quantified. This was done by selecting an area of interest (e.g. close to the M line) and measuring the signal intensity in that area. The data was from

the areas was plotted by assigning the area as the M line, the Z line, or in-between sometimes giving multiple readouts from the same cell, depending on the sarcomere length. Although the imaging laser power and staining protocols were consistent, different cell batches exhibited varying levels of overall TNI phosphorylation across the sarcomere (Fig. 3.3 B). Despite these variations, the signal of phospho-TNI at the Z line was consistently higher than the signal at the M line.

In the cells treated with ISO for 1 min (Fig. 3.3 C, J), a greater signal was observed along the proportion of the thin filament closer to the Z line than the portion closer to the M line. This suggests that after 1 minute of ISO treatment, phosphorylation of TNI occurs closer to the Z line than to the M line. Interestingly, samples treated with ISO for 5 min did not exhibit this distribution clearly (Fig. 3.3 D). Samples treated for 10 min showed a clear pattern similar to that observed in the samples treated for 1 min (Fig. 3.3 E, K). In samples treated with FSK and IBMX, there were no clear patterns of phospho-TNI across the sarcomere (Fig. 3.3 F).

Comparing phospho-TNI staining between samples, the data were first normalised to controls due to variations in staining between cell batches (Fig. 3.3 B). It was observed that cells treated with FSK and IBMX had the greatest phospho-troponin I content, as expected (as 25 µM FSK and 100 µM IBMX induces a large increase in cAMP which is demonstrated in subsequent FRET experiments)(Fig. 3.3 G). A transient increase in phosphorylation was observed between the untreated and treated samples, with the signal declining back to baseline (untreated) levels in the cells treated with ISO for 10 min (Fig. 3.3 G). This likely occurs due to PDE activity, which quickly degrades cAMP, leading to a transient cAMP increase, and/or phosphatase activity.

If the signalling pattern is indeed spatio-temporally controlled such that it is present only after 1 and 10 minutes of ISO treatment, but not in cells treated with a saturating stimulus, it could suggest two possibilities: a) a decoupling from cAMP-PKA control mediated by phosphatases, or b) PKA predominantly localises to the Z line, ensuring the highest levels of phosphorylation at all times. This would imply that, regardless of treatment, the phosphorylation levels at the M

and Z lines should remain consistent across all samples. Upon comparison, the differences between the samples were evident at the Z lines, where the samples treated with ISO for 1 and 5 minutes had significantly greater phospho-TNI content after normalisation to controls, than controls or 10 min ISO treated cells (Fig. 3.3 H). Significant differences were also observed at the M line (Fig. 3.3 I). Altogether, these data are consistent with cAMP forming a gradient in cells with elevated cAMP levels more prominently at the Z line after ISO treatment. Saturation after high dose FSK and IBMX treatment appears to overwhelm this gradient.

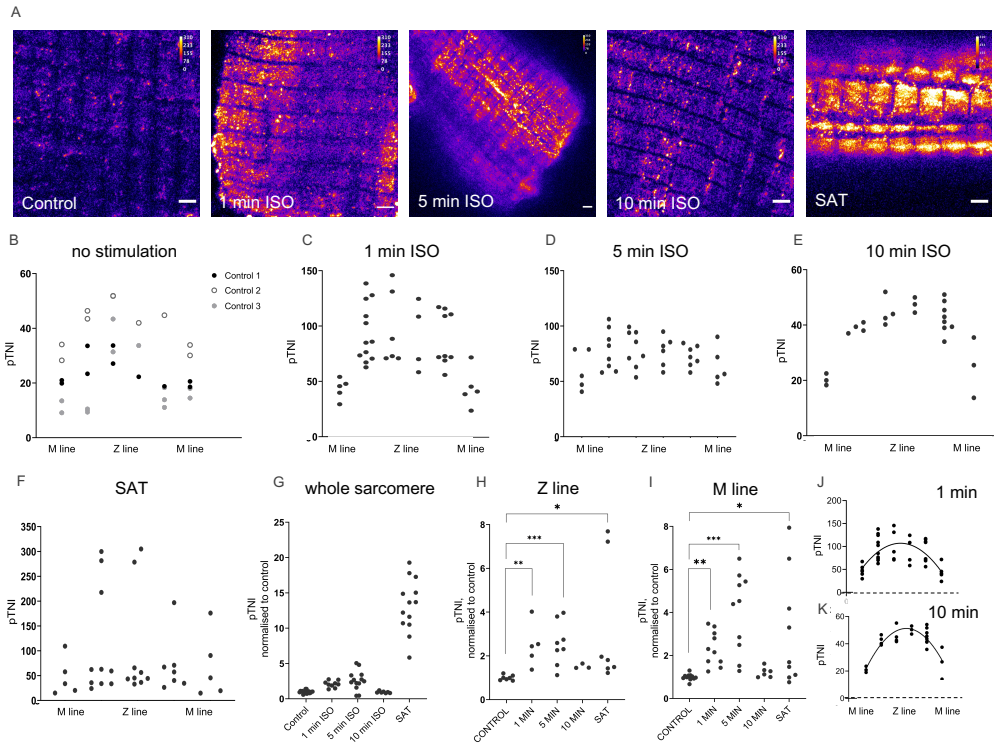


Figure 3.3: Quantification of phospho-troponin I distribution in ARVM samples. Scale bar: 1.25 μm. **A.** Representative images of phospho-troponin I staining in pseudo-colour in ARVM samples with different treatments, as indicated on the images. **B.** Phospho-TNI signal recorded in controls across the sarcomere, n=3 (individual cells imaged), N=3 (repeats, ARVM isolations), n=1-2 (measurements acquired form a single cell). **C.** Phospho-TNI signal recorded in 1 min 5 nM ISO treated cells across the sarcomere, n=3 (individual cells imaged), N=3 (repeats, ARVM isolations), n=1-4 (measurements acquired form a single cell). **D.** Phospho-TNI signal recorded in 5 min 5 nM ISO treated cells across the sarcomere. n=3 (individual cells imaged), N=3 (repeats, ARVM isolations), n=1-4 (measurements acquired form a single cell). **E.** Phospho-TNI signal recorded in 10 min 5 nM ISO treated cells across the sarcomere. n=3 (individual cells imaged), N=3 (repeats, ARVM isolations), n=1-3 (measurements acquired form a single cell). **F.** Phospho-TNI signal recorded in cells treated with 25 µM FSK and 100 µM IBMX across the sarcomere, n=3 (individual cells imaged), N=3 (repeats, ARVM isolations), n=1-4 (measurements acquired form a single cell). **G.** Quantification of phospho-troponin I signal normalised to control across the whole sarcomere between different samples, n=3 (individual cells), N=3 (repeats, ARVM isolations), n=1-5 (measurements acquired form a single cell). **H.** Quantification of phospho-troponin I signal normalised to control at the Z line compared between the different samples. Kruskal-Wallis test, Dunn's correction. Significant differences ($p<0.05$) between control (n=3 individual cells, N=3 (repeats, ARVM isolations), n=1-3 measurements acquired from a single cell) and 1 min (n=3 individual cells, n=1-2 measurements acquired from a single cell), 5 min (n=3 individual cells, N=3 (repeats, ARVM isolations), n=1-3 measurements acquired from a single cell), and SAT stimulus (n=3 individual cells, N=3 (repeats, ARVM isolations), n=1-3 measurements acquired from a single cell) treated samples; no significant differences between controls and 10 min ISO treated ($p>0.05$) samples. **I.** Quantification of phospho-troponin I signal normalised to control at the M line compared between the different samples. Kruskal- Wallis test, Dunn's correction. **Continued on next page.**

For comparisons between control (n=3 individual cells, N=3 (repeats, ARVM isolations), n=1-3 measurements acquired from a single cell) and 1 min (n=3 individual cells, N=3 (repeats, ARVM isolations), n=1-4 measurements acquired from a single cell), 5 min (n=3 individual cells, N=3 (repeats, ARVM isolations), n=1-4 measurements acquired from a single cell), and SAT stimulus (n=3 individual cells, N=3 (repeats, ARVM isolations), n=1-3 measurements acquired from a single cell) treated samples, $p<0.05$; no significant differences between controls and 10 min ISO treated samples. **J.** Phospho-TNI signal recorded in cells treated with 1 min 5 nM ISO across the sarcomere. A second-order polynomial model was used to describe the data non-linearly; adjusted $R^2 = 0.42$, RMSE = 4.32. **K.** Quantification of phospho-troponin I signal in cells treated with 10 min ISO across the sarcomere. Fitted with a second-order polynomial for non-linear representation; adjusted $R^2 = 0.74$, RMSE = 0.85.

3.3.2 Development and characterisation of the myofilament FRET sensors

To further investigate whether there is a TNI phosphorylation "wave" spreading across the sarcomere, functional cAMP FRET-based assays were conducted. The hypothesis here was that the TNI phosphorylation gradient from Z to M line is due to a similar cAMP gradient. To test this hypothesis, a cAMP FRET sensor targeted to troponin I was used. The sensor has been described before [34]. A MYBPC-CUTie sensor, developed by Dr Chao, was also employed.

In addition, a new sensor targeted to myomesin at the M line was developed. With this set of sensors it was possible to compare cAMP signalling at different sites of the myofilament: at I and A bands, excluding H zone (TNI-CUTie), C zone (MYBPC-CUTie), and at the M line (MYOM-CUTie) (Fig. 3.2 C).

The MYOM-CUTie sensor was developed by inserting the sequence coding for the 2nd and 3rd domains of the protein myomesin (domain 2-3 of myomesin 1, MYOM1, mRNA, NC-000018.10) into the backbone of the pEYFP-C1-CUTie plasmid. The myomesin sequence was inserted between the NheI restriction sites. The visualisation of the full sequence of the sensor is shown below (Fig. 3.4 A).

There are multiple challenges in developing targeted FRET sensors [199], further discussed in the Discussion. Before conducting experiments in cardiomyocytes, the MYOM-CUTie sensor was first characterised in HEK293T cells to confirm

its functionality as a cAMP reporter. While TNI-CUTie has been previously characterised, the MYBPC–CUTie sensor, a new sensor developed in the lab by Dr. Chao, had not been characterised before. The MYBPC-CUTie sensor is targeted to the C domain of MYBPC protein away from the MYBPC PKA phosphorylation site. To characterise MYBPC-CUTie and MYOM-CUTie in HEK293T cells, the FRET change induced by a saturating stimulus (25 µM forskolin (FSK) and 100 µM IBMX) was measured and compared between the sensors. This was done to: a) test if the newly developed MYOM-CUTie is functional as a FRET sensor, b) determine if there are intrinsic differences between these sensors in cells, and c) ensure that the response to the saturating stimulus achieves the same amplitude between the sensors, allowing for direct comparisons between the three sensors.

The MYOM-CUTie sensor was confirmed to function effectively as a FRET sensor (Fig. 3.4 B, D) in HEK293T cells, showing a maximal FRET change comparable to other CUTie sensors. The basal FRET ratios were significantly different across the various sensors (Fig. 3.4 C). This could be due to interactions between PDEs and sensors in HEK293T cells that do not occur in cardiomyocytes where the sensors localise to their respective targets (Fig. 3.6). Slower FRET change kinetics were observed in HEK293T cells expressing MYOM-CUTie than in cells expressing TNI-CUTie or MYBPC-CUTie in response to saturating stimulus (Fig. 3.4 D). As these differences were not present in ARVM cells (Fig. 3.5), it could be that MYOM-CUTie interacts with different proteins (e.g. PDEs) in HEK293T cells than in ARVM cells.

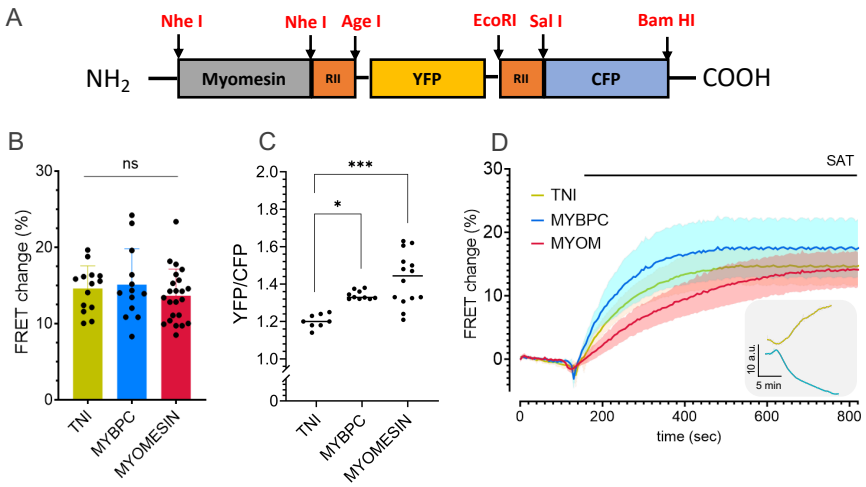


Figure 3.4: Characterisation of the FRET sensors. Newly developed MYOM-CUTie sensor enables cAMP measurements at the M line. **A.** Schematic of MYOM-CUTie sequence design. **B.** FRET change after saturating stimulation recorded in HEK293T cells expressing TNI (n=14 individual cells, N=2 repeats (HEK293T cultures)), MYBPC (n=12 individual cells, N=2 repeats (HEK293T cultures)), and MYOM (n=22 individual cells, N=2 repeats (HEK293T cultures)) CUTie sensors is not significantly different. Kruskal-Wallis test, Dunn's correction, $p>0.05$. **C.** Basal YFP/CFP ratios recorded in HEK293T expressing TNI (n=12 individual cells, N=2 repeats (HEK293T cultures)), MYBPC (n=12 individual cells, N=2 repeats (HEK293T cultures)), and MYOM (n=15 individual cells, N=2 repeats (HEK293T cultures)) CUTie sensors are significantly different, $p<0.05$, Kruskal-Wallis test, Dunn's correction. **D.** Average FRET change curve showing the kinetics of the response to SAT, saturating signal, comprised of 25 µM FSK and 100 µM IBMX measured with TNI (n=6 individual cells, N=2 repeats (HEK293T cultures)), MYBPC (n=7 individual cells, N=2 repeats (HEK293T cultures)), and MYOM (n=10 individual cells, N=2 repeats (HEK293T cultures)) CUTie sensors in HEK293T cells. Shaded areas represent the S.D. The inset shows the corresponding average CFP and YFP emission intensity curves for MYOM-CUTie.

3.3.3 Investigation of cAMP signalling from Z to M line

After initial characterisation, the sensors were used to test whether cAMP, following ISO stimulation, forms a "wave" from the Z to M line, as suggested by the TNI phosphorylation pattern observed in expansion microscopy experiments. First, sensors were found to localise in a striated manner in ARVMs (Fig. 3.5 C). Next, the response to 5 nM ISO was compared between the TNI, MYBPC, and MYOM sites in ARVMs expressing the respective targeted FRET sensors. The response appeared to be transient at the TNI site but not at the MYBPC or MYOM sites (Fig. 3.5 A). Quantification of the response showed that at 1 min after stimulation with 5 nM ISO, the increase in cAMP was similar at all three sites (Fig. 3.5 B). At 5 minutes, the response amplitude was significantly greater at the MYBPC and MYOM sites compared to the TNI site (Fig. 3.5 B).

These results do not support the generation of a cAMP wave diffusing from Z to M line across the sarcomere, as previously reported for calcium. Additionally, major differences in the kinetics of the ISO response are also observed. Therefore, it is unlikely that the cAMP signal across the sarcomere depends solely on a wave of second messenger generated at the T-tubules and propagating from the Z line to the M line.

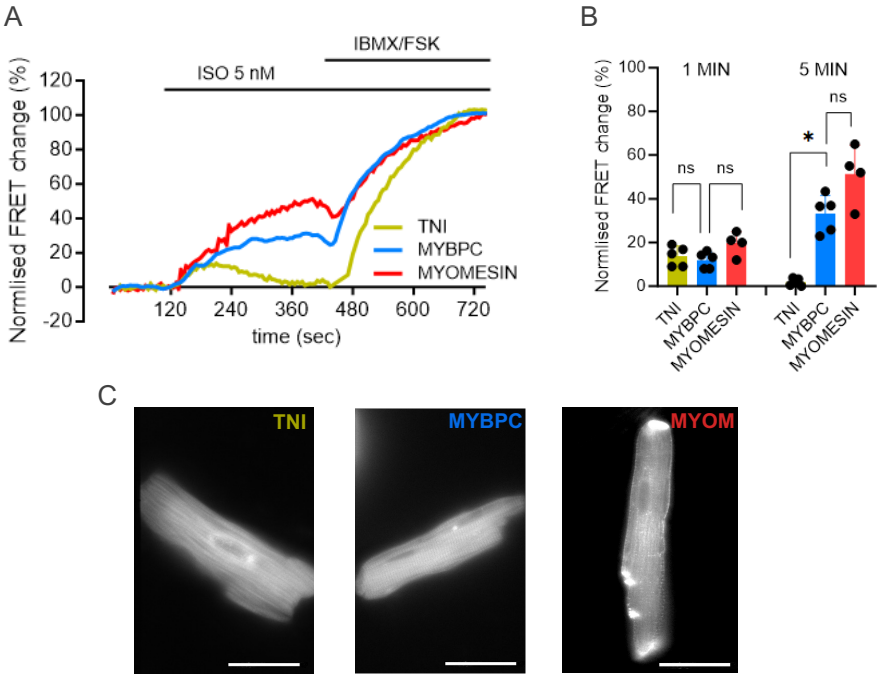


Figure 3.5: cAMP response following stimulation with ISO differs between TNI, MYBPC, and MYOM sites at the myofilament. The response does not follow a diffusion-like pattern. The experiments with the TNI-CUTie and MYBPC-CUTie sensors were performed by Dr. Chao, while the experiments with the MYOM-CUTie sensor were conducted by the author. **A.** Representative curves showing normalised FRET change after stimulation with 5 nM ISO and subsequent stimulation with 25 µM FSK and 100 µM IBMX measured with TNI-, MYBPC-, and MYOM-CUTie sensors in ARVMs. **B.** Quantification of the normalised FRET change measured with TNI- (n=5 individual cells, N=3 repeats (ARVM isolations)), MYBPC- (n=5 individual cells, N=3 repeats (ARVM isolations)), and MYOM- (n=4 individual cells, N=3 repeats (ARVM isolations)) CUTie sensors in ARVMs following the stimulation with 5 nM ISO for 1 min (Kruskal-Wallis test, FDR correction, $p>0.05$), and for 5 min (Kruskal-Wallis test, FDR correction, TNI vs. MYBPC: $p=0.03$; MYBPC vs. MYOM: $p=0.26$). **C.** Representative images of ARVMs expressing TNI-, MYBPC-, and MYOM-CUTie sensors. Scale bar: 20 µm.

Previous conclusions drawn from the experiments in ARVM were further supported by similar experiments conducted in NRVM. In NRVMs, the sensors were observed to show a striated localisation (Fig. 3.6 A) similar to that observed in ARVMs (Fig. 3.5 C). Despite the lack of T-tubules in this model system, NRVMs expressing the sensors exhibited cAMP response kinetics to ISO stimulation comparable to those in ARVMs (Fig. 3.6 A). Basal ratios at the myofilament were similar to those recorded at the cytosol with the cytosolic CUTie sensor (Fig. 3.6 B). The response kinetics showed a transient increase in cAMP after 1 nM ISO

stimulation at TNI, but not at MYOM or MYBPC sites (Fig. 3.6 C). The response at MYOM site was greater than at TNI site (Fig. 3.6 D).

3.3.4 PDE signalling across the sarcomere in NRVMs

It was next hypothesised that the differences in cAMP kinetics observed at TNI, MYBPC, and MYOM may be due to differences in cAMP hydrolysis at these locations. To test this, the response to IBMX was first investigated. IBMX inhibits all cAMP hydrolysing PDEs with the exclusion of PDE8. Application of IBMX after pre-stimulation with 1 nM ISO induced an increase in cAMP at all three sites, although it was lower at MYBPC than elsewhere (Fig. 3.6 E).

Without pre-stimulation with ISO, IBMX induced a robust increase in cAMP at the TNI, MYBPC, and MYOM sites (Fig. 3.6 F). However, the response was lower at the MYBPC site compared to the TNI and MYOM sites. The response to subsequent ISO stimulation also remained lower at the MYBPC site compared to the TNI and MYOM sites (Fig. 3.6 G). This lower response is due to IBMX inducing a smaller increase in cAMP at the MYBPC site, resulting in a lower cumulative effect of IBMX and ISO, as shown in the figure. Overall, these results suggest that PDE activity (excl. PDE8) is likely greater at the TNI and MYOM sites than at the MYBPC site. Additionally, it is possible that PDE8 activity is higher at the MYBPC site than at the other sites, which could help account for the differences observed with IBMX.

Even though PDE inhibition may not completely abolish the differences in cAMP kinetics observed at the three locations, altogether these results indicate that PDEs are a key determinant of the local cAMP differences observed between TNI, MYBPC, and MYOM. Therefore, further steps were taken to investigate and characterise PDE activity at the myofilament.

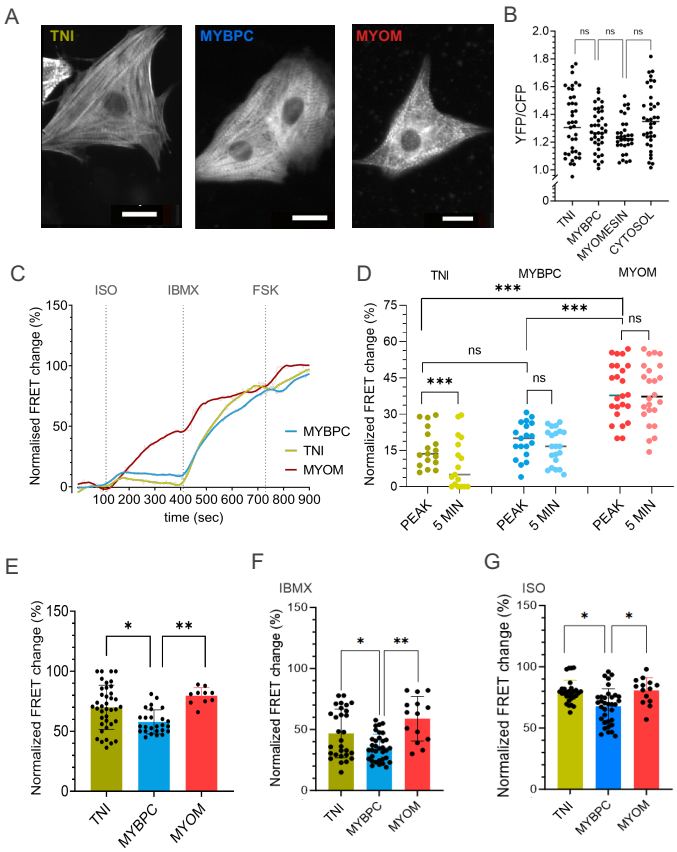


Figure 3.6: cAMP signalling across the sarcomere. **A.** Representative image of NRVMs expressing TNI- (left), MYBPC- (middle), and MYOM- (right) CUTie sensors. Scale bar: 20 µm. **B.** Basal YFP/CFP ratios recorded in NRVMs expressing TNI (n=38 individual cells, N=9 repeats (NRVM isolations)), MYBPC (n=41 individual cells imaged, N=9 repeats (NRVM isolations)), MYOM-CUTie (n=31 individual cells, N=4 repeats (NRVM isolations)), and cytosolic (n=38 individual cells, N=7 repeats (NRVM isolations)) CUTie sensors are not significantly different, p>0.05, Kruskal-Wallis test, Dunn's correction. **C.** Average curves showing smoothed normalised FRET change after stimulation with 1 nM ISO, 100 µM IBMX, and 25 µM FSK measured with TNI- (n=5 individual cells, N=3 repeats (NRVM isolations)), MYBPC- (n=5 individual cells, N=3 repeats (NRVM isolations)), and MYOM- (n=7 individual cells, N=3 repeats (NRVM isolations)) CUTie sensors in NRVMs. **D.** Normalised FRET change after 1 nM ISO stimulation is transient at the TNI site (n=17 individual cells imaged, N=5 repeats (NRVM isolations), Wilcoxon signed-rank test, p=0.0001), not transient at MYBPC site (n=19 individual cells, N=5 repeats (NRVM isolations) Wilxoson signed-rank test, p=0.19), and not transient at MYOM site (n=12 individual cells, N=4 repeats (NRVM isolations) Wilxoson signed-rank test, p<0.05). **E.** Normalised FRET change after 1 nM ISO stimulation + 100 µM IBMX is significantly different between TNI (n=29 individual cells, N=5 repeats (NRVM isolations)), MYBPC (n=30 individual cells, N=5 repeats (NRVM isolations)), and MYOM (n=6 individual cells, N=3 repeats (NRVM isolations)) sites. Kruskal-Wallis test, Dunn's correction, p<0.05. **F.** Normalised FRET change after IBMX recorded using TNI (n = 29 individual cells, N=5 repeats (NRVM isolations)), MYBPC (n = 34 individual cells, N=5 repeats (NRVM isolations)), and MYOM (n = 14 individual cells, N=3 repeats (NRVM isolations)) CUTie sensors. Kruskal-Wallis test, FDR correction, TNI vs. MYBPC: p=0.03; MYBPC vs. MYOM: p=0.004. **G.** Normalised FRET change after IBMX+ISO recorded using TNI (n = 29 individual cells, N=5 repeats (NRVM isolations)), MYBPC (n = 34 individual cells, N=5 repeats (NRVM isolations)), and MYOM (n = 14 individual cells, N=3 repeats (NRVM isolations)) CUTie sensors. Kruskal-Wallis test, FDR correction, TNI vs. MYBPC: p=0.04; MYBPC vs. MYOM: p=0.03.

3.3.5 Characterisation of the PDE involved in the regulation of cAMP signal at the sarcomere

To characterise PDE activity at the sarcomere, the response to different selective PDE inhibitors was recorded. First, the FRET change was captured before ISO stimulation, *i.e.*, the response to the inhibitor alone.

The experiments were conducted using TNI and MYBPC CUTie sensors to investigate differences in PDE signalling between these two sites. The activity of TNI and MYBPC, unlike myomesin, is regulated by PKA. Since previous experiments did not show a cAMP gradient from the Z to M line, and given that myomesin is not a direct target of PKA, subsequent experiments focused on investigating cAMP signalling specifically at the TNI and MYBPC locations.

It was observed that in the cytosol PDE4 accounts for the majority of the total PDE activity, as PDE4 inhibition induced the second-largest increase in cAMP. IBMX induced the greatest increase in cAMP. PDE2, PDE3, and PDE8 inhibition induced smaller increases (Fig. 3.7 A). A similar PDE contribution was observed at the TNI site (Fig. 3.7 B). In both locations, PDE4 inhibition could not fully account for total PDE activity, as significant differences remained between the effects of PDE4 inhibition and IBMX.

The signalling pattern was different at the MYBPC site. Although IBMX induced a robust response, inhibition of PDE2, PDE3, PDE4, and PDE8 did not produce similar effects (Fig. 3.7 C). This indicates that TNI-CUTie and MYBPC-CUTie detect signals from two separate cAMP domains under the regulation of distinct PDEs. Specifically, while PDE4 plays a prominent role in maintaining basal cAMP levels at TNI, this PDE does not regulate basal cAMP at MYBPC.

The response to PDE inhibition with various PDE inhibitors was compared between the TNI and MYBPC sites (Fig.3.7 D). This analysis uses previously described data (Fig.3.7 A-C) but the data is visualised differently. By doing so, it was found that the change induced by PDE2 and PDE3 inhibition is greater at the MYBPC site than at the TNI site, while the change induced by PDE4 inhibition and IBMX is greater at the TNI site than at the MYBPC site. There

were no statistically significant differences in the cAMP response induced by PDE8 inhibition between the two sites. The response to the combination of PDE4 and PDE3 inhibition was significantly higher at the TNI site than at the MYBPC site.

Despite the remaining differences between the TNI and MYBPC responses to the combination of PDE3 and PDE4 inhibition (Fig.3.7 D), the response was comparable to that induced by IBMX at both locations (Fig.3.7 E). In other words, inhibition of PDE4 and PDE3 together could potentially account for the total PDE activity at both sites, as there were no longer any significant differences between the response to IBMX and PDE4+PDE3 at either the TNI and at MYBPC sites. This aligns with previous findings suggesting a synergistic PDE3 and PDE4 control of intracellular cAMP and cardiac excitation-contraction coupling in porcine heart cells [200].

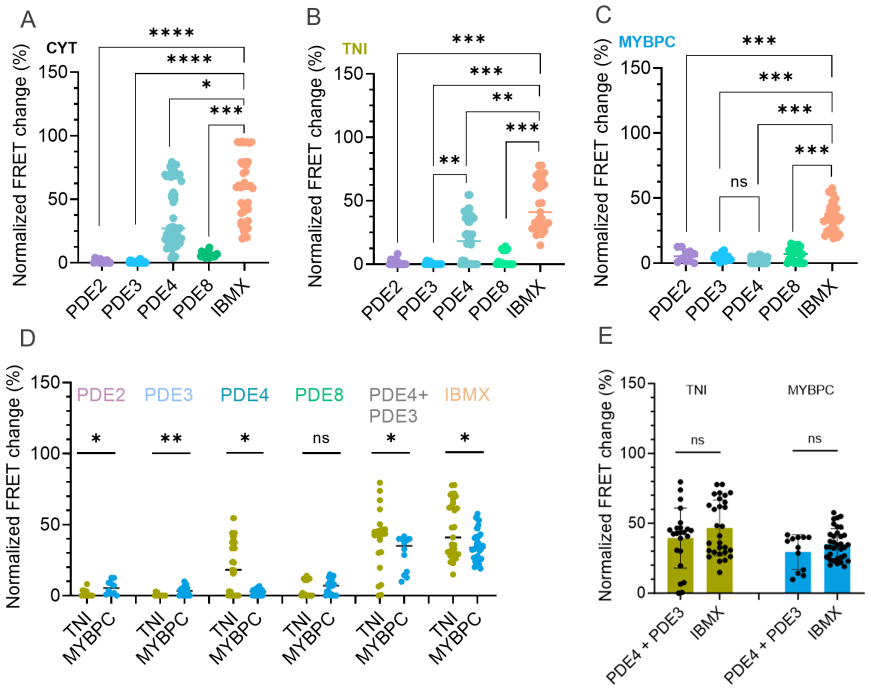


Figure 3.7: PDE contribution to determining cAMP levels at the myofilament in basal conditions. Here, PDE2 was inhibited with 10 nM Bay60-4204, PDE3 with 10 µM cilostamide, and PDE4 with 10 µM rolipram, PDE8 with 10 µM PF-04957325, and 100 µM IBMX was used. **A.** Normalised FRET change in the cytosol recorded with EPAC-SH187 sensor after PDE2 (n=12 individual cells, N=2 repeats (NRVM isolations)), PDE3 (n=28 individual cells, N=4 repeats (NRVM isolations)), PDE4 (n=67 individual cells, N=12 repeats (NRVM isolations)), PDE8 (n=18 individual cells, N=4 repeats (NRVM isolations)) inhibition, or IBMX (n=44 individual cells, N=5 repeats (NRVM isolations)). IBMX induces a greater increase in cAMP than PDE8 ($p<0.0001$), PDE4 ($p=0.02$), PDE3 ($p<0.0001$) or PDE2 ($p<0.0001$). Kruskal-Wallis test, Dunn's correction. **B.** Normalised FRET change at TNI after after PDE2 (n=12 individual cells, N=2 repeats (NRVM isolations)), PDE3 (n=14 individual cells, N=3 repeats (NRVM isolations)), PDE4 (n=37 individual cells, N=9 repeats (NRVM isolations)), PDE8 (n=14 individual cells, N=2 repeats (NRVM isolations)) inhibition, or IBMX (n=29 individual cells, N=5 repeats (NRVM isolations)). IBMX induces a greater increase in cAMP than PDE8 ($p<0.0001$), PDE4 ($p=0.0013$), PDE3 ($p<0.0001$) or PDE2 ($p<0.0001$). PDE4 inhibition induces a greater increase in cAMP than PDE2 ($p=0.042$) or PDE3 ($p=0.0025$). Kruskal-Wallis test, Dunn's correction. **C.** Normalised FRET change at MYBPC after after PDE2 (n=10 individual cells, N=2 repeats (NRVM isolations)), PDE3 (n=22 individual cells, N=3 repeats (NRVM isolations)), PDE4 (n=30 individual cells, N=9 repeats (NRVM isolations)), PDE8 (n=24 individual cells, N=3 repeats (NRVM isolations)) inhibition, or IBMX (n=34 individual cells, N=5 repeats (NRVM isolations)). IBMX induces a greater increase in cAMP than PDE8 ($p<0.0001$), PDE4 ($p<0.0001$), PDE3 ($p<0.0001$) or PDE2 ($p=0.009$). PDE4 inhibition does not induce a significantly different increase in cAMP than PDE2 ($p>0.99$) or PDE3 ($p>0.99$) inhibition. Kruskal-Wallis test, Dunn's correction. **D.** Comparison in responses to PDE inhibitors between TNI and MYBPC domains. PDE2 ($p=0.007$) and PDE3 ($p=0.0008$) induced a greater increase at MYBPC than at TNI site, but the change induced by PDE4 inhibition ($p<0.05$) and IBMX ($p<0.05$) is greater at TNI than at MYBPC site. PDE8 ($p=0.35$) induced a comparable increase in cAMP between MYBPC and TNI sites. **Continued on next page.**

Response to the combination of PDE4 and PDE3 inhibition was significantly higher ($p<0.05$) at TNI (n = 23 individual cells, N=3 repeats (NRVM isolations)) than at MYBPC (n=12 individual cells, N=3 repeats (NRVM isolations)) site. Mann-Whitney U test for comparisons between TNI and MYBPC. **E.** PDE3 and PDE4 can explain the total PDE activity at TNI (n=23 individual cells, N=3 repeats (NRVM isolations)) and MYBPC (n=12 individual cells, N=3 repeats (NRVM isolations)) sites. Mann-Whitney U test to compare IBMX and a combination of PDE3 + PDE4 activity at TNI ($p>0.05$) and MYBPC ($p>0.05$) sites separately.

3.3.6 PDE signalling and adrenergic stimulation

Next, the contribution of PDEs to regulation of the cAMP signal generated by βAR stimulation at the TNI and MYBPC sites was determined. The response to ISO alone was also recorded.

At the TNI site, it was observed that inhibition of PDE2, PDE4, and IBMX induced a greater increase in cAMP following inhibitor + ISO stimulation compared to ISO alone (Fig. 3.8 A). This was also true when both PDE3 and PDE4 were inhibited together, but not when PDE3 was inhibited alone (Fig. 3.8 A).

A similar pattern was observed at the MYBPC site (Fig. 3.8 B). In the cytosol, the response to ISO after PDE2, PDE3, or PDE8 inhibition did not induce a response greater than that of ISO alone (Fig. 3.8 C). In the cytosol, the response to ISO was greater after treatment with a PDE4 inhibitor and IBMX compared to ISO alone.

The response to PDE inhibitors after pre-stimulation with ISO was also compared between sites. It appeared that there are no significant differences between the TNI and MYBPC sites in their responses to ISO + PDE inhibitor in the case of PDE3 and PDE4 inhibitors (Fig. 3.8 D). This was not the case when the effects of inhibition were compared without the pre-stimulation of ISO (Fig. 3.7). There were also no significant differences between the TNI and MYBPC sites in their responses to ISO + PDE inhibitor in the case of PDE2 and PDE8 inhibitors (not shown on the figure). Altogether, this highlights the importance of studying PDE signalling at the myofilament with and without ISO pre-stimulation, as different PDE contributions and signalling patterns are observed. Nonetheless, the differences

between the TNI and MYBPC responses to IBMX remained with (Fig. 3.8 D) and without (Fig. 3.7 D) pre-stimulation with ISO .

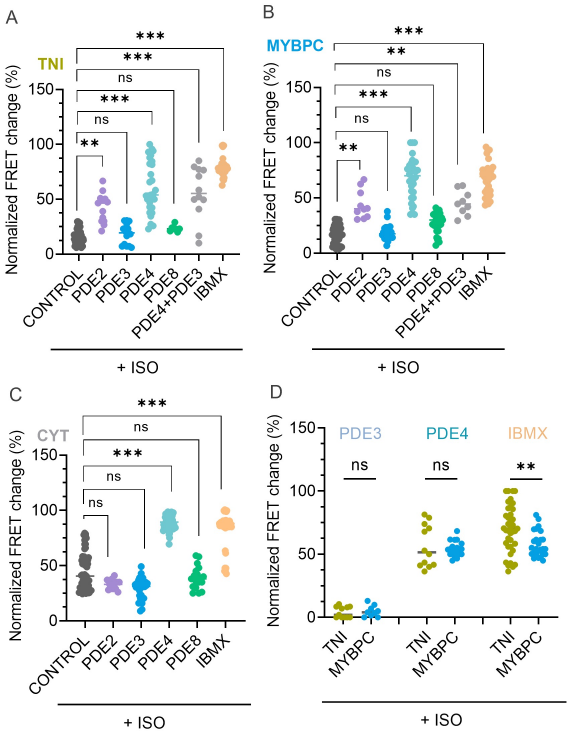


Figure 3.8: PDE signalling and adrenergic stimulation. Here, PDE2 was inhibited with 10 nM Bay60-4204, PDE3 with 10 µM cilostamide, PDE4 with 10 µM rolipram, and PDE8 with 10 µM PF-04957325, and 100 µM IBMX, and 1 nM ISO was used. The data is shown as % normalised FRET change from untreated baseline (including ISO + inhibitor induced FRET change). **A.** Normalised FRET change at TNI after stimulation with 1 nM ISO alone (n=62 individual cells, N=11 repeats (NRVM isolations)), of 1 nM ISO after PDE2 (n=12 individual cells, N=2 repeats (NRVM isolations)), PDE3 (n=14 individual cells, N=3 repeats (NRVM isolations)), PDE4 (n=29 individual cells, N=5 repeats (NRVM isolations)), PDE8 (n=7 individual cells, N=2 repeats (NRVM isolations)), or PDE3+PDE4 (n=12 individual cells, N=3 repeats (NRVM isolations)) inhibition, or IBMX (n=29 individual cells, N=5 repeats (NRVM isolations)). PDE2 ($p=0.0014$), PDE4 ($p<0.0001$), PDE3+PDE4 ($p=0.0001$) and IBMX ($p<0.0001$) inhibition induces a greater increase in cAMP after subsequent stimulation with ISO compared to ISO alone. The response to ISO after PDE3 ($p>0.99$) or PDE8 ($p=0.7$) inhibition is not significantly different to than that of ISO alone. Kruskal-Wallis test, Dunn's correction. **B.** Normalised FRET change at MYBPC site after stimulation with 1 nM ISO alone (n=62 individual cells, N=11 repeats (NRVM isolations)), of 1 nM ISO after PDE2 (n=10 individual cells, N=2 repeats (NRVM isolations)), PDE3 (n=22 individual cells, N=3 repeats (NRVM isolations)), PDE4 (n=30 individual cells, N=9 repeats (NRVM isolations)), PDE8 (n=22 individual cells, N=3 repeats (NRVM isolations)), PDE3+PDE4 (n=9 individual cells, N=3 repeats (NRVM isolations)) inhibition, or IBMX (n=34 individual cells, N=5 repeats (NRVM isolations)). PDE2 ($p=0.0047$), PDE4 ($p<0.0001$), PDE3+PDE4 ($p=0.005$) inhibition and IBMX ($p<0.0001$) induces an increase in response to subsequent stimulation with ISO compared to ISO alone. The response to ISO after PDE3 ($p>0.9$) or PDE8 ($p=0.25$) inhibition is not significantly different to than that of ISO alone. Kruskal-Wallis test, Dunn's correction. **C.** Normalised FRET change in the cytosol after stimulation with 1 nM ISO alone (n=60 individual cells, N=12 repeats (NRVM isolations)), of 1 nM ISO after PDE2 (n=12 individual cells, N=2 repeats (NRVM isolations)), PDE3 (n=28 individual cells, N=4 repeats (NRVM isolations)), PDE4 (n=67 individual cells, N=12 repeats (NRVM isolations)), PDE8 (n=18 individual cells, N=4 repeats (NRVM isolations)), or IBMX (n=44 individual cells, N=5 repeats (NRVM isolations)).**Continued on next page.**

PDE2 (p>0.9), PDE3 (p=0.12), or PDE8 (p>0.9) inhibition does not induce a significant increase in response to subsequent stimulation with ISO compared to ISO alone. The response to ISO after PDE4 inhibition (p<0.0001) and IBMX (p<0.0001) is significantly greater to than that of ISO alone. Kruskal-Wallis test, Dunn's correction. **D.** Normalised FRET change at TNI and MYBPC sites after 1 nM ISO + PDE inhibitor. There are no significant differences in responses to PDE3 or PDE4 inhibition after pre-stimulation with ISO between TNI (n=11-12 individual cells, N=3 repeats (NRVM isolations)) and MYBPC (n=9-20 individual cells, N=3 repeats (NRVM isolations)) sites (p>0.05). The response to IBMX after pre-stimulation with ISO is significantly lower at MYBPC (n=20 individual cells, N=5 repeats (NRVM isolations)) site compared to TNI (n=39 individual cells, N=5 repeats (NRVM isolations)) site (p=0.0045). Mann-Whitney U test for comparing TNI and MYBPC separately.

3.3.7 PDE4 at the sarcomere

Given the prominent role of PDE4 in regulating cAMP signalling at TNI, as observed in the previously described experiments (Fig. 3.7), further investigation into the role of PDE4 was conducted. A different visualisation of the data presented in Fig. 3.8 and Fig. 3.7 shows that the response to 10 µM rolipram, a PDE4 inhibitor, was significantly greater at the TNI site than at the MYBPC site (Fig.3.9 A).

The cAMP change after PDE4 inhibition also increased dramatically in the cytosol, with the increase in the cytosol being higher than at both, the TNI and MYBPC sites (Fig. 3.9 A). Notably, the substantial increase in cAMP induced by PDE4 inhibition in the cytosol did not affect cAMP levels at the MYBPC site, where PDE4 inhibition failed to elicit an increase in cAMP (*i.e.*, there is no 'spill-over' between the cytosolic and MYBPC domains). These differences between TNI and MYBPC sites were not observed when the response to PDE4 inhibition was recorded after pre-stimulation with 1 nM ISO (Fig. 3.9 B).

When analysing data, it was observed that not all cells respond to PDE4 inhibition in a similar manner. While the responses at the MYBPC site were consistently minimal, at the TNI site and in the cytosol, some cells exhibited a much larger cAMP increase than others. To investigate this further, the basal ratio (YFP/CFP), which indicates the cAMP levels at the specific site measured in the absence of any treatment, was compared between cells that did not show a

response to PDE4 inhibition (termed population 1, P1) and those that did (termed population 2, P2). PDE4 activity is known to be regulated by phosphorylation, where PKA-mediated PDE4 phosphorylation enhances PDE4 hydrolytic activity. Therefore, it was hypothesised that some cells might have higher starting cAMP levels, leading to greater PDE4 phosphorylation by cAMP-activated PKA, and thus, greater PDE4 activity.

To explore this, a histogram of the cytosolic dataset was created, revealing two distinct populations of cells (Fig. 3.9 C): P1, which responds with a low increase in cAMP following PDE4 inhibition, and P2, which responded with a large increase in cAMP. Basal ratios between the two populations were compared, demonstrating that in the cytosol, cells that responded with a large increase in cAMP after PDE4 inhibition had significantly higher basal cAMP ratios (Fig. 3.9 D), supporting the hypothesis of a population of cells with activated PDE4.

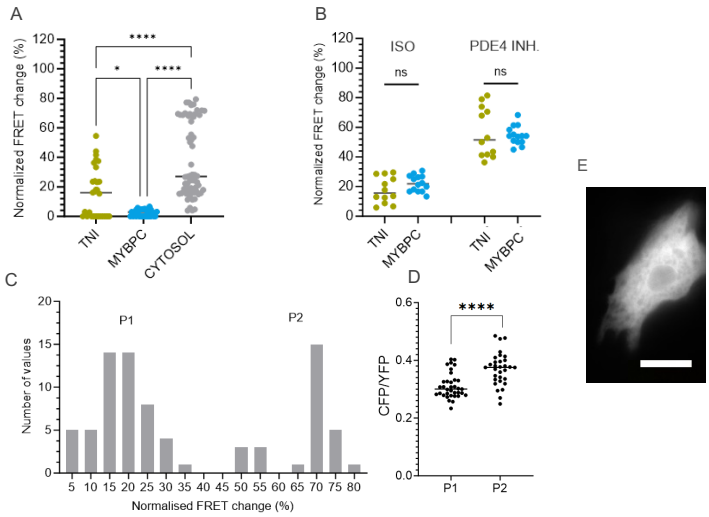


Figure 3.9: PDE4 signalling differs between TNI and MYBPC domains. **A.** Normalised FRET change after stimulation with 10 µM rolipram, a PDE4 inhibitor, compared between TNI-CUTie (n=20 individual cells, N=5 repeats (NRVM isolations)), MYBPC-CUTie (n=18 individual cells, N=5 repeats), and cytosolic EPAC-SH187 (n=67 individual cells, N=12 repeats (NRVM isolations)) sensors. PDE4 inhibition induces a greater response at the cytosol than at TNI ($p<0.0001$) or MYBPC ($p<0.0001$) sites; and the response at the TNI is greater than at MYBPC ($p=0.018$) site. Kruskal-Wallis test, Dunn's correction. **B.** Normalised FRET change recorded 1 minute after stimulation with 1 nM ISO (peak response) and subsequent stimulation with 10 µM rolipram, a PDE4 inhibitor, compared between TNI (n=12 individual cells, N=3 repeats (NRVM isolations)) and MYBPC (n=14 individual cells, N=3 repeats (NRVM isolations)) sites. Mann-Whitney U test to compare TNI with MYBPC responses to ISO ($p=0.19$) and rolipram ($p=0.7$) separately. **C.** Frequency distribution of the normalised FRET change values recorded in the cytosol after PDE4 inhibition. Histogram indicates two populations of cells, P1, which responds to PDE4 inhibition with a low change in FRET, and P2, which responds to PDE4 inhibition with a large change in FRET. **D.** Basal CFP/YFP ratios recorded in NRVM cells expressing cytosolic EPAC-SH187 sensor compared between the two populations, P1 (n=36 individual cells, N=12 repeats (NRVM isolations)) and P2 (n=31 individual cells, N=12 repeats (NRVM isolations)), as indicated in panel C. Mann-Whitney U Test, $p<0.0001$. **E.** Representative image of NRVM expressing EPAC-S-H187 sensor used for FRET experiments. Scale bar: 20 µm.

3.3.8 PDE4 and TNI interaction

In Fig. 3.9 it was observed that PDE4 plays a prominent role in controlling cAMP at TNI but not at MYBPC. It was hypothesised that there is a direct interaction between TNI and PDE4.

To test this, first, the expression of TNI was examined in NRVMs. It was found that NRVMs express both, mature form of TNI known as cTNI, and immature, or slow skeletal form of TNI, ssTNI (Fig. 3.10 A). To investigate which isoform of PDE4 is likely to be involved in TNI interactions, NRVM cells were transfected with PDE4D9 plasmid with a VSV tag, and with PDE4B1. PDE4D was weakly expressed in NRVMs (Fig. 3.10 C) and its molecular weight matched that of PDE4D9-VSV.

Then it was tested if PDE4D9 interacts with TNI. For co-immuno-precipitation in cell lysate with PDE4D9-VSV, TNI antibodies allowed to pull down PDE4D, and the PDE4D isoform that was pulled down was of the same molecular weight as PDE4D9 suggesting the interaction between PDE4D9 and TNI in NRVM cells expressing PDE4D9-VSV (Fig. 3.10 B).

Having established the interaction between PDE4D9 and TNI in NRVMs, it was tested if the same interaction occurs in human cardiomyocytes to increase the translational potential of the findings. For this purpose, human induced pluripotent stem cell derived cardiomyocytes (hiPSC-CM) were used. Further research translation capabilities were explored in later chapters (Chapter 5 and 6) where mathematical modelling was used to investigate hiPSC-CM features and the mechanical contraction regulation in these cells.

It was found that hiPSC-CM, just like NRVM, express both, mature cTNI and immature ssTNI (Fig. 3.10 A). PDE4D was also expressed in hiPSC-CM cells (Fig. 3.10 C). For co-immuno-precipitation, PDE4D was pulled down with TNI antibodies (Fig. 3.10 B) showing the interaction between TNI and PDE4D in hiPSC-CM cells. As the PDE4D isoform that was pulled down was of the same molecular weight as PDE4D9, it suggests that the interaction between PDE4D and TNI in hiPSC-CM cells involves PDE4D9.

To check if the interaction is PDE4D isoform-specific, the expression of PDE4B was tested in hiPSC-CM, and NRVMs transfected with PDE4B1. In hiPSC-CM, there appeared to be minimal expression of PDE4B (Fig. 3.10 D). A strong band was observed bellow 76 kDa in hiPSC-CM which was not observed in NRVM expressing PDE4B1. Upon pull-down with TNI antibodies, no PDE4B was detected in hiPSC-CM sample (Fig. 3.10 E). This suggests that in hiPSC-CM, there is an interaction between TNI and PDE4D, but not PDE4B.

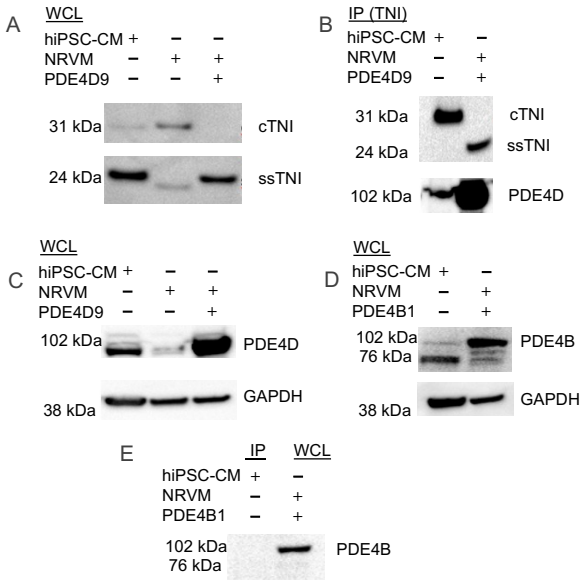


Figure 3.10: PDE4 expression and interactions in NRVMs and hiPSC-CMs. **A.** Western blot analysis showing cTNI and ssTNI expression in the whole cell lysates (WCL) from hiPSC-CM, NRVM, and lysates of NRVM transfected with PDE4D9-VSV, n=2 repeats. **B.** Western blot analysis showing cTNI, ssTNI, and PDE4D in the pull-down (IP) of endogenous TNI obtained from hiPSC-CM lysates and NRVM lysates expressing PDE4D9-VSV, n=2 repeats. **C.** Western blot analysis showing PDE4D expression in the whole cell lysates (WCL) of hiPSC-CM, NRVM, and NRVM transfected with PDE4D9-VSV, n=2 repeats. **D.** Western blot analysis showing PDE4B expression in the whole cell lysates (WCL) of hiPSC-CM and NRVM transfected with PDE4B1, n=2 repeats. **E.** Western blot analysis showing no interaction detected between TNI and PDE4B in hiPSC-CM lysates from the pull-down (IP) of endogenous TNI. PDE4B expression was detected in the whole cell lysates (WCL) of NRVMs expressing PDE4B1, n=2 repeats.

3.3.9 PDE4 signalling sequestration at the myofilament: role of PKA and AKAPs

cAMP compartmentalisation contributes to spatial regulation of PKA signalling. Other important players in cAMP-PKA signal compartmentalisation are AKAPs, A kinase anchoring proteins. They localise cAMP-PKA signalling machinery to the target protein, and can anchor PKA, PDEs, and other signalling molecules. It could be that AKAP-dependent PKA or PDE anchoring to the myofilament contributes to cAMP regulation at that site. However, the distinct contributions of AKAPs in controlling cAMP signalling at the myofilament are currently not completely clear. To address this, several experiments were performed to delineate the roles of PKA phosphorylation and AKAP-mediated anchoring in regulating cAMP dynamics within the myofilament.

First, it was examined if PKA-AKAP interaction disruption with HT31, a peptide that de-couples AKAPs from PKA, would affect cAMP signalling at the myofilament. Here, HT31 was introduced to the cells in a plasmid form. It was found that at TNI and MYBPC sites cAMP increase following the stimulation with ISO is not significantly altered after PKA-AKAP interaction disruption (Fig. 3.11 A, B). No notable differences in response kinetics were observed. Previously published data indicates the decrease in TNI and MYBPC phosphorylation levels after HT31 treatment [92].

PKA-AKAP interaction disruption affected PDEs. In HT31-treated cells, there were no longer any differences in the response to IBMX between TNI and MYBPC (Fig. 3.11 C). These differences were observed before in untreated control cells (Fig. 3.6 C). TNI response to IBMX was unchanged but the response to IBMX at the MYBPC site was increased.

To investigate the role of PKA-mediated phosphorylation in regulating cAMP signalling at the myofilament, PKA activity was inhibited using H89, a PKA inhibitor [201]. Following ISO stimulation, the cAMP response at both the TNI and MYBPC sites showed no significant differences between the two sites (Fig. 3.11 D).

However, when examining the effects of PDE4 inhibition after ISO pre-stimulation, a distinct pattern emerged. In H89-treated cells, the cAMP response at the TNI site was significantly reduced compared to untreated cells (Fig. 3.11 E), indicating that PKA activity may play a role in modulating PDE4-mediated cAMP degradation at this location. In contrast, no such reduction was observed at the MYBPC site, suggesting a site-specific interaction between PKA activity and PDE4 regulation.

PDE4-mediated cAMP signalling in disease

In some diseases, such as hypertrophic states and HF, there is a redistribution of cAMP signalling. This has been shown in animal models with pressure overload-induced cardiac hypertrophy and catecholamine-induced cardiac hypertrophy [39, 202]. It has been shown that the cAMP response at the myofilament in the TNI nanodomain is almost completely abolished in hypertrophy [34]. To further investigate PDE4 signalling at the myofilament in disease, PDE4 activity at TNI was examined in hypertophic cardiomyocytes.

It was found that the response to the PDE4 inhibitor rolipram was not significantly greater at the TNI site in hypertophic cells compared to control healthy cells (Fig. 3.11 F). However, unlike in control cells, there was no longer a bimodal distribution in the responses to PDE4 inhibition. In hypertrophic cells, all cells were responding to rolipram with an increase in cAMP at the TNI site. Subsequent application of ISO resulted in a greater response in the control cells than in hypertrophied cells. This could be due to the desensitisation of the βAR. Interestingly, there were no apparent differences in cAMP basal ratios at the TNI site between the control and hypertrophic cells (Fig. 3.11 G).

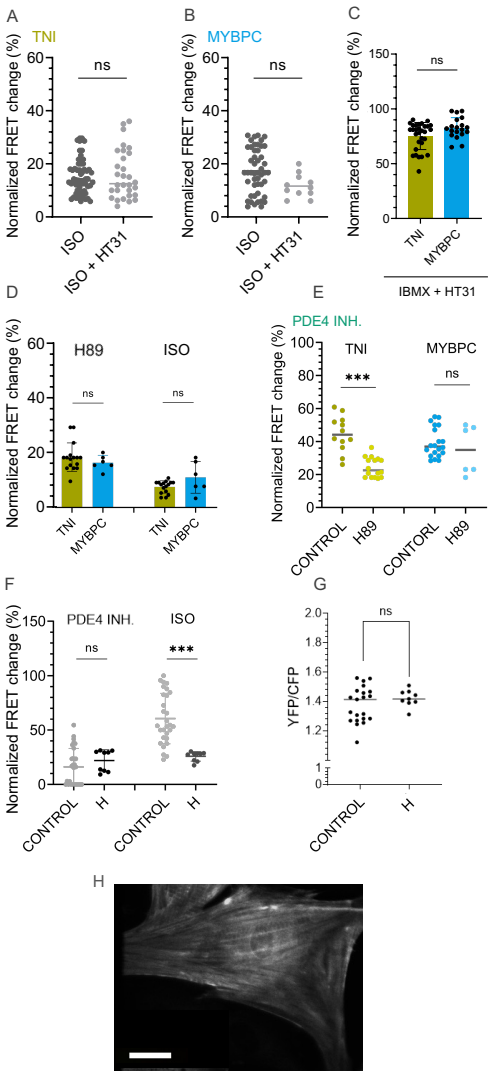


Figure 3.11: cAMP regulation at the myofilament in health and disease. Here H – hypertrophy. **A.** Normalised FRET change recorded 1 min after the application of 1 nM ISO (peak response) at TNI site in the cells not treated (n=62 individual cells, N=10 repeats (NRVM isolations)) and treated with HT31 peptide (n=30 individual cells, N=5 repeats (NRVM isolations)). No significant differences, t-test, $p>0.05$. **B.** Normalised FRET change recorded after the application of 1 nM ISO at MYBPC site in the cells not treated (n=48 individual cells, N=8 repeats (NRVM isolations)) and treated with HT31 peptide (n=11 individual cells, N=3 repeats (NRVM isolations)). No significant differences, t-test, $p>0.05$. **C.** Normalised FRET change recorded after the application of IBMX following the application of 1 nM ISO at TNI (n=30 individual cells, N=5 repeats (NRVM isolations)) and MYBPC (n=19 individual cells, N=3 repeats (NRVM isolations)) sites in the cells treated with HT31 peptide. No significant differences, t-test, $p>0.05$. **D.** Normalised FRET change recorded after the application of H89 with ISO, and the change induced by ISO alone at TNI (n=16 individual cells, N=3 repeats (NRVM isolations)) and MYBPC (n=6 individual cells, N=2 repeats (NRVM isolations)) sites. No significant differences between TNI and MYBPC, Mann-Whitney U test for comparisons between TNI and MYBPC sites in response to H89 ($p>0.05$) and ISO ($p>0.05$) separately.
Continued on next page.

E. Normalised FRET change recorded after the application of 10 μM rolipram, PDE4 inhibitor, in the cells pre-treated with H89 and ISO. The response at TNI site is significantly greater in the cells not treated (n=12 individual cells, N=3 repeats (NRVM isolations)) than treated with H89 (n=16 individual cells, N=3 repeats (NRVM isolations)), $p<0.001$. The response at MYBPC site is not significantly different between the cells not treated (n=20 individual cells, N=9 repeats (NRVM isolations)) and in the cells treated with H89 (n=6 individual cells, N=3 repeats (NRVM isolations)), $p>0.05$. Mann-Whitney U test. **F.** Normalised FRET change in control cells expressing TNI-CUTie (30-50 individual cells, N=9 repeats (NRVM isolations)) and hypertrophic (H) cells (n=9-21 individual cells, N=4 repeats (NRVM isolations)). Mann-Whitney U test indicates no significant differences in the response to 10 µM rolipram, PDE4 inhibitor, between the control and hypertrophic cells ($p>0.05$) and a significant difference in response to subsequent stimulation with 1 nM ISO ($p<0.001$). **G.** Basal YFP/CFP ratios recorded in NRVM control (n=21 individual cells, N=4 repeats (NRVM isolations)) and hypertrophic (n=9 individual cells, N=4 repeats (NRVM isolations)) cells expressing TNI-CUTie. No significant differences, $p>0.05$, Mann-Whitney U test. **H.** Representative image of hypetrophic NRVM expressing TNI-CUTie sensor that was used for FRET experiments. Scale bar: 20 µm.

3.4 Discussion

This chapter outlines the spatial and temporal dynamics of cAMP signalling in cardiomyocytes, particularly how this compartmentalised signalling regulates myofilament function. The findings highlight the importance of compartmentalised cAMP signalling, revealing distinct cAMP nanodomains within the sarcomere. These results help clarify the detailed regulation of cardiac function at the molecular level. The main findings in this chapter include:

1. After βAR stimulation, phospho-troponin I forms a spatio-temporal phosphorylation gradient across the sarcomere from the Z to the M line.

2. The development of a MYOM-CUTie sensor enables cAMP detection at the M line in cardiomyocytes.

3. cAMP response kinetics following β-adrenergic receptor stimulation differ between TNI, MYBPC, and MYOM sites, showing that the cAMP response at the TNI site is transient, while at the MYBPC or MYOM site, it is not.

4. PDE4 plays a predominant role in cAMP regulation at the TNI site but not at the MYBPC site.

5. PDE4 interacts with TNI, and PDE4 activity at TNI site is PKA-mediated.

Understanding cAMP regulation at the myofilament is critical for determining how cardiac contraction and relaxation are controlled, as cAMP-PKA signalling fine-tunes these processes. It is known that calcium, a key mediator of contraction, is distributed as a gradient across the sarcomere [192]. Based on this, it was hypothesised that cAMP follows a similar spatio-temporal distribution pattern. To investigate this, phospho-troponin I distribution, as a marker of cAMP-PKA signalling, was examined across the sarcomere. Expansion microscopy showed distinct TNI phosphorylation patterns after short (1 min) isoproterenol (ISO) exposure, with a significant increase in phosphorylation at the Z line compared to the M line. This suggests a rapid activation of cAMP-PKA signalling primarily at

the Z line immediately after adrenergic stimulation, or a difference in phosphatase activity. The Z-M line pattern dissipated at 5 minutes but reappeared after 10 minutes of treatment.

Interestingly, cells exposed to a high cAMP-inducing stimulus did not show clear patterns of phospho-TNI distribution. This could indicate a saturation effect, where maximal phosphorylation across all sites obscures differential localisation observed under more physiological conditions. The transient increase in phosphorylation levels, returning to baseline after 10 minutes of ISO treatment, supports the idea of a tightly regulated, dynamic phosphorylation process that rapidly adapts to changes in cellular signalling.

The observed differences between Z and M lines could stem from cAMP diffusion from plasmalemma-anchored adenylyl cyclases (ACs). To test this, functional FRET assays were performed in ARVMs. To detect a potential cAMP signal 'wave' from the Z to M line, sensors targeted to troponin (TNI-CUTie) [34], MYBPC (MYBPC-CUTie), localised to the thick filaments on the A bands, and myomesin (MYOM-CUTie) were used. MYOM-CUTie is a newly developed sensor targeted to myomesin at the M line to provide a third spatial point of reference.

The data obtained from the sensors revealed the differential cAMP responses to ISO at different subcellular sites. FRET data showed that signalling dynamics are not uniform across TNI, MYBPC, and MYOM domains. cAMP response kinetics at TNI were more transient compared to MYBPC and MYOM. This suggests that TNI and MYBPC, despite their proximity, function as separate cAMP nanodomains.

At 1 minute of ISO treatment, cAMP levels were comparable between the three sensors, despite the highest phospho-TNI content being at the Z line as indicated by expansion microscopy experiments. After 5 minutes of ISO treatment, cAMP content was highest at the M line and lowest at TNI, with phospho-TNI levels appearing uniform across the sarcomere.

These findings do not support the generation of a cAMP wave diffusing from Z to M line across the sarcomere. Instead, separate cAMP compartments emerged showing distinct cAMP response kinetics at TNI, MYBPC, and MYOM. Data

from the lab indicates that the transient cAMP increase at the TNI domain corresponds to a transient increase in TNI phosphorylation after ISO treatment, while phosphorylation at the MYBPC site is sustained [34]. This is consistent with expansion microscopy data, showing greater TNI phosphorylation in ARVM samples treated with ISO for 1 and 5 minutes compared to 10 minutes.

The differences in temporal cAMP control between TNI and MYBPC can be interpreted in the broader context of cAMP signalling. Previous lab data shows a transient cAMP response to 1 nM ISO at the AKAP18δ domain in the SR but not at the AKAP79 membrane domain [34]. While transience can be attributed to PDE activity, AKAP79 interacts with PDE4 and possibly other PDEs [203]. The lack of transience at the AKAP79 site could be due to its proximity to ACs, cAMP production sites. However, the absence of cAMP transience at the MYBPC site remains puzzling, as MYBPC is not known to be near cAMP sources. Future research should explore the functional implications of sustained MYBPC phosphorylation alongside limited TNI phosphorylation. In addition, delineating the role of phosphatases in controlling TNI and MYBPC phosphorylation patterns would be important.

Further exploration of cAMP dynamics in response to PDE inhibition with IBMX showed a lower cAMP response to IBMX at the MYBPC site. This suggests possibly lower PDE activity at MYBPC than at TNI which may be crucial for fine-tuning cAMP signals essential for myofilament function. The lower increase could be due to fewer PDEs that are active at the MYBPC site. Thus, inhibiting a smaller number of PDEs results in a less pronounced cAMP increase compared to TNI, where more PDEs are present, leading to a more significant rise in cAMP upon inhibition. This aligns with the lack of a transient ISO response at MYBPC, unlike at TNI, suggesting reduced PDE activity at MYBPC.

Further investigation into the differential PDE signalling between TNI and MYBPC sites showed a marked increase in cAMP at the TNI site following PDE4 inhibition with rolipram, compared to the MYBPC site, highlighting PDE4's role in modulating cAMP dynamics specifically at TNI. This suggests a targeted interaction

between PDE4 and TNI. This hypothesis was confirmed by co-immunoprecipitation experiments indicating a PDE4D9 interaction with TNI.

Interestingly, the cytosolic response to PDE4 inhibition showed a pronounced increase in cAMP, greater than that at TNI or MYBPC site. The absence of cAMP 'spill-over' from the cytosol to the MYBPC site during PDE4 inhibition underscores the effectiveness of compartmentalisation within the myofilament domains, ensuring localised signalling mechanisms remain insulated from broader cytosolic changes.

This finding contrasts with previous hypothesis suggesting lower PDE activity at the MYBPC site. If fewer PDEs are present at MYBPC, it would be unexpected that cAMP from the cytosol cannot reach this site. Either IBMX induces a non-uniform cAMP increase away from MYBPC, or there is significant, unidentified PDE activity at MYBPC. Despite a strong cAMP increase with IBMX, no significant response to PDE2, PDE3, PDE4, or PDE8 inhibition was observed at MYBPC.

The response of cAMP at TNI and MYBPC sites to βAR stimulation, modulated by specific PDE inhibition, reveals the role of PDEs in fine-tuning cardiac adrenergic responses. The observed cAMP increase at the TNI site following PDE inhibition after ISO stimulation shows that under normal physiological conditions, PDE2 and PDE4 actively regulate the adrenergic-induced cAMP increase, modulating the cardiac response. The lack of a significant effect following PDE3 or PDE8 inhibition suggests a less prominent role for these isoforms at the TNI site under these conditions.

At the MYBPC site, a similar modulation pattern by PDE2 and PDE4 indicates consistent regulatory mechanisms across sarcomeric domains. The differences between TNI and MYBPC in their response to IBMX persist even after ISO pre-treatment. These differences are first abolished when PKA is decoupled from AKAPs using HT31 peptide treatment. One would expect that removing PKA from the myofilament would reduce the activity of PKA-phosphorylatable PDEs like PDE4 and PDE3 [204], leading to an increased cAMP response to ISO which was not observed.

Due to PKA-AKAP interaction disruption, phosphorylation levels of TNI, phospholamban, and RYR were found to be reduced in HT31-treated cells [92]. Yet, the experiments in this chapter indicate that the cAMP levels at the myofilament remain unchanged after HT31 treatment. While the disruption of PKA-AKAP interactions did not affect the ISO response at the myofilament, it did augment the cAMP increase after IBMX at the MYBPC site, making it comparable to the TNI site.

It could be that compensatory mechanisms are activated and maintain or enhance PDE activity. This claim is supported by experiments suggesting that PDE3 and PDE4 may synergistically control cAMP activity at the myofilament. This hypothesis arose from observations of cAMP changes induced by various PDE inhibitors. No single inhibitor could account for the total PDE activity observed with IBMX treatment, but combined inhibition of PDE3 and PDE4 resulted in cAMP levels comparable to those after IBMX application. PDE3 might act as a first line of cAMP 'defence', given its high sensitivity to cAMP and ability to operate at low cAMP levels. However, PDE3 has a slow degradation rate, so any cAMP that bypasses PDE3 is likely captured by PDE4. Such dynamics have been described before in the nuclear domain [41].

The contribution of PKA-mediated phosphorylation to controlling cAMP signalling was evident, as inhibition of PKA with H89 altered the response to PDE4 inhibition at the TNI site after ISO stimulation. This demonstrates that PKA activity influences the sensitivity of the myofilament to PDE4 regulation. However, it is important to consider the limitations, such as H89's lack of specificity and potential off-target effects. Despite this, the selective sensitivity at the TNI site, but not the MYBPC site, underscores the differential regulatory mechanisms at these sarcomeric locations.

There could be therapeutic implications of these findings, particularly in conditions like hypertrophy and heart failure (HF), where altered cAMP signalling dynamics are documented. The uniform response to PDE4 inhibition in hypertrophic cells, unlike the bimodal response in control cells, may suggest a fundamental shift in cAMP signalling regulation in disease. Targeting PDE4 activity to restore

proper cAMP signalling at the TNI site could be crucial for maintaining effective cardiac function. This remains to be explored in the future. Altogether, these findings highlight the complex, regulated nature of signal propagation within cardiac myocytes and suggest mechanisms by which cells fine-tune their contractile response to hormonal stimuli.

3.4.1 Limitations

While this study provides significant insights into cAMP signalling and myofilament function in cardiomyocytes, several limitations must be considered. First, the majority of experiments were performed using neonatal rat ventricular myocytes (NRVMs), which are immature and may not fully represent the behavior of adult human cardiomyocytes. Although some experiments were conducted with adult rat ventricular myocytes (ARVMs), these cells, despite being mature, may not entirely reflect human physiology due to species differences. Furthermore, experiments with human-induced pluripotent stem cell-derived cardiomyocytes (hiPSC-CMs) were also included, but these cells are known to be immature compared to adult human cardiomyocytes, potentially limiting the translational potential of the findings. Despite these limitations, the results across NRVMs, ARVMs, and hiPSC-CMs were consistent, suggesting that the observed phenomena are robust across different models.

Second, the study primarily focused on PKA-mediated phosphorylation and did not extensively explore the regulation by other kinases or the impact of phosphatases (PPs). This is an important aspect of cAMP-PKA signalling, and future studies should consider these additional regulatory players.

Third, there is a lack of specificity of some reagents used in the experiments. For instance, H89, while effective in inhibiting PKA, is known to have off-target effects [205]. Moreover, the study's *in vitro* nature means that the complex interactions and environmental factors present *in vivo* are not fully captured. The use of FRET sensors to study cAMP signalling, while powerful, also have inherent limitations, such as potential steric hindrance effects in small compartments like the myofilament

[199]. To mitigate this, expansion microscopy was employed to complement the FRET experiments.

Finally, the study did not fully address the impact of altered cAMP signalling dynamics in specific disease contexts, such as heart failure (HF). While the findings suggest potential therapeutic implications, the specific changes in cAMP signalling in these pathological states were not comprehensively explored. Future research should focus on extending these findings to disease models to better understand how dysregulated cAMP signalling contributes to disease progression and to develop targeted therapeutic strategies.

3.5 Conclusions

The extensive exploration of cAMP signalling within cardiac myocytes presented in this chapter underscores the intricate and highly compartmentalised nature of cellular cardiac signalling mechanisms. Using advanced sensor technologies and imaging techniques, the work has revealed distinct cAMP signalling dynamics at sarcomeric sites, each finely tuned to the specific demands of cardiac physiology. The identification of differential PDE activity across the sarcomere, particularly the pivotal role of PDE4, highlights its impact on myocardial contractility and response to adrenergic stimuli.

The varying patterns of PDE inhibition between TNI and MYBPC sites, along with the unique interactions of PDE4D with TNI in both rat and human-derived cardiomyocytes, suggest a potential for therapeutic targeting in specific cardiac dysfunctions. Additionally, the development of the MYOM sensor to probe cAMP dynamics at the M line, and the use of expansion microscopy to visualise phosphotroponin distributions, mark significant advances in our ability to understand the molecular complexities of heart cells.

In conclusion, this chapter enhances our understanding of the molecular mechanisms underlying heart function and paves the way for developing targeted therapies to more effectively address cardiac pathologies.

4

PKA condensation and control of cAMP signalling at the myofilament

4.1 Introduction

4.1.1 cAMP buffering by PKA condensation

cAMP, produced in response to GPCR stimulation, regulates cardiac contraction and relaxation through various effector proteins, including PKA. To ensure hormonal specificity, cAMP-PKA signals are compartmentalised within the cell.

PKA is anchored to AKAPs, which localise PKA to specific intracellular sites, targeting proteins for phosphorylation. AKAPs enhance signalling specificity by anchoring PKA and binding other cAMP-associated proteins such as ACs, PDEs, and PPs, forming localised signalling hubs or signalosomes.

PDEs, responsible for cAMP degradation, play a key role in cAMP compartmentalisation. However, it is thought that PDE activity alone is insufficient to slow cAMP diffusion enough to confine the second messenger into discrete compartments. Different PDE isoforms have distinct enzymatic features, as discussed in Chapter 1 (Table 1.1). This is important to consider as for the cell to maintain cAMP nanodomains, cAMP signal must be precisely regulated. As previously discussed in Chapter 1, intracellular cAMP diffusion coefficient range from 10 to 780 $\mu m^2/s$ [35, 106] where in NRVMs it is estimated to be around 32 $\mu m^2/s$ [107].

Using experimentally established values, computational diffusion models indicate that PDEs alone cannot explain cAMP compartmentalisation as PDEs have relatively low catalytic rates that seem inadequate to effectively restrict the highly diffusible cAMP [106]. However, the cAMP diffusion and PDE catalytic rates used in the model were established *in vitro* and might not reflect catalytic rates *in vivo*.

Besides PDE-mediated cAMP compartmentalisation, cAMP signal control may depend on cAMP buffering. A significant molar excess of PKA regulatory subunits compared to catalytic subunits (around 17-fold) has been reported, potentially providing substantial cAMP binding and buffering [68]. A recent study showed that, at low concentrations, a fluorescent cAMP analogue diffuses slowly at 0–10 $\mu m^2/s$, increasing to 10–100 $\mu m^2/s$ with higher cAMP concentrations in HEK293 cells [35]. Similar results were reported in human airway smooth muscle cells, where the fluorescent cAMP analogue diffused at 4.0 ± 0.39 $\mu m^2/s$, doubling after treatment with HT31, a peptide that disrupts PKA-AKAP interactions [206].

A novel mechanism for cAMP buffering has been reported by Zhang et al. (2020), showing that PKA regulatory subunits type Iα (RIα) undergo liquid–liquid phase separation (LLPS) in the cytosol to form biomolecular condensates in various cell types, including neonatal cardiomyocytes [111] (Fig. 4.1). LLPS is a process where proteins self-assemble into liquid droplets, functioning as membraneless organelles to optimise reaction kinetics, buffer molecules, sense stress, and localise signals.

Study by Zhang et al. (2020) suggests that through LLPS, PKA RIα forms membraneless organelles that concentrate cAMP. This is supported by higher signals detected using FRET-based reporters of PKA activity in the RIα puncta compared to diffuse regions [111]. These organelles likely buffer cAMP and may include other cAMP signalling molecules, such as ACs and PDEs, although their involvement is not yet confirmed.

Fluorescence recovery after photobleaching (FRAP) of RIα-GFP experiments show slower fluorescence recovery within RIα condensates compared to the surrounding cytosol, with diffusivity around 0.004 $\mu m^2/s$ inside the droplets and over 100 $\mu m^2/s$ outside in basal conditions [111]. This suggests that RIα condensates

may act as cAMP buffers. Zhang et al. hypothesise that the binding of cAMP to RIα activates PKA C subunits, which are also present in the condensates, providing a model for localised cAMP signalling regulation [111].

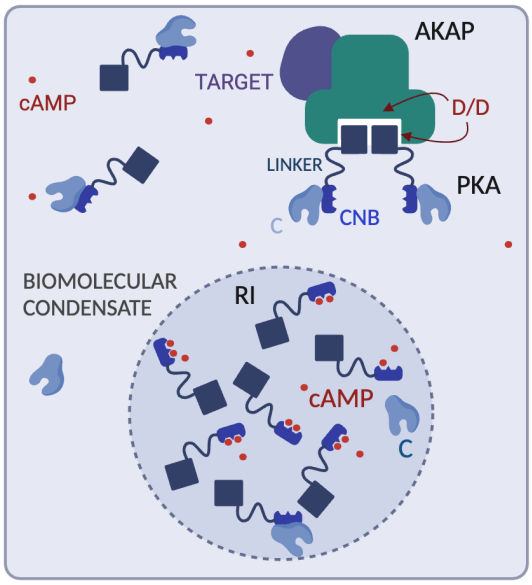


Figure 4.1: Schematic representation of PKA RIα biomolecular condensates.

So far, only RI, not RII, condensation has been described [111]. C subunits have been shown to associate with RI condensates and are co-recruited to RIα condensates upon cAMP elevation, challenging the canonical dissociation model of the PKA holoenzyme in the presence of cAMP. The molecular mechanisms and functional role of this co-recruitment are still unclear. Interestingly, PKA C appears not to undergo LLPS on its own but only in conjunction with RIα. The IS and D/D domains in RI contain sequence disorder, driving LLPS, while the CNB domain is crucial for cAMP-mediated LLPS promotion.

Importantly, the study also indicates that cAMP buffering enabled by PKA LLPS is essential for cAMP compartmentalisation, meaning that cAMP compartmentalisation cannot occur if PKA LLPS is disrupted. As indicated in the publication, LLPS disruption with 2.5% 1,6-hexanediol, a LLPS disrupting agent, leads to a greater cAMP signal induced by the AC activator forskolin around PDE4D2's catalytic site. The authors suggest that this means that RIα condensate disruption leads to decreased cAMP buffering and the PDEs are no longer able to provide effective

cAMP compartmentalisation because their hydrolytic activity is overwhelmed by the large amount of cAMP released from the disruption of RIα condensates.

These findings raise further questions about the function of RIα condensates in cells. While other biomolecular condensates are known to optimise enzymatic reactions, it is unclear whether and how LLPS affects PKA activity. Furthermore, PKA condensates might be serving other function besides cAMP buffering, and elucidating those is important for a comprehensive understanding of cardiac intracellular signalling.

4.1.2 Challenges in studying protein LLPS

While PKA LLPS promises new exciting research avenues, investigations are limited by the challenges in studying LLPS. Demonstration of phase separation in cells has technical constraints, such as challenges in studying proteins without overexpression or without fluorescent tags, and distinguishing between LLPS and aggregation. Effective *in vivo* models are also lacking. *In vitro* studies while useful, may not fully capture complex intracellular environment, raising concerns about the relevance of the findings to '*in vivo*' conditions. One key limitation is the absence of specific tools. Alberti et al. (2019) suggest crucial experiments for LLPS investigation, such as demonstrating fusion events of LLPS proteins with fluorescent tags in cells to complement *in vitro* studies [207]. However, different tags can affect LLPS, and caution in result interpretation is needed. GFP tagging is often considered safe, but in some cases, it can alter LLPS properties depending on whether the tag is placed at the C- or N-terminus of the protein, resulting in either promotion or disruption of LLPS [208].

Disrupting LLPS with 1,6-hexanediol (HEX) is a common approach to distinguish LLPS from aggregation. However, HEX has off-target effects, including altering membrane permeability, which could introduce artifacts in live-cell studies. Low exposure to HEX might minimise side effects but could also reduce its effectiveness in disrupting LLPS [207, 209].

Many researchers use FRAP experiments, and one common mistake is to assume that the recovery rate of FRAP reports only on the exchange rate between the dilute and dense phases. However, the FRAP recovery rate also depends on other parameters such as the size of the photobleached droplet, mobility within a droplet, and the size of bleach areas, which are often not taken into account [207].

Alberti et al. (2019) propose using mutations that affect LLPS but not protein functionality to investigate the role of LLPS in biological processes [207]. However, this has proven difficult with PKA, as mutations that alter LLPS often affect other functions [210]. New approaches to modulate PKA LLPS are needed to understand its function without confounding factors.

4.1.3 Open questions in PKA condensation research

Research by Zhang et al. (2020) prompts several important questions. It remains unclear whether PKA condensates provide substantial cAMP sequestration, as suggested by FRAP data. cAMP may simply bind to the abundant PKA within the condensates, which would not provide additional buffering compared to the same amount of RI subunit when free in the cytosol. If indeed cAMP is sequestered and contained in the condensates, this could be executed by "trapping" cAMP inside where cAMP would "bounce" from one PKA binding site to another. In this way, more cAMP molecules are contained inside the condensate than there are binding sites. Similar model has been proposed before for PDEs [37]. However, it could be that PKA condensates just bind cAMP without "trapping" which would provide the same amount of cAMP buffering as cAMP binding cytosolic PKA R subunits which are non-condensed. Therefore, differentiating between sequestration and binding is crucial for determining whether PKA condensation provides additional cAMP buffering. R subunit binds to AKAPs but the role of AKAPs in PKA LLPS has not been thoroughly explored.

Given the importance of the D/D domain in driving PKA condensation and AKAP interactions, it is of interest to investigate how AKAPs regulate PKA LLPS. Overexpression of smAKAP, a membrane-bound AKAP, sequesters PKA

RIα to the membrane, reducing the number of PKA puncta [210]. Based on these observations it has been suggested that RIα LLPS and AKAP anchoring represent distinct forms of spatial compartmentalisation within the cAMP/PKA pathway. However, the mechanism in adult heart cells or NRVMs, where PKA is largely anchored, remains unclear.

AKAP involvement in modulating cAMP diffusion also presents conflicting evidence. For instance, knockdown of AKAP2, a dual-specificity mitochondrial anchoring protein, increased cAMP diffusion [206]. The authors suggest that PKA-AKAP anchoring contributes to slowing down cAMP diffusion, which contrasts with previous findings from Zhang's lab showing that small membrane AKAP overexpression reduce PKA phase separation which should increase cAMP diffusion. This discrepancy may involve other structural factors, where AKAP2 knockdown affects the physical barriers governing cAMP diffusion, as AKAP2 is known to be located at the mitochondria [206]. Mitochondria has been previously identified as an organelle which provides physical barriers thereby slowing cAMP diffusion in cells [107].

HT31, a peptide disruptor of PKA-AKAP complexes, also increased cAMP diffusion, but no difference in cAMP levels was observed following isoproterenol stimulation as measured with the myrPALM-EPAC FRET sensor localised to the membrane [206]. Altogether, this highlights that the role of AKAPs in PKA LLPS is not completely understood and that AKAP role in modulating cAMP diffusion may depend on both the specific AKAP and its cellular context.

Peptides derived from the PKA-AKAP binding sequence have been used to disrupt PKA-AKAP interactions. HT31, a 24-amino acid peptide based on the sequence of AKAP-Lbc, binds RII and can disrupt both RI and RII AKAP complexes in cells and animal experiments. HT31 peptide binds RII with low nanomolar affinity (KD = 2.2 $\pm$ 0.03 nM) [86, 87]. The RIAD peptide was designed to be RI-specific by incorporating amino acids that sterically interfere with RII binding, while the core binding region fits both RI and RII D/D domains [89]. The SUPER-AKAP-IS peptide is RII-specific due to an aliphatic residue that does not fit into the first core

binding pocket of RIα [90]. These peptides allow detailed study of PKA-AKAP interactions and their role in cAMP compartmentalisation.

HT31 binds RII by interacting diagonally over one face of the D/D dimer, creating a solvent-excluded interaction site. As predicted by helical wheel analysis, the interaction of R-binding peptides with the D/D domain is mediated by aliphatic residues on one side of the peptide's α-helix, forming a hydrophobic ridge. This helix docks into a complementary hydrophobic groove formed by side chains from the N-terminal helices of both protomers of the RIIα D/D [88].

Zhang et al. (2020) demonstrated that deletion of the PKA dimerisation-docking (D/D) domain abolishes PKA RIα's ability to form puncta [111]. The D/D domain facilitates PKA-AKAP interactions, making it essential to understand how AKAPs influence this process. Both AKAP overexpression and knockdown have been shown to reduce cAMP buffering capacity in cells, raising questions about the precise mechanism at play.

While PKA condensation is proposed to act as a cAMP buffer, it remains to be clarified whether this mechanism operates in cardiomyocytes as it does in HEK293T cells. LLPS could influence the sequestration or exclusion of cAMP, possibly protecting catalytic subunits from activation. In cardiomyocytes, this mechanism could be critical for fine-tuning localised cAMP and PKA activity, thereby modulating contractility and protecting against excessive cAMP signalling, which is associated with cardiac disease such as hypertrophy and arrhythmias [211].

The previous chapter established that at least two distinct cAMP domains at the myofilament —TNI and MYBPC—exist, each with different PDE activity and distinct cAMP responses compared to the cytosol. This chapter aims to investigate whether PKA RIα biomolecular condensation contributes to cAMP compartmentalisation observed at the myofilament in the TNI and MYBPC domains.

4.2 Methods

4.2.1 Cell culture

The experiments were carried out in the human cell line (HEK293T) and in cardiomyocytes (NRVM). The cells were handled as outlined in General Methods, Chapter 2, Section 1. To address PKA RIα condensation in native conditions, HEK293T-RI cell line was employed [111]. This cell line was generated by introducing the 11^{th} strand of GFP (GFP11) [212] at the C terminus of RIα via CRISPR-Cas9 in HEK293 cells, yielding the HEK293T-RI cell line. This enables targeted reconstitution of intact GFP when the remainder of superfolder GFP (GFP1–10) is co-expressed. These cells were a gift from Prof Zhang (UCSD, USA) [111].

4.2.2 Plasmids, FRET biosensors, and imaging

To detect PKA condensation, PKA RIα and RIIβ plasmids were used. Additionally, PKA C subunit, and other plasmids were used to test the phase separation, and PKA localisation in cells. The full list of plasmids used is available in General Methods, Chapter 2, Section 1. To measure the effects on PKA condensation in cAMP dynamics in cells, cAMP FRET biosensors were used. The full list of biosensors used is available in General Methods, Chapter 2, Section 1. FRET and epiflourescence imaging was performed as outlined in General Methods, Chapter 2, Section 1. The imaging experiments were performed by the author, and by undergraduate students Jamie Adams and Samuel Santhouse under the author's supervision, where indicated.

4.2.3 PKA condensation modulating agents

2.5% 1,6-HEX was used to modulate PKA condensation, prepared in the imaging buffer (Ringer buffer). 1,6-HEX is known to disrupt weak intermolecular forces present in liquid-like assemblies and is widely used as a phase separation disrupting agent [209]. However, 1,6-HEX has off-site effects. Therefore, the treatment with 1,6-HEX was limited to a low concentration (2.5%) and a short 15 min duration as this particular time constrain has been shown to minimise off-target effects [209].

Still, currently there does not seem to be an agreement about the use of 1,6-HEX in phase separation studies, where 1,6-HEX has been shown to reduce [213], promote [214], and do nothing [215] to protein phase separation within 15 min treatment period.

To mitigate off-site effects 2,5-HEX [216] was used as an additional control. 2,5-HEX appears to have little to no effect on phase separation [216], although different opinions exist [213]. A publication by Alberti et al.(2019) recommendeds to use 1,6-HEX and 2,5-HEX for comprehensive phase separation studies [207].

4.2.4 PKA puncta counting methods

Number of PKA puncta in cells were established by counting manually the visible puncta in images acquired using ImageJ software. PKA puncta was counted by the author, and by undergraduate students (Jamie Adams and Sam Santhouse) under author's supervision, where indicated.

4.2.5 PDE activity assay

Colorimetric PDE activity assay reagents were purchased from Abcam, and imaged using Agilent BioTek Cytation C10 confocal imaging plate reader.

The basis for the assay is the cleavage of cAMP by a cyclic nucleotide phosphodiesterase. The 5'-nucleotide released is further cleaved into the nucleoside and phosphate by the enzyme 5'-nucleotidase. The phosphate released due to enzymatic cleavage is quantified using Green Assay Reagent in a modified Malachite Green assay. A nonspecific cyclic nucleotide phosphodiesterase inhibitor, 3-isobutyl-1-methylxanthine (IBMX) is included as a test control for inhibitor screening.

4.2.6 *In silico* protein disorder predictions

Disorder of different protein of interest, including RIα and RIIβ was predicted using PONDR (http://www.pondr.com/). Disorderliness of the amino acid sequence is a known predictor of its propensity to phase-separate [207]. The amino acid sequence used for disorderliness evaluation was from UniProt [217].

4.2.7 PKA condensation *in vitro*

In vitro PKA condesation assay was performed as described before [111]. The assay was performed in 150 mM KCl, 5 mM $MgCl_2$, 20 mM HEPES, pH 7.0, 1 mM ethyleneglycol-bil-N,N'-tetraacetic acid (EGTA), 1 mM dithiothreitol, 0.5 mM ATP, and 4% Polyethylene Glycol 4000 (unless specified otherwise). Purified PKA RIα protein (a gift from Prof Herberg, University of Kassel, Germany) and commercially available stearated HT31 peptide (Torcis Bioscience) were incubated at different concentrations at room temperature and imaged under DIC and/or fluorescence microscopy using confocal laser scanning microscope (TCS SP5 II; Leica, Germany, 20x air or 60x water immersion objective).

4.2.8 Statistical analysis

For the FRET analysis, each data point represents observations from individual cells or specific subcellular structures, as specified in the figure legends. This has been outlined in General Methods, Chapter 2, Section 1.

Sample sizes are indicated in the figure legends. All data presented in the figures were obtained from at least three separate NRVM isolations to ensure reproducibility and mitigate batch effects. For quantitative HEK293T, all the data acquired is from at least two different passages. Error bars and shaded areas in graphs represent standard deviations (SD), unless otherwise specified in the figure legends.

Due to the relatively small sample sizes, the unknown distribution of PKA puncta condensation data, and minimal existing biological insight, all the data was considered to be non-normally distributed. Consequently, all statistical tests performed were non-parametric, avoiding the assumption of normality. It is acknowledged that performing non-parametric tests on normally distributed data does not pose significant downsides, except that differences might be underestimated.

Otherwise, statistical procedures and data analysis was performed, and data visualised as outlined in General Mehtods, Chapter 2, Section 1.

4.3 Results

4.3.1 PKA condensation in HEK293T cells

PKA RIα condensation was first demonstrated in 2020 by Zhang et al. [111] showing the formation of condensates *in vitro*, and in cells, including HEK293T, NRVM, and neuronal cells, by over-expressing PKA RIα with a fluorescent tag. Endogenous PKA RIα condensation in HEK293T cells was also shown by tagging RIα using CRISPR.

To confirm these findings, and investigate if PKA RIIβ also forms condensates in cells, HEK293T cells were transfected with PKA RIα and RIIβ tagged with a fluorescent tag. Puncta-like structures were observed in living HEK293T cells expressing RIα-GFP, RIIβ-RFP, and RIα-RFP. Cat-YFP (without expression of RI or RII) also formed puncta in HEK293T cells. There were no apparent differences in the puncta appearance between RIα-RFP and RIα-GFP (Fig. 4.2 A, B). It appeared that there was minimal co-localisation between RI and RII puncta in HEK293T cells expressing RI-GFP and RII-RFP (Fig. 4.2 B).

To detect endogenous puncta-like patterns, immuno-staining was used, and a puncta-like distribution was observed (Fig. 4.2 C). This is in agreement with published data [218]. However, due to the limitations associated with investigating LLPS in fixed cells, further immuno-staining experiments were not performed [219].

To detect endogenous PKA RIα puncta-like distributions as described before [111], HEK293T-RI cell line was used where the line was generated by introducing the 11th strand of GFP (GFP11) [212] at the C terminus of RIα via CRISPR-Cas9 in HEK293A cells, yielding the HEK293T-RI cell line. However, the experiments with this cell line were not successful despite multiple attempts and optimisations in the transfection protocol, a good expression of RIα-GFP signal was never achieved (Appendix, Fig. A.2). Due to these limitations, subsequent experiments were performed in living cells with expression of exogenous proteins tagged with fluorescent constructs [219].

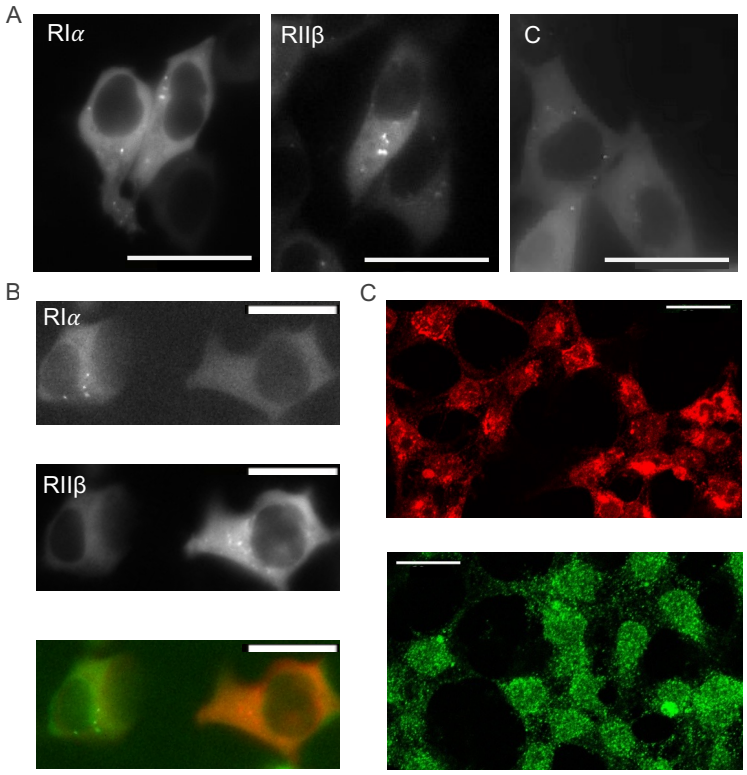


Figure 4.2: Appearance of puncta-like PKA structures in HEK293T cells. Imaging experiments with live cells were performed multiple times (n= at least 10). Scale bar: 20 µm. **A.** From left to right: Representative images of RIα-RFP, RIIβ-RFP, and C-YFP puncta in HEK293T cells. **B.** From top to bottom: representative images of RIα-GFP (top), RIIβ-RFP (middle) puncta in HEK293T cells, and the localisation of RIα-GFP relative to RIIβ-RFP (bottom). **C.** Representative images of immuno-stained HEK293T cells for PKA C subunit (top) and RIα (bottom). The immuno-staining experiments were performed once (n=1).

4.3.2 PKA puncta are dynamic

Next, the dynamics of PKA RIα and newly identified RIIβ puncta were investigated. Movement and merging of puncta are two of the key characteristics of LLPS [207]. Additional methods to test for LLPS include FRAP, disruption with 1,6-HEX treatment, and evaluating shape, where a round shape indicates a higher likelihood of the puncta being formed via LLPS. However, these methods have limitations. For example, diffraction-limited features often appear round, potentially obscuring the true structure, complicating roundness assessments. The limitations of FRAP in LLPS analysis have been discussed earlier. Hexanediol disrupts weak interactions associated with LLPS but also increases membrane permeability and can even

promote puncta formation [220]. Although each tool has its limitations, their combined use may provide more convincing evidence of protein phase separation.

Upon qualitative examination, both RIα and RIIβ puncta appeared to be round in shape (Fig. 4.2 A, B). Then it was tested if puncta respond to cAMP increase, as was indicated by previously published data, and if the puncta can be disrupted with 1,6-HEX.

It was observed that upon 25 µM FSK treatment for 15 min, the number of condensates observed in cells was significantly increased for both RIα and RIIβ subunits expressed in HEK293T cells (Fig. 4.3 A, D). This finding is in line with previously published data for RIα, and demonstrates a similar dynamic nature of RIIβ condensates.

Next, additional control experiments were performed to investigate if the effects observed are cAMP-specific. To test it, the change in puncta number was measured after increase in cGMP. Treatment with NO donor S-nitroso-N-acetylpenicillamine (SNAP) and guanylate cyclase stimulator BAY 41-2272, which induces and increase in cGMP, resulted in a small decrease in the number of PKA RIα, but not RIIβ condensates in cells (Fig. 4.3 B, E). This suggests that the increase in R subunit condensates is specifically cAMP-dependent.

1,6-HEX 2.5% treatment for 15 min reduced the number of RIα and RIIβ condensates in HEK293T cells (Fig. 4.3 C, F). The effect size was 15-30% reduction suggesting that 1,6-HEX treatment for 15 min disrupts some but not all PKA LLPS. A control agent, 2,5-HEX, did not have the same effect on PKA RIα condensates and induced no changes in the number of puncta per cell, as expected (Fig. 4.3 G).

Interestingly, stimulation with 10 nM ISO, βAR activator, did not induce a significantly increase in RIα condensates, unlike treatment with 25 µM FSK (Fig. 4.3 H). This suggests that either a greater increase in cAMP than elicited by 10 nM ISO is required to observe an increase in PKA condensation, or that the means used to observe and count the puncta are not sensitive enough to capture the differences in the number of puncta before and after the application of low cAMP stimulation. Another possibility is that ISO-induced cAMP increase does not affect puncta.

The dynamic nature of the condensates was further ascertained by observing their merging and moving in cells. Altogether, the results confirm PKA RIα phase separation in HEK293T and identify RIIβ as a PKA subunit that also forms liquid-like puncta in cells.

The modulation of puncta by either FSK or 1,6-HEX raises important questions about the biological significance of these findings. Despite the relatively low effect size, further experiments demonstrate that the 1,6-HEX-induced reduction in puncta is sufficient to alter cAMP signalling in the cell, including changes in response to adrenergic stimulation (Chapter 4, Results, subsection 4.3.8).

Future functional assays could be designed to investigate the biological relevance of these observations. For instance, establishing a cell line where PKA phase separation is abolished—achievable through genetic modifications such as those previously described [210]—could provide insight into how 1,6-HEX affects cAMP signalling. In such a model, no effect would be expected, as PKA would be unable to undergo liquid-liquid phase separation.

Additionally, FSK treatment, which increases the number of PKA puncta, is known to have various effects on cellular function, including enhanced and accelerated cell shortening, primarily through cAMP elevation. To determine whether these effects are mediated via PKA phase separation, it would be crucial to assess whether any new effects (or the absence of previously observed effects) occur upon FSK treatment in a cell line incapable of PKA condensation.

However, such assays are not without limitations. Currently available genetic mutations that disrupt PKA condensation (e.g., PKA RIα L50R [210]) are known to induce additional effects, such as interference with AKAP binding or cAMP binding [210]. These off-target effects could complicate the interpretation of results, necessitating careful experimental design and complementary approaches.

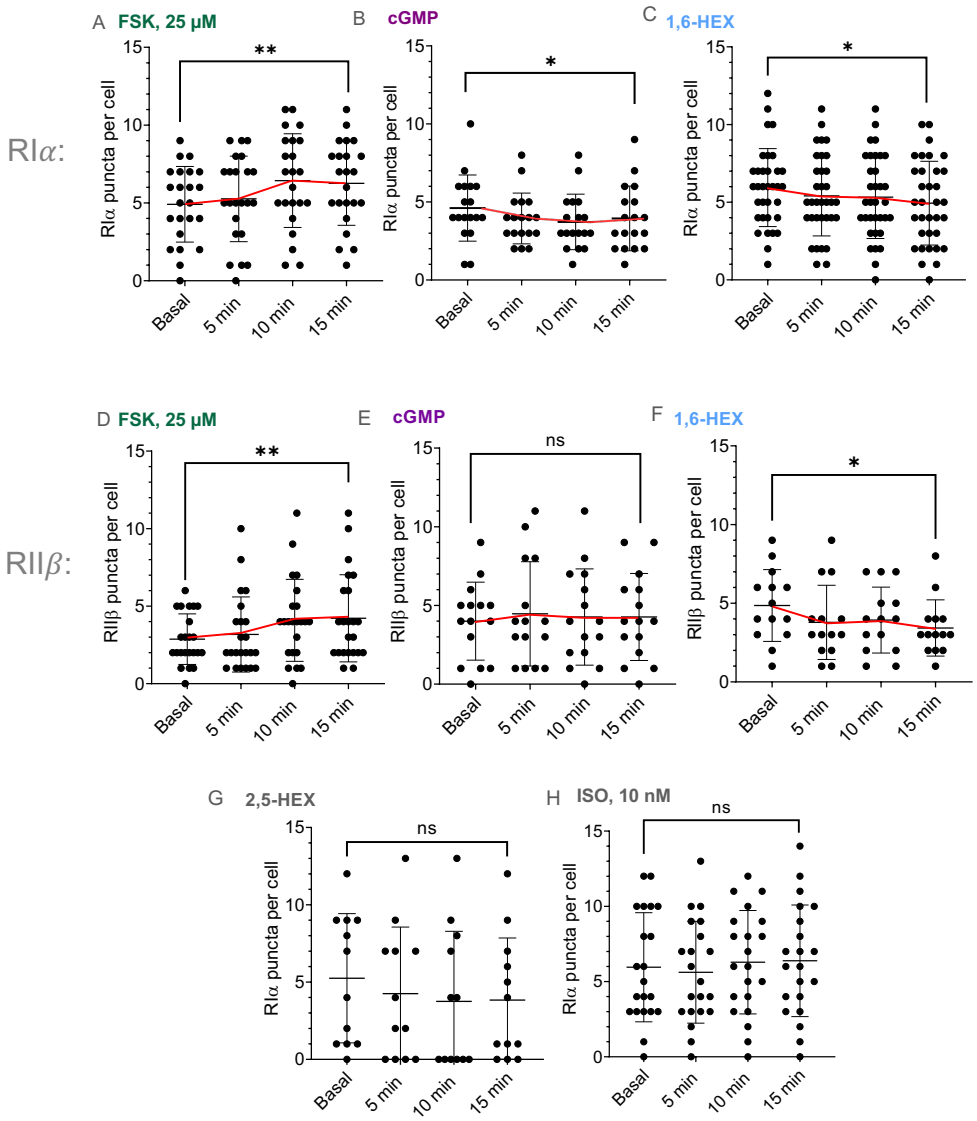


Figure 4.3: PKA puncta are dynamic in HEK293T cells. **A.** The number of RIα-GFP condensates (n=22 individual cells, N=5 HEK293T cultures) increases after treatment with 25 µM FSK for 15 min. Wilcoxon signed-rank test for Basal vs. 15 min, p=0.0005. **B.** RIα-GFP condensates (n=18 individual cells, N=4 repeats (HEK293T cultures)) decrease in number after treatment with SNAP and BAY 41-2272 for 15 min. Wilcoxon signed-rank test for Basal vs. 15 min, p=0.0337. **C.** RIα-GFP condensates (n=34 individual cells, N=3 repeats (HEK293T cultures)) decrease in number after treatment with 2.5% 1,6-HEX for 15 min. Wilcoxon signed-rank test for Basal vs. 15 min, p=0.0308. **D.** RIIβ-RFP condensates (n=20 individual cells, N=4 repeats (HEK293T cultures)) increase in number after treatment with 25 µM FSK for 15 min. Wilcoxon signed-rank test for Basal vs. 15 min, p=0.0262. **E.** The number of RIIβ-RFP condensates (n=15 individual cells, N=2 repeats (HEK293T cultures)) does not change significantly after treatment with SNAP and BAY 41-2272 for 15 min. Wilcoxon signed-rank test for Basal vs. 15 min, p=0.54. **F.** RIIβ-RFP condensates (n=15 individual cells, N=3 repeats (HEK293T cultures)) decrease in number after treatment with 2.5% 1,6-HEX for 15 min. Wilcoxon signed-rank test for Basal vs. 15 min, p=0.0078. **G.** The number of RIα-GFP condensates (n=12 individual cells, N=2 repeats (HEK293T cultures)) is not affected by 2.5% 2,5-HEX treatment for 15 min. Wilcoxon signed-rank test for Basal vs. 15 min, p>0.99. **H.** The number of RIα-GFP condensates (n=21 individual cells, N=4 repeats (HEK293T cultures)) is not affected by 10 nM ISO treatment for 15 min. Wilcoxon signed-rank test for Basal vs. 15 min, p=0.55.

4.3.3 PKA condensates as cAMP buffers

Next, it was investigated if and how PKA RIα condensates sequester cAMP. PKA RI condensates have been hypothesised to sequester and buffer cAMP in HEK293 cells [111]. The publication by Zhang et al. (2020) included experiments showing that cAMP content, as measured with a FluoSTEP-ICUE sensor targeted to the PKA RIα, is higher in the PKA puncta than in the diffuse PKA RIα regions.

Furthermore, LLPS disruption with 1,6-hexanediol (HEX) was found to result in a greater cAMP signal induced by the AC activator forskolin around PDE4D2's catalytic site. Based on this, the authors hypothesise that the disruption of RIα condensates leads to decreased cAMP buffering, overwhelming the ability of the PDEs to effectively compartmentalise cAMP. This suggests that the PKA RIα condensation is essential for the formation and maintenance of cAMP nanodomains.

First, using EPAC-SH187 sensor, it was examined if basal cAMP ratios are affected by puncta dissolution with 1,6-HEX. It was found that the basal cAMP ratio increases slightly in majority of the cells over the course of 15 min treatment (Fig. 4.4 C). The observed effect could be due to the release of cAMP from the PKA RI condensates upon their disruption, or due to PDE inhibition by 1,6-HEX, which is discussed later.

To test if PKA RI condensates sequester cAMP, RIα-CFP and C-YFP constructs were used [186]. In the presence of cAMP, RI-CFP undergoes a conformational change, increasing the distance between CFP and YFP, preventing resonance energy transfer and leading to a loss of the FRET signal (Fig. 4.4 A). Therefore, this sensor provides an ideal tool to directly measure the content of cAMP within the PKA condensates.

Using the snsor in HEK293T cells, PKA RIα-CFP and PKA C-YFP puncta were observed (Fig. 4.4 B). Using RI-CFP and C-YFP constructs, it was tested if cAMP content in the condensates is larger than in the cytosol. First, CFP and YFP intensities were quantified after direct excitation of CFP, and YFP, respectively. It was found that the PKA RI-CFP, and PKA C-YFP amount is greater in the puncta than outside the puncta in the cytosol (diffuse regions) (Fig. 4.4 D, E). This was

expected as puncta represent regions of condensed PKA. To establish if in puncta the relative amount of R-CFP and C-YFP was different from the surrounding cytosol, and thus eclude the possibility that the difference in FRET ration may dependent on this, the ratios of CFP (excited by CFP) over YFP (excited by YFP) were compared and revealed no differences between the diffuse and puncta regions (Fig. 4.4 F) indicating the same relative amount of R and C subunits in the puncta and the cytosol. Basal FRET cAMP ratios (CFP excitation) were found to be higher in puncta than in the cytosol (Fig. 4.4 G). This suggests that cAMP is present in the puncta in higher quantities than in the cytosol, and this difference is not driven by the different amount of the sensors components (RI-CFP and C-YFP) between the puncta and the diffuse cytosolic regions.

Previously published findings indicate that PKA RIα condensation disruption with 1,6-HEX results in an increased cAMP response to forskolin (FSK). To confirm this finding, cytosolic EPAC-SH-187 cAMP sensor was used in HEK293T cells. It was found that in the cells after 15 min 2,5% 1,6-HEX treatment, the increase in cAMP after 3 µM FSK treatment was greater than in non-treated cells (Fig. 4.4 H). This is in line with previously published findings.

The basal cytosolic cAMP ratios were also examined. The ratios were found to be lower in cells overexpressing PKA RIα than in controls (Fig 4.4 I). Finally, it was tested if overexpressing PKA RIα would result in higher cAMP sequestering, and therefore, attenuated response to adrenergic stimulation. No such effect was observed (Fig 4.4 J). Data suggest that PKA RI could provide cAMP sequestration, resulting in reduced basal cAMP ratios measured in the cytosol. However, the additional puncta are likely already saturated with cAMP and may not be effective at attenuating the cAMP response to ISO.

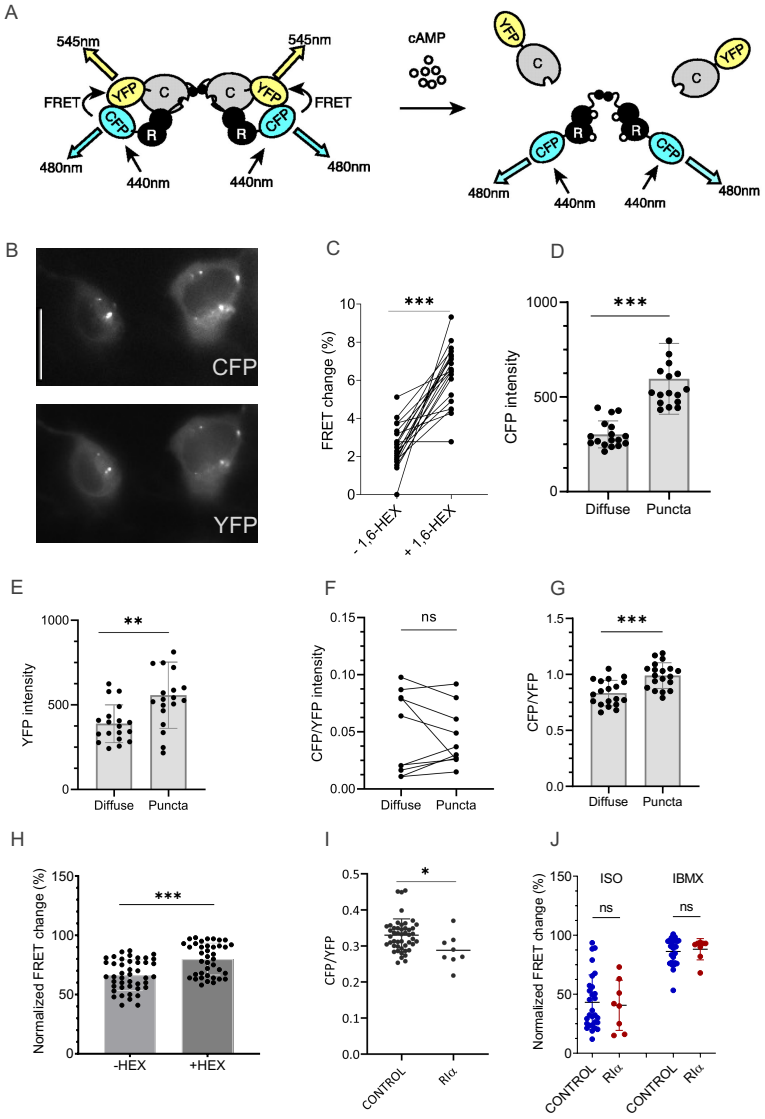


Figure 4.4: cAMP is sequestered inside the RI condensates. All the data shown here is from multiple puncta, multiple cells, and from at least three different passages of HEK293T cells. **A.** A schematic of the RI-CFP and C-YFP FRET cAMP sensor developed by Zaccolo et al. (2002). Schematic adapted from Zaccoolo et al. (2002), CC BY 4.0 [186]. **B.** Representative images of HEK293T cells expressing PKA RIα-CFP (top) and C-YFP (bottom) constructs. Scale bar: 20 µm. **C.** FRET change before and after 15 min 2.5% 1,6-HEX treatment in the cytosol of HEK293T cells measured with EPAC-SH187 sensor. Wilcoxon signed-rank test, n=19 individual cells, N=3 repeats (HEK293T cultures), p=0.0002. **D.** CFP intensity values recorded in HEK293T cells expressing RI-CFP and C-YFP are significantly higher in the puncta regions (n=17 puncta, N=4 repeats (HEK293T cultures)) than in diffuse regions (n=17) in cells. Mann-Whitney U test, $p<0.0001$. The data was acquired by S. Santhouse under the author's supervision. **E.** YFP intensity values recorded in HEK293T cells expressing RI-CFP and C-YFP after CFP excitation are significantly higher in the puncta regions (n=19 puncta, N=4 repeats (HEK293T cultures)) than in diffuse regions (n=19) in cells. Mann-Whitney U test, p=0.0043. The data was acquired by S. Santhouse under the author's supervision. **Continued on next page.**

F. Ratio of CFP (with CFP excitation) over YFP (YFP excitation) recorded in HEK293T cells expressing RI-CFP and C-YFP are not significantly different between the puncta (n=10 puncta, N=3 repeats (HEK293T cultures)) and diffuse regions (n=10 puncta). Wilcoxon signed-rank test, p=0.82. The data was acquired by S. Santhouse under author's supervision. **G.** CFP/YFP ratios recorded in HEK293T cells expressing RI-CFP and C-YFP are significantly higher in the puncta regions (n=19 puncta, N=3 repeats (HEK293T cultures)) than in diffuse regions (n=19) in cells. Mann-Whitney U test, p=0.0003. **H.** 15 min 2.5% 1,6-HEX treatment (n=44 individual cells, N=3 repeats (HEK293T cultures)) results in an amplified cAMP increase compared to controls (n=39 individual cells, N=3 repeats (HEK293T cultures)) following 3 µM FSK stimulation in the cytosol of HEK293T cells as measured with EPAC-SH187 sensor. Mann-Whitney U test, p<0.0001. **I.** Basal cAMP FRET ratios measured with EPAC-SH187 sensor is higher in the control cells (n=47 individual cells, N=7 repeats (NRVM isolations)) than cells expressing PKA RIα-RFP (n=8 individual cells, N=5 repeats (NRVM isolations)). Mann-Whitney U test, p=0.025. **J.** Normalised FRET change after 1 nM ISO stimulation recorded in the cytosol of NRVM does not differ significantly between control (n=29 individual cells, N=4 repeats (NRVM isolations)) and RI-RFP expressing cells (n=8 individual cells, N=4 repeats (NRVM isolations), p=0.8). There were no statistical differences between the control and RI-RFP expressing cells in their subsequent response to PDE inhibition with IBMX. Mann Whitney U test, p=0.98.

4.3.4 1,6-HEX affects PDE activity *in vitro*

Despite previous results providing evidence of cAMP sequestration inside the PKA puncta, some approaches to protein LLPS investigation have shortcomings. Namely, 1,6-HEX is known to induce off-target effect which could provide an alternative interpretation to the results. For example, if 1,6-HEX inhibited PDE activity, cAMP increase after 1,6-HEX could be explained by the reduced capacity of PDEs to degrade cAMP, and subsequent cAMP accumulation. To investigate if 1,6-HEX affects PDE activity, a colorimetric *in vitro* PDE activity assay was performed.

The basis for the assay is the cleavage of cAMP by a purified phosphodiesterase *in vitro*. The 5'-AMP released is further cleaved into the adenosine and phosphate by 5'-nucleotidase. The phosphate released due to enzymatic cleavage is quantified using Green Assay Reagent in a modified Malachite Green assay.

After establishing a standard curve, the potential inhibitory activity of a compound such as 1,6-HEX can be measured by recording the change in optical

density (OD) induced by the exposure to the compound, and comparing the results with the standard curve, and a known PDE inhibitor, such as IBMX.

First, it was tested if 1,6-HEX does not alter the activity of any reagents used in the assay alone (the Green Assay Reagent). This was done by quantifying the OD signal produced by the combination of cAMP, Green Assay Reagent, 5'-nucleotidase, and 1,6-HEX. As no PDEs were added in this case, no change in OD signal was expected as there are no enzymes to hydrolyse cAMP into 5'-AMP. However, it was found that 1,6-HEX alters Green Assay Reagent activity and produces a change in OD signal (Fig. 4.5 A). 1,6-HEX amplified OD signal measured where the OD signal produced by dye-1,6-HEX interaction alone remain constant over time.

Therefore, a mathematical correction on the assay data was performed by subtracting the change in OD produced by 1,6-HEX alone from all the recorded data points in the 1,6-HEX group. After the correction, it appeared that 2.5% 15 min 1,6-HEX treatment inhibits PDE activity to a similar level as 40 µM IBMX application which was used as a control (Fig. 4.5 B).

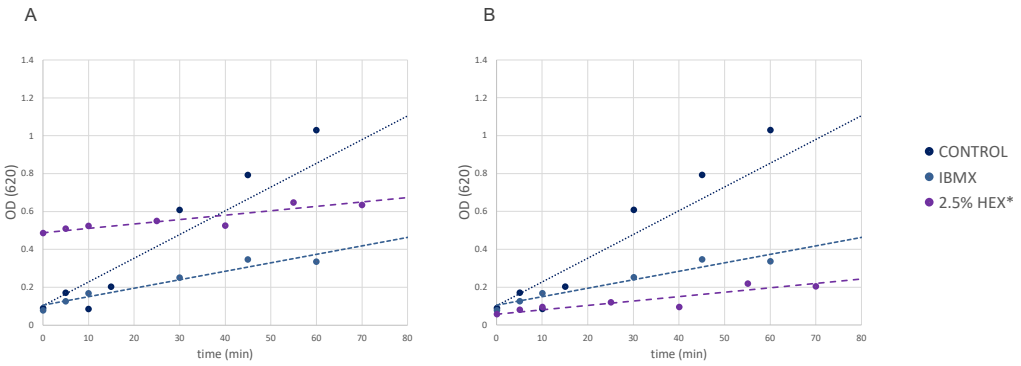


Figure 4.5: 1,6-HEX inhibits PDE activity *in vitro* **A.** Linear relationship between the recorded results in the respective groups. Due to the non-specific interaction between the assay dye reagent and 1,6-HEX, a change in OD signal occurred even without a PDE present resulting in different starting conditions between the groups. **B.** 2.5% 1,6-HEX application results in the reduced PDE hydrolytic activity compared to controls. 40 µM IBMX induces a similar inhibition of the PDE activity after around 15 min incubation. The linear relationship is visualised after fitting the curves after the mathematical correction of the data as described above.

4.3.5 Manipulation of PKA-AKAP interaction affects PKA phase separation

Given the limitations of methods used to disrupt PKA phase separation discussed above, new approaches for modulation of PKA condensation modulation are needed. It is known that PKA D/D domain is essential for PKA phase separation as the deletion of the domain has been shown to abolish PKA puncta formation ability in cells [111]. D/D is also a domain that permits PKA-AKAP interactions. Exploiting this feature, it was tested if manipulation of PKA-AKAP interactions could provide an alternative way to affect PKA LLPS.

In silico investigation of protein propensity to phase-separate

First, an *in silico* analysis of the level of the disorderliness in the amino acid sequence of proteins involved in cAMP signalling cascade was carried out. Sequence disorderliness serves as a positive indicator of LLPS [207]. The analysis was performed using PONDR software (http://www.pondr.com/), which is an algorithm used for predicting the naturally disordered region, widely used in LLPS research [111, 221]. PONDR uses neural networks to analyse sequence attributes (e.g. hydropathy) across windows of 9 to 21 amino acid residues. These attributes are averaged over each window and input into the neural network to predict the level of disorder across the entire protein sequence, where disorder scores range from 0 (ordered) to 1 (fully disordered).

The analysis was done prior to the investigations in cells to test the potential involvement of AKAPs, and other proteins involved in cAMP signalling cascade in LLPS. It was observed that RIIβ has a lower sequence disorderliness score than RIα (Fig. 4.6 A). Interestingly, it was also observed that a large number of different isoforms of AKAPs have a high sequence disorderliness (Fig. 4.6 A). LLPS of AKAP95 has been reported where the region driving phase separation was found to be in the amino acid sequence position 200-300 which is the PKA binding region [222]. Another AKAP with identified high sequence disorder was AKAP12, which is known to interact with PDE8 [72] (Fig. 4.6 A).

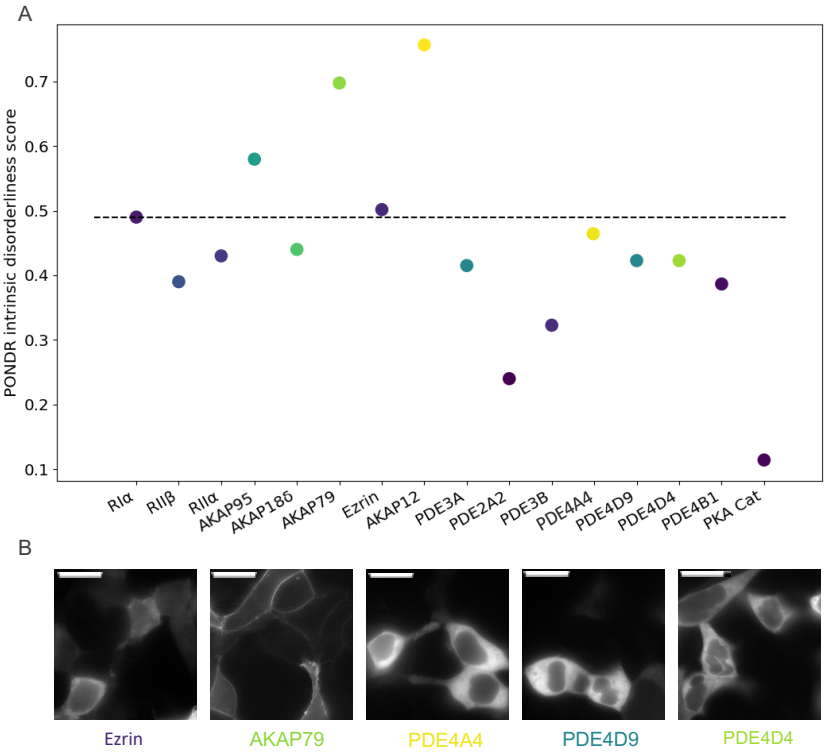


Figure 4.6: Investigation of LLPS of other proteins in cAMP signalling cascade. **A.** In silico assessment of amino acid sequence disorder of various proteins implicated in cAMP signalling cascade. **B.** From left to right: ezrin, AKAP79, PDE4A4, PDE4D9, and PDE4D4 localisation in HEK293T cells. Scale bar: 20 µm.

The sequence disorder of some PDEs was also examined, and it was found that in general, they have a lower sequence disorderliness score than PKA and AKAPs (Fig. 4.6 A). To investigate potential AKAP and PDE involvement in the phase separation, HEK293T cells were transfected with various AKAP and PDE constructs available in the laboratory, but no puncta-like appearance was observed (Fig. 4.6 B).

PKA RIα liquid-liquid phase separation *in vitro*

Next, it was investigated if PKA-AKAP interactions play a role in PKA condensation. To do that, PKA-AKAP interaction disrupting peptides were used. First the experiments were performed *in vitro* with purified RIα protein, and then in cells.

Overexpression of smAKAP was found to sequester PKA RIα to the membrane

and to reduce the number of PKA puncta [210]. Therefore, it was hypothesised that PKA-AKAP interaction disruption with disrupting peptide will reduce the number of PKA puncta. Disrupting peptides are designed based on the endogenous AKAP sequences and competitively bind PKA preventing it from anchoring to the endogenous AKAPs. It was thought that the peptides will serve as artificial AKAPs, and that AKAP-PKA, or disrupting peptide-PKA binding will sequester PKA and reduce the number of free PKA subunits available for PKA puncta formation thereby reducing the number of PKA puncta in cells, and *in vitro*.

To investigate the involvement of PKA-AKAP interactions in controlling PKA LLPS, stearated HT31 peptide was used to modulate RIα phase separation *in vitro*. The assay was carried out using varying concentration of purified RIα protein, and using a commercially available stearated HT31 peptide. Increasing the concentration of RIα resulted in greater number of condensates observed (Fig. 4.7 A). No phase separation was observed at 3.125 µM RIα concentrations, and condensation appeared after the concentration was increased to 6.5 µM.

To test if RIα condensation can be disrupted *in vitro*, 2.5% 1,6-HEX was applied for 15 min. After the application, the condensation was disrupted where RIα condensates appeared to become elongated and not round (Fig. 4.7 B, as indicated on the figure). This is in line with known 1,6-HEX properties allowing protein LLPS disruption.

Knowing the interaction of HT31 with the D/D of RIα, varying amounts of HT31 were added to 6.5 µM RIα solutions. It was observed that 6.5 µM RIα condensation was abolished with 6.5 µM HT31. However, when HT31 concentration was increased, low levels of RIα condensation were observed again (Fig. 4.7 B).

This could be explained by a non-linear relationship between the interactions of D/D of RIα and HT31 with condensation propensity regulation. It could be that HT31-PKA binding induces allosteric changes in PKA that initially block LLPS. At higher concentrations HT31 may engage in multivalent interactions that restore or promote PKA LLPS [223]. Alternatively, a limitation of the assay is the stearation of HT31, which could alter LLPS properties independently from specific D/D

interactions. As the non-stearated form of the peptide is not commercially available, and to validate the effects of HT31 on RI LLPS, further experiments were performed in cells rather than *in vitro*, using HT31 peptide encoded in a plasmid form.

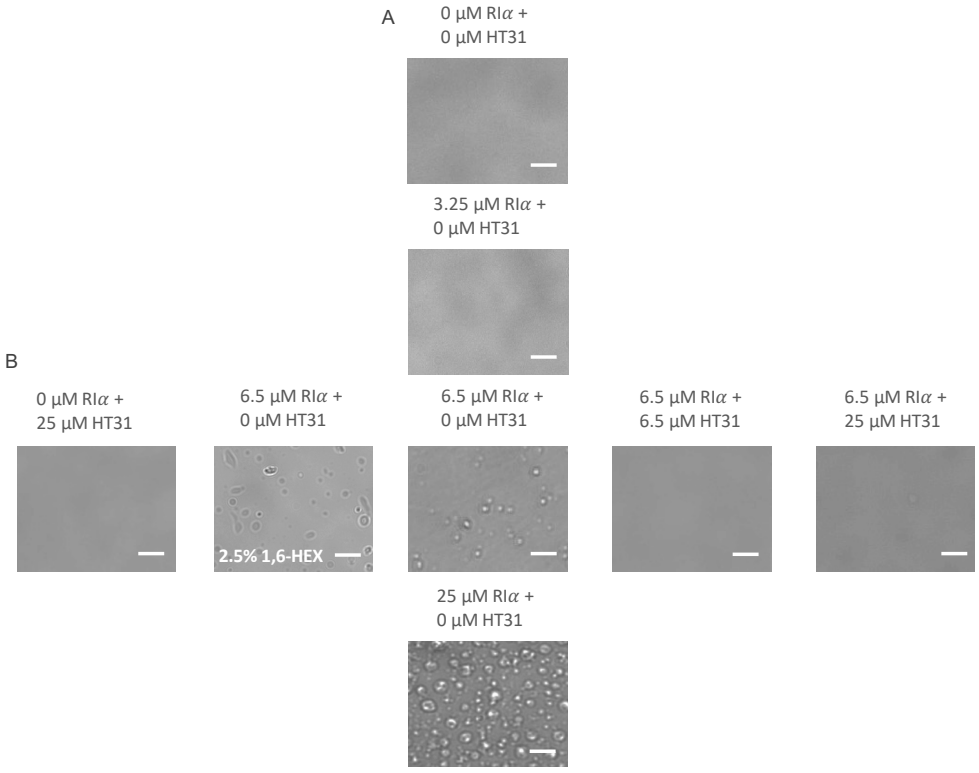


Figure 4.7: RIα phase separates *in vitro*. Scale bar: 10 µm. All *in vitro* experiments were performed at least 5 times, each with 3 technical replicates. **A.** Representative images (vertically from top to bottom) showing liquid droplet formation by purified RI at the indicated concentrations *in vitro*. **B.** Representative images (horizontally from left to right) showing RI liquid droplet dissolution by HT31 at the indicated concentrations *in vitro*. At larger concentrations, such as 25 µM of HT31, RIα liquid droplets become observable again. Second image from the left (as indicated): a representative image showing RIα liquid droplet dissolution after 15 min 2.5% 1,6-HEX application *in vitro*.

Disruption of AKAP-PKA interaction reduces PKA condensation in cells

The effect of disrupting PKA-AKAP interaction on PKA condensation was tested in cells. In addition to allowing to test the hypotehsis that PKA-AKAP interaction disruption with disrupting peptides would reduce the number of PKA puncta in cells, this approach allows to avoid potential caveats associated with using stearated HT31 in the *in vitro* assay.

It appeared that upon expression of HT31 (plasmid), PKA-AKAP interaction disrupting peptide, in HEK293T cells, the number of PKA condensates in cells was significantly reduced (Fig. 4.8 A). This was true for RIα-GFP, but not for RIIβ-

RFP (Fig. 4.8 B). The number of RIα-GFP puncta was found to be greater than RIIβ-RFP on average (Fig. 4.8 C). To test the acute effects of HT31 application, a stearated HT31 peptide was added to HEK293T cells expressing PKA RIα-GFP, and the puncta number was tracked over time. A reduction in puncta numbers was observed within 15 min (Appendix, Fig. A.3 C).

Experiments with RIα-RFP showed a similar trend to those performed with RIα-GFP (Fig. 4.8 D). As fluorescent tag can have an effect on LLPS properties [208], similar findings with GFP and RFP give credibility to the results. RIAD, a specific RI-AKAP interaction disruptor showed a more pronounced effect than HT31 for RIα (Fig. 4.8 D). SUSPER-AKAP-IS (SUPER-IS), a selective disruptor of RII-AKAP interaction, and HT31P, a control peptide for HT31 that does not bind to D/D, had no effect of the number of RIα puncta (Fig. 4.8 D). HT31P is used as a negative control and contains 2 prolines substituted for 2 hydrophobic residues within the PKA R binding domain. This disrupts the secondary structure of the amphipathic helix necessary for PKA binding and does not bind PKA, providing no disruption to PKA-AKAP binding. In the case of RIIβ, different disrupting peptides did not have an effect on the number of puncta (Fig. 4.8 E).

Next, the investigation was moved onto examining the functional roles of PKA LLPS in cardiomyocytes, specifically aiming to determine whether PKA LLPS contributes to cAMP compartmentalisation via cAMP buffering.

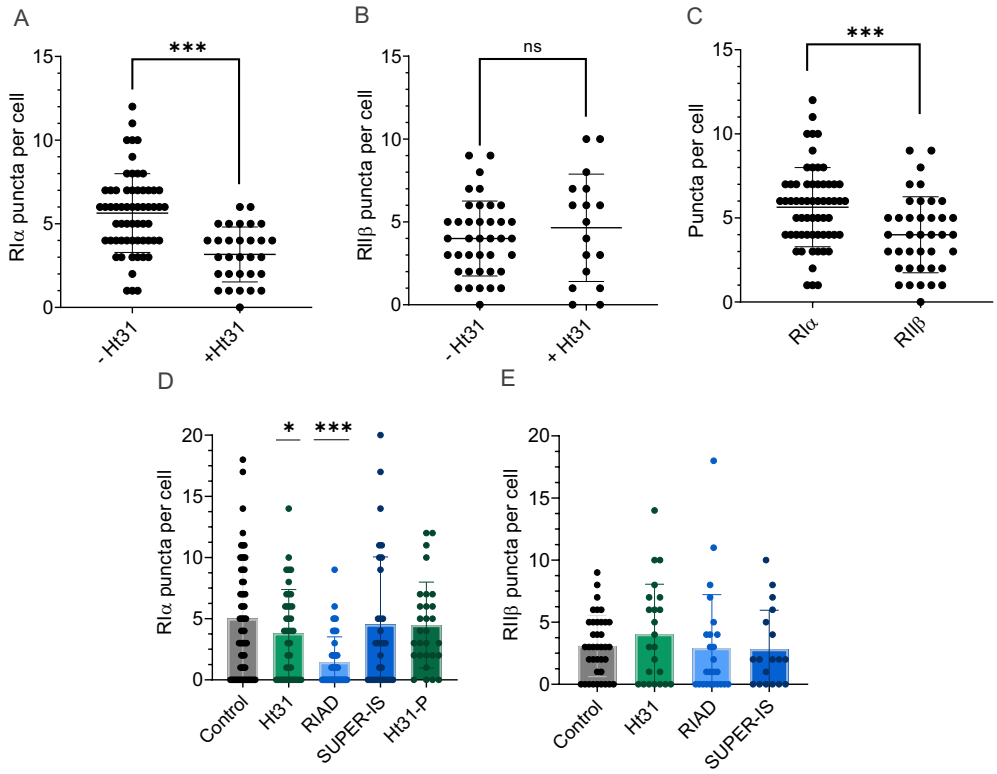


Figure 4.8: PKA-AKAP interactions control PKA LLPS. Here PKA-AKAP interactions were disrupted using different peptides introduced to the cells in a plasmid form. **A.** There are significantly fewer PKA RIα-GFP condensates in HEK293T cells with HT31 (n=43 individual cells, N=3 repeats (HEK293T cultures)) than in the cells without (n=30 individual cells, N=3 repeats (HEK293T cultures)) HT31. Mann-Whitney U test, p<0.0001. **B.** Expression of HT31 does not affect the number of PKA RIIβ-RFP condensates (n=17-24 individual cells, N=3 repeats (HEK293T cultures)) in HEK293T cells. Mann-Whitney U test, p=0.53. **C.** The number of PKA RIα-GFP condensates (n=43 individual cells, N=3 repeats (HEK293T cultures)) is significantly greater than PKA RIIβ-RFP (n=24 individual cells, N=3 repeats (HEK293T cultures)) in HEK293T cells. Mann-Whitney U test, p=0.0008. **D.** PKA-AKAP interaction disruption with HT31 (n=40 individual cells, N=3 repeats (HEK293T cultures)) and RIAD (n=47 individual cells, N=3 repeats (HEK293T cultures)) significantly reduces the number of PKA RIα-RFP condensation in HEK293T cells compared to controls (n=62 individual cells, N=3 repeats (HEK293T cultures)) (p<0.05), but HT31P (n=29 individual cell, N=3 repeats (HEK293T cultures)) and SUPER-AKAP-IS (n=31 individual cell, N=3 repeats (HEK293T cultures)) do not have the same effect. Kruskal-Wallis test, Dunn's correction. **E.** PKA-AKAP interaction disruption with HT31 (n=23 individual cells, N=3 repeats (HEK293T cultures)), RIAD (n=25 individual cells, N=2 repeats (HEK293T cultures)), or SUPER-AKAP-IS (n=18 individual cells, N=2 repeats (HEK293T cultures)) does not affect the number of PKA RIIβ-RFP condensates (control n=38 individual cells, N=3 repeats (HEK293T cultures)) in HEK293T cells. Kruskal-Wallis test, Dunn's correction, p=0.49.

4.3.6 PKA condenses in cardiomyocytes

After observing PKA RIα and RIIβ condensates in HEK293T cell, the investigations were continued to test if, as a consequence of their ability to buffer cAMP, thus enabling PDEs to effectively work as cAMP sinks, PKA condensates contribute to cAMP compartmentalisation at the myofilament. First, it was explored if the condensation can be observed in cardiac cells such as NRVMs. Primary cardiomyocytes were transfected with RIα-RFP, RIα-GFP, or RIIβ-RFP constructs, and puncta like distribution of RIα and RIIβ was observed in NRVM (Fig. 4.9 A, B). Puncta were round in appearance and moved across the cell showing merging and liquid-like behaviour (Fig. 4.9 B).

Due to the lack of availability of RI and RII viral constructs it was not possible to determine whether PKA condensation can be observed in adult cardiomyocytes. Immuno-staining was used to determine PKA RIα and C subunit distribution. The staining appeared to show dotted distribution of PKA, although this could not be interpreted as an indication of PKA condensation due to limitations involved when fixing cells, as fixing is known to affect LLPS properties [219] (Fig. 4.9 A).

4.3.7 PKA puncta are dynamic in cardiomyocytes

The properties of PKA condensates observed in NRVM cells were then examined. First, it was observed that on average, there were 40 ($\pm$ 10) RIα-RFP puncta per cell, and 35 ($\pm$ 10) RIIβ-RFP puncta per cell in NRVM. This is significantly more than observed in HEK293T cell (5.5 ($\pm$ 3) and 4 ($\pm$ 2), respectively), likely reflecting difference in the size of the cell where NRVM cell is on average 10 times larger than HEK293T cell.

Similarly to the observations made in HEK293T cells, treatment with HT31 or RIAD (plasmids) induced a decrease in the number of RIα but not RIIβ puncta in NRVM (Fig. 4.10 A, B, C). Control peptide HT31P did not have the puncta-reducing effect of HT31 on RIα condensation (Fig. 4.10 A). More cells did not have any RIα puncta in the presence of HT31 or RIAD (Fig. 4.10 D) than in

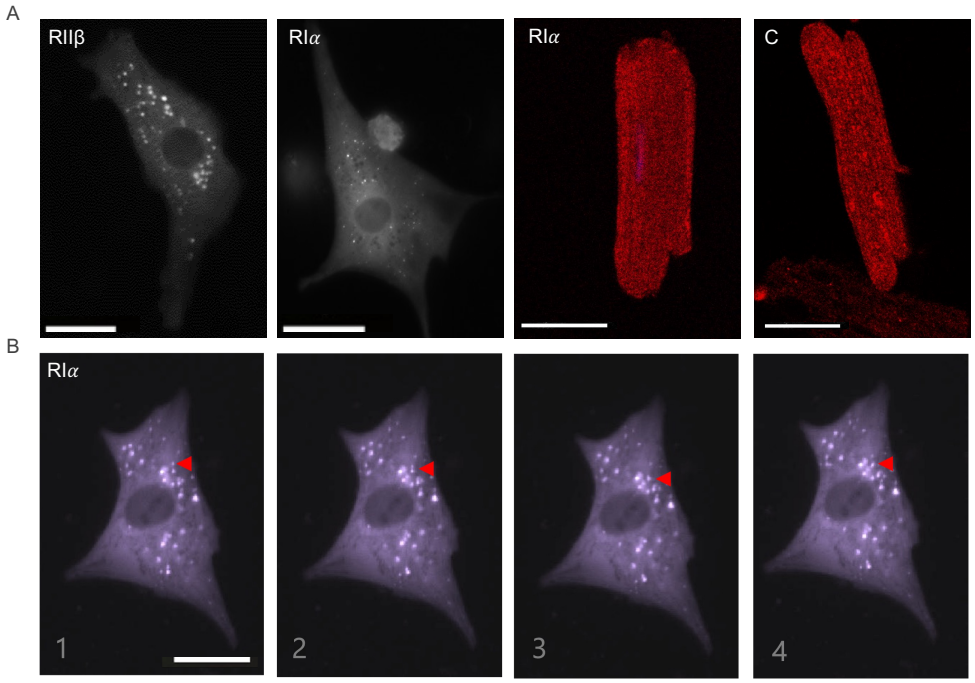


Figure 4.9: Representative images of PKA localisation in cardiomyocytes. Scale bar: 20 µm. Imaging experiments with were performed multiple times (n= at least 10 individual cells, N= at least 5 NRVM isolations). **A.** From left to right: PKA RIIβ-RFP and PKA RIα-GFP form liquid-like puncta in living NRVM cells; immuno-staining of PKA RIα and PKA C in ARVM show dotted appearance in fixed ARVM. **B.** PKA RIα-RFP form liquid-like puncta in living NRVM cells, and puncta move across the cells, and merge together, showing LLPS-like qualities. Numbers 1 to 4 indicate puncta merging sequence (merging starting at 1 and finishing in the image number 4).

controls. This was not observed with RIIβ where the presence of HT31 did not have any significant effect (Fig. 4.10 E).

2.5% 1,6-HEX treatment was found to reduce the number of RIα but not RIIβ puncta in NRVM (Fig. 4.10 F, H). This is unlike HEK293T cells, where 1,6-HEX treatment resulted in a decrease in the number of condensates for both, RI and RII (Fig. 4.3 B, E). The control agent 2,5-HEX did not have an effect on the puncta numbers in NRVM cells (Fig. 4.10 G, I). Similar to HEK293T cells, FSK was found to significantly increase the number of puncta in NRVM for both, RIα and RIIβ (Fig. 4.10 J, K).

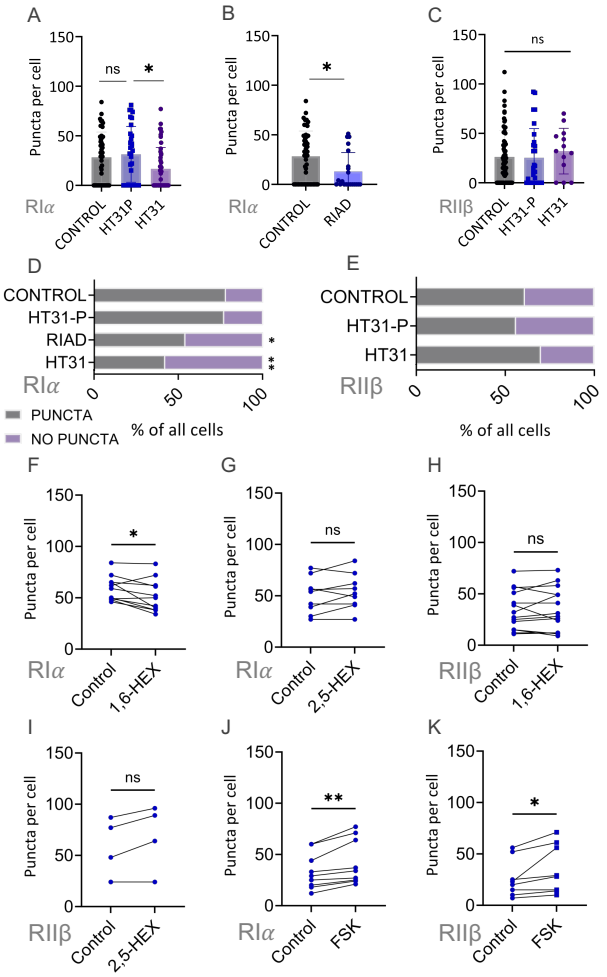


Figure 4.10: PKA puncta in NRVMs are dynamic. **A.** The number of PKA RIα-RFP puncta is reduced after transfection with HT31 (n=49 individual cells, N=7 repeats (NRVM isolations), p=0.039) but unaffected by the transfection with HT31P (n=32 individual cells, N=7 repeats (NRVM isolations), p=0.99). Kruskal-Wallis test, Dunn's correction. **B.** The number of PKA RIα-RFP puncta is reduced after transfection with RIAD (n=21 individual cells, N=3 repeats (NRVM isolations), p=0.0405). Mann-Whitney U test. **C.** The number of RIIβ-RFP condensates is unaffected by the transfection with HT31P (n=27 individual cells, N=3 repeats (NRVM isolations)) or HT31 (n=12 individual cells, N=3 repeats (NRVM isolations)) in NRVM. Kruskal-Wallis test, Dunn's correction, p=0.5281. **D.** The number of NRVM cells that have RIα-RFP puncta is lower when transfected with RIAD or HT31 compared to controls. Chi-sq test, $X^2 = 8.24$, p=0.016 for control, HT31 and RIAD. **E.** The number of NRVM cells that have RIIβ-RFP puncta is unaffected by the transfection with Ht31 compared to controls. Chi-sq test, $X^2 = 5.8$, p=0.054 for control, HT31 and HT31P. **F.** The number of RIα-RFP puncta (n=11 individual cells, N=3 repeats (NRVM isolations)) is decreased after 2.5% 1,6-HEX treatment. Wilcoxon signed-rank test, p=0.024. **G.** The number of RIα-RFP puncta (n=9 individual cells, N=3 repeats (NRVM isolations)) is unaffected by 2.5% 2,5-HEX treatment. Wilcoxon signed-rank test, p=0.3125. **H.** The number of RIIβ-RFP puncta (n=14 individual cells, N=3 repeats (NRVM isolations)) in NRVM is unaffected by 2.5% 1,6-HEX treatment. Wilcoxon signed-rank test, p=0.199. **I.** The number of RIIβ-RFP puncta (n=4 individual cells, N=2 repeats (NRVM isolations)) in NRVM is unaffected by 15 min 2.5% 2,5-HEX treatment. Wilcoxon signed-rank test, p=0.25. **Continued on next page.**

J. The number of RIα-RFP puncta (n=9 individual cells, N=4 repeats (NRVM isolations)) is increased after 15 min 25 µM FSK treatment. Wilcoxon signed-rank test, p=0.0039. **K.** The number of RIIβ-RFP puncta (n=8 individual cells, N=4 repeats (NRVM isolations)) is increased after 25 µM FSK treatment. Wilcoxon signed-rank test, p=0.0156.

4.3.8 PKA condensation does not impact cAMP compartmetalisation and cAMP signalling at the myofilament

Based on their initial findings, Zhang et al. (2020) suggest that PKA condensation is essential for cAMP compartmentalisation: PDEs cannot cope with the excess cAMP released on disruption of PKA condensates leading to the disruption of cAMP nanodomains [111]. Building on this interpretation, it was hypothesised that disruption of PKA condensation would result in the loss of cAMP compartmentalisation at the myofilament, which was characterised in the previous chapter (Chapter 3, Fig. 3.5 and Fig. 3.6).

To test this hypothesis, the response to 1 nM ISO stimulation was compared between controls, HT31 (plasmid), and 1,6-HEX treated NRVMs in different cAMP signalling domains, including the plasmalemma, SR, and the myofilament. This was achieved using targetted FRET reporters localised to the plasmalemma by AKAP79; to SR by AKAP18δ, to troponin I, and to MYBPC.

The examination of cAMP signalling after 1 nM ISO stimulation showed that the cAMP response to βAR activation is compartmentalised, with a higher cAMP level detected at plasmalemma and SR than at the myofilament, confirming previous findings [34]. When the signalling in the presence of PKA condensation disruption was examined, no difference was detected at the different domains, indicating that cAMP compartmentalisation is unaffected by the disruption of PKA condensation (Fig. 4.11 A). The response to subsequent PDE inhibition with IBMX was also not statistically different between treatment and control, except at MYBPC site (Fig. 4.11 B). No notable differences in cAMP response kinetics after IBMX application were observed in cells treated with HT31.

Similar findings were corroborated by disruption of PKA condensation with 1,6-HEX. It was found that the response to 1 nM ISO stimulation was unchanged, as observed in HT31 treated cells (Fig. 4.11 C). However, the PDE signalling was inhibited, unlike in cells treated with HT31 (Fig. 4.11 D). The cAMP response kinetics appeared to be slower in cells treated with 1,6-HEX than in control cells.

Comparison of the basal cAMP ratios between the cells with and without HT31 showed no statistical differences (Fig. 4.11 E). No differences were observed in the case of 1,6-HEX treatment as well (Fig. 4.11 F).

Altogether, these data suggests that PKA condensation disruption does not significantly influence cAMP compartmentalisation. Myofilament cAMP signalling does not appear to be affected by PKA condensation disruption. In the case of 1,6-HEX-mediated disruption, the results suggests that even though PDE activity is inhibited, it is still sufficient to maintain tight cAMP signalling control and dictate the level of cAMP achieved in the different compartments, both at basal conditions and on agonist application.

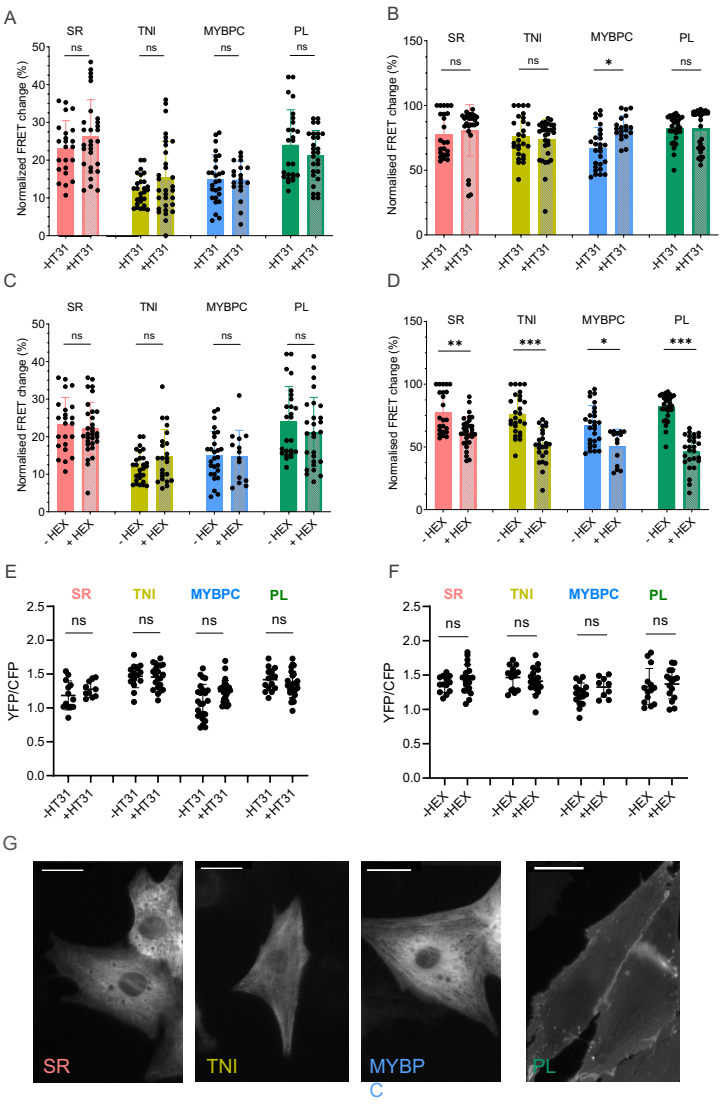


Figure 4.11: HT31 and 1,6-HEX treatment does not affect the adrenergic cAMP signal in the compartments at SR, plasmalemma (PL), and myofilament. **A.** Normalised FRET change after 1 nM ISO application measured with targeted cAMP CUTie sensors at the SR (n=23-29 individual cells, N=3 repeats (NRVM isolations), p=0.36), TNI (n=27-31 individual cells, N=5 repeats (NRVM isolations), p=0.44), MYBPC (n=19-27 individual cells, N=5 repeats (NRVM isolations), p=0.94), and PL (n=25-28, individual cells, N=3 repeats (NRVM isolations), p=0.38) sites shows no statistically significant differences in control cells and cells transfected with HT31. Mann-Whitney U test. **B.** Normalised FRET change after 100 µM IBMX after 1 nM ISO application measured with targeted cAMP CUTie sensors at the SR (n=23-29 individual cells, N=3 repeats (NRVM isolations), p=0.6), TNI (n=27-31 individual cells, N=5 repeats (NRVM isolations), p=0.7), MYBPC (n=19-27 individual cells, N=5 repeats (NRVM isolations), p=0.006), and PL (n=25-28 individual cells, N=3 repeats (NRVM isolations), p=0.168) shows no statistically significant differences in control cells and cells transfected with HT31 except for MYBPC. Mann-Whitney U test. **C.** Normalised FRET change after 1 nM ISO application measured with targeted cAMP CUTie sensors at the SR (n=23-31 individual cells, N=3 repeats (NRVM isolations), p=0.6), TNI (n=23-27 individual cells, N=5 repeats (NRVM isolations), p=0.19), MYBPC (n=14-27 individual cells, N=5 repeats (NRVM isolations), p=0.8), and PL (n=25-27 individual cells, N=3 repeats (NRVM isolations), p=0.2) sites shows no statistically significant differences in the cells treated and not treated with 2.5% 1,6-HEX. Mann-Whitney U test. **Continued on next page.**

D. Normalised FRET change after 100 µM IBMX after 1 nM ISO application measured with targeted cAMP CUTie sensors at the SR (n=23-31 individual cells, N=3 repeats (NRVM isolations), p=0.0016), TNI (n=23-27 individual cells, N=5 repeats (NRVM isolations), p<0.0001), MYBPC (n=14-27 individual cells, N=5 repeats (NRVM isolations), p=0.0062), and PL (n=25-27 individual cells, N=3 repeats (NRVM isolations), p<0.0001) is significantly lower in the cells treated than not treated with 2.5% 1,6-HEX. Mann-Whitney U test. **E.** Basal cAMP FRET ratios measured with targeted cAMP CUTie sensors at the SR (n=10-12 individual cells, N=3 repeats (NRVM isolations), p=0.2), TNI (n=15-21 individual cells, N=5 repeats (NRVM isolations), p=0.8), MYBPC (n=24-27 individual cells, N=5 repeats (NRVM isolations), p=0.055), and PL (n=15-24 individual cells, N=3 repeats (NRVM isolations), p=0.5) sites shows no statistically significant differences in control cells and cells transfected with HT31. Mann-Whitney U test. **F.** Basal cAMP FRET ratios measured with targeted cAMP CUTie sensors at the SR (n=12-19 individual cells, N=3 repeats (NRVM isolations), p=0.2), TNI (n=15-18 individual cells, N=5 repeats (NRVM isolations), p=0.4), MYBPC (n=9-16 individual cells, N=5 repeats (NRVM isolations), p=0.12), and PL (n=14-16 individual cells, N=3 repeats (NRVM isolations), p=0.7) sites no statistically significant differences in the cells treated and not treated with 2.5% 1,6-HEX. Mann-Whitney U test. **G.** Representative images of different sensors expressed in NRVM cells used for FRET experiments including (from the left): AKAP18δ-CUTie (SR), TNI-CUTie, MYBPC-CUTie, and AKAP79-CUTie (PL).

4.3.9 PKA condensation enables adrenergic signal transduction in the cytosol of NRVMs

In the previous chapter, clear differences in cAMP signalling were observed between the TNI, MYBPC, MYOM nanodomains, and the cytosol (Chapter 3, Fig. 3.6, Fig. 3.4). To investigate the effects of PKA condensation in the cytosol, the PKA condensation was disrupted with 15 min 2.5% 1,6-HEX treatment or with expression of HT31. It was hypothesised that upon PKA condensation disruption, cAMP will no longer be buffered, and cAMP levels in the cytosol will increase, resulting in an amplified response to adrenergic stimulation. To test this hypothesis, the response to adrenergic stimulation was measured in the cytosol of NRVMs using the cAMP FRET reporter EPAC-SH-187.

Unexpectedly, the results showed that upon disruption of PKA condensation, unlike what was observed in the compartments, the response to 1 nM ISO stimulation in the cytosol was significantly reduced in the cells treated with 1,6-HEX, or in cells treated with HT31 (Fig. 4.12 A-D). Similar effect was observed in the presence of RIAD (Fig. 4.12 E, F). Notably, disruption of LLPS impacted prominently the

peak cAMP response but not the subsequent plateau. HT31P, a control peptide, did not have such an effect (Fig. 4.12 C, D). Control agent 2,5-HEX did not affect the cAMP increase following ISO stimulation (Fig. 4.12 A, B). Treatments with 1,6-HEX, HT31, and RIAD resulted in slower cAMP response kinetics to PDE inhibition by IBMX, applied after ISO, but not when the cells were treated with HT31P or 2,5-HEX (Fig. 4.12 A, C, E).

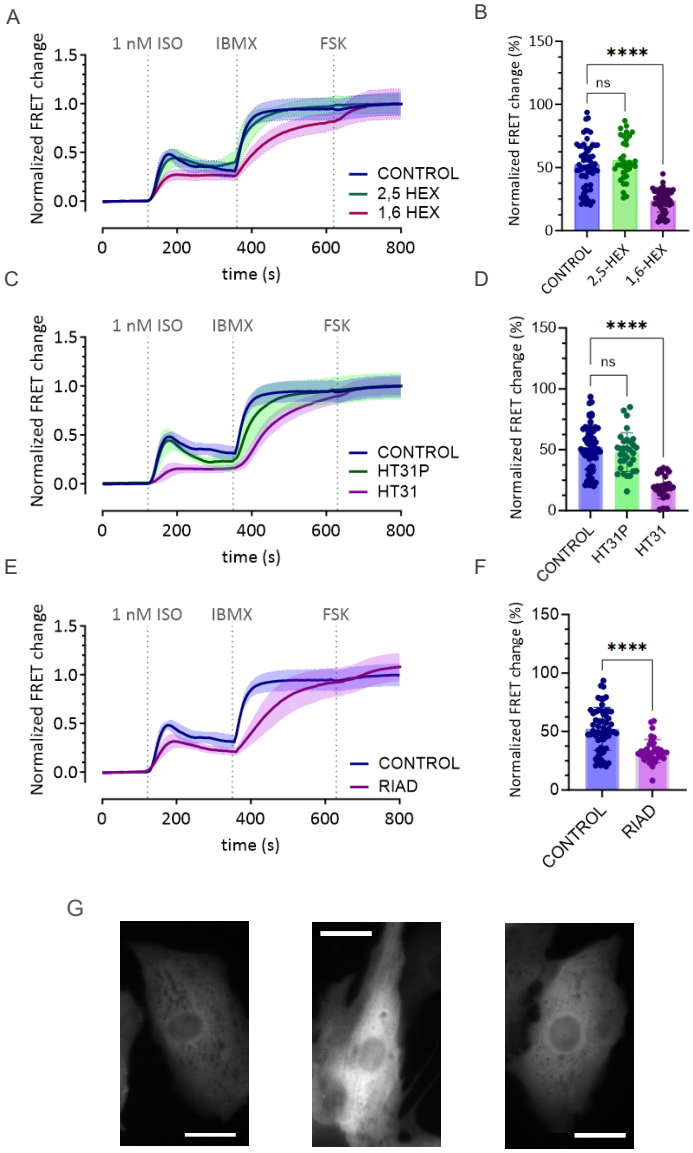


Figure 4.12: HT31 and 1,6-HEX diminishes adrenergic cAMP signal in the NRVM cytosol. **A.** FRET change following 1 nM ISO application with subsequent application of 100 µM IBMX and 25 µM FSK in NRVM cytosol measured with EPAC-SH187 in control cells, cells treated with 1,6-HEX, or 2,5-HEX. **B.** Quantification of FRET change induced by ISO application shows a lower response in cells treated with 1,6-HEX (n=53 individual cells, N=5 repeats (NRVM isolations), $p<0.0001$) than in controls (n=59 individual cells, N=12 repeats (NRVM isolations)) or cells treated with 2,5-HEX (n=34 individual cells, N=4 repeats (NRVM isolations)), $p>0.99$). Kruskal-Wallis test, Dunn's correction. **C.** FRET change curve following 1 nM ISO application with subsequent application of 100 µM IBMX and 25 µM FSK in NRVM cytosol measured with EPAC-SH187 in control cells, cells with HT31, or cells with HT31P. Part of the data was acquired by J. Adams under the author's supervision. **D.** Quantification of FRET change induced by ISO application shows a lower response in cells expressing HT31 (n=24 individual cells, N=7 repeats (NRVM isolations), $p<0.0001$) than in controls (n=59 individual cells, N=12 repeats (NRVM isolations)) or cells with HT31P (n=32 individual cells, N=7 repeats (NRVM isolations), $p>0.99$). Kruskal-Wallis test, Dunn's correction. Part of the data was acquired by J. Adams under the author's supervision.**Continued on next page.**

E. FRET change curve following 1 nM ISO application with subsequent application of 100 µM IBMX and 25 µM FSK in NRVM cytosol measured with EPAC-SH187 in control cells and cells with RIAD. **F.** Quantification of FRET change induced by ISO application shows a lower response in cells expressing RIAD (n=37 individual cells, N=3 repeats (NRVM isolations)) than in controls (n=59 individual cells, N=12 repeats (NRVM isolations)). Mann-Whitney U test, $p<0.0001$. **G.** Representative images of NRVM cells expressing EPAC-SH-187 sensor used for FRET experiments. Scale bar: 20 µm.

4.3.10 PKA condensation effects on the ACs and PDEs in NRVM

A possible explanation for the unexpected reduction in the cAMP response to ISO, measured in the cytosol upon disruption of PKA condensation, is the effect on the activity of proteins involved in the signalling pathway (e.g. PDEs, ACs).

First, it was examined if PDE activity was upregulated, which would result in greater cAMP degradation. The response to IBMX, pan-PDE inhibitor that does not inhibit PDE8, was reduced not only by 1,6-HEX treatment but also by HT31 (plasmid) treatment. This shows that the increase in cAMP induced by PDE inhibition was lower in cells treated with 1,6-HEX or transfected with HT31 than in controls (Fig. 4.13 A). To further understand the effects on PDEs, the activity of PDE4 was assessed in NRVMs. PDE4 is the predominant PDE isoform in NRVMs [43]. Similar to the findings with IBMX, the activity of PDE4 was found to be reduced in cells treated with 1,6-HEX and in the presence of HT31 (Fig. 4.13 C). It is known that PDE4, alongside other PDEs, can be activated by PKA-dependent phosphorylation, and, therefore, the reduction in PDE phosphorylation, secondary to the attenuated cAMP response, could explain the reduced PDE activity.

Next, it was investigated if cAMP generation by cyclases was impaired by the lack of PKA condensation. cAMP generation capacity appeared intact as the response to 7 µM FSK, which elicits a FRET change of 50% ±15% on average, similar to that of 1 nM ISO in the cytosol (50% ±18%, Fig. 4.12), when measured with EPAC-SH187, was slightly increased by 1,6-HEX treatment, and was elevated in the presence of HT31 (Fig. 4.13 B).

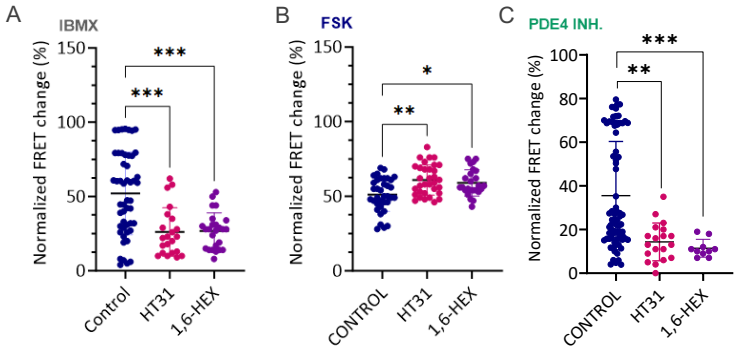


Figure 4.13: PKA condensation disruption affects ACs and PDE activity. **A.** Normalised FRET change recorded with cytosolic cAMP sensor EPAC-SH187 after stimulation with 100 µM IBMX, a pan-PDE inhibitor, compared between control (n=50 individual cells, N=6 repeats (NRVM isolations)), HT31 (n=22 individual cells, N=4 repeats (NRVM isolations), p =0.0001), and 1,6-HEX treated (n=25 individual cells, N=5 repeats (NRVM isolations), p=0.0006) cells. Kruskal-Wallis test, Dunn's correction. **B.** Normalised FRET change recorded with cytosolic cAMP sensor EPAC-SH187 after stimulation with 7 µM FSK, an AC activator, compared between control (n=36 individual cells, N=5 repeats (NRVM isolations)), HT31 (n=33 individual cells, N=3 repeats (NRVM isolations), p=0.0022), and 1,6-HEX treated (n=25 individual cells, N=3 repeats (NRVM isolations), p=0.0351) cells. Kruskal-Wallis test, Dunn's correction. **C.** Normalised FRET change recorded with cytosolic cAMP sensor EPAC-SH187 after stimulation with 10 µM rolipram, a PDE4 inhibitor, compared between control (n=79 individual cells, N=12 repeats (NRVM isolations)), HT31 (n=19 individual cells, N=3 repeats (NRVM isolations), p=0.001), and 1,6-HEX (n=10 individual cells, N=3 repeats (NRVM isolations), p=0.001) treated cells. Kruskal-Wallis test, Dunn's correction.

4.3.11 Attenuated cAMP signal after the disruption of PKA condensation involves PDE8 activation

To further investigate the mechanisms that lead to cAMP signal attenuation in the cytosol upon disruption of PKA condensation, the effects of PDE8 signalling was explored. Channelling of cAMP between PDE8 and PKA RIα has been previously reported [74], making PDE8 a likely target which activity could be altered by disruption of PKA condensation. Furthermore, previous data indicated that the attenuation of cAMP signal in the cytosol upon disruption of PKA condensation is not a result of impaired AC activity or activation of other PDEs that can be inhibited by IBMX, as the cAMP response to IBMX inhibition was reduced and not amplified after PKA condensation disruption (Fig. 4.13). This evidence collectively suggests

that PDE8 is the most likely mediator involved in modulating cAMP signalling in the cytosol following the disruption of PKA condensation. Therefore, it was hypothesised that PDE8 activity in the cytosol increases after PKA condensation disruption, leading to the observed attenuation of the cAMP signal.

It was observed that the cAMP increase after 1 nM ISO following PDE8 inhibition was no longer significantly different between the control cells and cells treated with HT31 (Fig. 4.14 A). This suggests that PDE8 activity is indeed altered in cells with HT31 which in turn explains the attenuation of the cAMP signal induced by the ISO stimulation in HT31 treated cells (Fig. 4.12). PDE8 inhibition with PF05871564 (1 µM) alone did not induce a noticeable change in cAMP in the cytosol, and the induced cAMP increase did not differ between controls, HT31, and HT31P transected cells, although the kinetics of cAMP response in cells with HT31P showed no transience (Fig. 4.14 A, B).

Nonetheless, if PDE8 is indeed activated in cells treated with HT31, then it is unclear why increased response to PDE8 inhibition alone was not observed in the cells with HT31. It was hypothesised that at basal conditions, PDE8 does not play a pivotal role in maintaining cAMP levels, and the contribution of PDE8 might become apparent after the pre-stimulation with ISO. Indeed, the cAMP increase following PDE8 inhibition after 1 nM ISO pre-stimulation was significantly higher in HT31 cells than in control or HT31P cells (Fig. 4.14 C, D).

As cAMP channelling effect has been previously demonstrated between PDE8 and PKA RIα *in silico* and *in vitro* [74], the interaction between PDE8 and RIα was examined in HEK293T cells. It was found that in HEK293T cells, PDE8 is expressed at undetectable levels, whereas PKA RIα could be clearly observed (Fig. 4.14 F). Therefore, the interaction between PDE8 and RIα was tested after transfection of PDE8-RFP. It was found that PDE8 interacts with endogenous PKA RIα (Fig. 4.14 J). However, this interaction was only observed in conditions where cAMP is increased (after 25 µM FSK treatment) and not when cAMP is low (no interaction in controls with no FSK treatment) (Fig. 4.14 G). Quantification of the interaction

revealed a trend where the interaction between PDE8 and PKA RIα is stronger in cells with HT31 and weaker in cells with HT31P, than controls (Fig. 4.14 I, H).

Next, it was tested if PDE8 activation could explain the attenuated cAMP signal after 1,6-HEX treatment. Unlike in HT31 case, it was found that the stimulation with ISO following the pre-stimulation with 10 µM PDE8 inhibitor results in an attenuated increase in cAMP (Fig. 4.14 E). In this case, 10 µM PDE8 inhibitor dose was selected as preliminary data with 1 µM PDE8 inhibitor showed no effect.

Due to the similarities between the catalytic domains of PDEs, it was tested if the PDE activation effect is specific to PDE8. PDE4 activity was found to be inhibited rather than increased in cells with HT31 (Fig. 4.13).

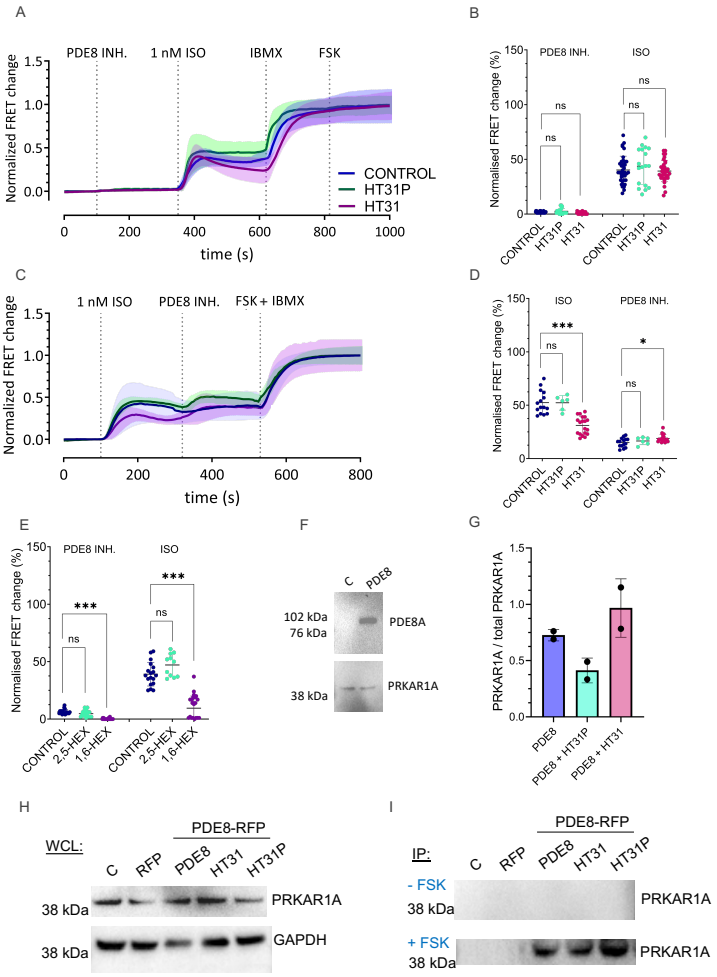


Figure 4.14: PDE8 is activated in cells with HT31. Scale bar: 20 µm. **A.** FRET change curve following PDE8 inhibition with 1 µM PF-04957325, 1 nM ISO application with subsequent application of 100 µM IBMX and 25 µM FSK in NRVM cytosol measured with EPAC-SH187 in control cells, cells with HT31, or HT31P. **B.** Quantification of FRET change induced by PDE8 inhibition with 1 µM PF-04957325 is not significantly different between controls (n=37 individual cells, N=3 repeats (NRVM isolations)), cells with HT31P (n=18 individual cells, N=3 repeats (NRVM isolations), p>0.99), or with HT31 (n=34 individual cells, N=3 repeats (NRVM isolations), p=0.15). Subsequent change induced by the 1 nM ISO application shows no significant differences between cells with HT31 (n=34 individual cells, N=3 repeats (NRVM isolations), p=0.77), HT31P (n=18 individual cells, N=3 repeats (NRVM isolations), p>0.99), or controls (n=37 individual cells, N=3 repeats (NRVM isolations)). Kruskal-Wallis test, Dunn's correction. **C.** FRET change curve following 1 nM ISO application, PDE8 inhibition with 1 µM PF-04957325 with subsequent application of 100 µM IBMX and 25 µM FSK in NRVM cytosol measured with EPAC-SH187 in control cells, cells with HT31, or HT31P. **D.** Quantification of FRET change induced by 1 nM ISO application is significantly lower in cells with HT31 (n=19 individual cells, N=3 repeats (NRVM isolations), p<0.0001) than in cells with HT31P (n=6 individual cells, N=2 repeats (NRVM isolations), p>0.99), or controls (n=15 individual cells, N=3 repeats (NRVM isolations)). Kruskal-Wallis test, Dunn's correction. Subsequent change induced by PDE8 inhibition with 1 µM PF-04957325 is significantly higher in cells with HT31 (n=19, p=0.035) than in cells with HT31P (n=6, p=0.8) or controls (n=15). Kruskal-Wallis test, Dunn's correction. **Continued on next page.**

E. Quantification of FRET change induced by PDE8 inhibition with 10 µM PF-04957325 is greater in control cells (n=18 individual cells, N=3 repeats (NRVM isolations)) and 2,5-HEX treated cells (n=11 individual cells, N=2 repeats (NRVM isolations), p=0.5) than in cells treated with 1,6-HEX (n=26 individual cells, N=3 repeats (NRVM isolations), p<0.0001). Subsequent change induced by the 1 nM ISO application is significantly lower in cells treated with 1,6-HEX (n=26, p<0.0001) than in cells treated with 2,5-HEX (n=11, p=0.64), or controls (n=18). Kruskal-Wallis test, Dunn's correction. **F**. Analysis of Western blot (WB) data, collected together with Dr Yadav, showing PDE8A and PRKAR1A (PKA RIα) expression in HEK293T lysates transfected with PDE8-RFP. Endogenous PRKAR1A was, and PDE8 was not detected. N=2 repeats. **G.** Quantification of the WB (panel I) results where the pull-down PRKAR1A levels are normalised to total PRKAR1A detected in the cell lysates (panel H). N=2 repeats. **H.** Analysis of WB data, collected together with Dr Yadav, showing PRKAR1A expression in different samples in whole cell lysates (WCL) of HEK293T cells. Bottom blot shows GAPDH. N=2 repeats. **I.** Analysis of WB data, collected together with Dr Yadav, showing that no PRKAR1A was detected in the pull-down (IP) of PDE8-RFP obtained from HEK293T lysates by pulling down with RFP in the absence of FSK treatment. The bottom blot shows PRKAR1A in the pull-down of PDE8-RFP obtained from HEK293T lysates by pulling down with RFP from the cells treated with 25 µM FSK. Here, C refers to pull-down from a control HEK293T lysate, no transfection, RFP - pull-down from a lysate of cells transfected with RFP only, PDE8 - pull-down from a lysate transfected with PDE8-RFP, HT31 - from transfected with PDE8-RFP and HT31, HT31P - from transfected with PDE8-RFP and HT31P. N=2 repeats.

Besides protein-protein interactions, the localisation of PDE8 in cells was also investigated. It is known that PDE8 interacts with AKAP12 at the membrane [72]. Previously, PDE8 has been identified to interact with AC6 [224], β2AR [224], and to be localised in the cytosol [225], membrane [225], mitochondria [226], and functionally involved in SR cAMP signalling regulation [224].

The localisation of PDE8-RFP was analysed in living HEK293T and NRVM cells transfected with PDE8-RFP, and membrane enrichment was observed (Fig. 4.15 A, B, C). The enriched areas did not appear to co-localise with PKA puncta (Fig. 4.15 B, C). In addition, puncta-like distribution of PDE8-RFP was observed in NRVMs (Fig. 4.15 A). The localisation of PDE8 did not appear to change between HT31 expressing and non-expressing samples (Fig. 4.15 B, C). In HEK293T cells, clear membrane-like localisation was observed (Appendix, Fig. A.3 A). Transfection with PDE8-RFP resulted in a significantly reduced number of PKA RIα puncta observed in HEK293T cells (Appendix, Fig. A.3 B).

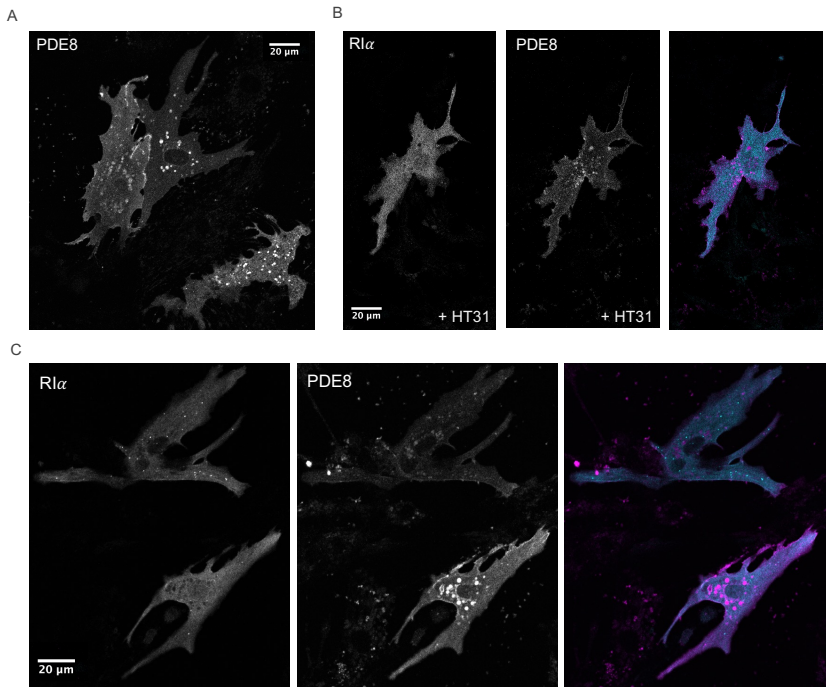


Figure 4.15: PDE8 localisation in NRVM. Imaging experiments with live cells were performed multiple times (n= at least 3).**A.** Representative image of PDE8-RFP in NRVMs. **B.** Representative image of NRVMs transfected with HT31, PKA RIα-GFP (left) and PDE8-RFP (middle), and overlap between PKA RIα-GFP in cyan and PDE8-RFP in magenta (right). **C.** Representative image of NRVMs transfected with PKA RIα-GFP (left) and PDE8-RFP (middle), and overlap between PKA RIα-GFP in cyan and PDE8-RFP in magenta (right).

4.3.12 PKA condensation in hypertrophic cardiomyocytes

PKA and AKAP signalling is disorganised in disease conditions. Therefore, it was investigated if PKA condensation is altered in hypertrophic NRVMs. LLPS has been shown to be involved in multiple pathological states, including cardiac failure [227], HCM [228], and other cardiac disorders [229].

An *in vitro* NRVM hypertrophy model was used where NRVMs were treated for 48 h with norepinephrine to induce cell hypertrophy, as described in Methods, Chapter 2. An increase in cell size was observed (Fig. 4.16 E, F). PKA RIα-RFP and RIIβ-RFP signal was quantified and it was found that PKA RIα but not RIIβ form significantly more condensates in hypertrophic cardiomyocytes (Fig. 4.16

A, B). It was also observed that the number of puncta is directly proportional to the cell size (Fig. 4.16 D).

This could be due to cAMP involvement in stress signalling, in which LLPS is widely implicated, and due to elevated cAMP levels after norepinephrine treatment, which contributes to promoting PKA LLPS, as shown before (Fig. 4.10 A).

It was also investigated if PKA LLPS disruption with HT31 would correct for the increase in puncta. Indeed, it was found that HT31 successfully lowers the number of RIα puncta in hypertrophic NRVMs (Fig. 4.16 C). However, HT31 did not affect cell size and the cell remained hypetrophied. NRVMs were transfectd with HT31 at the same time as norepinephrine treatment was started (48 hours prior to imaging).

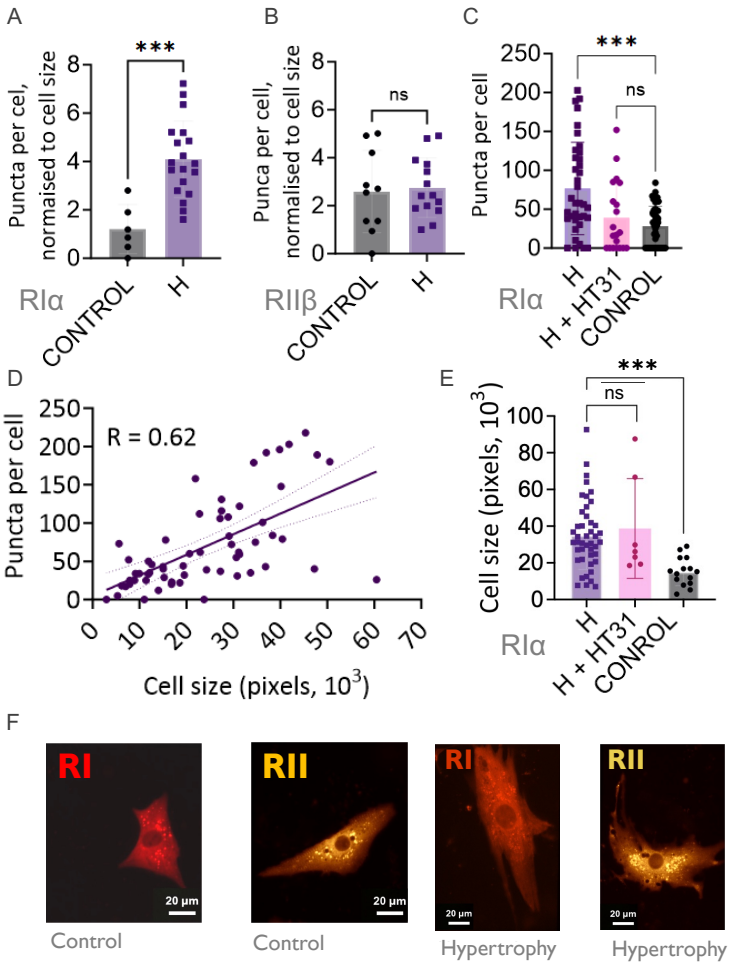


Figure 4.16: PKA RIα condensation is increased in hypertorphy. Scale bar: 20 µm. **A.** The number of PKA RIα condensates after the normalisation to the cell size is greater in hypertrophic (H) (n=19 individual cells, N=4 repeats (NRVM isolations)) cardiomyocytes than controls (n=6 individual cells, N=4 repeats (NRVM isolations)). Mann-Whitney U test, p=0.004. The data was acquired by J. Adams under author's supervision. **B.** The number of PKA RIIβ condensates after the normalisation to the cell size is not statistically different between hypertrophic (H) (n=14 individual cells, N=4 repeats (NRVM isolations)) cardiomyocytes compared to controls (n=10 individual cells, N=4 repeats (NRVM isolations)). Mann-Whitney U test, p=0.79. The data was acquired by J. Adams under author's supervision. **C.** The number of PKA RIα condensates is greater in hypertrophic cardiomyocytes (H) (n=37 individual cells, N=5 repeats (NRVM isolations), p=0.0006) than controls (n=48 individual cells, N=4 repeats (NRVM isolations)), and HT31 (H+HT31) (n=20 individual cells, N=2 repeats (NRVM isolations)) induces a reduction in PKA condensation in hypertrophic cardiomyocytes after which there is no significant difference in the number of PKA p=condensates between controls and hypertrophic cardiomyocytes with HT31 (p>0.99). Kruskal-Wallis test, Dunn's correction. Part of the data was acquired by J. Adams under author's supervision. **D.** There is a positive correlation between the cell size and PKA condensation. Linear regression, Spearman's correlation, adjusted $r^2 = 0.62$. The data was acquired by J. Adams under author's supervision. **E.** Hypertrophic cardiomyocytes (H) (n=39 individual cells, N=5 repeats (NRVM isolations)) are larger (p=0.002) than control cells (n=15 individual cells, N=5 repeats (NRVM isolations)). Hypertrophic cells with HT31 (H+HT31) did not show a significant reduction in size (n=7 individual cells, N=2 repeats (NRVM isolations), p=0.2). Kruskal-Wallis test, Dunn's correction. Part of the data was acquired by J. Adams under author's supervision. **Continued on next page.**

F. From left to right: representative image of PKA RIα and PKA RIIβ condensation in control NRVM; representative image of PKA RIα and PKA RIIβ condensation in hypertrophic NRVM.

4.3.13 Technical considerations when measuring cAMP signalling

After PKA condensation disruption, cAMP signal attenuation was observed in the cytosol (Fig. 4.12 A, B) but not at specific subcellular compartments (Fig. 4.11). This attenuation was observed after 1 nM ISO stimulation, but not after stimulation with FSK (Fig. 4.13, 4.12).

As PKA condensation disruption affected FSK-induced and ISO-induced cAMP response in a different way in the cytosol, it was tested what effect would PKA disruption have on the FSK-induced cAMP response in the specific subcellular compartments. To investigate this, the response to 7 µM FSK was recorded in different cAMP signalling domains. Similarly to stimulation with 1 nM ISO, no difference was found in cAMP response between controls and 1,6-HEX treated cells where PKA condensation was disrupted (Fig. 4.17 A). Interestingly, similar to ISO, the response to 7 µM FSK was lower at the myofilament than at the plasma membrane or SR.

To assess whether the attenuation in cAMP increase observed in the cytosol upon PKA condensation disruption was specific to βAR pathway stimulation, an additional control experiment was performed using a non-βAR pathway. The cAMP response to GLP1 receptor stimulation was tested using 3 µM semaglutide, a GLP1 receptor activator. It appeared that after stimulation with semaglutide, the cAMP increase was significantly lower in the cells treated with 1,6-HEX or HT31 compared to controls (Fig. 4.17 B). This is similar to the findings collected with 1 nM ISO stimulation (Fig. 4.12 A, B). This suggests that PKA condensation disruption affects cAMP signalling across different receptor pathways, not limited to βAR activation.

There are also inherent differences between the cAMP sensors used to study cAMP in nanodomains and cytosol. Namely, the cytosolic cAMP sensor is a loss

of FRET sensor whereas the targeted CUTie sensors are gain of FRET sensors. CUTie and EPAC-SH187 sensors have been well-characterised and compared before [108]. It has been shown that with EPAC-SH187, 0.71µM cAMP is sufficient to elicit a detectable FRET change, whereas that cAMP concentration would not result in a FRET change when measured with CUTie sensors. For CUTie sensors, the concentration of cAMP required to detect a FRET change is at least 1.14µM. For CUTie, the Hill coefficient is 1.071 and the EC50 of cAMP binding is 7.385. For EPAC-SH187, the hill coefficient is 1.750, resulting in a higher binding co-operativity, and EPAC-SHA187 has an EC50 of 7.406 [108]. The change in FRET when measured with EPAC-SH187 therefore will occur more rapidly compared to CUTie for changes in cAMP concentration around the EC50 value. The EC50 values being very close (7.385 vs. 7.406) means that both sensors have similar cAMP affinities, but the binding cooperativity difference will cause the EPAC-SH187 sensor to have a sharper response.

Given these considerations, it could be that the differences in the response to ISO between the controls and 1,6-HEX treated cells are missed in the domains due to the slower response kinetics of the CUTie sensor. One way to overcome this limitation is to work with concentrations of cAMP that are away from the EC50s of the sensors. Since the change in FRET for CUTie is slower near its EC50 compared to EPAC-SH187, this could mask subtle differences in cAMP levels. To minimise this limitation, it is better to work with cAMP concentrations that are away from the EC50 values of the sensors. Specifically, at concentrations near the EC50, the differences in cAMP response between the two sensors may be amplified where EPAC-SH187, with its higher binding cooperativity, can detect more rapid changes than CUTie.

This is relevant because the change induced by 1 nM ISO is around 50% of the maximal response when measured with EPAC-SH187 (Fig. 4.12 B), which may reduce the ability to detect differences between treated and control cells with the CUTie sensor. To account for this, cAMP levels in the cytosol were measured using both EPAC-SH187 and cytosolic CUTie sensors. After 1 nM ISO stimulation,

the cytosolic CUTie sensor showed a lower increase in cAMP in 1,6-HEX-treated cells compared to controls, but the difference was not statistically significant (Fig. 4.17 E). However, when the ISO concentration was increased to 3 nM, the cAMP response measured by both CUTie (Fig. 4.17 D) and EPAC-SH187 sensors (Fig. 4.17 C) was significantly lower in 1,6-HEX-treated cells than in controls.

To test if indeed the effects of PKA condensation disruption where under-reported when measuring cAMP with CUTie sensors after 1 nM ISO stimulation, the response to 3 nM ISO stimulation was compared using TNI-CUTie and MYBPC-CUTie sensors. No significant differences were found in the cAMP response in these domains when comparing control and 1,6-HEX treated cells (Fig. 4.17 F). Altogether, this suggests that despite potential technical limitations, the previously collected data remains valid: disruption of PKA condensation does not significantly affect the cAMP response to ISO at the myofilament, indicating that cAMP compartmentalisation remains intact.

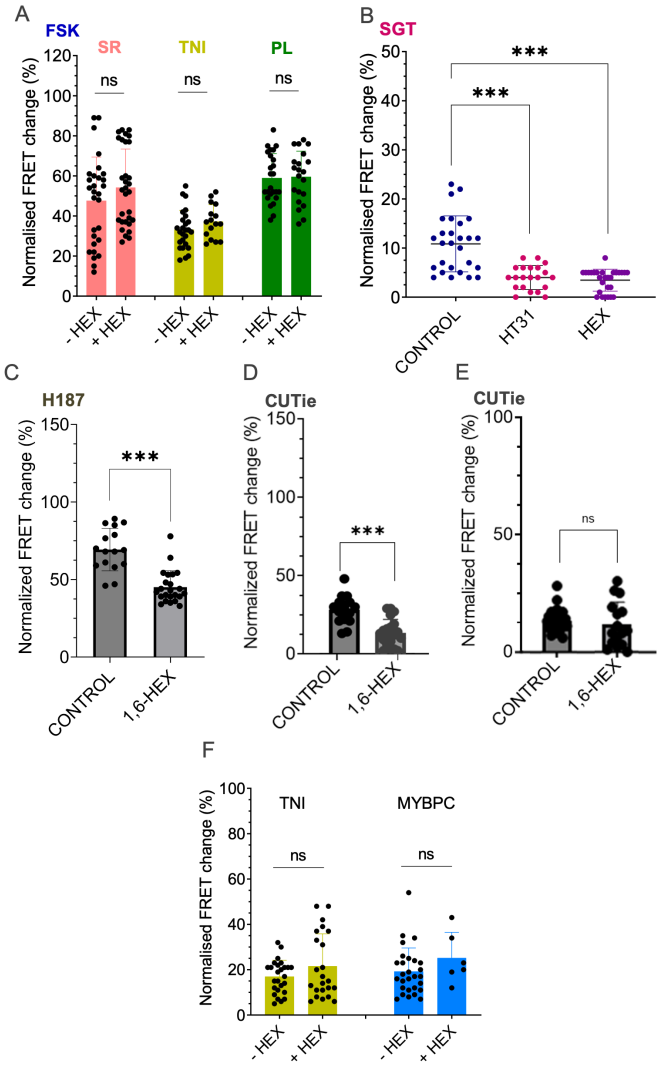


Figure 4.17: Technical considerations for studying PKA condensation disruption effects with FRET sensors. **A.** Normalised FRET change after 7 µM FSK application measured with targeted cAMP CUTie sensors at the SR (n=29-31 individual cells, N=3 repeats (NRVM isolations), p=0.29), TNI (n=16-26 individual cells, N=4 repeats (NRVM isolations), p=0.13), and PL (n=21-25 individual cells, N=3 repeats (NRVM isolations), p=0.79) shows no statistically significant differences in the cells treated and not treated with 2.5% 1,6-HEX. Mann-Whitney U test. **B.** Normalised FRET change after 3 µM semaglutide (SGT) application measured with the cytosolic EPAC-SH187 sensor is lower in the cells treated with 1,6-HEX (n=28 individual cells, N=3 repeats (NRVM isolations), p<0.0001) and HT31 (n=21 individual cells, N=3 repeats (NRVM isolations), p<0.0001) than in controls (n=27). Kruskal-Wallis test, Dunn's correction. **C.** Normalised FRET change after 3 nM ISO application in the cytosol measured with EPAC-SH187 is lower in the cells treated with 1,6-HEX (n=23 individual cells, N=2 repeats (NRVM isolations), p<0.0001) than in controls (n=16 individual cells, N=2 repeats (NRVM isolations)). Mann-Whitney U test. **D.** Normalised FRET change after 3 nM ISO application in the cytosol measured with the cytosolic CUTie sensor is lower in the cells treated with 1,6-HEX (n=20 individual cells, N=3 repeats (NRVM isolations), p=0.002) than in controls (n=16 individual cells, N=3 repeats (NRVM isolations)). Mann-Whitney U test. **Continued on next page.**

E. Normalised FRET change after 1 nM ISO application in the cytosol measured with the cytosolic CUTie is not significantly different between the cells treated with 1,6-HEX (n=17 individual cells, N=4 repeats (NRVM isolations), p>0.05) and controls (n=14 individual cells, N=4 repeats (NRVM isolations)). Mann-Whitney U test. **F.** Normalised FRET change after 3 nM ISO application measured with targeted cAMP CUTie sensors at the TNI and MYBPC shows no statistically significant differences in control cells (n=26-29 individual cells, N=3 repeats (NRVM isolations)) and cells treated with 1,6-HEX (n=6-24 individual cells, N=3 repeats (NRVM isolations)). Mann-Whitney U test, p>0.05.

4.4 Discussion

The main findings outlined in this chapter include:

1. PKA RI and RII form puncta-like structures, with features consistent with liquid-liquid phase separation, in cardiomyocytes.

2. Treatment with HT31 is an effective and PKA-specific method to disrupt PKA condensation.

3. PKA condensation does not play a role in cAMP compartmentalisation at the myofilament, SR, or plasmalemma.

4. PKA phase separation is required for maximal adrenergic response in the cytosol of cardiomyocytes where the disruption of PKA condensation using either 1,6-HEX or HT31 results in a reduced cAMP increase following adrenergic stimulation.

5. Disruption of PKA condensation via PKA-AKAP de-coupling activates PDE8 and reduces cAMP signal transduction in the cytosol following adrenergic stimulation.

6. An interaction between endogenous PKA RI and PDE8 was discovered in cells, supporting the idea of a channelling effect where PDE8 effectively removes cAMP in proximity to PKA RI.

7. A significant increase in PKA RIα condensates in hypertrophic NRVMs suggests a potential role in disease states.

In this chapter, the effects of PKA condensation on cAMP signalling were examined. PKA RIα condensation, first reported in 2020 [111], has previously been observed in 2011, though it was referred to as "multivesicular bodies" [230]. In this study, the puncta-like appearance of PKA RIα was confirmed, and the formation of RIIβ condensates was also observed.

The PKA puncta were found to be highly dynamic in living HEK293T cells and cardiomyocytes, suggesting that PKA condensation is a reversible process that responds to changes in cellular conditions. Zhang et al. (2020) proposed a cAMP buffering function for these PKA condensates [111]. The results of this study show that cAMP concentration is higher within PKA puncta compared to the cytosol, as measured using the PKA RI-CFP and C-YFP sensors.

Zhang et al. (2020) also proposed that the cAMP buffering function of PKA condensates is essential for enabling PDEs to form cAMP nanodomains. They showed that the cAMP increase at PDE4D2 is amplified when cells are treated with 1,6-HEX, which disrupts LLPS. The authors hypothesised that the reduced PDE catalytic activity is due to decreased cAMP buffering caused by the disruption of PKA RIα condensation. In the current study, it was found that 1,6-HEX inhibits PDE activity *in vitro*. Results in cells are consistent with these findings, as the cAMP response to IBMX and the PDE4 inhibitor rolipram was lower in cells treated with 1,6-HEX. This provides a potential alternative explanation to Zhang's findings, suggesting that the cAMP increase observed at PDE4D2 may be due to 1,6-HEX-mediated PDE inhibition rather than solely due to cAMP buffering disruption.

Further investigation into PKA condensation revealed that multiple AKAPs have a high degree of amino acid sequence disorder, an indicator of LLPS propensity. As AKAPs can potentially form condensates, they could aid or be involved in PKA LLPS. Therefore, it could be that disrupting PKA-AKAP interactions reduces puncta. Indeed it was observed that HT31 or RIAD (peptides that disrupt PKA-AKAP interactions) reduce the number of PKA puncta in cells. However, other studies have found that overexpression of smAKAP also results in a reduction of PKA puncta [210]. Interpreting this data together suggests that HT31 might be acting as an AKAP, competing with endogenous AKAPs for RI binding, and thereby reducing PKA condensation. In this way, HT31 and RIAD mimic AKAP-RI interactions, sequestering RI from the condensates and consequently reducing the number of the PKA puncta.

After establishing a novel method to specifically disrupt PKA puncta using HT31 or RIAD, the effects of this disruption were investigated. It was hypothesised that if PKA buffers cAMP, and this buffering is essential for maintaining cAMP nanodomains, then disrupting PKA would lead to the loss of cAMP compartmentalisation. However, it was found that disrupting PKA condensation, either with HT31 or 1,6-HEX, did not alter the cAMP response to ISO or FSK in cAMP domains, including the myofilament, plasmalemma, or SR. The cAMP nanodomains, where cAMP response induced by ISO is higher at plasmalemma than at the myofilament [34], were maintained after the disruption of PKA condensates.

cAMP nanodomains were maintained despite PDE inhibition following 1,6-HEX treatment, highlighting the ample ability of PDEs to ensure compartmentalised cAMP signalling. Interestingly, after PKA condensation disruption, adrenergic signal transduction in the cytosol was affected. Specifically, abolishing PKA condensation resulted in a reduced ISO-induced cAMP increase in the cytosol. This was unexpected, given that cytosolic PDE activity was reduced following PKA condensation disruption.

It was hypothesised that the reduced cytosolic adrenergic signal transduction was driven by altered PDE8 activity. The results confirmed that PDE8 activity was indeed amplified in cells where PKA condensation was disrupted with HT31. Interestingly, this amplification did not occur under basal conditions; PDE8 inhibition led to a greater increase in cAMP in HT31-treated cells only when pre-stimulated with isoproterenol. PDE8 is known to be activated by PKA phosphorylation, and a study has demonstrated a channelling effect between PDE8 and PKA RI, where cAMP is more effectively removed from RI and hydrolysed when PDE8 is in proximity [74]. In this study, an interaction between endogenous PKA RI and PDE8 was also found in HEK293T cells.

Altogether, the findings indicate that PDE8-RI interactions are important in modulating adrenergic signal transduction and that disrupting PKA condensation alters PDE8 activity, and, ultimately, cAMP levels. However, PDE8 activation alone does not appear to fully explain the 1,6-HEX-induced reduction in cAMP

signalling in the cytosol. This suggests that the mechanisms underlying PKA condensation disruption may differ between those mediated by 1,6-HEX and by PKA-AKAP interaction disruption.

Preliminary investigations into PKA condensation in hypertrophic NRVMs revealed a significant increase in PKA RIα condensates. It remains to be determined whether this represents an adaptive response to the disease or a factor contributing to its progression. Future studies should replicate these results in more relevant *in vivo* models and examine whether the amplification of PKA condensation in hypertrophy affects myofilament cAMP signalling. A recent study outlines that RI expression is decreased in failing human hearts [231]. Authors also indicate that a conditional heart RI knock out in adult mice results in a decreased total cAMP compared with control, amplified PKA phosphorylation activity, and after 6 months, the mice developed cardiac hypertrophy, fibrosis, and reduced ejection fraction. While these findings suggest that disrupted PKA signalling plays a role in heart failure, the increase in PKA condensation observed in hypertrophic NRVMs may reflect a distinct mechanism in hypertrophy. Further investigation using relevant *in vivo* models is required to explore whether this increase in condensation acts as a protective mechanism in early hypertrophy or contributes to disease progression. Relevant in vivo models could include transverse aortic constriction (TAC)-induced pressure overload models, which would allow exploration of early and late-stage heart failure states to determine if this increase in condensation acts as a protective mechanism in early hypertrophy or contributes to disease progression. Additionally, genetic models that recapitulate genetic hypertrophic cardiomyopathy could be used to investigate phase separation and its impact on hypertrophy.

These findings are crucial as they shed light on the fundamental mechanisms regulating cAMP signalling, highlighting the critical role of PKA LLPS in maintaining cellular homeostasis. Furthermore, the potential role of PKA condensation in cardiac hypertrophy opens up new avenues for exploring therapeutic strategies targeting LLPS dynamics, offering a promising direction for treating cardiac diseases.

4.4.1 Limitations

One limitation of this study is the reliance on overexpression of PKA constructs to observe PKA LLPS, as studying endogenous PKA condensation using CRISPR cell lines posed technical challenges.

Another limitation is the inability to study PKA condensation in adult cardiomyocytes. This was due to the lack of viral PKA constructs. Future studies should focus on examining PKA condensation in adult cardiomyocytes to gain insights into its role in a more native cellular environment.

The study also faced challenges in terms of the methods available to disrupt PKA condensation. The widely used LLPS disruptor, 1,6-HEX, is known to have off-target effects, as it is not PKA-specific and can affect other membraneless organelles formed via LLPS. Minimal off-target effects were expected with the 15-minute 2.5% 1,6-HEX treatment used in this study [209].

Additionally, this study explored the role of AKAPs in PKA condensation. It was found that disrupting PKA-AKAP interactions with HT31 reduces the number of condensates in cells but replication of these findings *in vitro* has been difficult due to the stearation of commercially available HT31, which may influence LLPS properties. Synthesis of non-stearated HT31 peptide in future experiments could help clarify the true effects of HT31 on PKA condensation.

4.5 Conclusions

This chapter elucidates the critical role of PKA condensation in regulating cAMP signalling within cardiomyocytes. While PKA condensation substantially influences cAMP transduction in the cytosol, its effect at the myofilament appears minimal under physiological conditions. The findings suggest that PKA condensates may act as cAMP buffers only under high cAMP concentrations, conditions that are unlikely to be typically encountered at the myofilament.

Although RI condensates appear to be enriched in cAMP and may act as a buffer, this buffering does not contribute to cAMP compartmentalisation. The

results from this study also uncover a new mechanism in which RI condensation enables the maximal amplitude of the cytosolic cAMP response by limiting cAMP degradation by PDE8.

A deeper understanding of these mechanisms could lead to novel therapeutic approaches for cardiac diseases, particularly those associated with aberrant cAMP signalling and PKA activity. Future research should aim to validate these findings in more physiologically relevant models and explore the therapeutic potential of targeting PKA condensation for cardiac disease management.

5

In silico human induced pluripotent stem cell derived cardiomyocyte electromechanical modelling

5.1 Introduction

Myofilament function and its regulation has been explored using experimental and computational tools. Different existing mathematical models have been useful for testing and generating new hypothesis related to myofilament mechanics, as discussed in the Introduction chapter (Chapter 1).

Mathematical models enable studies on human cardiac function that are otherwise challenging due to the limited availability of healthy human heart tissue. However, validating simulation results from adult human cardiomyocyte models remains difficult because of restricted access to human cells and the variability between human and animal cardiomyocyte physiology.

Human induced pluripotent stem cell derived cardiomyocytes (hiPSC-CM) offer a way to circumvent these issues by allowing human-based cardiac studies. Having been utilised in the lab settings, hiPSC-CM mathematical models have been proven as useful tools for mechanistic investigations, drug testing, and disease modelling. Modelling hiPSC-CMs also allows for straightforward validation experimentally due

to the availability of the cells. However, hiPSC-CMs also have limitations, such as immature phenotypes compared to adult cardiomyocytes.

While many computational studies traditionally focus on the electrical properties of these cells [160–162], there is a significant gap in understanding their mechanical responses, such as contraction and relaxation, which are essential for evaluating heart medications and elucidating mechanisms of heart disease. Developing models that include contractility is crucial because mechanical properties play a vital role in assessing the efficacy and safety of cardiac drugs. Conversely, contractility-only models based on human adult cardiomyocyte data exist, but they do not include extensive electrophysiology signalling pathways which may render the simulation results less accurate [168]. Although contractility can be measured experimentally, *in silico* models allow for more efficient, scalable, and cost-effective drug testing, and they enable the exploration of scenarios that might be challenging to replicate experimentally.

The goal of this study is to develop and validate an electromechanical hiPSC-CM model to facilitate the investigations of electromechanical regulation processes. The model aims to provide a platform that could integrate and extend experimental findings using *in silico* tools.

This chapter outlines the development and validation of the Integrated Cardiomyocyte Electromechanical Model (iCEM) for hiPSC-CMs, focusing on its potential to investigate the regulation of contractile cell function. The iCEM provides a flexible method for modelling the electromechanical properties of hiPSC-CMs, which can be adapted for a wide range of applications in cardiac research.

5.2 Methods

5.2.1 hiPSC-CM electro-mechanical model coupling and calibration

The previously published hiPSC-CM electrophysiology Paci model [160] was coupled with the human adult cell tension Land model [168]. The electrophysiology model reflects different currents and their dynamics observed in hiPSC-CMs and features

two compartments, cytosol and sarcoplasmic reticulum, without T-tubules which is also observed in hiPSC-CMs. The ion currents and pumps included in the model are the fast Na^+ current (INa), the late Na^+ current (INaL), the funny current (If), the L-type Ca^2+ current (ICaL), the transient outward K^+ current (Ito), the rapid and slow delayed rectifier K^+ currents (IKr and IKs), the inward rectifier K^+ current (IK1), the Na^+/Ca^2+ exchanger (INCX), the Na^+/K^+ pump (INaK), the sarcolemmal Ca^2+ pump (IpCa), and the Na^+ and Ca^2+ background currents (IbNa and IbCa). The SR compartment exchanges calcium with cytosol through three fluxes: RyR-sensitive release current (Irel), the SERCA pump (Iup), and the leakage current (Ileak). The Paci electrophysiology model is a model of a ventricular-like hiPSC-CM [160].

The human cardiomyocyte contractility model developed by Land et al. (2017) was used for active tension generation [168]. The model is based on measurements obtained from adult human cardiomyocytes at body temperature and includes troponin C (TRPN) and tropomyosin kinetics as well as a three-state crossbridge model that also accounts for crossbridge distortion (Fig. 5.1). Three states in the model are unbound cross-bridge state U, the pre-power-stroke state W, and the force-generating state S. To address the differences observed in the active tension generation in hiPSC-CMs and adult human cardiomyocytes, the parameters of the adult cell in the contractility model were later calibrated to create a hiPSC-CMs tension model. Coupling of the two models was implemented by using intracellular calcium concentration from the electrophysiological model as an input for the Land model. In turn, the amount of calcium bound to TRPN in the contractility model was used in the electrophysiology model to update the free intracellular calcium concentration. This approach has been previously described and is illustrated bellow (Fig. 5.1). The biomarkers computed after each simulation included time to peak for active tension (TP), action potential (APTP) and calcium transient (CTTP), time to 50% and 90 % decay for active tension (RT50/RT90), calcium transient (CTD50/CTD90) and action potential (APD50 and APD90)(Fig. 5.1).

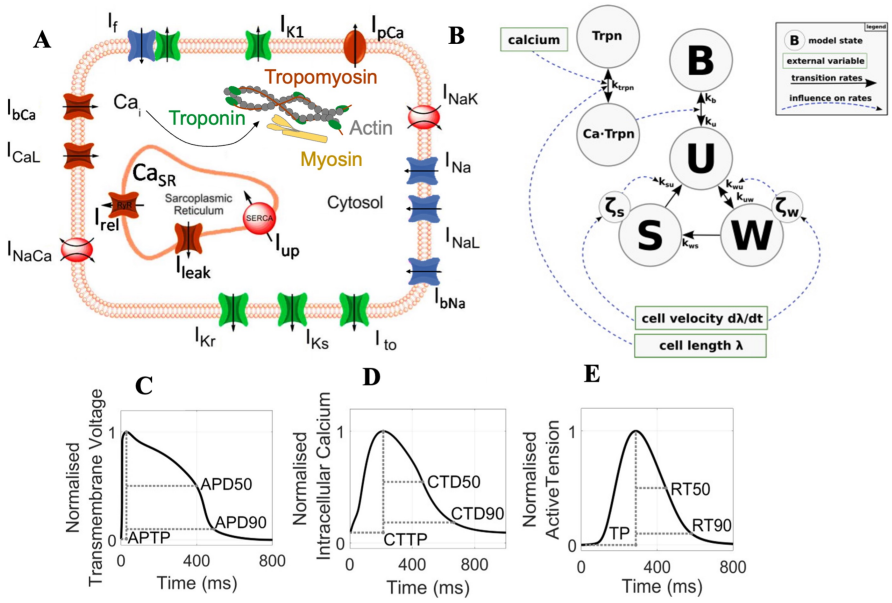


Figure 5.1: Schematic representation of hiPSC-CM electromechanical model (iCEM). **A.** The schematic representation of the model is adapted from Paci et al. (2012) [160] **B.** Schematic representation of active tension model adapted from Land et al. (2017) [168]. States of the model include the 'blocked' state 'B', the unbound crossbridge state 'U', the pre-powerstroke state 'W', and the force-generating state 'S'. States ζw and ζs keep track of the mean distortion of crossbridges. Calcium binding to troponin C (TRPN) drives the transition between states 'B' and 'U'. **C.** Representative action potential waveform and biomarkers computed which include APTP, APD50 and APD90. **D.** Representative calcium transient waveform and biomarkers computed which include CTTP, CTD50 and CTD90. **E.** Representative active tension waveform and biomarkers computed which include TP, RT50 and RT90.

First, to couple the electrophysiology and contractility models, equations describing calcium buffering in the electrophysiology model were altered to account for buffering by troponin and calmodulin. Briefly, the total calcium concentration change over time in the cell ($\left[\mathrm{Ca}^{2+}\right]_{\mathrm{total}}$) can be decomposed as the sum of intracellular free calcium ($\left[\mathrm{Ca}^{2+}\right]_{i}$), calcium bound to calmodulin (CMDN, ($\left[\mathrm{Ca}^{2+}\right]_{\mathrm{CMDN}}$), and to troponin C (TRPN, ($\left[\mathrm{Ca}^{2+}\right]_{\mathrm{TRPN}}$), such that:

$$\frac{d\left[\mathrm{Ca}^{2+}\right]_{\mathrm{total}}}{dt} = \frac{d\left[\mathrm{Ca}^{2+}\right]_{i}}{dt} + \frac{d\left[\mathrm{Ca}^{2+}\right]_{\mathrm{CMDN}}}{dt} + \frac{d\left[\mathrm{Ca}^{2+}\right]_{\mathrm{TRPN}}}{dt} \quad (1)$$

Equivalently, changes in total calcium are described in the electrophysiology model as:

$$\frac{d\left[\mathrm{Ca}^{2+}\right]_{\mathrm{total}}}{dt} = [\mathrm{Ca}]_{i,\mathrm{bufc}}\left(I_{\mathrm{leak}} - I_{\mathrm{up}} + I_{\mathrm{rel}} - \frac{(I_{\mathrm{CaL}}+I_{\mathrm{bCa}}+I_{\mathrm{pCa}}-2I_{\mathrm{NaCa}})}{2FV_c}C_m\right) \quad (2)$$

where I_{leak} represents calcium release by leakage, I_{up} represents calcium uptake by SR and I_{rel} – release via RyR. I_{CaL} represents L-type Ca^{2+} current, I_{pCa} - calcium pump current, I_{bCa} – calcium background current and I_{NaCa} – Na^+/Ca^{2+} exchanger current. F here is Faraday's constant, V_c is cytoplasmic volume and C_m is mean membrane capacitance. $[\text{Ca}]_{i,\text{bufc}}$ is total intracellular calcium that is buffered in the cytoplasm.

To couple electrophysiology and contractility models, $[\text{Ca}]_{i,\text{bufc}}$ was defined as a sum of calcium buffered by troponin C and calmodulin, two main calcium buffers in the cytoplasm besides SERCA (which is represented by I_{up}):

$$\left[\text{Ca}^{2+}\right]_{i,\text{bufc}} = \left[\text{Ca}^{2+}\right]_{\text{TRPN}} + \left[\text{Ca}^{2+}\right]_{\text{CMDN}} \quad (3)$$

Initial electrophysiology model formula for $[\text{Ca}]_{i,\text{bufc}}$ describes its dynamics in such a way that:

$$\left[\text{Ca}^{2+}\right]_{i,\text{bufc}} = \frac{1}{1 + \frac{\text{Buf}_c \cdot K_{\text{bufc}}}{(\left[\text{Ca}^{2+}\right]_i + K_{\text{bufc}})^2}} \quad (4)$$

Considering equations (3) and (4) together yields:

$$[\text{Ca}]_{i,\text{bufc}} = \frac{1}{1 + \frac{\left[\overline{\text{CMDN}}\right] K_{\text{CMDN}}}{(\left[\text{Ca}^{2+}\right]_i + K_{\text{CMDN}})^2} + \frac{\left[\overline{\text{TRPN}}\right] K_{\text{TRPN}}}{(\left[\text{Ca}^{2+}\right]_i + K_{\text{TRPN}})^2}} \quad (5)$$

where $\left[\overline{\text{CMDN}}\right]$ and $\left[\overline{\text{TRPN}}\right]$ refer to the CMDN and TRPN concentrations that can bind calcium. Given that, the initial equation for calcium change over time in the cell becomes:

$$\frac{d\left[\text{Ca}^{2+}\right]_{\text{total}}}{dt} = \frac{d\left[\text{Ca}^{2+}\right]_i}{dt} + \frac{d\left[\text{Ca}^{2+}\right]_{\text{CMDN}}}{dt} + \frac{d\left[\text{Ca}^{2+}\right]_{\text{TRPN}}}{dt} = \frac{d\left[\text{Ca}^{2+}\right]_i}{dt}\left(1 + \frac{\left[\overline{\text{CMDN}}\right] K_{\text{CMDN}}}{(\left[\text{Ca}^{2+}\right]_i + K_{\text{CMDN}})^2} + \frac{\left[\overline{\text{TRPN}}\right] K_{\text{TRPN}}}{(\left[\text{Ca}^{2+}\right]_i + K_{\text{TRPN}})^2}\right) \quad (6)$$

yielding

$$\frac{d\left[\text{Ca}^{2+}\right]_i}{dt} = [\text{Ca}]_{i,\text{bufc}}\left(I_{\text{leak}} - I_{\text{up}} + I_{\text{rel}} - \frac{(I_{\text{CaL}} + I_{\text{bCa}} + I_{\text{pCa}} - 2I_{\text{NaCa}})}{2FV_c} C_m\right) \quad (7)$$

where $[\mathrm{Ca}]_{i,\mathrm{bufc}}$ is described by equation (5).

In order to implement the electro-mechanical coupling, dynamic calcium buffering for troponin C was included. This was achieved by defining calcium bound to troponin C $\left[\mathrm{Ca}^{2+}\right]_{\mathrm{TRPN}}$ as the fraction of troponin C units with calcium bound to its regulatory binding site (CaTRPN) multiplied by a constant maximum concentration of calcium ions that can bind to troponin C. The maximum concentration was derived as described bellow in the section *Approximation of calcium buffering efficiencies* giving $\left[\mathrm{Ca}^{2+}\right]_{\mathrm{TRPN,max}} = 0.42\,\mathrm{mM}$. Dynamic calcium buffering by troponin C was described as:

$$\frac{d\left[\mathrm{Ca}^{2+}\right]_{\mathrm{TRPN}}}{dt} = \left[\mathrm{Ca}^{2+}\right]_{\mathrm{TRPN,max}} \frac{d\mathrm{CaTRPN}}{dt} \quad (8)$$

The formulation provided by Land and colleagues [168] was then adopted to describe the dynamic binding of calcium to troponin C:

$$\frac{d\mathrm{CaTRPN}}{dt} = k_{\mathrm{TRPN}} \left(\left(\frac{\left[\mathrm{Ca}^{2+}\right]_i}{\left[\mathrm{Ca}^{2+}\right]_{T50}} \right)^{n_{\mathrm{TRPN}}} (1 - \mathrm{CaTRPN}) - \mathrm{CaTRPN} \right) \quad (9)$$

where k_{TRPN} represents the unbinding rate, and n_{TRPN} the cooperativity of the calcium-troponin C binding rate. The parameter $\left[\mathrm{Ca}^{2+}\right]_{T50}$ describes the half-activation point. The final formulation for the transient of the free intracellular calcium then becomes:

$$\frac{d\left[\mathrm{Ca}^{2+}\right]_i}{dt} = [\mathrm{Ca}^*]_{i,\mathrm{bufc}} \left(I_{\mathrm{leak}} - I_{\mathrm{up}} + I_{\mathrm{rel}} - \frac{(I_{\mathrm{CaL}} + I_{\mathrm{bCa}} + I_{\mathrm{pCa}} - 2I_{\mathrm{NaCa}})}{2FV_c} C_m \right) - \frac{d\left[\mathrm{Ca}^{2+}\right]_{\mathrm{TRPN}}}{dt} \quad (10)$$

where

$$[\mathrm{Ca}^*]_{i,\mathrm{bufc}} = \frac{1}{1 + \frac{\mathrm{CMDN} \cdot K_{\mathrm{CMDN}}}{(\left[\mathrm{Ca}^{2+}\right]_i + K_{\mathrm{CMDN}})^2}} \quad (11)$$

Approximation of calcium buffering efficiencies

As per equation 3, total buffered calcium in the cytosol can be described as the sum of calcium buffered by troponin C (TRPN) and CMDN. In ToR-ORd [156], total calcium buffered by TRPN alone equals 0.07 mM, and by CMDN equals 0.05 mM. Assuming the proportions of maximal calcium that can be buffered by TRPN and CMDN remain the same and assuming that Km for both buffers are unchanged, the final concentrations of TRPN and CMDN were derived. First, the TRPN:CMDN ratio was established based on adult cardiomyocyte model data:

$$\left[\overline{\text{CMDN}}\right] = 0.05\,\text{mM}; \quad \left[\overline{\text{TRPN}}\right] = 0.07\,\text{mM}; \quad \left[\overline{\text{CMDN}}\right] : \left[\overline{\text{TRPN}}\right] = 5 : 7$$

Given that TRPN can buffer 1.4 times more calcium (as outlined above), CMDN concentration for the hiPSC-CM electromechanical model (iCEM) was found by utilising the genetic algorithm (`ga`) function on MATLAB with default parameters. The `ga` function was used to find the lowest value of a cost function which was outlined as:

$$d_t = d(\texttt{tp}, [217]) + d(\texttt{amplitude}, [0.152])$$

where the distances d between calcium transient biomarkers `tp` and `amplitude`, and the corresponding calcium transient biomarker values extracted after running electrophysiology model simulations, were computed and summed to obtain the total cost d_t which was then minimised. This allowed finding CMDN and TRPN concentrations that provide the best fit between hiPSC-CM electromechanical (iCEM) and electrophysiology model's calcium transients, which was later validated by comparing remaining calcium transient biomarkers, RT50 and RT90, between the two models, and with experimentally established biomarker ranges. The values for TRPN and CMDN concentrations were:

$$[\text{TRPN}] \approx 0.42\,\text{mM}$$

$$[\text{CMDN}] \approx 0.3\,\text{mM}$$

Calibration of the hiPSC-CM electromechanical model (iCEM)

After the coupling of the models, the hiPSC-CM electromechanical model (iCEM) was established. To calibrate it according to the experimental active tension hiPSC-CMs data, parameters in the adult human cardiomyocyte contractility (Land) model were changed to represent the active tension phenotype observed in hiPSC-CMs.

To identify the influence of different parameters on the biomarkers of interest, the values of different parameters in the contractility (Land) model were varied by $\pm 10\%$. Out of 17 parameters used to describe active tension in the contractility model, the sensitivity analysis was done on 7 parameters. Other 10 were excluded due to different reasons. First, six of them are related to length changes and would not affect model outputs in an isometric setup. The *Tref* parameter, which is the tension developed at maximal activation for an extension ratio (λ) equal to 1, would only scale the model output, and therefore was not considered for sensitivity analysis, and was kept unchanged. Parameters that significantly affected calcium transient were excluded from the candidates for further fitting as well. These were *nTRPN* and *ca50*, a parameter describing the cooperativity of the calcium-troponin C binding rate and a parameter describing calcium-troponin C half-activation point, respectively. No sensitivity analysis was performed on *TRPN50* as it has an important length-dependent effect which was not tested in this study, and so the parameter was kept unchanged.

Two parameters were selected for future fitting: *nTm* and *ku*, representing the Hill coefficient of cooperative activation and the tropomyosin rate constant, respectively (Table 5.1). This was partly based on the results obtained after the sensitivity analysis indicating that *nTm* had the greatest influence on the biomarker values. The second greatest influence was elicited by the parameter *rs* which describes a steady-state duty ratio *i.e.* the ratio of myosin heads in the power stroke state sliding actin (S) over the number of myosin heads in states U, W,

and *S*. However, *rs* was based on experimental values from myosin dimer and therefore, was left unchanged [168].

Next parameters that had the greatest influence on active tension biomarkers were *rw*, *kuw* and *kws*. *Rw* describes a steady-state ratio between myosin heads in the pre-power stroke and unblocked states. *Kuw* describes the rate at which model moves from the state *U* to the state *W*, *i.e.* how quickly unblocked myosin heads bind to actin going into pre-power stroke state. *Kws* describes the rate at which model moves from the state *W* to the state *S*, *i.e.* how quickly myosin heads start sliding the actin moving from the pre-power stroke state to the power-stroke. Fitting these parameters showed active tension biomarkers that are within the experimental ranges, but the fit was not as good as the one achieved when fitting parameter *ku*. Therefore, the second parameter chosen for fitting was *ku*, and fitting *nTm* and *ku* values to reproduce the contractile phenotype of hiPSC-CMs allowed to acquire the biomarker values that were in line with ranges established from experimental data (Table 5.1).

Table 5.1: Model parameters fitted in the calibration process.

	ku	***nTm***
Parameter Meaning	the rate at which myosin binding sites on actin move from blocked (B) to unbound (U) state	Hill coefficient of the cooperative Hill curve describing a steady-state relation between troponin C units with calcium bound (CaTRPN) the fraction of unblocked myosin binding sites on actin
Parameter range	0.01 - 2	1.5 - 2.5
Original value	1	5
Calibrated iCEM	1.96	2.3

The selected parameters were fitted by changing their values to reproduce contractile phenotype of hiPSC-CMs. This was achieved by minimizing the cost function value. Cost function includes TP, RT50, maximum and minimum active tension values, and they were extracted after running simulations and computing active tension using the hiPSC-CM electromechanical model (iCEM). The cost

function used here was an altered formula of the cost function used by Land et al. (2017) [168]:

$$d_t = d\,(\mathrm{TP}, [169, 215]) + d\,(\mathrm{RT50}, [141, 178]) + 10d\,(\max(\mathrm{AT}), [0.21, 6.5]) + 25\min(\mathrm{AT}))$$

where the distances d between each biomarker and the corresponding experimental ranges were computed and summed to obtain the total cost d_t, which was then minimised. The function was altered by eliminating one term that was included in the original formulation: $d\,(\mathrm{rt90}, [\,])$. This was done because of the lack of availability of hiPSC-CMs studies reporting RT90. The weights in the cost function that multiply minimal (25) and maximal (10) active tension were chosen by Land et al. (2017) to prioritise good activation and relaxation, and were kept unvaried here [168]. However, the elimination changes the relative weight of each term used in the summation. Despite this, the minimisation of the cost function allowed finding parameter values such that the biomarkers of the simulations would be in line with the experimental data ranges as detailed in the Results section of this chapter.

The ranges of biomarkers chosen as targets for this calibration procedure are $[0.21, 6.5]$ for active tension peak ($\mathrm{mN/mm^2}$), $[169, 215]$ for TP (ms) and $[141, 178]$ for RT50 (ms) based on Table 5.2. To minimise the cost function, the MATLAB function `ga` was used. It finds the minimum of a cost function using a genetic algorithm. The values of the parameters fitted using the `ga` function are outlined in Table 5.1. The calibrated electromechanical model was then used for simulations and hiPSC-CMs contractile phenotype investigations *in silico*.

5.2.2 hiPSC-CM electromechanical model calibration and experimental evaluation

The summary of experimental data used for the experimental model evaluation (Table 5.3) and calibration (Table 5.2) is provided bellow.

The hiPSC-CMs engineered heart tissue (EHT) data from Schawan et al. (2016) and Sewanan et al. (2019) was used for calibrating the model using active tension

parameters TP, RT50 and active tension amplitude reported [232, 233]. Other data was used for calibration of the model using the active tension amplitude only, since other parameters were not reported.

Contractile hiPSC-CM data for the validation of the simulation outputs (peak force, time to peak force, time to 50% relaxation) of the model was collected by Marilù Casini, Manuel Koch, Ursula Ravens, and Remi Peyronnet in the Hospital Universitario y Politecnico La Fe, Valencia, Spain.

The initial iteration of hiPSC-CM computer model was presented at Computing in Cardiology 2021, and figures, where indicated, are reproduced with permission form the authors [234].

Table 5.2: The summary of the experimental data used for model calibration from hiPSC-CMs only (human embryonic stem cell (hESC) data not included). Here TP: time to peak tension; RT50: time to 50% decay; AT: Active Tension; RT: room temperature; EBs: embryoid bodies; CMs: cardiomyocytes; FBS: foetal bovine serum; EHTs: engineered human tissues; PDMS-M: polydimethylsiloxane elastomer mold; hiPSC: human induced pluripotent stem cells; Lmax: cell length at which maximum twitch force is reached; n: sample size. The data was collected from hiPSC-CM derived EBs, EHTs and other constructs unless stated otherwise. The data are reported as Mean ± Standard Deviation (SD).

Reference	**Cell preparation methods**	**Measurement protocol**	**Cell maturity**	**Data type**	**Biomarkers**
[235]	Paced at 1 Hz hiPSC line from dermal fibroblasts. Reprogrammed by retroviral vectors encoding SOX2, KLF4 and OCT4. Differentiated by the growth factors, EB-based process.	Single-cell force-measurement system (2 micromanipulators, an optical force transducer and a piezoelectric length controller). hiPSC-CM were attached to the coated fibers at cell's edges, separated from the substrate, and lifted.	Experiments performed at d.22 post differentiation.	Mean AT was measured at baseline cell length with subsequent stretching reaching 40% stretch.	Mean AT at baseline length: 0.51 ± 0.06 mN/mm^2; Maximal AT after stretch: 1.24 ± 0.08 mN/mm^2. Peak total tension: 1.82 ± 0.25 mN/mm^2. Peak passive tension: 0.58 ± 0.07 mN/mm^2.
[236]	HiPSC differentiation and EB formation induced by antibiotic-mediated selection of CMs using G418 to generate human iPSC-derived bioartificial cardiac tissues with Matrigel and collagen scaffold. Paced at 1 Hz, RT.	Constructs were placed into a custom-made bioreactor for force measurements. Tissue constructs were subject to constant static stress due to fixation at both ends.	Measurements performed at d.14-21 post differentiation.	Contraction forces at Lmax; forces after stretching (5-10%); AT.	AT: 4.4 mN/mm^2. Contraction force: 0.62 ± 0.03 mN on d14; 0.75 ± 0.06 mN on d21. Force after cyclical stretching: 0.77 ± 0.07 mN (n = 5); after static: 0.97 ± 0.08 mN (n = 8).

Continued on next page

Reference	Cell preparation methods	Measurement protocol	Cell maturity	Data type	Biomarkers
[233]	HiPSCs from T cells differentiated by modulating Wnt signaling. HiPSC-CMs used for ETHs generation. Measured at 35°C, paced at 1 Hz.	Force dynamics assessed like in Schwan et al. (2016) (entry bellow). ETHs were mounted on a testing setup consisting of a force transducer and a linear actuator which was mobile enabling muscle stretching.	Measurements performed at d.15 post differentiation.	Active force generated by gradual stretch (0.015 mm/s to 10% stretch).	TP: 211 ± 4 ms; RT50: 143 ± 2 ms; peak twitch force: 0.05 ± 0.01 mN; peak stress: 0.22 ± 0.1 mN/mm^2.
[232]	HiPSC-CMs from peripheral blood mononuclear cells differentiated using a Sendai virus and a monolayer differentiation protocol. Cells seeded on scaffolds forming ETHs. Measured at 35°C, paced at 1 Hz.	Clips holding EHT were ejected from the frame and picked up by motorized micromanipulators with claw-like extensions, leaving the muscle suspended between an anchoring attachment claw and a force transducer on a second claw; EHTs immersed in a perfusion bath.	Measurements performed at d.23 post differentiation	AT at 8% stretch.	Average (n=8) peak stress: 2.2 ± 0.76 mN/mm^2; Maximum peak stress recorded: 6.5 mN/mm^2; TP: 181 ± 12 ms; RT50: 168 ± 10 ms.
[237]	HiPSCs from a lung fibroblast line differentiated by monolayer-based protocol. Paced at 2 Hz, 37°C. HiPSC-CMs used for cardiac construct (3D scaffolds) generation.	Constructs were dissected into sections and suspended on stainless steel hooks attached to a force transducer and a length controller in a chamber perfused with Tyrode solution.	Measurements performed at d.14-21 post differentiation.	AT determined by stretching the structure in small increments (4% length) to 125% of initial length.	Twitch amplitude: 0.37 mN/mm^2.

Table 5.3: The summary of the experimental data used for model validation. Same abbreviations are used here as in the Table 5.2. Here PDMS-M: polydimethylsiloxane elastomer mold, APD50 and APD90: action potential (AP) duration at 50% and 90% repolarisation, respectively; CaT: calcium transient; CTD50 and CTD90: CaT duration at 50% and 90% decay, respectively; CTTP: CaT time to peak; bpm: beats per minute; FBS: foetal bovine serum.

Reference	**Cell preparation methods**	**Measurement protocol**	**Cell maturity**	**Data type**	**Biomarkers**
[238]	HiPSC-CM from peripheral blood mononuclear cells (n=37) differentiated with Sendai virus and a 2D monolayer protocol.	Recordings made using patch clamping at 36-37°C, paced at 0.5 Hz.	Measurements performed at d.30-50 post differentiation.	CaT, AP.	CaT: TP (245.0±81.3 ms); CTD50 (450±100 ms); CTD95 (990 ±50 ms); AP: AP amplitude (111.26 ±0.99mV); APD90 (367.17±19.62 ms); APD50 (308.33±17.09 ms).
[239]	HiPSC-CM on structured PDMS-M and non-structured substrates paced at 0.5 and 1 Hz at 37°C. Both constructs had similar mechanical properties. HiPSC-CMs acquired from iCell®.	AP was measured using a current clamp system. CaT was measured under field stimulation using an external pacing generator.	Measurements performed at d.14 post hiPSC-CM seeding.	CaT, AP.	CaT: Non-structured at 0.5 Hz: CTTP (200 ± 10 ms); CTD50 (255±10 ms); CTD90 (500±20 ms). At 1 Hz: CTTP (242± 10 ms); CTD50: (280± 10 ms); CTD90 (610 ±10 ms). Structured at 0.5 Hz: CTTP 9145±5 ms); CTD50 (230±10 ms); CTD90 (510±10 ms). At 1 Hz: CTTP (195±10 ms); CTD50 (285±20 ms); CTD90 (670± 20 ms). AP: Non-structured: APD90 (550±10ms). Structured: APD90 (548±12ms).

Continued on next page

Reference	Cell preparation methods	Measurement protocol	Cell maturity	Data type	Biomarkers
[240]	HiPSC from skin fibroblasts reprogrammed using retroviruses encoding OCT3/4, SOX2, KLF4, and c-MYC; differentiation induced by co-culturing hiPSC with murine visceral endoderm-like cell line END2. Measured at 37°C.	Whole-cell current clamp technique with an EPC-9 amplifier was used for AP measurements.	Measurements performed at d.20-30 post differentiation.	AP.	APD90 for ventricular-like cells: 297.70 ± 60.53 ms; APD50: 175.45 ±43.25 ms.
[241]	HiPSC from fibroblasts reprogrammed with retrovirus encoding Oct3/4, Sox2, Klf4, and c-Myc. EBs formed and differentiation induced by differentiation medium. Measured at RT.	After colony disassociation, single cells were patch-clamped to measure AP.	Measurements performed at d.28-44 post differentiation.	AP.	APD90: 429 ± 34 ms, APD50: 357 ± 29 ms, amplitude: 101.5 ± 2 mV.

Continued on next page

Reference	Cell preparation methods	Measurement protocol	Cell maturity	Data type	Biomarkers
[242]	HiPSC from fibroblasts, reprogramed by retroviral vectors with sox7, oct4, nanog, and lin28. Diff. when cultured in suspension with zebrafish basic fibroblast growth factor and FBS. Measured at 35-37°C, paced at 1Hz.	APs were recorded from single cardiomyocytes with perforated whole cell patch-clamp technique.	Measurements performed at d.10-21 post differentiation.	AP.	APD90: 414.7±21.8 ms.

5.2.3 Simulation protocols

Simulations were conducted using MATLAB (Mathworks Inc. Natwick, MA, USA) using the ordinary differential equation solver ode15s. For the simulations in paced mode, stimulus currents of 5 ms duration and 550 pA amplitude were used. The cell length was kept unchanged meaning that the extension ratio (sarcomere length over sarcomere length at rest) was set to 1. For simulations in the paced mode (1 Hz) at 37^{o}C, biomarkers were computed in the steady state (after 800 s). For simulations in a non-paced mode to investigate the responses in spontaneously beating cells, biomarkers were also computed after 800s.

To assess the changes on action potentials, calcium transients, and contraction, different biomarkers were extracted. Action potential biomarkers included action potential duration at 50, and 90% of repolarization (APD50, APD90); action potential amplitude (APA) and cycle length (CL). Calcium biomarkers extracted included CTD50 and CTD90. Active tension biomarkers extracted included force amplitude, time to 50 and 90% relaxation (RT50 and RT90) (fIG. 5.1 C-E).

5.3 Results

5.3.1 Experimental evaluation of the hiPSC-CM electromechanical model

Figure 5.2 shows the comparison of newly developed hiPSC-CM electromechanical and electrophysiology-only [160] model outputs. Electro-mechanical coupling does not alter the normal morphology of action potential and calcium dynamics. However, the non-calibrated electromechanical model did not produce active tension biomarkers as desired.

The calibration of model parameters improved the contractility performance of the electromechanical model. In particular, active tension amplitude increased from 0.04 kPa to 0.4 kPa in simulated paced cell (1 Hz) after calibration. The time to peak tension remained largely the same, 201 ms (experimental range: 169-215 ms), and the relaxation time (RT50) changed from 158 ms to 164 ms (experimental

range: 141-178 ms). The simulated active tension biomarkers after calibration are in agreement with experimental data (Fig. 5.2, Table 5.4). Similar results were obtained from the simulations in a spontaneously beating cell mode.

After calibration, the calcium and action potential biomarkers are also within the experimental hiPSC-CM biomarker ranges in the paced mode (Fig. 5.2): an increase in calcium transient duration (CTD90) by 3% and a 3% decrease in calcium transient peak amplitude were present in calibrated electromechanical model when compared to the electrophysiology-only model. Similar results were observed in the spontaneously beating mode as well (Fig. 5.2, Table 5.4). These differences fall within the expected range, demonstrating our model's capability for simulating hiPSC-CM electromechanical behaviour that is physiological as detailed in the calibration process.

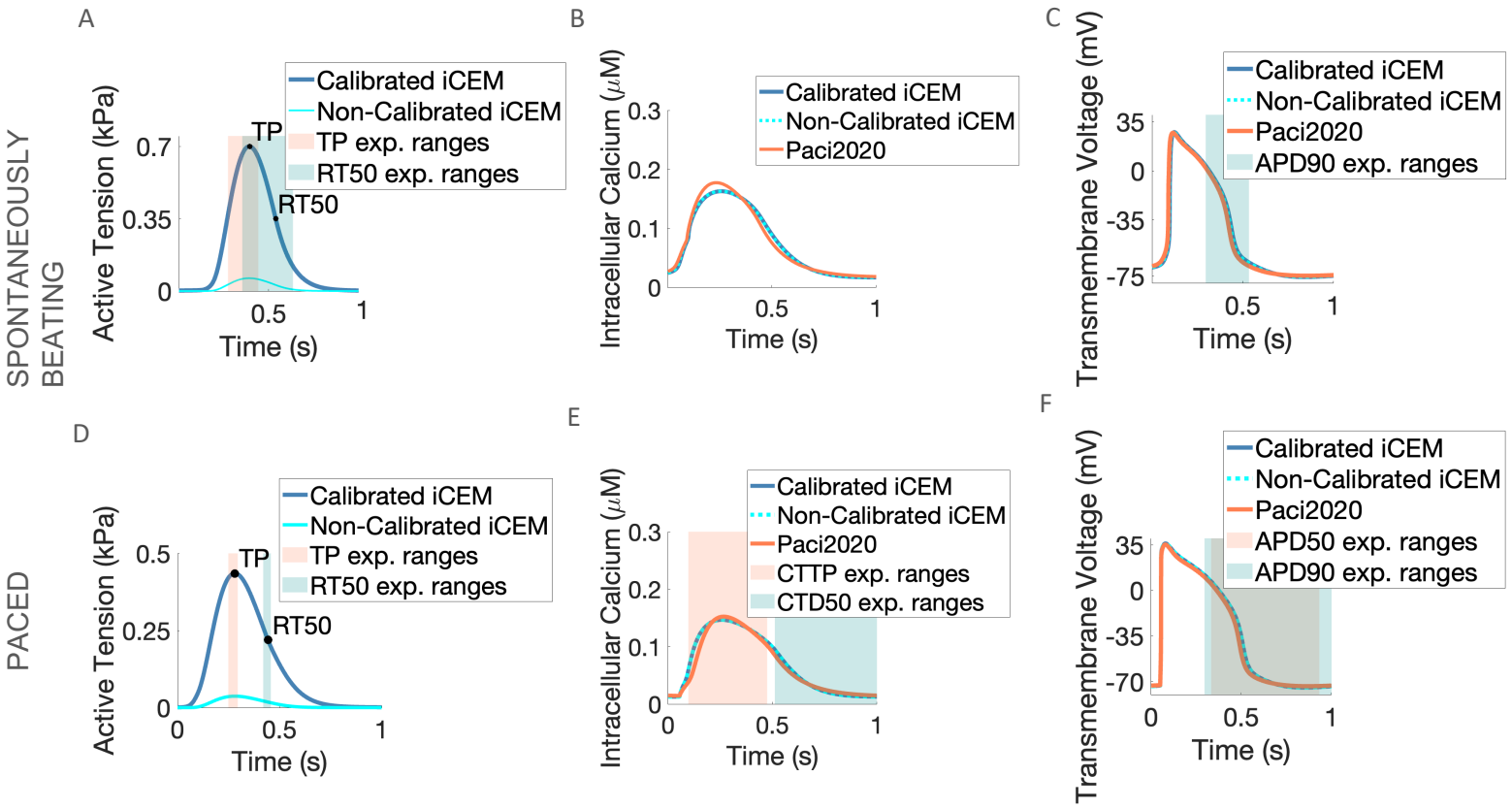


Figure 5.2: Experimental evaluation of the electromechanical hiPSC-CM (iCEM) model. In cases where calibrated (dark blue) and non-calibrated (bright dashed cyan) model simulations results in the very similar outputs, the line is visualised as dashed lines. Experimental ranges for biomarkers are denoted as shaded areas. **A.** The biomarkers of simulated active tension including TP and RT50 in the spontaneously beating cell mode are within the experimental biomarker ranges after the calibration of the model. **B.** There are minor differences between the outputs of the electrophysiology-only (Paci2020) and iCEM models in simulated calcium transient in spontaneously beating cells. **C.** The biomarkers of simulated action potential including APD90 in the spontaneously beating cell mode are within the experimental biomarker ranges. **D.** The biomarkers of simulated active tension including TP and RT50 in the paced cell mode are within the experimental biomarker ranges after the calibration of the model. **E.** The biomarkers of simulated calcium transient including CTTP and CTD90 in the paced cell mode are within the experimental biomarker ranges. **F.** The biomarkers of simulated action potential including APD50 and APD90 in the paced cell mode are within the experimental biomarker ranges.

Table 5.4: Active tension, calcium transient, and action potential biomarker values generated from simulations with hiPSC-CM electrophysiology [160], adult contractility [168], adult cardiomyocyte electromechanical [156] models; uncalibrated iCEM with original parameter values, and calibrated iCEM models. Experimental ranges are based on hiPSC-CM data established from literature search (Chapter 5, Methods), and acquired experimentally in the lab for this study, as indicated with *. Land model describes mechanical adult ventricular cardiomyocyte behaviour, ToR-ORd-Land describes electromechanical adult cardiomyocyte behaviour, Paci describes electrophysiology of hiPSC-CM, and iCEM is the newly established hiPSC-CM electromechanical model, and Paci-Rice is iPSC-CM electromechanical model based on contractile model established using experimental contractile data from rabbit cardiomyocytes [169].

Biomarkers	**Paced**						**Spontaneously Beating**				
	Land	**ToR-ORd-Land**	**Paci**	**Uncalib. iCEM**	**Calib. iCEM**	**Exp. ranges**	**Paci**	**Uncalib. iCEM**	**Calib. iCEM**	**Exp. ranges**	**Paci-Rice**
Active Tension (AT)											
TP, ms	175	169	N/A	201.5	201	169-215	N/A	219.7	214	63.7–232*	
RT50, ms	121	116	N/A	158	164	141-178	N/A	143	147	69.2-182*	161
RT90, ms	234	227	N/A	286	329		N/A	258	287		
Max AT, kPa	51.2	24	N/A	0.04	0.44	0.21-6.5	N/A	0.062	0.7		0.055
Min AT, kPa	0.0078	0.075	N/A	0	0	0-0.58	N/A	0	0		
Calcium Transient											
CTTP, ms	124	42.4	207.3	200.4	201	97-474	218	232	232		
CTD50+TP, ms	337	201.9	369.6	427	427.5	511-1168	345.9	387.7	387.6		
CTD90+TP, ms	567	355.4	613.3	631.3	632.7	310-1803	550.4	576	576		
Amplitude, µM	0.6	0.475	0.152	0.147	0.147	0.16	0.177	0.163	0.163		
Action Potential											
APD50, ms	N/A	219.5	393.3	408	408	333-932	300.5	303.5	303.5		
APD90, ms	N/A	273.5	483.5	505.2	505	296-1398	390.4	397.7	397.5	296-534	403
Amplitude, mV	N/A	121.63	108.8	110.6	110.6	98-112	102	103.3	103.3	98-110	103

5.3.2 Comparison of hiPSC-CM and human adult cardiomyocytes

Human induced pluripotent stem cell-derived cardiomyocytes (hiPSC-CM) and adult human cardiomyocytes exhibit different contractile phenotypes. Therefore, it was aimed to (a) quantitatively assess the differences in contractile biomarkers between hiPSC-CM and adult human cardiomyocyte *in silico* and to (b) investigate the drivers of those differences in the Land contractile model framework. This was achieved by comparing hiPSC-CM electromechanical (iCEM) model with two other human adult cardiomyocyte models: contractility (Land) and electromechanical (ToR-ORd-Land) model [156, 168]. These models simulate electrophysiological and mechanical behaviours in adult human cardiomyocytes, providing a basis for identifying key differences with hiPSC-CM.

Comparison of the active tension and calcium transient biomarkers between adult cardiomyocyte mechanical (Land), electromechanical (ToR-ORd-Land), and hiPSC-CM electromechanical (iCEM) models reveals major differences between the three (Fig. 5.3, Table 5.4). The differences between the biomarker values computed from hiPSC-CM electromechanical and adult cardiomyocyte mechanical models were the results of the hiPSC-CM electromechanical model calibration.

The quantitative assessment was carried out by comparing the active tension biomarkers simulated from different models in order to establish whether the model can be used for active tension biomarker data translation from stem to adult cells. Upon comparison with experimental data from adult cells, it appeared that the relative difference in TP and RT50 active tension biomarker values between hiPSC-CM electromechanical (iCEM) and adult cardiomyocyte mechanical (Land), and electromechanical (ToR-ORd-Land) models is in agreement with the relative differences observed experimentally (Fig. 5.3). This is quite interesting given the differences in calcium transients between adult cardiomyocyte electromechanical (ToR-ORd-Land) and mechanical (Land) models (Fig. 5.3).

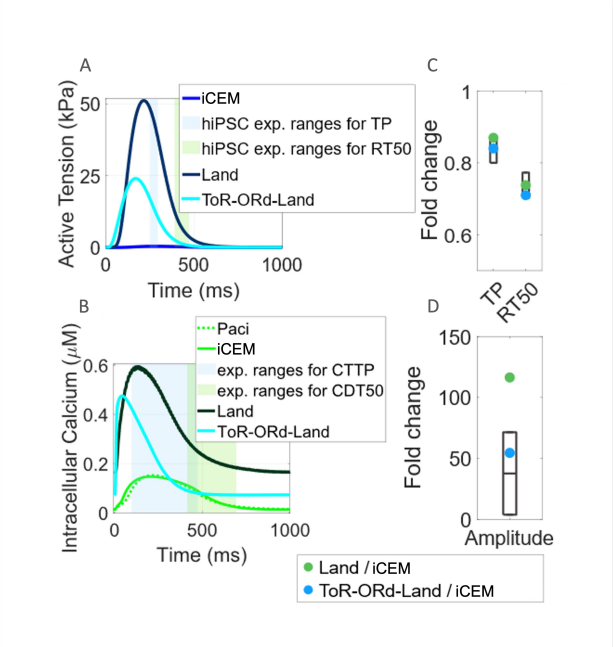


Figure 5.3: The differences between hiPSC-CM electromechanical (iCEM) and adult contractility (Land), and adult electrophysiology (ToR-ORd-Land) models. The figure has been updated and reproduced with a permission from Folkmanaite et al. (2021) [234]. **A.** Active tension waveforms differ between hiPSC-CM and adult human cardiomyocyte models highlighting the differences in the contractile phenotype observed experimentally between hiPSC-CMs and human adult cardiomyocyte. **B.** Calcium transient waveforms differ between hiPSC-CM and adult models. Here exp. ranges refer to experimental ranges for TP and RT50 established in hiPSC-CMs. **C.** Fold change in biomarker values TP and RT50 between simulated adult cardiomyocyte and hiPSC-CM biomarkers by dividing biomarker values from adult by the values from hiPSC-CM. Box plots represent the ranges of the fold changes in experimental values acquired by dividing experimental adult cardiomyocyte biomarker values by hiPSC-CM biomarker values. HiPSC-CM experimental values are detailed in Table 5.4, and adult human experimental values are detailed in the Methods. **D.** Fold change in simulated active tension amplitude from adult cardiomyocyte and hiPSC-CM biomarkers. Box plots represent the ranges of the fold changes in experimental values.

The relative difference in active tension amplitude between hiPSC-CM electromechanical (iCEM) and adult cardiomyocyte electromechanical (ToR-ORd-Land), but not adult cardiomyocyte mechanical (Land) models aligns with the experimentally observed values (Fig. 5.3). This is because the amplitude of active tension in the adult cardiomyocyte mechanical (Land) model is higher than the experimental active tension amplitudes involved in this figure. Although both, adult cardiomyocyte mechanical (Land) and electromechanical (ToR-ORd-Land) models simulate active tension that is physiological, the electromechanical (ToR-ORd-Land) model considers the majority of the current available adult experimental data whereas the experimental dataset used for the mechanical (Land) model is more limited.

Overall, the agreement between experimental and simulated biomarkers demonstrates that the hiPSC-CM electromechanical (iCEM) model can be used to address the active tension differences between hiPSC-CM and adult human cells in most cases.

5.4 Discussion

This chapter outlines:

1. the development of a hiPSC-CM electromechanical model, including model coupling and calibration;

2. the simulation of hiPSC-CM action potentials, calcium transients, and active tension, with evaluation against experimental hiPSC-CM data;

3. the comparison of hiPSC-CM and adult human cardiomyocyte contraction *in silico*.

Myofilament function and its regulation have been explored using experimental and computational tools. Due to the complicated nature of cellular signalling events leading to contraction generation and the modulation of force generation processes at the myofilament, computer models offer an excellent way to investigate these processes in detail.

For those investigations, a hiPSC-CM electromechanical model has been developed to provide a platform that integrates and extends experimental findings using *in silico* tools. First, the electromechanical model demonstrates performance comparable to the established electrophysiology-only model [160] in terms of action potential and calcium transient features, indicating that the electro-mechanical coupling does not alter normal electrophysiological behaviour. Action potential and calcium transient biomarkers remain within experimental ranges after model calibration. Detailed comparisons of simulated and experimental hiPSC-CM data show that the electromechanical model accurately captures the electromechanical properties of hiPSC-CMs.

The hiPSC-CM electromechanical model enables simulations of hiPSC-CM electrophysiology and mechanics, an aspect often overlooked but critically important. Although models of human ventricular cardiomyocyte electromechanics exist [156], there is a lack of human-data-based electromechanical hiPSC-CM models. Developing such models is a crucial step towards more accurate pre-clinical studies,

reducing reliance on animal models, and enabling more precise predictions of drug effects in humans. Furthermore, unlike human ventricular cardiomyocyte models, the results of hiPSC-CM electromechanical simulations can be directly tested in the lab due to the availability of hiPSC-CM cells, which is challenging with human cardiomyocytes. Additionally, hiPSC-CMs can be patient-derived, holding the same genetic information as the donor, making hiPSC-CM-based *in silico* and wet lab experiments personalised and useful for developing patient-specific treatment options. Finally, these experiments can be high-throughput due to the ample availability of hiPSC-CM cells, making them ideal for drug screening, unlike human cardiomyocytes, which are a scarce resource.

To assess whether the established model can facilitate translation of hiPSC-CM contractile data to adult cardiomyocytes, comparisons were made between the hiPSC-CM and human adult cardiomyocyte models. Quantitative differences in active tension biomarkers between these models reflect the experimental differences observed between the two cell types. This finding suggests that the hiPSC-CM electromechanical model can be used alongside adult cardiomyocyte *in silico* models to translate contractility data from hiPSC-CMs to adult human cell phenotypes in most cases.

In summary, this chapter presents a calibrated and experimentally evaluated hiPSC-CM electromechanical model capable of simulating physiological contraction properties. This model establishes a foundation for future hiPSC-CM-based electromechanical *in silico* studies.

5.4.1 Limitations

While the model represents a significant methodological advancement, it is not without limitations. Further refinement of the model could allow to more closely mirror signalling pathways in the heart cells.

Refinement could include modelling additional signalling pathways that play an important role in mediating cellular contraction such as MYBPC signalling, phosphorylation cascade, and hiPSC-CM specific aspects such as differences in the

expression of various protein isoforms. For example, it is known that the predominant troponin I isoform in hiPSC-CMs is immature and not the mature form found in adult cardiomyocytes, which can affect contraction dynamics. Incorporating these isoform differences can improve the accuracy of the model.

Further enhancements could involve the integration of biomechanical properties specific to hiPSC-CMs, such as detailed cytoskeletal dynamics and the influence of extracellular matrix components on cellular contraction. Incorporating multi-scale modelling approaches that bridge cellular and tissue-level dynamics might also address some of the current model limitations, providing a representation of cardiac organoid function.

5.5 Conclusions

The new electromechanical model offers a robust framework for studying the mechanisms of cardiomyocyte contraction regulation and electrophysiology, particularly when complemented by experimental data. The model provides a strong foundation for future hiPSC-CM-based *in silico* studies in health and disease, as well as investigations of pharmacological mechanisms.

6

Investigating the mechanisms regulating contraction with hiPSC-CM electromechanical modelling and simulation

6.1 Introduction

Human-induced pluripotent stem cell-derived cardiomyocytes (hiPSC-CMs) have emerged as crucial tools in cardiovascular research, providing a patient-specific platform for drug testing and disease modeling.

Simulating contractility using computer models allows for the investigation of mechanical properties which play a vital role in assessing the efficacy and safety of cardiac drugs. Although contractility can be measured experimentally, *in silico* models offer for more efficient, scalable, and cost-effective approach to drug testing, enabling the exploration of scenarios that might be challenging to replicate experimentally.

The Comprehensive in Vitro Proarrhythmia Assay (CiPA) initiative highlights the importance of assessing drug-induced effects through a combination of *in silico* approaches and lab-based assays [243]. However, only a few existing models integrate electrophysiology and contractility aspects, which could be critical for a compre-

hensive assessment [156]. In addition, there is a lack of electromechanical models based on human data. Existing hiPSC-CM models incorporate contractile elements from animal data, limiting their translational value to human physiology [169].

To address this gap, the hiPSC-CM electromechanical model (iCEM), described in the previous chapter, is employed. By integrating and extrapolating sparse experimental data, this model serves as a platform for mechanistic studies, offering insights into the molecular drivers of drug responses, which is crucial for the design of safer and more effective cardiac therapies.

While current experimental approaches provide insights into drug mechanisms, they are often limited by the complexity of intracellular signalling. The main objective of this study is to provide further validation of the model by simulating drug effects on contraction. A key focus of this chapter is to evaluate whether the hiPSC-CM electromechanical (iCEM) model can accurately predict drug effects. This facilitates the exploration of contractile function regulation and provides validity to the model. Additionally, the model's ability to simulate drug effects in both paced and spontaneously beating cells provides insights into rate-dependent behaviours, offering valuable mechanistic understanding of how pacing conditions influence calcium handling and contractility.

This chapter outlines the application of the hiPSC-CM electromechanical (iCEM) model, aiming to advance mechanistic understanding of cellular behaviours and serve as an advanced computational tool for drug efficacy testing and cardiotoxicity predictions. The model offers a flexible and translatable platform that can be modified and applied broadly to various hiPSC-CM studies.

6.2 Methods

The main simulation were performed using the newly developed hiPSC-CM electromechanical (iCEM) model, as described in Chapter 5. Here, the methods used to evaluate the hiPSC-CM electromechanical model, *in silico* drug assay design, experimental approaches used for *in silico* assay validation, and simulation protocols, are described. For the adult cardiomyocyte simulations, ToR-ORd-Land model

was used [156]. Experimental adult human cardiomyocyte biomarkers used in this study include the peak force (11.9 - 25 kPa), time to peak force (147-172 ms), and time to 50% relaxation (110-126 ms) [156].

6.2.1 *In silico* drug assay design

Two groups of compounds were selected to assess the accuracy of the hiPSC-CM model in simulating drug effects on contractility. Group 1 contains 7 compounds, and their simulated effects were compared with available experimental data from hiPSC-CM contractile studies (Fig. 6.1). The compounds were selected based on availability of experimental hiPSC-CM contractile studies reporting the effects of the compounds on the force of contraction of hiPSC-CMs. The experimental studies outlined the changes in calcium transient duration (CTD90), and the peak force amplitude. The compounds include: Bay-K8644, a single channel activator (ICaL), E-4031, IKr blocker, and multiple channel (ICaL, IKr, INa) blockers sunitinib, bepridil, lidocaine, nifedipine, and verapamil.

Group 2 includes 63 compounds where the simulated inotropic effects were compared to known clinical and experimental data. The list includes antiarrhythmic drugs and other drugs used for different purposes but with known effects on cardiac ion channels including antipsychotics, antibiotics, kinase inhibitors, antivirals, and other. Most of these drugs have a multichannel action, which makes prediction and interpretation of cardiotoxicity challenging.

Drug effects were simulated using a simple pore-block model based on the availability of IC50 and Hill coefficient (h) for each drug-ion channel.

$$I(X) = \frac{100}{1 + \left(\frac{X}{IC_{50}}\right)^h}\% \tag{6.1}$$

where I(X)% denotes the percentage of ionic current remaining after the block, IC50 is the inhibitory concentration 50%, X is the concentration of the drug, and h is the Hill coefficient.

The experimental IC50 and h used for the drug assays for different ion channels were considered: fast $Na+$ current (INa), rapid/slow delayed rectified $K+$ current

(IKr/IKs), transient outward $K+$ current (Ito), L-type $Ca2+$ current (ICaL), inward rectifier $K+$ current (IK1), and late $Na+$ current (INaL). This was based on the availability of the data, where these inputs were successfully used for the *in silico* drug assays before. The data was from Passini et al. (2017), Forouzandehmehr et al. (2021) and Tomek et al. (2019) [154, 169, 244].

For the compounds that were included in more than one of these datasets, multiple profiles were considered to investigate the impact of variability in drug characterization. Each IC50 and h set was simulated separately, resulting in 87 different drug trials (as detailed in the Appendix). Generally, there was a good agreement between the results of compounds with multiple profiles.

Multiple concentrations were investigated for each compound, chosen to match those used in the experimental drug assays, as well as to explore different multiples of the maximal effective free therapeutic concentration (EFTPCmax), up to 100-fold. The EFTPCmax values were taken from literature. The full list of compounds, together with the IC50, Hill coefficient and the EFTPCmax used for in silico drug trials is provided in the Appendix (Table. B.1).

Simulated drug effects were considered as positive or negative inotropic when the change in peak force amplitude was greater than 10% of baseline to ensure only robust changes were registered as positive and negative.

6.2.2 Experimental data for the evaluation of the *in silico* drug trials

In silico drug simulation results were compared to experimental data as outlined in Fig. 6.1 and the Appendix (Table B.1). All experimental results are presented as percentage changes with respect to the baseline.

As the inotropic effects of some simulated drugs were previously unknown, additional experiments were performed in hiPSC-CM for some representative compounds to assess the changes in intracellular calcium dynamics after the addition of varying concentrations of duloxetine hydrochloride (ThermoFisher) and paliperidone (Cambridge Bioscience). First, human induced pluripotent stem

cells (hiPSCs) were cultured and differentiated into cardiomyocytes as described in General Methods, Chapter 2. Dr Koschinski and Ms Hong provided help in differentiating and culturing hiPSC-CMs.

Seeded hiPSC-CM were incubated with Fura-2 (1 μM, 15 min, 37^{o}C degrees). For calcium imaging, cells were kept in a imaging buffer (NaCl 125 mmol/L, KCl 5 mmol/L, HEPES 20 mmol/L, glucose 5.5 mmol/L, CaCl2 1 mmol/L, and pH 7.4) and imaged on an Olympus IX71 inverted microscope using a PlanApoN, $\times$40, oil immersion objective (numerical aperture 1.4, 0.17/field number 26.5, Olympus) using IonOptix hardware and software, in 0.5 Hz pacing, and in spontaneously beating modes at room temperature. Data was analysed and plotted using MATLAB (Mathworks Inc. Natwick, MA, USA).

6.2.3 Simulation protocols

For *in silico* drug trials, simulations were run in a spontaneously beating cell mode to also investigate drug-induced effects on the spontaneous beating frequency. Simulations were conducted using MATLAB (Mathworks Inc. Natwick, MA, USA) using the ordinary differential equation solver ode15s. For the simulations in paced mode, stimulus currents of 5 ms duration and 550 pA amplitude were used. For simulations in the paced mode (1 Hz) at 37^{o}C, biomarkers were computed in the steady state (after 800 s). For simulations in a non-paced mode to investigate the responses in spontaneously beating cells, biomarkers were also computed after 800s. Additional simulations were run in the paced mode (0.5 Hz) at 20^{o}C for additional comparisons with the experimental dataset (Appendix).

To assess the changes on action potentials, calcium transients, and contraction, different biomarkers were extracted. Drug-induced changes in those biomarkers are presented as percentage change with drug, compared to control (no drug). Single and multiple early afterdepolarizations (EADs) were defined as extrapeaks greater than $-55\,\mathrm{mV}$ in between two consecutive action potential upstrokes. Repolarisation failure was identified in spontaneously beating cells when a stable ($\frac{dV}{dt_{\max}} < 0.1\,\mathrm{V/s}$) membrane potential greater than $-40\,\mathrm{mV}$ was observed during the last 15 s of

simulation. Irregular rhythm in spontaneously beating cells was identified when the difference in cycle length between two consecutive action potentials was greater than 150%. Quiescence, *i.e.* when a model does not produce spontaneous action potentials, was also assessed. This was defined as a model of spontaneously beating cells which during the last 15 s has an average membrane potential smaller than $-40\,\mathrm{mV}$.

6.3 Results

6.3.1 Simulation of drug-induced inotropic effects agree with experimental hiPSC-CM data

To evaluate the hiPSC-CM electromechanical (iCEM) model, and to test the effects of drugs on the myofilament signalling and contraction generation, the drug-induced inotropic effects in hiPSC-CM electromechanical simulations were compared with experimental hiPSC-CM contractility and calcium data.

This was achieved by evaluating the consistency between the simulated and experimental calcium transient durations and inotropic responses for the first group of drugs (7 reference compounds in group 1) with varied actions on ion channels (including single and multichannel blockers).

For Bay-K8644, a single channel activator (ICaL) and sunitinib, a multiple channel blocker (ICaL, IKr, INa), simulations showed an increase in force which has also been observed experimentally [245, 246] (Fig. 6.1). For E-4031, which was simulated as a 70% IKr block at 1 μM, repolarization failure was observed in some cases in hiPSC-CM experiments [247], consistent with simulation results. For multiple channel blockers bepridil, lidocaine, nifedipine, and verapamil the simulation results show a decrease in force, in good general agreement with the experimental data [145, 245–249] (Fig. 6.1).

Despite the minimal input information (IC50s and Hill coefficients), the simulations revealed a good qualitative agreement with experimental data, highlighting the model's ability to capture drug-specific responses (Fig. 6.1).

	Bay-K8644	Bepridil	E-4031	Lidocaine	Nifedipine	Sunitinib	Verapamil
CTD90							
Experimental hiPSC-CM data		↑	EADs, RF	↑	↓		↓
iCEM simulation data	↑	↑	RF	↑	↓	↑	↓
Inotropy (force)							
Experimental hiPSC-CM data	↑	↓	↓	↓	↓	↑	↓
iCEM simulation data	↑	↓	↓	↓	↓	↑	↓

Figure 6.1: Simulation of calcium transients and active tension changes induced by 7 reference compounds in group 1 are in a qualitative agreement with experimental data. Simulated force amplitude and CTD90 were compared with the corresponding experimental data from different hiPSC-CM studies [145, 245–249]. Here: EADs - early after depolarisations, RF - repolarisation failure

6.3.2 Comparison of simulated drug-induced inotropic effects with clinical and adult cell experimental data

In addition to the available hiPSC-CM contractility experiments of drug effects, the comparisons were extended to include clinical reports and adult cell experiments. 47 compounds, which included single and multiple channel blockers, in the group 2 were clinically or experimentally characterised before for their effects on the active tension.

The experimental data used for comparison are mostly qualitative reports of inotropic effects without detailed calcium signalling or active tension measurements available. Fig. 6.2 shows all the tested compounds classified by their effects on simulated active tension amplitude, and includes a comparison with known experimental data.

Among 47 drugs with known clinical or experimental inotropic characteristics, simulations accurately identified the effects of 37 drugs: 29 out of 32 with negative inotropic effects, 4 out of 6 with positive inotropic effects, and 4 out of 9 with no effects. This accuracy rate demonstrates that the electromechanical model is

particularly robust in predicting the effects of ion channel blockage on contractility when considering negative inotropic drugs. For positive inotropy classification, additional inputs beyond IC50s and Hill coefficients might be required to achieve higher accuracy in simulations.

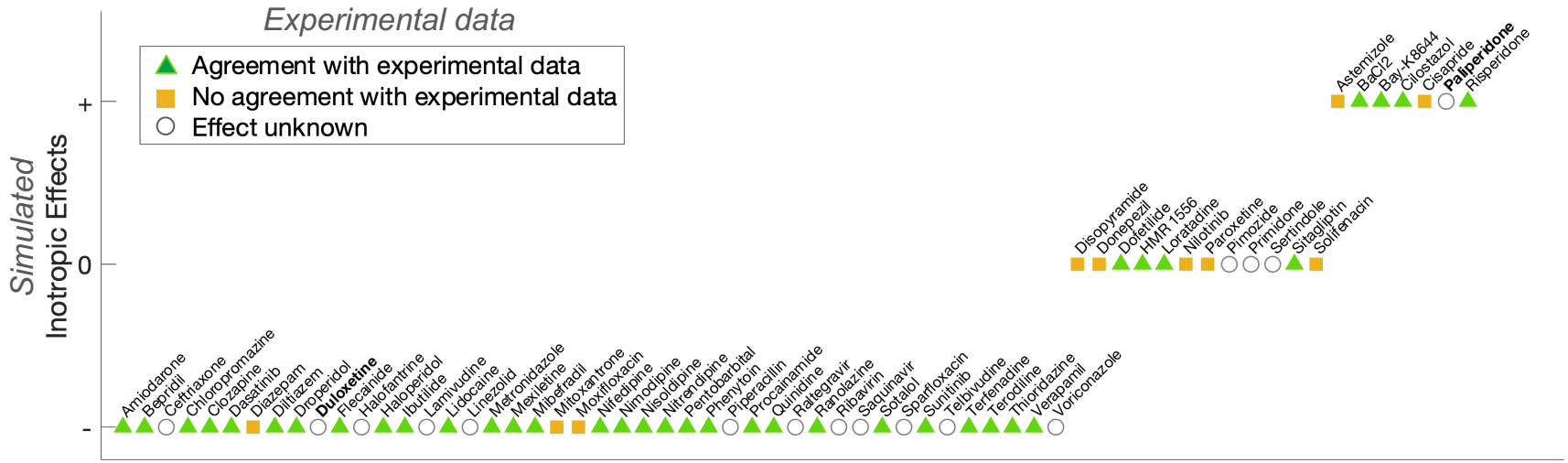


Figure 6.2: Comparison of the simulated inotropic effects from the electromechanical model with experimental and clinical data from various cell types. Simulation results of active tension changes from spontaneously beating hiPSC-CM cell are plotted, and they are in a qualitative agreement with experimental and/or clinical data (as denoted in the legend) in most cases. Here, the simulated effects are plotted on y axis, and green triangles indicate an agreement between the experimental and simulation data, orange squares indicate no agreement with experimental data, and grey circles indicate the compounds with unknown inotropic effects. Compounds highlighted in bold were selected for further validation.

6.3.3 Comparing experimental and simulated drug inotropic effects in paced hiPSC-CMs

Having evaluated the performance of the model under drug action of known inotropic effects, the model was used to simulate potential inotropic effects of drugs that have not been tested experimentally in hiPSC-CM before. Simulations of the activity of 16 drugs of unknown inotropic effect predicted several of these compounds to have positive or negative inotropic effects (Fig. 6.2).

Two drugs, duloxetine and paliperidone, were selected for further investigation to validate the predictions of the model (highlighted in bold in Fig. 6.2). Duloxetine and paliperidone were selected as representative compounds of multichannel action and single channel action, respectively, both with unknown inotropic effects. Duloxetine was simulated as a multichannel inhibitor (ICaL, INa, IKr) at 100-fold effective free therapeutic plasma concentration (EFTPCmax), and as a ICaL and IKr inhibitor at 10-fold EFTPCmax based on literature [154]. Paliperidone at its EFTPCmax, and at 10-fold EFTPCmax, is a single IKr channel blocker.

Simulations of paced hiPSC-CMs show that 0.1 µM and 1 µM duloxetine, a serotonin-norepinephrine reuptake inhibitor, has a negative inotropic effect (EFTPCmax = 0.016 µM, Fig. 6.3 A). To validate the predictions, the effects of duloxetine were tested in hiPSC-CM measuring the change in the calcium transients. Simulations show that duloxetine induces small reduction in calcium transient duration, and this was then also observed experimentally when measuring 50% and 90% of calcium transient duration (CTD50 and CTD90) (Fig. 6.3 B, C, D). Furthermore, both simulations and experimental data indicate a reduction in the calcium transient peak after the application of duloxetine, demonstrating qualitative agreement between the experimental observations and simulation results.

Comparison of *in silico* simulation and experimental data acquired in the lab shows good qualitative agreement in predicting duloxetine effects on calcium transient duration and peak. In addition to predicting calcium transient biomarkers, hiPSC-CM electromechanical model also predicted the shortening of action potential duration and a decrease in force (Appendix, Fig. B.1).

Simulations of 0.1 µM and 1 µM paliperidone (EFTPCmax = 0.069 µM), an antipsychotic, in paced hiPSC-CM cell suggest it has a negative effect on inotropy, and prolongs the calcium transient duration (Fig. 6.3 E). To further validate these predictions, the effects on calcium transient were tested experimentally in paced cells. The experimental calcium traces in paced cells also showed a prolonged calcium transient duration following paliperidone application in a dose-dependent manner, consistent with *in silico* results (Fig. 6.3 F, G, H).

Altogether, this demonstrates that the hiPSC-CM electromechanical model provides a robust platform for simulating drug-induced inotropic effects with good agreement between experimental and simulation results. Mechanistically, the observed negative inotropic effects of duloxetine and paliperidone can be attributed to their respective actions on ion channels: duloxetine's inhibition of ICaL (and other channels), and paliperidone's selective IKr blockade, which prolong calcium transients and reduce contractile force. Compared to simpler models, this approach captures the complex interactions between ion channel modulation and contraction control, providing a more comprehensive and mechanistic understanding of drug effects. Furthermore, unlike machine learning models, this framework can not only simulate novel drug effects, but also offer an interpretable tool for drug testing.

6.3.4 Inotropic drug effects are affected by the hiPSC-CM cell pacing mode

Similar as in the paced mode in Fig. 6.3, when simulated in a spontaneously beating hiPSC-CM cell mode, duloxetine has a negative inotropic effect (Appendix, Fig. B.1). Unlike for duloxetine, the effects of paliperidone were different between the pace and the non-paced modes. Although the calcium transient durations were prolonged in both modes following paliperidone application (Fig. 6.4 A, C), the paced mode predicted a reduction in the peak force and calcium transient (Fig. 6.4 A, B), whereas the non-paced mode showed a mild increase of contractility (Fig. 6.4 C-D).

Next, the model was used to explore what gives rise to the differences in calcium signalling and inotropy between paced and non-paced cells. It was hypothesised

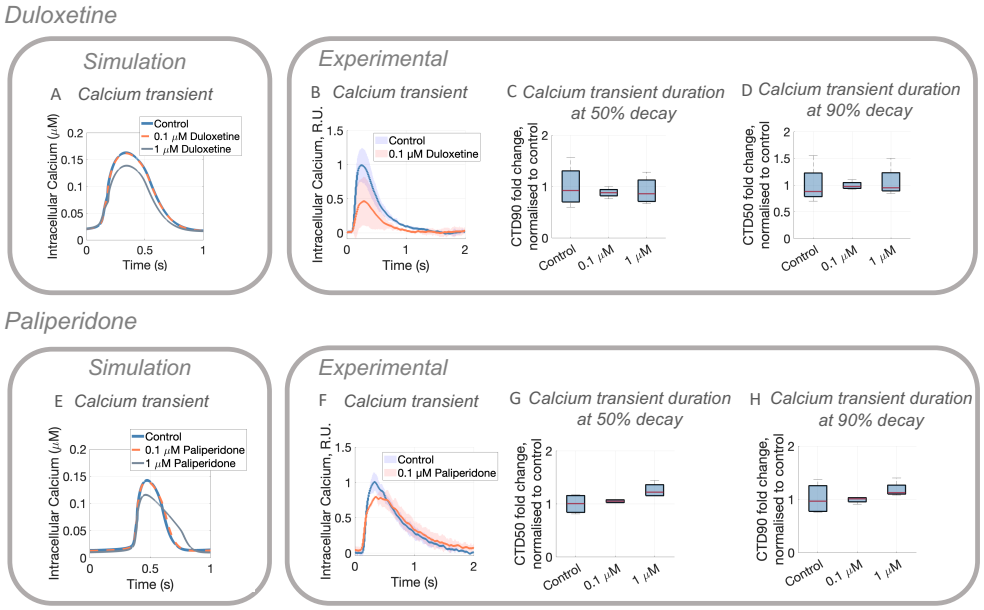


Figure 6.3: Comparison of experimental and simulation calcium data. **A.** Simulated hiPSC-CM calcium transient following the application of duloxetine. **B.** Average experimental hiPSC-CM calcium transient following the application of duloxetine. **C.** Experimental hiPSC-CM (n=3 individual cells, N=2 repeats (hiPSC-CM differentiations), n= at least 5 calcium transients averaged) data showing CTD50 following duloxetine application. **D.** Experimental hiPSC-CM data showing CTD90 following duloxetine application (n=3 individual cells, N=2 repeats (hiPSC-CM differentiations), n= at least 5 calcium transients averaged). **E.** Simulated hiPSC-CM calcium transient following the application of paliperidone. **F.** Average experimental hiPSC-CM calcium transient following the application of paliperidone. **G.** Experimental hiPSC-CM data showing CTD50 following paliperidone application (n=3 individual cells, N=2 repeats (hiPSC-CM differentiations), n= at least 5 calcium transients averaged). **H.** Experimental hiPSC-CM data showing CTD90 following paliperidone application (n=3 individual cells, N=2 repeats (hiPSC-CM differentiations), n= at least 5 calcium transients averaged). Shaded areas and error bars represent the SD.

that the differences might come from drug induced changes in ICaL. Greater ICaL availability would result in a greater calcium content in the cell, leading to increased inotropy, higher calcium transient peak, and longer calcium transient duration. It could also be that the differences might come from upstroke difference between the two pacing modes, or a more significant action potential prolongation induced by IKr blockade allowing for increased calcium entry during the plateau phase. To test these hypotheses, the cycle length in paced versus non-paced cells was compared. Non-paced cells have greater cycle length, and the cycle length

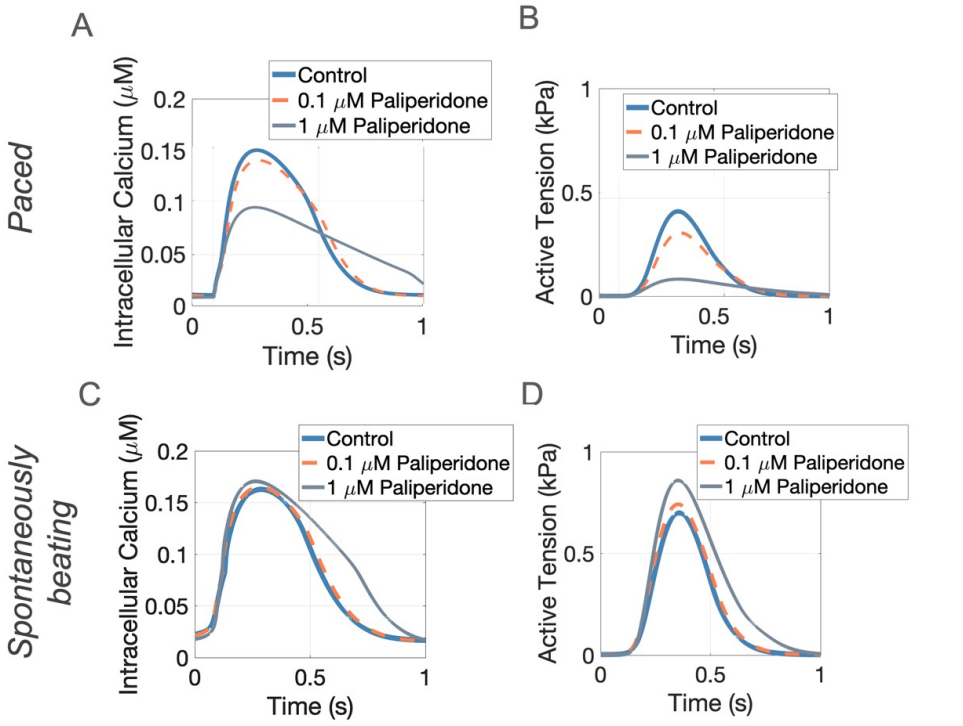


Figure 6.4: Paliperidone effects on active tension and calcium transient are dependent on pacing. **A.** Simulated calcium transient after paliperidone application in paced cells. **B.** Simulated active tension after paliperidone application in paced cells. **C.** Simulated calcium transient after paliperidone application in spontaneously beating cells. **D.** Simulated active tension after paliperidone application in spontaneously beating cells.

increases with increasing doses of paliperidone (paced: 1000 ms vs. 1856 ms in non-paced at 1 µM paliperidone).

Further comparisons of the action potential prolongations as well as the different currents between paced and non-paced cells were then performed. Action potentials were prolonged to a greater degree in paced than spontaneously beating cells (Fig. 6.5 A, B). Therefore, it was concluded that the increased calcium amplitude in the spontaneous beating mode is not due to a more significant action potential prolongation induced by the IKr blockade.

Generally, non-paced cells had a greater ICaL peak than paced cells. Since the longer plateau phase does not appear to correspond to a bigger ICaL in the paced cells (Fig. 6.5 A-D), the bigger ICaL amplitude in Fig. 6.5D is therefore

likely driven by the greater ICaL availability.

IKr currents were smaller and longer when affected by the drug, and these differences were driven by IKr current blockage ((Fig. 6.5 E, F). Changes in IKr prolongs the repolarisation phase and potentially delays the time until the pacemaker current can depolarise the cell to threshold again for the non-paced mode. This lengthening cycle leads to a more prolonged diastolic interval in the non-paced cells, allowing more time for the calcium handling system to recover, leading to increased ICaL channel availability and a greater ICaL peak, as well as a prolonged calcium reuptake into the sarcoplasmic reticulum in the non-paced mode.

Consistent with this hypothesis, paliperidone induces an increased reuptake in non-paced cells and reduced reuptake in paced cells (Fig. 6.5 I, J). Significantly reduced ICaL current in paced cells results in a lower amount of calcium being taken back to SR and a reduced subsequent release in paced cells. This is unlike in spontaneously beating cells where greater ICaL availability results in a greater amount of cytosolic calcium that can be taken back to the SR leading to a greater subsequent release. The calcium content in the SR is higher in the non-paced mode than in the paced mode (Fig. 6.5 K, L), which could be due to both, higher ICaL amplitude, and longer Iup. The elevated calcium loading state in the SR of the non-paced cell model subsequently leads to higher amplitude of calcium release (Irel) (Fig. 6.5 G, H). This mechanism can explain why calcium transient peaks are not reduced but are slightly greater in non-paced cells, as more calcium available in the SR can lead to more substantial releases during each excitation.

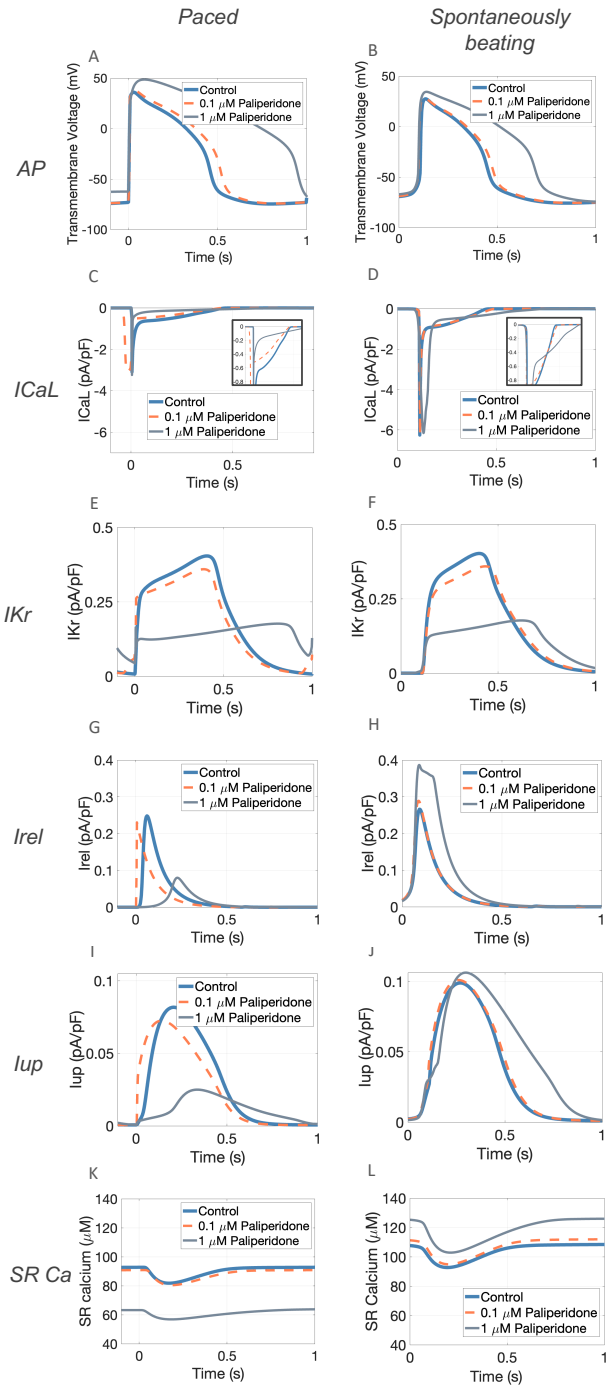


Figure 6.5: Paliperidone-induced changes are dependent on the cell beating rate. **A.** Paliperidone-induced action potential changes in paced cell. **B.** Paliperidone-induced action potential changes in spontaneously beating cell. **C.** ICaL changes following paliperidone application in paced cell. **D.** ICaL changes following paliperidone application in spontaneously beating cell. **E.** IKr current changes following paliperidone application in paced cell. **F.** IKr current changes following paliperidone application in spontaneously beating cell. **G.** Irel current changes following paliperidone application in paced cell. **H.** Irel current changes following paliperidone application in spontaneously beating cell. **I.** Iup current changes following paliperidone application in paced cell. **J.** Iup current changes following paliperidone application in spontaneously beating cell. **K.** SR calcium loading changes following paliperidone application in paced cell. **L.** SR calcium loading changes following paliperidone application in spontaneously beating cell.

To verify the above mechanisms, it was tested whether slower pacing with paliperidone would lead to similar inotropic effects as observed in the spontaneous mode. Upon prolonging the cycle length, it was observed that the negative inotropic effects of paliperidone were no longer present (Fig. 6.6 A, B, C).

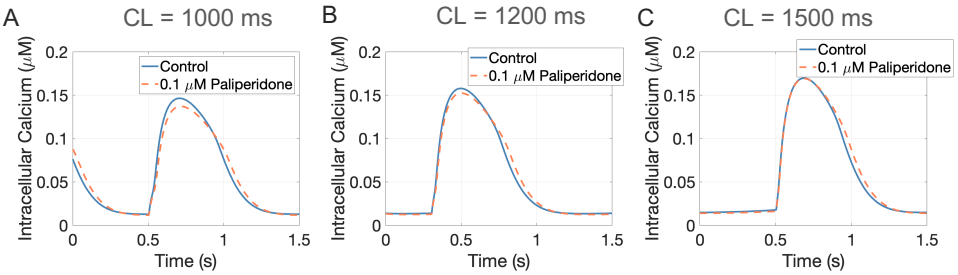


Figure 6.6: The effects of paliperidone are beating rate-dependent. Here CL - cycle length. **A.** Paliperidone induces a reduction in calcium transient peak in cell paced at 1 Hz. **B.** Paliperidone induces a reduction in calcium transient peak in cell paced at 50 beats per minute. The reduction in calcium transient amplitude is less pronounced than in cell paced at 60 beats per minute. **C.** Paliperidone does not induce a reduction in calcium transient peak in cell paced at 40 beats per minute unlike in cells paced at 60 beats per minute (panel A).

In summary, the simulations show that the differences in paliperidone-induced inotropic effects between the spontaneously-beating and paced cells arise from their differences in ICaL availability. Altogether, this demonstrates that the model enables mechanistic investigations of drug-induced signalling. In this case, simulations demonstrate that the drug effects on calcium dynamics and contractility are beating rate dependent.

6.4 Discussion

This study describes the experimental evaluation of an electromechanical hiPSC-CM model. The results demonstrate the utility of the model in simulating the contractile properties of hiPSC-CMs. The key findings described in this chapter are:

1. the hiPSC-CM electromechanical model simulates drug-induced inotropic effects, showing good qualitative agreement with experimental data.

2. the simulations identify previously unknown drug effects, which were later confirmed experimentally.

3. mechanistic insights from the model reveal that paliperidone-induced effects are linked to calcium handling processes, with key differences observed between paced and non-paced cells.

This study highlights that the electromechanical model accurately simulates drug-induced inotropic effects providing validity to the model. The good qualitative agreement with experimental data suggests that the model effectively represents the pathways that regulate myofilament activation and force production.

The simulation results were evaluated by comparing drug-induced changes in calcium transient duration and peak force *in silico* with experimental hiPSC-CM data, showing good agreement. By integrating *in silico* results with *in vitro* data, the model provides a mechanistic understanding of hiPSC-CM behaviour under pharmacological interventions together with a framework that can be continuously refined through iterative simulations and experimental data. The integrated approach enables novel insights into the mechanisms driving drug-induced inotropic effects, thus advancing beyond the limitations of standard drug screening models

Using a pore block model that inputs only IC50s and Hill coefficients, the electromechanical model successfully predicted the drug responses of seven reference compounds, showing good qualitative agreement with experimental data. This highlights the model's effectiveness in simulating drug responses despite minimal input, addressing a critical challenge in pharmacological modelling.

Model performance is comparable to that of adult cardiomyocyte models [154]. Before this study, extensive pharmacological studies were not carried out using hiPSC-CM electromechanical models. Previously established electrophysiology hiPSC-CM models have been evaluated against experimental data following drug application, showing good agreement with experimental hiPSC-CM data in most cases [160].

For the integration of the hybrid *in vitro-in silico* system, the model predictions of drug action for compounds with unknown effects on calcium were tested. Notably, the model successfully predicted calcium transient changes for duloxetine and paliperidone. Experimental verification confirmed *in silico* predictions qualitatively, highlighting the model's capacity to bridge gaps in our understanding despite the quantitative discrepancies, which are expected due to parameter variability and differences in experimental setups. This successful prediction illustrates the model's capacity to fill critical knowledge gaps in drug-cardiomyocyte interactions, offering a powerful tool for early-phase drug safety assessment.

There are several experimental and clinical reports detailing rate-dependent drug effects. For instance, studies have shown that class 1c antiarrhythmic drug flecainide increases atrial action potential duration to a greater extent at faster heart rates [250]. Flecainide's sodium channel-blocking effect becomes more pronounced with faster heart rates, leading to greater suppression of arrhythmias. However, this rate dependency can also increase the risk of pro-arrhythmic effects, especially in patients with structural heart disease.

The hiPSC-CM electromechanical model (iCEM) is capable of simulating rate-dependent effects, which is critical for accurate drug safety assessments. The study demonstrates that paliperidone has distinct effects in paced and spontaneously beating cells. Specifically, it was shown that the decrease in inotropic response in paced cells, which was not observed in spontaneously beating cells, likely results from paliperidone-induced effects on L-type calcium current. It could be that the increased ICaL availability results in greater calcium content in the cell. This could lead to increased inotropy and a higher calcium transient peak in spontaneously beating cells,

but not in paced cells. This rate-dependent behaviour highlights the importance of considering pacing conditions when evaluating drug effects on contractile function.

Currently, the contractile effects of duloxetine and paliperidone in human cardiac cells are unknown. Testing these effects and understanding the underlying mechanisms is important, especially given the wide prescription of duloxetine, one of the first-line antidepressants used globally, and its designation as a drug against hot flushes [251] and menopause-related symptoms [252]. This is the first time the inotropic effects of duloxetine and paliperidone have been established *in silico* in hiPSC-CMs and validated with a new calcium experimental dataset. Understanding these drugs' inotropic effects could lead to safer prescribing practices and potentially guide the development of new therapeutic strategies.

The hiPSC-CM electromechanical model provides a more comprehensive assessment of drug effects than purely electrophysiological models [160]. Additionally, unlike previous studies with adult cardiomyocytes, the model enables hiPSC-CM-specific simulations, which are increasingly relevant in personalised medicine and early drug testing [154]. Studies by Li et al. (2020) and Ovics et al. (2020) [253, 254] focus on hiPSC-CM for drug screening, highlighting the relevance of this work. Compared to these studies, the presented *in silico* approach, with the integration of mechanical responses, offers an advancement in understanding drug-cardiomyocyte interactions, addressing a critical gap in current hiPSC-CM research.

Furthermore, the model framework extends the capabilities of testing drug activity in the lab by offering simulations of inotropy, action potential, and ionic currents in a quick, accurate, and user-friendly manner. Achieving similar results through traditional wet-lab methods would require significantly more time, labour, and cost. The model's capabilities not only reinforce the value of integrating electromechanical aspects into hiPSC-CM drug testing frameworks but also facilitates easier and more efficient validation of *in silico* predictions through subsequent wet-lab experiments. This streamlined process supports the broader application of the model framework in drug discovery and safety pharmacology.

6.4.1 Limitations

The framework provides a new important approach for mechanistic signalling investigations in cardiomyocytes, but it is not without limitations. Further refinement is necessary to enhance the accuracy of simulating responses for positive inotropes, which will depend on acquiring more detailed experimental data on drug-specific mechanisms and kinetic contraction data.

Refinement could include modelling additional signalling pathways that play an important role in mediating cellular contraction. Another area for improvement is the inclusion of more sophisticated drug-binding kinetics beyond Hill coefficients and IC50s, and detailed pharmacodynamic models to better predict the temporal aspects of drug action, albeit more detailed models may or may not have better performance depending on the model structure. Additionally, expanding the model to incorporate additional mechanical-electrical feedback mechanisms between electrical activity and mechanical responses could enhance the simulation of complex drug effects. By incorporating these refinements, the hiPSC-CM electromechanical model (iCEM) could achieve greater accuracy and reliability in predicting cardiomyocyte behaviour under various pharmacological interventions.

6.5 Conclusions

In conclusion, this study demonstrates that the hiPSC-CM electromechanical model is a powerful tool that integrates and complements experimental findings. It can serve as a bridge between theoretical simulations and practical applications in cardiac safety and efficacy studies.

The model enhances our understanding of the electromechanical behaviour of hiPSC-CMs under pharmacological interventions. It accurately predicts drug-induced changes in action potentials, calcium transients, and inotropic effects, which are crucial for assessing cardiac drug safety. The model's ability to simulate drug responses using minimal input data highlights its practical utility for early-phase drug screening. This approach could contribute to the development of safer,

more effective therapeutic strategies while enhancing our understanding of the mechanisms regulating force generation.

7 Discussion

In this chapter, the thesis aims outlined in Section 1.6 are revisited and the key findings of the work are discussed in the context of their broader implications.

The primary goal of this thesis was to understand how the regulation of myofilament function is achieved in cardiomyocytes. In greater detail, this thesis aimed to a) assess cAMP signalling at the myofilament; b) characterise the impact of PKA phase separation on myofilament cAMP signalling, and c) develop and validate a model that could integrate and extend the experimental findings for cardiac contractility regulation studies.

The first major finding of this research is the discovery that the sarcomere contains multiple distinct cAMP nanodomains. It was observed that troponin I phosphorylation occurs in a gradient-like manner across the sarcomere. However, this gradient is not static but varies over time. This dynamic control of troponin phosphorylation is likely regulated by the interplay between cAMP-PKA signalling and phosphatases, rather than by cAMP directly following the gradient dynamics. Instead, distinct cAMP signalling domains were identified at the sites of troponin I, myosin-binding protein C, and myomesin. Particularly, PDE4 was found to be essential for controlling cAMP levels specifically at the troponin site, but not at the myosin-binding protein C site.

These findings were made possible by the development of a new FRET sensor specifically targeted to myomesin at the M line of the sarcomere. This novel tool not only advances our understanding of cAMP regulation at the M line—a region of the sarcomere that remains largely uncharacterised—but also holds potential for broad applications in other studies [255]. The differences in cAMP control between troponin I and myosin-binding protein C suggest new therapeutic strategies, particularly in disease states such as heart failure where sarcomeric proteins, including troponin I, are hypo-phosphorylated [85]. Disruption of the PDE4-troponin I interaction could selectively modulate cAMP signalling at troponin I without affecting global cAMP levels, offering a targeted approach in conditions where troponin I hypo-phosphorylation occurs. This could have a significant impact, as current treatments do not address the issue of hypo-phosphorylation, and no curative treatments for heart failure currently exist.

The second key finding of this work demonstrates that PKA condensation, hypothesised to buffer cAMP [111], does not affect cAMP signalling following β-adrenergic receptor (βAR) stimulation at the moyfilament, or other cAMP nanodomains, such as the phospholamban domain at the sarcoplasmic reticulum or plasmalemma. Although PKA was found to form condensates in cardiac cells, a novel finding showing puncta-like structures of both RI and RII isoforms, these condensates do not appear to affect cAMP signalling at the myofilament. However, PKA phase separation effects were evident in the cytosol, where disruption of PKA condensation significantly reduced the cAMP response following βAR stimulation. This discovery reveals that PKA condensation is crucial for maximal adrenergic response in the cytosol of cardiomyocytes, a previously unknown aspect of cardiac signalling that this work has identified for the first time.

Additionally, this research identified A-kinase anchoring proteins (AKAPs) as key regulators of PKA phase separation. The peptide HT31, which disrupts PKA-AKAP interactions, emerged as a novel, 1,6-HEX-independent, PKA-specific method to disrupt PKA condensation. Interestingly, the disruption of PKA condensation through PKA-AKAP de-coupling was also found to alter PDE8 activity, leading

to a reduction in cAMP signal transduction in the cytosol following adrenergic stimulation. This was further contextualised by the discovery of an interaction between endogenous PKA RI and PDE8, supporting the concept of a channelling effect where PDE8 efficiently removes cAMP in proximity to PKA RI [74]. This finding uncovers a novel role for PKA liquid-liquid phase separation in regulating PKA-PDE interactions.

These findings have significant implications for our understanding of PKA signalling in both healthy and diseased hearts. In particular, the observation of a significant increase in PKA RIα condensates in hypertrophic myocytes suggests a potential role for PKA condensation in disease states. Further investigation is required to determine whether this increase in PKA condensates is an adaptive response or a factor that drives pathogenicity. Future research should also focus on replicating these findings in more physiologically relevant *in vivo* models to better understand the impact of PKA condensation on myofilament cAMP signalling in hypertrophy and other cardiac pathologies.

The third key achievement of this research is the development of a new hiPSC-CM electromechanical model capable of replicating key features of hiPSC-CM action potentials, calcium transients, and contraction. The hiPSC-CM electromechanical model (iCEM) was developed by integrating hiPSC-CM electrophysiology with an adult cardiomyocyte contractile model [160, 168]. This model was created based on a defined set of calibration criteria and subsequently experimentally evaluated.

The morphology of simulated action potentials, calcium transients, and active tension aligns well with experimental data from various hiPSC-CM studies. Further validation of the model confirms its ability to accurately simulate the effects of drug-induced calcium transient changes and active tension modulation. Replicating both positive and negative inotropic drug effects, the model proves valuable for simulating and investigating the mechanisms by which drugs affect contraction generation in cardiomyocytes. As a result, it holds promise for use in drug safety testing.

A key attribute of a model is its predictive power, and validation using data not involved in the calibration process is crucial for establishing credibility [244].

The fact that hiPSC-CM electromechanical model (iCEM) accurately reproduces a wide range of behaviours consistent with experimental findings, despite not being explicitly optimised for these scenarios, shows its robustness and gives further credibility. Furthermore, the simulations with the model contributed novel insights, such as the observation of previously unknown rate-dependent drug effects.

Using the model, inotropic effects of paliperidone and duloxetine were simulated and subsequently validated through calcium imaging experiments. Notably, the model revealed that paliperidone's inotropic effects are dependent on the beating rate, with L-type calcium channel activity playing a central role. This mechanistic insight enhances our understanding of how these drugs regulate contraction. Such findings are essential for assessing the clinical implications of drug-mediated cardiac function, especially under varying heart rates and exercise conditions, which may influence therapeutic efficacy and safety.

These findings underscore the utility of the modelling and simulation in uncovering the mechanisms of the drug action. These discoveries were made possible by the hiPSC-CM electromechanical model, which is expected to have broad utility due to its user-friendly design. It is a valuable tool for developing integrated *in silico-in vitro* platforms. These platforms align with the goals of the Comprehensive In Vitro Proarrhythmia Assay (CiPA) initiative, aimed at improving clinical trial design and drug toxicity testing in the pharmaceutical industry [243].

Looking forward, several avenues for future research emerge from these findings. First, further studies should focus on validating the role of PDE4-troponin I interactions in cAMP compartmentalisation using more physiologically relevant *in vivo* models. For example, genetically modified mouse models, such as PDE4 knockout mice or transgenic mice expressing PDE4-targeting biosensors, could provide insights into how PDE4 regulates cAMP dynamics and troponin I function under normal and hypertrophic conditions. Additionally, pressure overload models like transverse aortic constriction (TAC) can simulate pathological stress to evaluate PDE4-troponin I interactions during disease progression. Other relevant models would include those that develop diastolic dysfunction, such as animal models of

HFpEF. This could help determine the therapeutic potential of targeting these interactions in disease states like heart failure. Additionally, the mechanisms underlying PKA condensation and its selective impact on cytosolic versus myofilament cAMP signalling warrant deeper exploration. Future studies should also investigate whether the observed increase in PKA RIα condensates in hypertrophic myocytes is an adaptive or pathogenic response. Also, investigating PKA condensation in adult cardiomyocytes as well as human cardiomyocytes would be useful for better understanding the translational potential of the results. Moreover, extending the computational modelling work to include the modelling of additional signalling pathways could aid in the prediction of potential drug side effects in clinical settings, and extend the current understanding of intracellular signalling pathways, and their effect on myofilament function control. Finally, expanding the application of the hiPSC-CM electromechanical model to cardiac disease modelling and integrating it with patient-specific data could enhance its utility in precision medicine, enabling more tailored and effective therapeutic strategies.

8 Conclusions

Taken together, findings outlined in this thesis significantly advance the understanding of cAMP signalling compartmentalisation and its impact on cardiac function. The research outlined in the thesis demonstrates that cAMP signalling is highly localised within cardiomyocytes, with distinct nanodomains at the sarcomere, such as those at troponin I and myosin-binding protein C. The critical role of PDE4 in regulating cAMP levels specifically at troponin I, without affecting other regions like myosin-binding protein C, highlights the intricate and precise nature of cAMP signalling. This compartmentalised control offers new therapeutic possibilities, particularly in conditions such as heart failure, where selective modulation of cAMP at TNI could correct hypo-phosphorylation without disrupting global cAMP dynamics.

Furthermore, the work has revealed the crucial role of PKA condensation in modulating cAMP signalling within the cytosol, while notably not affecting cAMP levels at the myofilament. This finding challenges the previously held notion that PKA condensates universally buffer cAMP across all cellular domains. Instead, the findings outlined in the thesis show that PKA phase separation plays a significant role in enhancing adrenergic responses in the cytosol, with AKAPs being key regulators of this process. The discovery that PKA-AKAP interaction disruption leads to PDE8 activation and alters cAMP signalling further underscores the complexity of these regulatory mechanisms.

In addition to these experimental findings, the computational modelling and simulation provided critical insights into the effects of drug-induced modulation of cardiac function. The use of the hiPSC-CM electromechanical model enabled the simulations with a subsequent confirmation of previously uncharacterised inotropic effects of clinically used drugs, such as paliperidone and duloxetine. The simulations revealed that drug effects on cardiac contraction are highly dependent on the beating rate. The integration of computational modelling and simulation with experimental validation underscores the value of *in silico* approaches in uncovering novel drug effects and understanding their action mechanisms.

In summary, the integration of these experimental and computational findings provides a comprehensive view of how endogenous (cAMP compartmentalisation and PKA condensation), and exogenous (drug-induced) modulation collectively shape cardiac signalling and function. This work not only contributes to the fundamental understanding of cardiac biology but also opens up new avenues for therapeutic intervention aimed at modulating specific aspects of cAMP signalling and cardiac function in disease contexts.

Appendices

A
Appendix

A.1 cAMP signalling at the myofilament

Specificity of the antibodies used for ARVM staining and expansion microscopy in Chapter 3 was tested showing no non-specific binding of the secondary antibody (Fig. A.1).

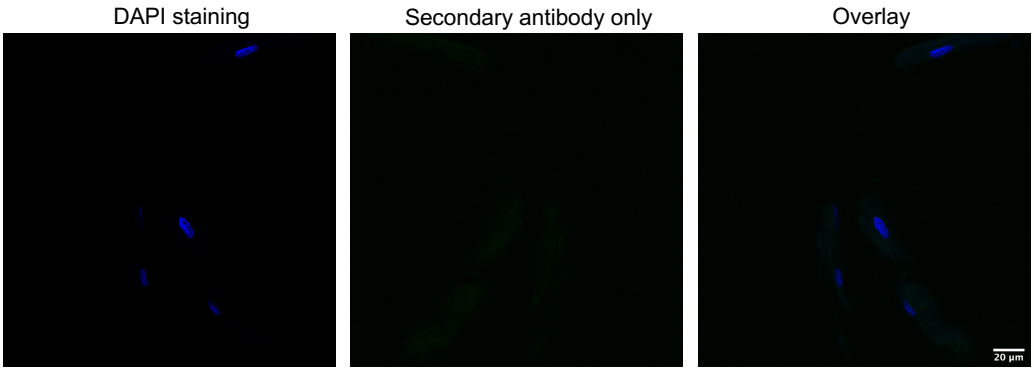


Figure A.1: Secondary antibody staining control. Scale bar: 20 µm. Negative controls constituted ARVMs labeled with DAPI stain and the secondary antibody only, in the absence of primary antibodies.

A.2 PKA phase separation

A.2.1 Endogenous PKA RIα phase separation

Endogenous PKA RIα condensation was examined in HEK293T-RI cell line, as described before [111]. The transfection of the cell line was not successful despite multiple optimisations to the transfection protocol (Fig. A.2 A, B).

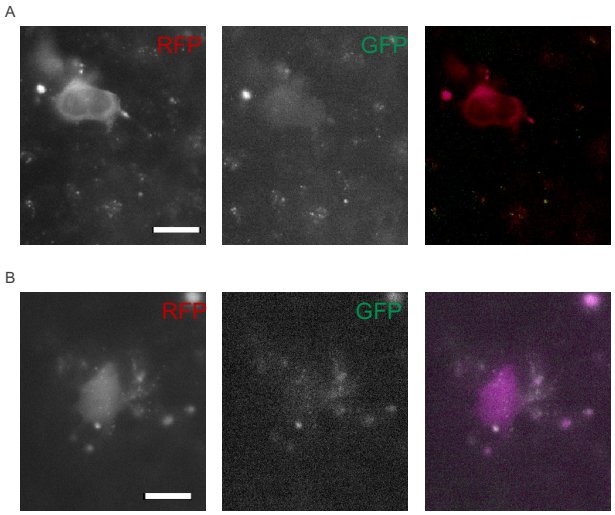


Figure A.2: HEK293T-RI cells transfected with FlouSTEP sensors. Scale bar: 20 µm. **A.** From left to right: a representative FluoSTEP AKAR-RFP, endogenous PKA RIα-GFP, and composite image (AKAR in pink, RI in green) of HEK293T-RI cells transfected with FluoSTEP AKAR sensor. **B.** From left to right: a representative FluoSTEP ICUE-RFP, endogenous PKA RIα-GFP, and composite image (ICUE in pink, RI in cyan) of HEK293T-RI cells transfected with FluoSTEP ICUE sensor.

A.2.2 PDE8 localises at the membrane in HEK293T cells

PKA RIα and PDE8 localisation was examined in HEK293T cells (Fig. A.3 A). In addition, the effects of PDE8-RFP expression and stearated HT31 peptide application on PKA puncta were examined (Fig. A.3 B, C).

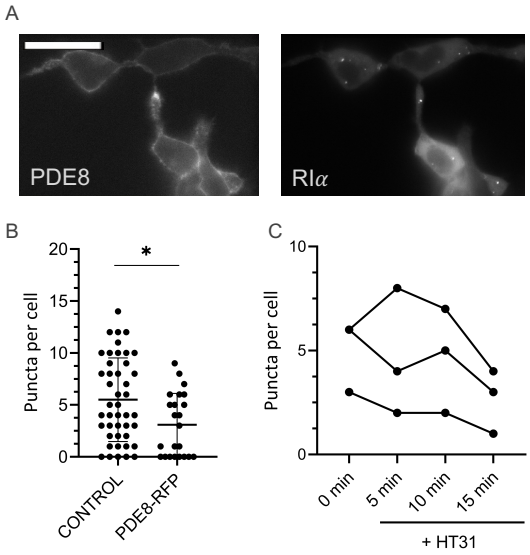


Figure A.3: HEK293T cells expressing PDE8-RFP and PKA RIα-GFP. **A.** A representative image of living HEK293T cells expressing PDE8-RFP (left) and PKA RIα-GFP (right). Scale bar: 20 µm. **B.** The number of PKA RIα puncta is lower in cells co-expressing PDE8-RFP (n=24) than in cells expressing PKA RIα-GFP only (n=44). Wilcoxon signed-rank test, p=0.02. **C.** The number of PKA RIα puncta is reduced by the application 10 µM of stearated HT31 within 15 min.

B
Appendix

B.1 IC50 and Hill coefficients for *in silico* drug trials

IC50 and Hill coefficient (h) values were used as inputs for the *in silico* drug trials. For each compound, the EFTPCmax is also included. Data come from different sources, and all the references are listed bellow. The table bellow also includes experimental and/or clinical data available regarding the inotropic response induced by the compound. Finally, the table summarises the information available from hiPSC-CM experimental studies. The data sources are outline bellow.

Table B.1: IC50 and Hill coefficient (h) values used as inputs for the in silico drug trials. Here * refers to the IC50 concentration which was not reached in the experiments, and therefore an estimate was computed from the percentage of block at the maximum tested concentration, with h equal to 1.

Data extended from Passini et al. (2017) & Tomek et al. (2019)										**Experimental data**	
			IC50 (Hill coeficient)								
Compound List	**Description**	**EFTPC max (µM)**	**I_{Na}**	**I_{Kr}**	**I_{CaL}**	**I_{NaL}**	**I_{Ks}**	**I_{to}**	**I_{K1}**	**Inotropic effect (clinical & experimental data)**	**hiPSC-CM force amplitude**
Amiodarone I	Antiarrhythmic class III	0.155	15.9 (0.97)	0.86 (1.09)	1.9 (0.69)					negative	unknown
Amiodarone II	Antiarrhythmic class III	0.155	4.577 (0.7)	0.941 (0.6)	1.281 (0.6)	9.423 (0.4)		3.758 (0.4)		negative	unknown
Astemizole	H1-receptor antagonist, an anti-allergic agent	0.0003	3 (1.95)	0.004 (0.78)	1.1 (1.66)					no effect	unknown
$BaCl_2$	Potassium channel blocker	1		257 (1)*					4.5 (1)	positive	increase
Bay-K8644	Calcium channel activator				17.3 (1.25)					positive	increase
Bepridil	Calcium channel blocker	0.035	2.929 (1.2)	0.149 (0.9)	2.808 (0.6)	1.814 (1.4)				negative	decrease
Ceftriaxone	Antibiotic	23.17		445.7 (1)	153.8 (1)					unknown	unknown

Continued on next page

Continued from previous page

Data extended from Passini et al. (2017) & Tomek et al. (2019)										**Experimental data**	
			IC50 (Hill coefficient)								
Compound List	**Description**	**EFTPC max (μM)**	**I_{Na}**	**I_{Kr}**	**I_{CaL}**	**I_{NaL}**	**I_{Ks}**	**I_{to}**	**I_{K1}**	**Inotropic effect (clinical & experimental data)**	**hiPSC-CM force amplitude**
Chloropromazine I	Antipsychotic	0.038		1.5 (1.4)	3.4 (1.73)					negative	unknown
Chloropromazine II	Antipsychotic	0.038		1.118 (0.9)	8.192 (0.8)	4.56 (0.9)		9.27 (0.7)		negative	unknown
Cilostazol	Anticoagulant (antiplatelet)	0.128		13.8 (0.91)	91.2 (1)					positive	unknown
Cisapride I	Gastroprokinetic	0.003		0.02 (1.04)	11.8 (1)					negative	decrease
Cisapride II	Gastroprokinetic	0.003		0.012 (1.3)						negative	decrease
Clozapine	Antipsychotic	0.071	15.1 (1.14)	2.3 (0.97)	3.6 (1)					negative	unknown
Dasatinib	Tyrosine kinase inhibitor	0.041	76.3 (1.43)	24.5 (1.16)	81.1 (1)					negative	unknown
Diazepam	Benzodiazepine	0.029	306.4 (1)	53.2 (1.07)	30.5 (0.89)					positive	unknown
Diltiazem	Calcium channel blocker	0.1275	22.4 (1.29)	13.2 (1.16)	0.76 (1.14)					negative	decrease

Continued on next page

Continued from previous page

Data extended from Passini et al. (2017) & Tomek et al. (2019)										**Experimental data**	
			IC50 (Hill coefficient)								
Compound List	**Description**	**EFTPC max (µM)**	**I_{Na}**	**I_{Kr}**	**I_{CaL}**	**I_{NaL}**	**I_{Ks}**	**I_{to}**	**I_{K1}**	**Inotropic effect (clinical & experimental data)**	**hiPSC-CM force amplitude**
Disopyramide	Antiarrhythmic class Ia	0.742	168.4 (1.09)	14.4 (0.91)	1036.7 (1)					negative	unknown
Dofetilide I	Antiarrhythmic class III	0.0021	31.9 (0.54)	0.013 (1.56)	201 (1)*		135 (1)*	300 (1)*		no effect	decrease
Dofetilide II	Antiarrhythmic class III	0.0021	162.1 (1)	0.03 (1.2)	26.7 (1)					no effect	decrease
Dofetilide III	Antiarrhythmic class III	0.0021		0.001 (0.6)						no effect	decrease
Donepezil	Acetylcholinesterase inhibitor	0.007	38.5 (1)	0.7 (0.98)	34.3 (0.83)					negative	unknown
Droperidol	Butyrophenone antipsychotic drug	0.016	22.7 (1.24)	0.06 (1.1)	7.6 (1.16)					negative	unknown
Duloxetine	Serotonin-norepinephrine reuptake inhibitor	0.016	5.1 (1.66)	3.8 (1.39)	2.8 (1.41)					unknown	unknown

Continued on next page

Continued from previous page

Data extended from Passini et al. (2017) & Tomek et al. (2019)										**Experimental data**	
			IC50 (Hill coefficient)								
Compound List	**Description**	**EFTPC max (μM)**	**I_{Na}**	**I_{Kr}**	**I_{CaL}**	**I_{NaL}**	**I_{Ks}**	**I_{to}**	**I_{K1}**	**Inotropic effect (clinical & experimental data)**	**hiPSC-CM force amplitude**
Flecainide I	Antiarrhythmic class Ic	0.752	3.19 (0.71)	1.64 (0.81)	27.1 (0.97)					negative	decrease
Flecainide II	Antiarrhythmic class Ic	0.752	6.2 (1.14)	1.5 (0.88)	27.1 (0.97)					negative	decrease
Flecainide III	Antiarrhythmic class Ic	0.752	6.677 (1.9)	0.692 (0.8)	25.599 (1.4)	18.87 (0.6)		9.266 (0.7)		negative	decrease
Halofantrine	Antimalarial	0.172	331.2 (1)	0.38 (1.31)	1.9 (0.99)					unknown	unknown
Haloperidol	Antipsychotic	0.004	4.3 (1.58)	0.04 (1.18)	1.3 (1.38)					negative	decrease
HMR 1556	IKs channel blocker						90 (1)*			no effect	no effect
Ibutilide	Antiarrhythmic class III	0.14	42.5 (1.03)	0.018 (1.53)	62.5 (1.16)					negative	unknown
Lamivudine	Nucleoside reverse transcriptase inhibitor	19.54	1571.4 (1)	2054 (1)	54.2 (0.89)					unknown	unknown

Continued on next page

Continued from previous page

Data extended from Passini et al. (2017) & Tomek et al. (2019)										**Experimental data**	
			IC50 (Hill coefficient)								
Compound List	**Description**	**EFTPC max (µM)**	**I_{Na}**	**I_{Kr}**	**I_{CaL}**	**I_{NaL}**	**I_{Ks}**	**I_{to}**	**I_{K1}**	**Inotropic effect (clinical & experimental data)**	**hiPSC-CM force amplitude**
Lidocaine I	Antiarrhythmic class Ib	2.6	44 (0.94)	300 (1)*						negative	decrease
Lidocaine II	Antiarrhythmic class Ib		44 (0.94)	300 (1)*		10.79 (1.3)				negative	decrease
Linezolid	Antibiotic	59.11	2644.5 (1)	1147.2 (1)	105.4 (0.94)					unknown	unknown
Loratadine	H1-antihistamine	0.0004	28.9 (1.64)	6.1 (1.44)	11.4 (1.38)					no effect	unknown
Metronidazole	Antibiotic	187	2073.2 (1)	1340.2 (1)	177.9 (0.66)					negative	unknown
Mexiletine I	Antiarrhythmic class Ib	2.5	49.7 (0.94)	69.4 (1.11)	203 (0.75)		32.6 (0.92)	367 (0.91)		negative	unknown
Mexiletine II	Antiarrhythmic class Ib	2.5	49.7 (0.94)	69.4 (1.11)	203 (0.75)	8.957 (1.4)	32.6 (0.92)	367 (0.91)		negative	unknown
Mibefradil I	Calcium channel blocker	0.012	5.6 (1.53)	1.7 (1.38)	0.51 (1.44)					negative	unknown
Mibefradil II	Calcium channel blocker	0.012	5.866 (1)	0.307 (0.9)	0.652 (1.1)	3.628 (1.2)				negative	unknown

Continued on next page

Continued from previous page

Data extended from Passini et al. (2017) & Tomek et al. (2019)										**Experimental data**	
			IC50 (Hill coefficient)								
Compound List	**Description**	**EFTPC max (μM)**	**I_{Na}**	**I_{Kr}**	**I_{CaL}**	**I_{NaL}**	**I_{Ks}**	**I_{to}**	**I_{K1}**	**Inotropic effect (clinical & experimental data)**	**hiPSC-CM force amplitude**
Mitoxantrone	Antineoplastic	0.225	93.5 (1.05)	539.4 (1)	22.5 (0.64)					positive	unknown
Moxifloxacin I	Antibiotic	10.96	1563 (1)*	79 (1)	173 (1)					no effect	unknown
Moxifloxacin II	Antibiotic	10.96	1112 (1)	86.2 (0.94)	173 (1)					no effect	unknown
Moxifloxacin III	Antibiotic	10.96		93.041 (0.6)		382.34 (1.1)	50.321 (1)			no effect	unknown
Nifedipine	Calcium channel blocker	0.008	88.5 (0.71)	44 (0.8)	0.012 (1.02)					negative	decrease
Nilotinib I	Tyrosine kinase inhibitor	0.172	13.3 (2.11)	1 (0.96)	17.5 (1)					negative	unknown
Nilotinib II	Tyrosine kinase inhibitor	0.172		0.091 (0.8)		4.706 (1.9)				negative	unknown
Nimodipine	Calcium channel blocker	0.001		45.6 (1)*	0.139 (0.63)					negative	unknown
Nisoldipine	Calcium channel blocker	0.0001	45 (0.72)	49.3 (0.84)	0.009 (0.71)	61.7 (0.71)	52.8 (1.03)			negative	unknown

Continued on next page

Continued from previous page

Data extended from Passini et al. (2017) & Tomek et al. (2019)										**Experimental data**	
			IC50 (Hill coefficient)								
Compound List	**Description**	**EFTPC max (µM)**	**I_{Na}**	**I_{Kr}**	**I_{CaL}**	**I_{NaL}**	**I_{Ks}**	**I_{to}**	**I_{K1}**	**Inotropic effect (clinical & experimental data)**	**hiPSC-CM force amplitude**
Nitrendipine	Calcium channel blocker	0.003	21.6 (1.25)	24.6 (0.82)	0.025 (0.78)					negative	unknown
Paliperidone	Antipsychotic	0.069	109 (1.33)	0.78 (1.01)	193.9 (1)					unknown	unknown
Paroxetine	Selective serotonin reuptake inhibitor	0.014	9.8 (1.34)	1.9 (1.26)	3.9 (1.39)					positive	unknown
Pentobarbital	Barbiturate	5.171	2686 (1)	1433.9 (1)	299 (1.38)					negative	unknown
Phenytoin	Anticonvulsant	4.36	72.4 (1.06)	147 (1)	21.9 (0.99)					negative	unknown
Pimozide	Antipsychotic	0.0005	1.1 (1.05)	0.04 (1.16)	0.24 (1.49)					unknown	unknown
Piperacillin	Antibiotic	114	2433.8 (1)	3405.1 (1)	1226 (1)					unknown	unknown
Primidone	Anticonvulsant	20.6	640 (1)*	3360 (1)*						unknown	unknown

Continued on next page

Continued from previous page

Data extended from Passini et al. (2017) & Tomek et al. (2019)										**Experimental data**	
			IC50 (Hill coefficient)								
Compound List	**Description**	**EFTPC max (μM)**	**I_{Na}**	**I_{Kr}**	**I_{CaL}**	**I_{NaL}**	**I_{Ks}**	**I_{to}**	**I_{K1}**	**Inotropic effect (clinical & experimental data)**	**hiPSC-CM force amplitude**
Procainamide	Antiarrhythmic class Ia	54.18	746.6 (1)	272.4 (1)	389.5 (0.83)					negative	unknown
Quinidine	Antiarrhythmic class Ia	3.237	14.6 (1.22)	0.72 (1.06)	6.4 (0.68)					negative	decrease
Quinidine	Antiarrhythmic class Ia	3.237		0.343 (1)		4.899 (1.4)	3.487 (1.3)			negative	decrease
Raltegravir	Antiretroviral	7	824.2 (1)	782.8 (1)	246.7 (1)					unknown	unknown
Ranolazine	Antianginal	1.95	30.2 (0.8)	10.9 (0.9)	172 (0.6)	5.9 (1)				negative	increase
Ranolazine	Antianginal	1.95		6.49 (0.8)		7.887 (0.9)				negative	increase
Ribavirin	Antiviral	27.88	2997.5 (1)	967 (1)	622.5 (1)					unknown	unknown
Risperidone	Antipsychotic	0.002	43.3 (0.98)	0.26 (0.99)	34.2 (0.79)					positive	unknown
Saquinavir I	Antiretroviral	0.4172	12.1 (2.34)	16.9 (1.72)	1.9 (1.15)					unknown	unknown

Continued on next page

Continued from previous page

Data extended from Passini et al. (2017) & Tomek et al. (2019)										**Experimental data**	
			IC50 (Hill coefficient)								
Compound List	**Description**	**EFTPC max (μM)**	**I_{Na}**	**I_{Kr}**	**I_{CaL}**	**I_{NaL}**	**I_{Ks}**	**I_{to}**	**I_{K1}**	**Inotropic effect (clinical & experimental data)**	**hiPSC-CM force amplitude**
Saquinavir II	Antiretroviral	0.4172	15.568 (1.2)	3.477 (1)	3.161 (1.4)	7.088 (1.2)				unknown	unknown
Sertindole I	Antipsychotic	0.002	6.9 (1.19)	0.033 (1.25)	6.3 (1.29)					unknown	unknown
Sertindole II	Antipsychotic	0.002	0.011 (0.8)							unknown	unknown
Sitagliptin	Antidiabetic	0.442	1220.8 (1)	174.7 (1)	147.1 (1)					no effect	unknown
Solifenacin	Antimuscarinic	0.003	1.5 (1.32)	0.28 (0.9)	4.3 (1.47)					negative	unknown
Sotalol I	Antiarrhythmic Class III, beta blocker	14.69	7013.9 (1)	111.4 (0.73)	193.3 (1)					negative	decrease
Sotalol II	Antiarrhythmic Class III, beta blocker	14.69		86.369 (0.9)						negative	decrease
Sparfloxacin I	Antibiotic	1.766	1465 (1)*	17.7 (0.99)	88.8 (1)					unknown	unknown

Continued on next page

Continued from previous page

Data extended from Passini et al. (2017) & Tomek et al. (2019)										**Experimental data**	
			IC50 (Hill coefficient)								
Compound List	**Description**	**EFTPC max (μM)**	**I_{Na}**	**I_{Kr}**	**I_{CaL}**	**I_{NaL}**	**I_{Ks}**	**I_{to}**	**I_{K1}**	**Inotropic effect (clinical & experimental data)**	**hiPSC-CM force amplitude**
Sparfloxacin II	Antibiotic	1.766	2555 (1)	22.1 (0.93)	88.8 (1)					unknown	unknown
Sunitinib	Tyrosine kinase inhibitor	0.013	16.5 (1.22)	1.2 (1)	33.4 (1.09)					negative	unknown
Telbivudine	Antiviral	19.72	1095.2 (1)	422.7 (1)	713.9 (1)					unknown	unknown
Terfenadine I	Antihistamine	0.009	2 (1.81)	0.05 (1.15)	0.93 (1.8)					negative	unknown
Terfenadine II	Antihistamine	0.009		0.019 (0.6)	0.7 (0.7)					negative	unknown
Terodiline	Potassium channel blocker	0.145	7.4 (1.23)	0.65 (1.02)	4.8 (1.01)					negative	unknown
Thioridazine	Antipsychotic	0.98	1.4 (1.11)	0.5 (0.98)	3.5 (1.35)					negative	unknown
Verapamil I	Antiarrhythmic class IV	0.088	32.5 (1.33)	0.25 (0.89)	0.2 (0.8)					negative	unknown
Verapamil II	Antiarrhythmic class IV	0.088	7.2 (0.95)	0.83 (1.17)	0.1 (0.7)	6.1 (1.24)	65.6 (0.92)		9.03 (1)	negative	unknown

Continued on next page

Continued from previous page

Data extended from Passini et al. (2017) & Tomek et al. (2019)										**Experimental data**	
			IC50 (Hill coefficient)								
Compound List	**Description**	**EFTPC max (µM)**	**I_{Na}**	**I_{Kr}**	**I_{CaL}**	**I_{NaL}**	**I_{Ks}**	**I_{to}**	**I_{K1}**	**Inotropic effect (clinical & experimental data)**	**hiPSC-CM force amplitude**
Verapamil III	Antiarrhythmic class IV	0.088		0.499 (1.1)	0.202 (1.1)					negative	unknown
Voriconazole	Antifungal	7.563	1550.5 (1)	490.9 (1)	414.2 (1)					unknown	decrease

References

1. Kramer, J. et al. MICE models: superior to the HERG model in predicting Torsade de Pointes. Sci. Rep. 3, 2100 (2013).

2. Passini et al. Human In Silico Drug Trials Demonstrate Higher Accuracy than Animal Models in Predicting Clinical Pro-Arrhythmic Cardiotoxicity. Front. Physiol. 8, September (2017).

3. Crumb, W. J., Vicente, J., Johannesen, L. and Strauss, D. G. An evaluation of 30 clinical drugs against the comprehensive in vitro Proarrhythmia assay proposed ion channel panel. J. Pharmacol. Toxicol. Methods 81, 251–262 (2016).

4. Schram, G., Pourrier, M., Wang, Z., White, M. and Nattel, S. Barium block of Kir2 and human cardiac inward rectifier currents: evidence for subunit-heteromeric contribution to native currents. Cardiovasc. Res. 59, 328–338 (2003).

5. Xu, W. and Lipscombe, D. Neuronal Ca(V)1.3alpha(1) L-Type Channels Activate at Relatively Hyperpolarized Membrane Potentials and Are Incompletely Inhibited by Dihydropyridines. J. Neurosci. 21, 5944–5951 (2001).

6. Antzelevitch, C. et al. Electrophysiological effects of ranolazine, a novel antianginal agent with antiarrhythmic properties. Circulation 110, 904–910 (2004).

7. Obejero-Paz, C. A. et al. Quantitative Profiling of the Effects of Vanoxerine on Human Cardiac Ion Channels and its Application to Cardiac Risk. Sci. Rep. 5, 17623 (2015).

8. Giardina M. et al. Amiodarone: Clinical uses. In: UpToDate, Dardas (Ed), Wolters Kluwer. (2023)

9. Sugiyama, A. et al. Effects of Nonsedating Antihistamine, Astemizole, on thein SituCanine Heart Assessed by Cardiohemodynamic and Monophasic Action Potential Monitoring. Toxicology and Applied Pharmacology, vol. 143, no. 1. Elsevier BV, pp. 89–95 (1997).

10. Paci, M. et al. All-Optical Electrophysiology Refines Populations of In Silico Human iPSC-CMs for Drug Evaluation. Biophysical Journal, vol. 118, no. 10. Elsevier BV, pp. 2596–2611 (2020).

11. Nguyen, N. et al. Adult Human Primary Cardiomyocyte Model for the Simultaneous Prediction of Drug-induced Inotropic and Pro-arrhythmia Risk. AnaBios Corporation. (2022).

12. Ruan, J-L. et al. Mechanical Stress Conditioning and Electrical Stimulation Promote Contractility and Force Maturation of Induced Pluripotent Stem Cell-Derived Human Cardiac Tissue. Circulation, vol. 134, no. 20. Ovid Technologies (Wolters Kluwer Health), pp. 1557–1567 (2016)

13. Saleem, U. et al. Force and Calcium Transients Analysis in Human Engineered Heart Tissues Reveals Positive Force-Frequency Relation at Physiological Frequency. Stem Cell Reports, vol. 14, no. 2. Elsevier BV, pp. 312–324 (2020)

14. Blinova, K. et al. International Multisite Study of Human-Induced Pluripotent Stem Cell-Derived Cardiomyocytes for Drug Proarrhythmic Potential Assessment. Cell Reports, vol. 24, no. 13. Elsevier BV, pp. 3582–3592, (2018).

15. Forouzandehmehr, M. et al. A mathematical model of hiPSC cardiomyocytes electromechanics," Physiological Reports, vol. 9, no. 22. Wiley, Nov. (2021).

16. Juriavicius I. Inotropic effect of chlorpromazine on the frog atrium. Fiziol Zh (1978).

17. Schrör, K. The pharmacology of cilostazol," Diabetes, Obesity and Metabolism, vol. 4, no. s2. Wiley, Mar. (2002).

18. Lee, E.K. et al., "Machine Learning of Human Pluripotent Stem Cell-Derived Engineered Cardiac Tissue Contractility for Automated Drug Classification," Stem Cell Reports, vol. 9, no. 5. Elsevier BV, pp. 1560–1572, Nov. (2017).

19. Keller, N. et al. Cardiovascular effects of cisapride and prucalopride on human 5-HT4 receptors in transgenic mice," Naunyn-Schmiedeberg's Archives of Pharmacology, vol. 391, no. 9. Springer Science and Business Media LLC, pp. 975–985, Jun. 09, (2018).

20. Abdel-Wahab, B.A. Clozapine-induced cardiotoxicity in rats: Involvement of tumour necrosis factor alpha, NF- and caspase-3," Toxicology Reports, vol. 1. Elsevier BV, pp. 1213–1223, (2014).

21. Motokawa, T. et al. Comparison of Dasatinib- and Imatinib-Related Cardiotoxic Adverse Events in Japanese Patients With Chronic Myeloid Leukemia and Gastrointestinal Stromal Tumor. Circulation Reports, vol. 4, no. 1. Japanese Circulation Society, pp. 1–8, Jan. 07, (2022).

22. Martinez, E. Diazepam potentiates the positive inotropic effect of isoprenaline in rat ventricle strips: role of cyclic AMP," European Journal of Pharmacology, vol. 282, no. 1–3. Elsevier BV, pp. 169–175, Aug. (1995).

23. Talreja, O. Diltiazem. StatPearls Publishing; PMID: 30422532. (2023).

24. Zeng, H. et al. Resolving the Reversed Rate Effect of Calcium Channel Blockers on Human-Induced Pluripotent Stem Cell-Derived Cardiomyocytes and the Impact on In Vitro Cardiac Safety Evaluation. Toxicological Sciences, vol. 167, no. 2. Oxford University Press (OUP), pp. 573–580, Oct. 26, (2018).

25. Lan, H. et al. Ionic Mechanisms of Disopyramide Prolonging Action Potential Duration in Human-Induced Pluripotent Stem Cell-Derived Cardiomyocytes From a Patient With Short QT Syndrome Type 1. Frontiers in Pharmacology, vol. 11. Frontiers Media SA, Oct. 12, (2020).

26. Blair, C. A. and Pruitt, B. L. Mechanobiology Assays with Applications in Cardiomyocyte Biology and Cardiotoxicity. Advanced Healthcare Materials, vol. 9, no. 8. Wiley, Apr. (2020).

27. Kijlstra, J. D. et al. Integrated Analysis of Contractile Kinetics, Force Generation, and Electrical Activity in Single Human Stem Cell-Derived Cardiomyocytes. Stem Cell Reports, vol. 5, no. 6. Elsevier BV, pp. 1226–1238, Dec. (2015).

28. Page, R. L. et al. Drugs That May Cause or Exacerbate Heart Failure. Circulation, vol. 134, no. 6. Ovid Technologies (Wolters Kluwer Health), Aug. 09 (2016).

29. Shiga, T., Yong, S., Carino, J., Murray, P. A., Damron, D. S. Droperidol Inhibits Intracellular Ca2+, Myofilament Ca2+Sensitivity, and Contraction in Rat Ventricular Myocytes. Anesthesiology, vol. 102, no. 6. Ovid Technologies (Wolters Kluwer Health), pp. 1165–1173, Jun. 01 (2005).

30. Yang, P.-C., Giles, W. R., Belardinelli, L., Clancy, and C. E. Mechanisms of flecainide induced negative inotropy: An in silico study. Journal of Molecular and Cellular Cardiology, vol. 158. Elsevier BV, pp. 26–37, Sep. (2021).

31. Hatip-Al-Khatib, I., Bolukbaşi-Hatip, F. Modulation of the Negative Inotropic Effect of Haloperidol by Drugs with Positive Inotropic Effects in Isolated Rabbit Heart. Pharmacology, vol. 66, no. 1. S. Karger AG, pp. 19–25, (2002).

32. Zhao, Q., Wang, X., Wang, S., Song, Z., Wang, J., Ma, J. Cardiotoxicity evaluation using human embryonic stem cells and induced pluripotent stem cell-derived cardiomyocytes. Stem Cell Research and Therapy, vol. 8, no. 1. Springer Science and Business Media LLC, Mar. 09 (2017).

33. Mannhardt, I. et al. Human Engineered Heart Tissue: Analysis of Contractile Force. Stem Cell Reports, vol. 7, no. 1. Elsevier BV, pp. 29–42, Jul. (2016).

34. Kaufman, L. J., Kofalvi, A. E., Hong, R. A., Moreno-Cabral, C. E., Low, L. L. Cardioversion of atrial fibrillation with ibutilide in an orthotopic heart transplant patient. The Journal of Heart and Lung Transplantation, vol. 18, no. 10. Elsevier BV, pp. 1018–1020, Oct. (1999).

35. Wilson, R. A., Soei, L. K., Bezstarosti, K., Lamers, J. M. J., Verdouw, P. D. Negative inotropy of lidocaine: possible biochemical mechanisms. European Heart Journal. vol. 14, no. 2. Oxford University Press (OUP), pp. 284–289, Feb. 02, (1993).

36. Pousti, A., Malihi, G., Abdollahi, A. The Comparative Effects of Four Antihistamines on Isolated Rat Atria. Iranian Journal of Pharmacology and Therapeutics (ISSN: 1735-2657) Vol 1 Num 2 (2002).

B.2 Simulations of cell activity following duloxetine application in paced cells

Simulations were run in the paced mode (1 Hz) to simulate AP, CaT, and active tension changes induced by duloxetine application (Fig. B.1).

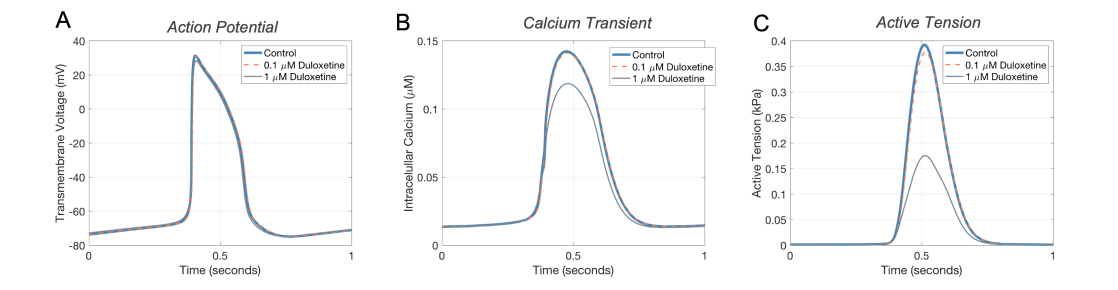


Figure B.1: *In silico*, duloxetine-induced action results in calcium transient shortening and reduction in the calcium transient peak. **A.** *In silico* iCEM simulations in paced mode show a change in action potentials following increasing doses of DXT, duloxetine. **B.** *In silico* iCEM simulations in paced mode show a change in calcium transients following increasing doses of DXT, duloxetine. **C.** *In silico* iCEM simulations in paced mode show a change in active tension following increasing doses of DXT, duloxetine.

Simulations were also run in the paced mode (0.5 Hz) at 20^{o}C for additional comparisons with the experimental dataset for both, paliperidone and duloxetine (Fig. B.2).

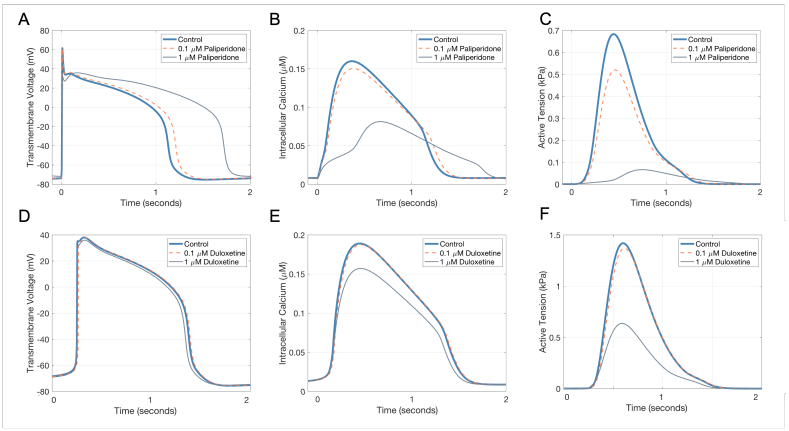


Figure B.2: Simulations predict duloxetine and paliperidone effects at 20^{o}C in paced cells (0.5Hz). **A.** *In silico* iCEM simulations in paced mode show a change in action potentials following increasing doses of peliperidone. **B.** *In silico* iCEM simulations in paced mode show a change in calcium transients following increasing doses of paliperidone. **C.** *In silico* iCEM simulations in paced mode show a change in active tension following increasing doses of paliperidone. **D.** *In silico* iCEM simulations in paced mode show a change in action potentials following increasing doses of duloxetine. **E.** *In silico* iCEM simulations in paced mode show a change in calcium transients following increasing doses of duloxetine. **F.** *In silico* iCEM simulations in paced mode show a change in active tension following increasing doses of duloxetine.

Bibliography

[1] Nuo Sun and Toren Finkel. 'Cardiac mitochondria: A surprise about size'. In: *Journal of Molecular and Cellular Cardiology* 82 (2015), pp. 213–215.

[2] Gina L Galli. 'Design and Physiology of the Heart'. In: *Encyclopedia of Physiology* (2011), pp. 1006–1014.

[3] Thomas G Martin and Jonathan A Kirk. 'Under construction: The dynamic assembly, maintenance, and degradation of the cardiac sarcomere'. In: *Journal of Molecular and Cellular Cardiology* 148 (2020), pp. 89–102.

[4] Claudia Crocini and Michael Gotthardt. 'Cardiac sarcomere mechanics in health and disease'. In: *Biophysical Reviews* 13.5 (2021), pp. 637–652.

[5] Douglas A Rowen, Aaron D Likens and Nick Stergiou. 'Revisiting a classic: Muscles, reflexes, and locomotion by McMahon'. In: *Biomechanics and Gait Analysis* (2020), pp. 149–224.

[6] Samantha K Barrick and Michael J Greenberg. 'Cardiac myosin contraction and mechanotransduction in health and disease'. In: *Journal of Biological Chemistry* 297.5 (2021), p. 101297.

[7] Saffie Mohran, Kristina Kooiker, Max Mahoney-Schaefer, Christian Mandrycky, Kerry Kao, An-Yue Tu, Jeremy Freeman, Farid Moussavi-Harami, Michael Geeves and Michael Regnier. 'The biochemically defined super relaxed state of myosin—A paradox'. In: *Journal of Biological Chemistry* 300.1 (2024), p. 105565.

[8] Lata Govada, Liz Carpenter, Paula C da Fonseca, John R Helliwell, Pierre Rizkallah, Emily Flashman, Naomi E Chayen, Charles Redwood and John M Squire. 'Crystal Structure of the C1 domain of Cardiac Myosin Binding Protein-C: Implications for Hypertrophic Cardiomyopathy'. In: *Journal of Molecular Biology* 378.2 (2008), pp. 387–397.

[9] James W McNamara, Rohit R Singh and Sakthivel Sadayappan. 'Cardiac myosin binding protein-C phosphorylation regulates the super-relaxed state of myosin'. In: *Proceedings of the National Academy of Sciences* 116.24 (2019), pp. 11731–11736.

[10] Alessio V Inchingolo, Samantha Beck Previs, Michael J Previs, David M Warshaw and Neil M Kad. 'Revealing the mechanism of how cardiac myosin-binding protein C N-terminal fragments sensitize thin filaments for myosin binding'. In: *Proceedings of the National Academy of Sciences* 116.14 (2019), pp. 6828–6835.

[11] Ivanka R Sevrieva, Saraswathi Ponnam, Ziqian Yan, Malcolm Irving, Thomas Kampourakis and Yin-Biao Sun. 'Phosphorylation-dependent interactions of myosin-binding protein C and troponin coordinate the myofilament response to protein kinase A'. In: *Journal of Biological Chemistry* 299.1 (2023), p. 102767.

[12] David J Hartshorne and Helmut Mueller. 'Fractionation of troponin into two distinct proteins'. In: *Biochemical and Biophysical Research Communications* 31.5 (1968), pp. 647–653.

[13] Godfrey L Smith and David A Eisner. 'Calcium Buffering in the Heart in Health and Disease'. In: *Circulation* 139.20 (2019), pp. 2358–2371.

[14] David A Eisner, Erwin Neher, Holger Taschenberger and Godfrey L Smith. 'Physiology of intracellular calcium buffering'. In: *Physiological Reviews* 103.4 (2023), pp. 2767–2845.

[15] Kyung Chan Park, David C Gaze, Paul O Collinson and Michael S Marber. 'Cardiac troponins: from myocardial infarction to chronic disease'. In: *Cardiovascular Research* 113.14 (2017), pp. 1708–1718.

[16] Martin M LeWinter and Henk Granzier. 'Cardiac Titin: A Multifunctional Giant'. In: *Circulation* 121.19 (2010), pp. 2137–2145.

[17] Maya Noureddine and Katja Gehmlich. 'Structural and signaling proteins in the Z-disk and their role in cardiomyopathies'. In: *Frontiers in Physiology* 14 (2023).

[18] Ekaterina P Lamber, Pascale Guicheney and Nikos Pinotsis. 'The role of the M-band myomesin proteins in muscle integrity and cardiac disease'. In: *Journal of Biomedical Science* 29.1 (2022).

[19] Janette F Strasburger and Annette Wacker-Gussmann. 'Developmental Electrophysiology in the Fetus and Neonate'. In: *Fetal and Neonatal Physiology* (2017), 522–539.e3.

[20] Saleet M Jafri. 'Models of Excitation–Contraction Coupling in Cardiac Ventricular Myocytes'. In: *Bioinformatics and Drug Discovery* (2012), pp. 309–335.

[21] Hugh E Huxley. 'Sliding filaments and molecular motile systems'. In: *Journal of Biological Chemistry* 265.15 (1990), pp. 8347–8350.

[22] Donald M Bers. 'Cardiac excitation–contraction coupling'. In: *Nature* 415.6868 (2002), pp. 198–205.

[23] Yin-Biao Sun and Malcolm Irving. 'The molecular basis of the steep force–calcium relation in heart muscle'. In: *Journal of Molecular and Cellular Cardiology* 48.5 (2010), pp. 859–865.

[24] Paul J M Wijnker and Jolanda van der Velden. 'Mutation-specific pathology and treatment of hypertrophic cardiomyopathy in patients, mouse models and human engineered heart tissue'. In: *BBA Molecular Basis of Disease* 1866.8 (2020), p. 165774.

[25] Sydney W Patterson and Ernest H Starling. 'On the mechanical factors which determine the output of the ventricles'. In: *Journal of Physiology* 48.5 (1914), pp. 357–379.

[26] Guoxia Liu, Arianne Papa, Alexander N. Katchman, Sergey I. Zakharov, Daniel Roybal, Jessica A. Hennessey, Jared Kushner, Lin Yang, Bi-Xing Chen, Alexander Kushnir, Katerina Dangas, Steven P. Gygi, Geoffrey S. Pitt, Henry M. Colecraft, Manu Ben-Johny, Marian Kalocsay and Steven O. Marx. 'Mechanism of adrenergic CaV1.2 stimulation revealed by proximity proteomics'. In: *Nature* 577.7792 (2020), pp. 695–700.

[27] Gaia Calamera, Lise Román Moltzau, Finn Olav Levy and Kjetil Wessel Andressen. 'Phosphodiesterases and compartmentation of cAMP and cGMP signaling in regulation of cardiac contractility in normal and failing hearts'. en. In: *International Journal of Molecular Sciences* 23.4 (2022), p. 2145.

[28] John S Hayes, Laurence L Brunton and Steven E Mayer. 'Selective activation of particulate cAMP-dependent protein kinase by isoproterenol and prostaglandin E1'. In: *Journal of Biological Chemistry* 255.11 (1980), pp. 5113–5119.

[29] Giulietta Di Benedetto, Anna Zoccarato, Valentina Lissandron, Anna Terrin, Xiang Li, Miles D. Houslay, George S. Baillie and Manuela Zaccolo. 'Protein Kinase A Type I and Type II Define Distinct Intracellular Signaling Compartments'. In: *Circulation Research* 103.8 (2008), pp. 836–844.

[30] Viacheslav O Nikolaev, Moritz Bünemann, Eva Schmitteckert, Martin J Lohse and Stefan Engelhardt. 'Cyclic AMP imaging in adult cardiac myocytes reveals far-reaching beta1-adrenergic but locally confined beta2-adrenergic receptor-mediated signaling'. en. In: *Circulation Research* 99.10 (2006), pp. 1084–1091.

[31] Trudy A Kohout, Hideyuki Takaoka, Patricia H McDonald, Stephen J Perry, Lan Mao, Robert J Lefkowitz and Howard A Rockman. 'Augmentation of Cardiac Contractility Mediated by the Human 3 -Adrenergic Receptor Overexpressed in the Hearts of Transgenic Mice'. In: *Circulation* 104.20 (2001), pp. 2485–2491.

[32] Dagoberto Soto, Vania De Arcangelis, Jin Zhang and Yang Xiang. 'Dynamic protein kinase a activities induced by beta-adrenoceptors dictate signaling propagation for substrate phosphorylation and myocyte contraction'. en. In: *Circulation Research* 104.6 (2009), pp. 770–779.

[33] Milda Folkmanaite and Manuela Zaccolo. 'Regulation of cardiac function by cAMP nanodomains'. en. In: *Bioscience Reports* 43.2 (2023).

[34] Nicoletta C Surdo, Marco Berrera, Andreas Koschinski, Marcella Brescia, Matias R Machado, Carolyn Carr, Peter Wright, Julia Gorelik, Stefano Morotti, Eleonora Grandi, Donald M Bers, Sergio Pantano and Manuela Zaccolo. 'FRET biosensor uncovers cAMP nano-domains at -adrenergic targets that dictate precise tuning of cardiac contractility'. In: *Nature Communications* 8.1 (2017).

[35] Andreas Bock, Paolo Annibale, Charlotte Konrad, Annette Hannawacker, Selma E Anton, Isabella Maiellaro, Ulrike Zabel, Sivaraj Sivaramakrishnan, Martin Falcke and Martin J Lohse. 'Optical Mapping of cAMP Signaling at the Nanometer Scale'. In: *Cell* 182.6 (2020), 1519–1530.e17.

[36] Selma E Anton, Charlotte Kayser, Isabella Maiellaro, Katarina Nemec, Jan Möller, Andreas Koschinski, Manuela Zaccolo, Paolo Annibale, Martin Falcke, Martin J Lohse and Andreas Bock. 'Receptor-associated independent cAMP nanodomains mediate spatiotemporal specificity of GPCR signaling'. en. In: *Cell* 185.7 (2022), 1130–1142.e11.

[37] Ying-Chi Chao, Nicoletta C Surdo, Sergio Pantano and Manuela Zaccolo. 'Imaging cAMP nanodomains in the heart'. In: *Biochemical Society Transactions* 47.5 (2019), pp. 1383–1392.

[38] Katharina Schleicher and Manuela Zaccolo. 'Axelrod symposium 2019: Phosphoproteomic analysis of G-protein-coupled pathways'. en. In: *Molecular Pharmacology* 99.5 (2021), pp. 383–391.

[39] Gunasekaran Subramaniam, Katharina Schleicher, Duangnapa Kovanich, Anna Zerio, Milda Folkmanaite, Ying-Chi Chao, Nicoletta C Surdo, Andreas Koschinski, Jianshu Hu, Arjen Scholten, Albert J R Heck, Maria Ercu, Anastasiia Sholokh, Kyung Chan Park, Enno Klussmann, Viviana Meraviglia, Milena Bellin, Sara Zanivan, Svenja Hester, Shabaz Mohammed and Manuela Zaccolo. 'Integrated Proteomics Unveils Nuclear PDE3A2 as a Regulator of Cardiac Myocyte Hypertrophy'. In: *Circulation Research* 132.7 (2023), pp. 828–848.

[40] Matthew Movsesian, Faiyaz Ahmad and Emilio Hirsch. 'Functions of PDE3 Isoforms in Cardiac Muscle'. In: *Journal of Cardiovascular Development and Disease* 5.1 (2018), p. 10.

[41] Terri Clister, Eric C Greenwald, George S Baillie and Jin Zhang. 'AKAP95 organizes a nuclear microdomain to control local cAMP for regulating nuclear PKA'. en. In: *Cell Chemical Biology* 26.6 (2019), 885–891.e4.

[42] Andrey D Bondarev, Misty M Attwood, Jörgen Jonsson, Vladimir N Chubarev, Vadim V Tarasov, Wen Liu and Helgi B Schiöth. 'Recent developments of phosphodiesterase inhibitors: Clinical trials, emerging indications and novel molecules'. In: *Frontiers in Pharmacology* 13 (2022).

[43] Wito Richter, Moses Xie, Colleen Scheitrum, Judith Krall, Matthew A Movsesian and Marco Conti. 'Conserved expression and functions of PDE4 in rodent and human heart'. en. In: *Basic Research Cardiology* 106.2 (2011), pp. 249–262.

[44] Delphine Mika, Pierre Bobin, Martine Pomérance, Patrick Lechêne, Ruth E Westenbroek, William A Catterall, Grégoire Vandecasteele, Jérôme Leroy and Rodolphe Fischmeister. 'Differential regulation of cardiac excitation–contraction coupling by cAMP phosphodiesterase subtypes'. In: *Cardiovascular Research* 100.2 (2013), pp. 336–346.

[45] Peter Molenaar, Torsten Christ, Rizwan I Hussain, Andreas Engel, Emanuel Berk, Katherine T Gillette, Lu Chen, Alejandro Galindo-Tovar, Kurt A Krobert, Ursula Ravens, Finn Olav Levy and Alberto J Kaumann. 'PDE3, but not PDE4, reduces β_1- and β_2-adrenoceptor-mediated inotropic and lusitropic effects in failing ventricle from metoprolol-treated patients'. en. In: *British Journal of Pharmacology* 169.3 (2013), pp. 528–538.

[46] Andrew T Bender and Joseph A Beavo. 'Cyclic nucleotide phosphodiesterases: molecular regulation to clinical use'. en. In: *Pharmacology Reviews* 58.3 (2006), pp. 488–520.

[47] Peter Molenaar, Torsten Christ, Emanuel Berk, Andreas Engel, Katherine T Gillette, Alejandro Galindo-Tovar, Ursula Ravens and Alberto J Kaumann. 'Carvedilol induces greater control of β_2- than β_1-adrenoceptor-mediated inotropic and lusitropic effects by PDE3, while PDE4 has no effect in human failing myocardium'. en. In: *Naunyn-Schmiedeberg's Archives of Pharmacology* 387.7 (2014), pp. 629–640.

[48] Claire Y Zhao, Joseph L Greenstein and Raimond L Winslow. 'Interaction between phosphodiesterases in the regulation of the cardiac β-adrenergic pathway'. en. In: *Journal of Molecular and Cellular Cardiology* 88 (2015), pp. 29–38.

[49] Peter B Snyder, Vincent A Florio, Ken Ferguson and Kate Loughney. 'Isolation, Expression and Analysis of Splice Variants of a Human Ca2+/Calmodulin-Stimulated Phosphodiesterase (PDE1A)'. In: *Cellular Signalling* 11.7 (1999), pp. 535–544.

[50] Fabrice Vandeput, Sharon L Wolda, Judith Krall, Ryan Hambleton, Lothar Uher, Kim N McCaw, Przemyslaw B Radwanski, Vincent Florio and Matthew A Movsesian. 'Cyclic nucleotide phosphodiesterase PDE1C1 in human cardiac myocytes'. en. In: *Journal of Biological Chemistry* 282.45 (2007), pp. 32749–32757.

[51] Marco Mongillo, Carlo G Tocchetti, Anna Terrin, Valentina Lissandron, York-Fong Cheung, Wolfgang R Dostmann, Tullio Pozzan, David A Kass, Nazareno Paolocci, Miles D Houslay and Manuela Zaccolo. 'Compartmentalized phosphodiesterase-2 activity blunts beta-adrenergic cardiac inotropy via an NO/cGMP-dependent pathway'. en. In: *Circulation Research* 98.2 (2006), pp. 226–234.

[52] André Iffland, Darcy Kohls, Simon Low, Jing Luan, Yan Zhang, Michael Kothe, Qing Cao, Ajith V Kamath, Yuan-Hua Ding and Tom Ellenberger. 'Structural determinants for inhibitor specificity and selectivity in PDE2A using the wheat germ in vitro translation system'. en. In: *Biochemistry* 44.23 (2005), pp. 8312–8325.

[53] Youn Wook Chung, Claudia Lagranha, Yong Chen, Junhui Sun, Guang Tong, Steven C Hockman, Faiyaz Ahmad, Shervin G Esfahani, Dahae H Bae, Nazari Polidovitch, Jian Wu, Dong Keun Rhee, Beom Seob Lee, Marjan Gucek, Mathew P Daniels, Christine A Brantner, Peter H Backx, Elizabeth Murphy and Vincent C Manganiello. 'Targeted disruption of PDE3B, but not PDE3A, protects murine heart from ischemia/reperfusion injury'. en. In: *Proceedings of the National Academy of Sciences* 112.17 (2015), E2253–62.

[54] S H Soderling, S J Bayuga and J A Beavo. 'Cloning and characterization of a cAMP-specific cyclic nucleotide phosphodiesterase'. en. In: *Proc. Natl. Acad. Sci. U. S. A.* 95.15 (1998), pp. 8991–8996.

[55] Huanchen Wang, Zier Yan, Serena Yang, Jiwen Cai, Howard Robinson and Hengming Ke. 'Kinetic and Structural Studies of Phosphodiesterase-8A and Implication on the Inhibitor Selectivity'. In: *Biochemistry* 47.48 (2008), pp. 12760–12768.

[56] Huanchen Wang, Yudong Liu, Jing Hou, Meiyan Zheng, Howard Robinson and Hengming Ke. 'Structural insight into substrate specificity of phosphodiesterase 10'. In: *Proceedings of the National Academy of Sciences* 104.14 (2007), pp. 5782–5787.

[57] Emmanuel Vazquez-Rivera, Brenda L Rojas, Jessica C Parrott, Anna L Shen, Yongna Xing, Patrick R Carney and Christopher A Bradfield. 'The aryl hydrocarbon receptor as a model PAS sensor'. In: *Toxicology Reports* 9 (2022), pp. 1–11.

[58] Ahleah S Gustina and Matthew C Trudeau. 'HERG potassium channel regulation by the N-terminal eag domain'. In: *Cellular Signalling* 24.8 (2012), pp. 1592–1598.

[59] Paul J A Erbel, Paul B Card, Ozgur Karakuzu, Richard K Bruick and Kevin H Gardner. 'Structural basis for PAS domain heterodimerization in the basic helix–loop–helix-PAS transcription factor hypoxia-inducible factor'. In: *Proceedings of the National Academy of Sciences* 100.26 (2003), pp. 15504–15509.

[60] Enrico Patrucco, Masami Shimizu Albergine, Luis F Santana and Joseph A Beavo. 'Phosphodiesterase 8A (PDE8A) regulates excitation-contraction coupling in ventricular myocytes'. en. In: *Journal of Molecular and Cellular Cardiology* 49.2 (2010), pp. 330–333.

[61] Grace K Muller, Joy Song, Vivek Jani, Yuejin Wu, Ting Liu, William P D Jeffreys, Brian O'Rourke, Mark E Anderson and David A Kass. 'PDE1 inhibition modulates Cav1.2 channel to stimulate cardiomyocyte contraction'. en. In: *Circulation Research* 129.9 (2021), pp. 872–886.

[62] Alessandra Stangherlin, Frank Gesellchen, Anna Zoccarato, Anna Terrin, Laura Ashley Fields, Marco Berrera, Nicoletta C Surdo, Margaret Anne Craig, Godfrey Smith, Graham Hamilton and Manuela Zaccolo. 'cGMP signals modulate cAMP levels in a compartment-specific manner to regulate catecholamine-dependent signaling in cardiac myocytes'. en. In: *Circulation Research* 108.8 (2011), pp. 929–939.

[63] Si Chen, Yishuai Zhang, Janet K Lighthouse, Deanne M Mickelsen, Jiangbin Wu, Peng Yao, Eric M Small and Chen Yan. 'A novel role of cyclic nucleotide phosphodiesterase 10A in pathological cardiac remodeling and dysfunction'. en. In: *Circulation* 141.3 (2020), pp. 217–233.

[64] Hind Mehel, Julius Emons, Christiane Vettel, Katrin Wittköpper, Danilo Seppelt, Matthias Dewenter, Susanne Lutz, Samuel Sossalla, Lars S Maier, Patrick Lechêne, Jérôme Leroy, Florence Lefebvre, Audrey Varin, Thomas Eschenhagen, Stanley Nattel, Dobromir Dobrev, Wolfram-Hubertus Zimmermann, Viacheslav O Nikolaev, Grégoire Vandecasteele, Rodolphe Fischmeister and Ali El-Armouche. 'Phosphodiesterase-2 is up-regulated in human failing hearts and blunts β-adrenergic responses in cardiomyocytes'. en. In: *Journal of the American College of Cardiology* 62.17 (2013), pp. 1596–1606.

[65] Rigney E Turnham and John D Scott. 'Protein kinase A catalytic subunit isoform PRKACA; History, function and physiology'. In: *Gene* 577.2 (2016), pp. 101–108.

[66] Donald M Bers, Yang K Xiang and Manuela Zaccolo. 'Whole-Cell cAMP and PKA Activity are Epiphenomena, Nanodomain Signaling Matters'. In: *Physiology* 34.4 (2019), pp. 240–249.

[67] Matthew G Gold. 'Swimming regulations for protein kinase A catalytic subunit'. In: *Biochemical Society Transactions* 47.5 (2019), pp. 1355–1366.

[68] Ryan Walker-Gray, Florian Stengel and Matthew G Gold. 'Mechanisms for restraining cAMP-dependent protein kinase revealed by subunit quantitation and cross-linking approaches'. In: *Proceedings of the National Academy of Sciences* 114.39 (2017), pp. 10414–10419.

[69] Wes Yonemoto, Maria L McGlone and Susan S Taylor. 'N-myristylation of the catalytic subunit of cAMP-dependent protein kinase conveys structural stability.' In: *Journal of Biological Chemistry* 268.4 (1993), pp. 2348–2352.

[70] Ece C Gaffarogullari, Larry R Masterson, Emily E Metcalfe, Nathaniel J Traaseth, Erica Balatri, Musa M Musa, Daniel Mullen, Mark D Distefano and Gianluigi Veglia. 'A Myristoyl/Phosphoserine Switch Controls cAMP-Dependent Protein Kinase Association to Membranes'. In: *Journal of Molecular Biology* 411.4 (2011), pp. 823–836.

[71] Kimberly L. Dodge-Kafka, Joseph Soughayer, Genevieve C Pare, Jennifer J Carlisle Michel, Lorene K Langeberg, Michael S Kapiloff and John D Scott. 'The protein kinase A anchoring protein mAKAP coordinates two integrated cAMP effector pathways'. In: *Nature* 437.7058 (2005), pp. 574–578.

[72] Hanan Qasim, Mehrdad Rajaei, Ying Xu, Arfaxad Reyes-Alcaraz, Hala Y. Abdelnasser, M. David Stewart, Satadru K. Lahiri, Xander H.T. Wehrens and Bradley K. McConnell. 'AKAP12 Upregulation Associates With PDE8A to Accelerate Cardiac Dysfunction'. In: *Circulation Research* 134.8 (2024), pp. 1006–1022.

[73] Srinath Krishnamurthy, Balakrishnan Shenbaga Moorthy, Lim Xin Xiang, Lim Xin Shan, Kavitha Bharatham, Nikhil Kumar Tulsian, Ivana Mihalek and Ganesh S Anand. 'Active Site Coupling in PDE:PKA Complexes Promotes Resetting of Mammalian cAMP Signaling'. In: *Biophysical Journal* 107.6 (2014), pp. 1426–1440.

[74] Nikhil Kumar Tulsian, Srinath Krishnamurthy and Ganesh S Anand. 'Channeling of cAMP in PDE-PKA Complexes Promotes Signal Adaptation'. In: *Biophysical Journal* 112.12 (2017), pp. 2552–2566.

[75] Kristoffer Søberg and Bjørn Steen Skålhegg. 'The Molecular Basis for Specificity at the Level of the Protein Kinase a Catalytic Subunit'. In: *Frontiers in Endocrinology* 9 (2018).

[76] Omar Torres-Quesada, Johanna E Mayrhofer and Eduard Stefan. 'The many faces of compartmentalized PKA signalosomes'. In: *Cellular Signalling* 37 (2017), pp. 1–11.

[77] Susan S. Taylor, Jian Wu, Jessica G.H. Bruystens, Jason C. Del Rio, Tsan-Wen Lu, Alexandr P. Kornev and Lynn F. Ten Eyck. 'From structure to the dynamic regulation of a molecular switch: A journey over 3 decades'. In: *Journal of Biological Chemistry* 296 (2021), p. 100746.

[78] Carla Mucignat-Caretta and Antonio Caretta. 'Protein Kinase A Catalytic and Regulatory Subunits Interact Differently in Various Areas of Mouse Brain'. In: *International Journal of Molecular Sciences* 21.9 (2020), p. 3051.

[79] Michael Plank, Nicole Carmiol, Bassam Mitri, Austin A Lipinski, Paul R Langlais and Andrew P Capaldi. 'Systems level analysis of time and stimuli specific signaling through PKA'. In: *Molecular Biology of the Cell* 35.4 (2024).

[80] Frank Christian, Márta Szaszák, Sabine Friedl, Stephan Drewianka, Dorothea Lorenz, Andrey Goncalves, Jens Furkert, Carolyn Vargas, Peter Schmieder, Frank Götz, Kerstin Zühlke, Marie Moutty, Hendrikje Göttert, Mangesh Joshi, Bernd Reif, Hannelore Haase, Ingo Morano, Solveig Grossmann, Anna Klukovits, Judit Verli, Róbert Gáspár, Claudia Noack, Martin Bergmann, Robert Kass, Kornelia Hampel, Dmitry Kashin, Hans-Gottfried Genieser, Friedrich W. Herberg, Debbie Willoughby, Dermot M F Cooper, George S Baillie, Miles D Houslay, Jens Peter von Kries, Bastian Zimmermann, Walter Rosenthal and Enno Klussmann. 'Small Molecule AKAP-Protein Kinase A (PKA) Interaction Disruptors That Activate PKA Interfere with Compartmentalized cAMP Signaling in Cardiac Myocytes'. In: *Journal of Biological Chemistry* 286.11 (2011), pp. 9079–9096.

[81] Elisabeth Jarnæss, Anja Ruppelt, Anne Jorunn Stokka, Birgitte Lygren, John D. Scott and Kjetil Taskén. 'Dual Specificity A-kinase Anchoring Proteins (AKAPs) Contain an Additional Binding Region That Enhances Targeting of Protein Kinase A Type I'. In: *Journal of Biological Chemistry* 283.48 (2008), pp. 33708–33718.

[82] Leslie A Piggott, Andrea L Bauman, John D Scott and Carmen W Dessauer. 'The A-kinase anchoring protein Yotiao binds and regulates adenylyl cyclase in brain'. In: *Proceedings of the National Academy of Sciences* 105.37 (2008), pp. 13835–13840.

[83] Poopak Banky, Melinda Roy, Marceen G Newlon, Dimitrios Morikis, Nina M Haste, Susan S Taylor and Patricia A Jennings. 'Related Protein–Protein Interaction Modules Present Drastically Different Surface Topographies Despite A Conserved Helical Platform'. In: *Journal of Molecular Biology* 330.5 (2003), pp. 1117–1129.

[84] Maen D Abou Ziki, Neha Bhat, Arpita Neogi, Tristan P Driscoll, Nelson Ugwu, Ya Liu, Emily Smith, Johny M Abboud, Salah Chouairi, Martin A Schwartz, Joseph G Akar and Arya Mani. 'Epistatic interaction of PDE4DIP and DES mutations in familial atrial fibrillation with slow conduction'. In: *Human Mutation* 42.10 (2021), pp. 1279–1293.

[85] Yuanyuan Dai, Asset Amenov, Nadezda Ignatyeva, Andreas Koschinski, Hang Xu, Poh Loong Soong, Malte Tiburcy, Wolfgang A. Linke, Manuela Zaccolo, Gerd Hasenfuss, Wolfram-Hubertus Zimmermann and Antje Ebert. 'Troponin destabilization impairs sarcomere-cytoskeleton interactions in iPSC-derived cardiomyocytes from dilated cardiomyopathy patients'. In: *Scientific Reports* 10.1 (2020).

[86] Friedrich W Herberg, Ariane Maleszka, Turid Eide, Lutz Vossebein and Kjetil Tasken. 'Analysis of A-kinase anchoring protein (AKAP) interaction with protein kinase A (PKA) regulatory subunits: PKA isoform specificity in AKAP binding'. In: *Journal of Molecular Biology* 298.2 (2000), pp. 329–339.

[87] Marceen G Newlon. 'A novel mechanism of PKA anchoring revealed by solution structures of anchoring complexes'. In: *The EMBO Journal* 20.7 (2001), pp. 1651–1662.

[88] Francis S Kinderman, Choel Kim, Sventja von Daake, Yuliang Ma, Bao Q Pham, Glen Spraggon, Nguyen-Huu Xuong, Patricia A Jennings and Susan S Taylor. 'A Dynamic Mechanism for AKAP Binding to RII Isoforms of cAMP-Dependent Protein Kinase'. In: *Molecular Cell* 24.3 (2006), pp. 397–408.

[89] Cathrine Rein Carlson, Birgitte Lygren, Torunn Berge, Naoto Hoshi, Wei Wong, Kjetil Taskén and John D Scott. 'Delineation of Type I Protein Kinase A-selective Signaling Events Using an RI Anchoring Disruptor'. In: *Journal of Biological Chemistry* 281.30 (2006), pp. 21535–21545.

[90] Ganapathy N Sarma, Francis S Kinderman, Choel Kim, Sventja von Daake, Lirong Chen, Bi-Cheng Wang and Susan S Taylor. 'Structure of D-AKAP2:PKA RI Complex: Insights into AKAP Specificity and Selectivity'. In: *Structure* 18.2 (2010), pp. 155–166.

[91] Ali El-Armouche, Lutz Pohlmann, Saskia Schlossarek, Jutta Starbatty, Yung-Hsin Yeh, Stanley Nattel, Dobromir Dobrev, Thomas Eschenhagen and Lucie Carrier. 'Decreased phosphorylation levels of cardiac myosin-binding protein-C in human and experimental heart failure'. In: *Journal of Molecular and Cellular Cardiology* 43.2 (2007), pp. 223–229.

[92] Bradley K McConnell, Zoran Popovic, Niladri Mal, Kwangdeok Lee, James Bautista, Farhad Forudi, Raul Schwartzman, J-P Jin, Marc Penn and Meredith Bond. 'Disruption of Protein Kinase A Interaction with A-kinase-anchoring Proteins in the Heart in Vivo'. In: *Journal of Biological Chemistry* 284.3 (2009), pp. 1583–1592.

[93] Mona El Refaey, Hassan Musa, Nathaniel P Murphy, Ellen R Lubbers, Michel Skaf, Mei Han, Omer Cavus, Sara N Koenig, Michael J Wallace, Daniel Gratz, Elisa Bradley, Katherina M Alsina, Xander H Wehrens, Thomas J Hund and Peter J Mohler. 'Protein Phosphatase 2A Regulates Cardiac Na + Channels'. In: *Circulation Research* 124.5 (2019), pp. 737–746.

[94] Silvio Weber, Stefanie Meyer-Roxlau, Michael Wagner, Dobromir Dobrev and Ali El-Armouche. 'Counteracting Protein Kinase Activity in the Heart: The Multiple Roles of Protein Phosphatases'. In: *Frontiers in Pharmacology* 6 (2015).

[95] Malay Chaklader and Beverly A Rothermel. 'Calcineurin in the heart: New horizons for an old friend'. In: *Cellular Signalling* 87 (2021), p. 110134.

[96] Sean T DeGrande, Sean C Little, Derek J Nixon, Patrick Wright, Jedidiah Snyder, Wen Dun, Nathaniel Murphy, Ahmet Kilic, Robert Higgins, Philip F Binkley, Penelope A Boyden, Cynthia A Carnes, Mark E Anderson, Thomas J Hund and Peter J Mohler. 'Molecular Mechanisms Underlying Cardiac Protein Phosphatase 2A Regulation in Heart'. In: *Journal of Biological Chemistry* 288.2 (2013), pp. 1032–1046.

[97] Naina Bhasin, Shane R Cunha, Malkanthi Mudannayake, Marisa S Gigena, Terry B Rogers and Peter J Mohler. 'Molecular basis for PP2A regulatory subunit B56 targeting in cardiomyocytes'. In: *American Journal of Physiology-Heart and Circulatory Physiology* 293.1 (2007), H109–H119.

[98] Xiaoke Yin, Friederike Cuello, Ursula Mayr, Zhiqi Hao, Martin Hornshaw, Elisabeth Ehler, Metin Avkiran and Manuel Mayr. 'Proteomics Analysis of the Cardiac Myofilament Subproteome Reveals Dynamic Alterations in Phosphatase Subunit Distribution'. In: *Molecular amp; Cellular Proteomics* 9.3 (2010), pp. 497–509.

[99] Stephanie M Stanford and Nunzio Bottini. 'Targeting protein phosphatases in cancer immunotherapy and autoimmune disorders'. In: *Nature Reviews Drug Discovery* 22.4 (2023), pp. 273–294.

[100] Danielle Abdallah, Nipun Malhotra and Mona El Refaey. 'Protein Phosphatase Signaling in Cardiac Myocytes'. In: *Cardiovascular Signaling in Health and Disease*. Springer International Publishing, 2022, pp. 175–196.

[101] Joanne Layland, R John Solaro and Ajay M Shah. 'Regulation of cardiac contractile function by troponin I phosphorylation'. en. In: *Cardiovascular Research* 66.1 (2005), pp. 12–21.

[102] Alexander Dutsch, Paul J. M. Wijnker, Saskia Schlossarek, Felix W. Friedrich, Elisabeth Krämer, Ingke Braren, Marc N. Hirt, David Brenière-Letuffe, Alexandra Rhoden, Ingra Mannhardt, Thomas Eschenhagen, Lucie Carrier and Giulia Mearini. 'Phosphomimetic cardiac myosin-binding protein C partially rescues a cardiomyopathy phenotype in murine engineered heart tissue'. In: *Scientific Reports* 9.1 (2019).

[103] Mohit Kumar, Kobra Haghighi, Evangelia G. Kranias and Sakthivel Sadayappan. 'Phosphorylation of cardiac myosin–binding protein-C contributes to calcium homeostasis'. In: *Journal of Biological Chemistry* 295.32 (2020), pp. 11275–11291.

[104] O'Neal Copeland, Sakthivel Sadayappan, Andrew E. Messer, Ger J.M. Steinen, Jolanda van der Velden and Steven B. Marston. 'Analysis of cardiac myosin binding protein-C phosphorylation in human heart muscle'. In: *Journal of Molecular and Cellular Cardiology* 49.6 (2010), pp. 1003–1011.

[105] Srboljub M Mijailovich, Boban Stojanovic, Djordje Nedic, Marina Svicevic, Michael A Geeves, Thomas C Irving and Henk L Granzier. 'Nebulin and titin modulate cross-bridge cycling and length-dependent calcium sensitivity'. In: *Journal of General Physiology* 151.5 (2019), pp. 680–704.

[106] Pei-Chi Yang, Britton W Boras, Mao-Tsuen Jeng, Steffen S Docken, Timothy J Lewis, Andrew D McCulloch, Robert D Harvey and Colleen E Clancy. 'A Computational Modeling and Simulation Approach to Investigate Mechanisms of Subcellular cAMP Compartmentation'. In: *PLOS Computational Biology* 12.7 (2016), e1005005.

[107] Mark Richards, Oliver Lomas, Kees Jalink, Kerrie L. Ford, Richard D Vaughan-Jones, Konstantinos Lefkimmiatis and Pawel Swietach. 'Intracellular tortuosity underlies slow cAMP diffusion in adult ventricular myocytes'. In: *Cardiovascular Research* 110.3 (2016), pp. 395–407.

[108] Andreas Koschinski and Manuela Zaccolo. 'Activation of PKA in cell requires higher concentration of cAMP than in vitro: implications for compartmentalization of cAMP signalling'. In: *Scientific Reports* 7.1 (2017).

[109] Hiroshi Satoh, Leanne M Delbridge, Lothar A Blatter and Donald M Bers. 'Surface:volume relationship in cardiac myocytes studied with confocal microscopy and membrane capacitance measurements: species-dependence and developmental effects'. In: *Biophysical Journal* 70.3 (1996), pp. 1494–1504.

[110] Kimberly J McCabe and Padmini Rangamani. 'Computational modeling approaches to cAMP/PKA signaling in cardiomyocytes'. In: *Journal of Molecular and Cellular Cardiology* 154 (2021), pp. 32–40.

[111] Jason Z. Zhang, Tsan-Wen Lu, Lucas M Stolerman, Brian Tenner, Jessica R Yang, Jin-Fan Zhang, Martin Falcke, Padmini Rangamani, Susan S Taylor, Sohum Mehta and Jin Zhang. 'Phase Separation of a PKA Regulatory Subunit Controls cAMP Compartmentation and Oncogenic Signaling'. In: *Cell* 182.6 (2020), 1531–1544.e15.

[112] Nicol Birsa, Matthew Peter Bentham and Pietro Fratta. 'Cytoplasmic functions of TDP-43 and FUS and their role in ALS'. In: *Seminars in Cell and Developmental Biology* 99 (2020), pp. 193–201.

[113] Clifford P Brangwynne, Christian R Eckmann, David S Courson, Agata Rybarska, Carsten Hoege, Jöbin Gharakhani, Frank Jülicher and Anthony A Hyman. 'Germline P Granules Are Liquid Droplets That Localize by Controlled Dissolution/Condensation'. In: *Science* 324.5935 (2009), pp. 1729–1732.

[114] Dimitri Scholz, Catalin F Baicu, William J Tuxworth, Lin Xu, Harinath Kasiganesan, Donald R Menick and George Cooper. 'Microtubule-dependent distribution of mRNA in adult cardiocytes'. In: *American Journal of Physiology-Heart and Circulatory Physiology* 294.3 (2008), H1135–H1144.

[115] Joshua R Wheeler, Tyler Matheny, Saumya Jain, Robert Abrisch and Roy Parker. 'Distinct stages in stress granule assembly and disassembly'. In: *eLife* 5 (2016).

[116] Daniel Mateju, Titus M Franzmann, Avinash Patel, Andrii Kopach, Edgar E Boczek, Shovamayee Maharana, Hyun O Lee, Serena Carra, Anthony A Hyman and Simon Alberti. 'An aberrant phase transition of stress granules triggered by misfolded protein and prevented by chaperone function'. en. In: *EMBO J.* 36.12 (2017), pp. 1669–1687.

[117] Helen V Edwards, John D Scott and George S Baillie. 'PKA phosphorylation of the small heat-shock protein Hsp20 enhances its cardioprotective effects'. In: *Biochemical Society Transactions* 40.1 (2012), pp. 210–214.

[118] Vanesa Tudisca, Clare Simpson, Lydia Castelli, Jennifer Lui, Nathaniel Hoyle, Silvia Moreno, Mark Ashe and Paula Portela. 'PKA isoforms coordinate mRNA fate during nutrient starvation'. In: *Journal of Cell Science* (2012).

[119] Adriana Marcelo, Rebekah Koppenol, Luís Pereira de Almeida, Carlos A Matos and Clévio Nóbrega. 'Stress granules, RNA-binding proteins and polyglutamine diseases: too much aggregation?' In: *Cell Death and Disease* 12.6 (2021).

[120] Damian Szklarczyk, Rebecca Kirsch, Mikaela Koutrouli, Katerina Nastou, Farrokh Mehryary, Radja Hachilif, Annika L Gable, Tao Fang, Nadezhda T Doncheva, Sampo Pyysalo, Peer Bork, Lars J Jensen and Christian von Mering. 'The STRING database in 2023: protein–protein association networks and functional enrichment analyses for any sequenced genome of interest'. In: *Nucleic Acids Research* 51.D1 (2022), pp. D638–D646.

[121] Jay W Schneider, Saji Oommen, Muhammad Y Qureshi, Sean C Goetsch, David R Pease, Rhianna S Sundsbak, Wei Guo, Mingming Sun, Han Sun, Hidehito Kuroyanagi, Dennis A Webster, Alexander W Coutts, Kimberly A Holst, Brooks S Edwards, Nikolas Newville, Matthew A Hathcock, Tamene Melkamu, Francesca Briganti, Wu Wei, Maria G Romanelli, Scott C Fahrenkrug, Doug E Frantz, Timothy M Olson, Lars M Steinmetz, Daniel F Carlson, Timothy J Nelson, Susana Cantero Peral, Sarah Edgerton, Joan Wobig, Boyd Rasmussen, Jodi A Scholz, Frank Cetta, Scott H Suddendorf, Joanne M Pedersen, Steve Krage, Craig S Frisk, Chelsea L Reece, Angela R Miller, Sara E Martineau, Rebecca K Johnson, Amanda L Breuer and Janell K Fox. 'Dysregulated ribonucleoprotein granules promote cardiomyopathy in RBM20 gene-edited pigs'. In: *Nature Medicine* 26.11 (2020), pp. 1788–1800.

[122] Xiaodong Cheng. 'Protein SUMOylation and phase separation: partners in stress?' In: *Trends in Biochemical Sciences* 48.5 (2023), pp. 417–419.

[123] Ali El-Armouche, Peter Boknik, Thomas Eschenhagen, Lucie Carrier, Michael Knaut, Ursula Ravens and Dobromir Dobrev. 'Molecular Determinants of Altered Ca 2+ Handling in Human Chronic Atrial Fibrillation'. In: *Circulation* 114.7 (2006), pp. 670–680.

[124] Norio Fukuda, Yiming Wu, Preetha Nair and Henk L Granzier. 'Phosphorylation of Titin Modulates Passive Stiffness of Cardiac Muscle in a Titin Isoform-dependent Manner'. In: *The Journal of General Physiology* 125.3 (2005), pp. 257–271.

[125] Federica Barbagallo, Bing Xu, Gopireddy R Reddy, Toni West, Qingtong Wang, Qin Fu, Minghui Li, Qian Shi, Kenneth S Ginsburg, William Ferrier, Andrea M Isidori, Fabio Naro, Hemal H Patel, Julie Bossuyt, Donald M Bers and Yang K Xiang. 'Genetically Encoded Biosensors Reveal PKA Hyperphosphorylation on the Myofilaments in Rabbit Heart Failure'. In: *Circulation Research* 119.8 (2016), pp. 931–943.

[126] Bo Ding, Jun-ichi Abe, Heng Wei, Qunhua Huang, Richard A. Walsh, Carlos A. Molina, Allan Zhao, Junichi Sadoshima, Burns C. Blaxall, Bradford C. Berk and Chen Yan. 'Functional Role of Phosphodiesterase 3 in Cardiomyocyte Apoptosis: Implication in Heart Failure'. In: *Circulation* 111.19 (2005), pp. 2469–2476.

[127] Hou Tee Lu, Jiyen Kam, Rusli Bin Nordin, Surinder Kaur Khelae, Jing Mein Wang, Chun Ngok Choy and Chuey Yan Lee. 'Beta-blocker use and risk of symptomatic bradyarrhythmias: a hospital-based case-control study'. en. In: *Journal of Geriatric Cardiology* 13.9 (2016), pp. 749–759.

[128] Adam C Vandergriff, Michael Taylor Hensley and Ke Cheng. 'Isolation and Cryopreservation of Neonatal Rat Cardiomyocytes'. In: *Journal of Visualized Experiments* 98 (2015).

[129] Tobias Opthof, Carol Ann Remme, Esther Jorge, Francisco Noriega, Rob F. Wiegerinck, Arlin Tasiam, Leander Beekman, Jesus Alvarez-Garcia, Cristian Munoz-Guijosa, Ruben Coronel and Juan Cinca. 'Cardiac activation–repolarization patterns and ion channel expression mapping in intact isolated normal human hearts'. In: *Heart Rhythm* 14.2 (2017), pp. 265–272.

[130] Sharon Siedner, Martina Kruger, Mechthild Schroeter, Doris Metzler, Wilhelm R Roell, Bernd K Fleischmann, Juergen Hescheler, Gabriele Pfitzer and Robert Stehle. 'Developmental changes in contractility and sarcomeric proteins from the early embryonic to the adult stage in the mouse heart'. In: *The Journal of Physiology* 548.2 (2003), pp. 493–505.

[131] Chao Yuan, Quanhu Sheng, Haixu Tang, Yixue Li, Rong Zeng and R. John Solaro. 'Quantitative comparison of sarcomeric phosphoproteomes of neonatal and adult rat hearts'. In: *American Journal of Physiology-Heart and Circulatory Physiology* 295.2 (2008), H647–H656.

[132] Valiery Kuznetsov, Elena Pak, Richard B Robinson and Susan F Steinberg. ' 2 -Adrenergic Receptor Actions in Neonatal and Adult Rat Ventricular Myocytes'. In: *Circulation Research* 76.1 (1995), pp. 40–52.

[133] Angela K Peter, Maureen A Bjerke and Leslie A Leinwand. 'Biology of the cardiac myocyte in heart disease'. In: *Molecular Biology of the Cell* 27.14 (2016), pp. 2149–2160.

[134] Paul Simpson. 'Norepinephrine-stimulated hypertrophy of cultured rat myocardial cells is an alpha 1 adrenergic response.' In: *Journal of Clinical Investigation* 72.2 (1983), pp. 732–738.

[135] Dimitrios Papadimitriou, Theodoros Xanthos, Ismene Dontas, Pavlos Lelovas and Despina Perrea. 'The use of mice and rats as animal models for cardiopulmonary resuscitation research'. In: *Laboratory Animals* 42.3 (2008), pp. 265–276.

[136] Nima Milani-Nejad and Paul M L Janssen. 'Small and large animal models in cardiac contraction research: Advantages and disadvantages'. In: *Pharmacology amp; Therapeutics* 141.3 (2014), pp. 235–249.

[137] Hong Bian, Ji Zhang, Ping Wu, Lori A. Varty, Yanlin Jia, Todd Mayhood, John A. Hey and Peng Wang. 'Differential type 4 cAMP-specific phosphodiesterase (PDE4) expression and functional sensitivity to PDE4 inhibitors among rats, monkeys and humans'. In: *Biochemical Pharmacology* 68.11 (2004), pp. 2229–2236.

[138] William B Johnson, Sidath Katugampola, Sarah Able, Carolyn Napier and Sian E Harding. 'Profiling of cAMP and cGMP phosphodiesterases in isolated ventricular cardiomyocytes from human hearts: Comparison with rat and guinea pig'. In: *Life Sciences* 90.9–10 (2012), pp. 328–336.

[139] Anna Astashkina, Brenda Mann and David W Grainger. 'A critical evaluation of in vitro cell culture models for high-throughput drug screening and toxicity'. In: *Pharmacology and Therapeutics* 134.1 (2012), pp. 82–106.

[140] Steven J Kattman, Alec D Witty, Mark Gagliardi, Nicole C Dubois, Maryam Niapour, Akitsu Hotta, James Ellis and Gordon Keller. 'Stage-specific optimization of activin/nodal and BMP signaling promotes cardiac differentiation of mouse and human pluripotent stem cell lines'. en. In: *Cell Stem Cell* 8.2 (2011), pp. 228–240.

[141] Fabian Zanella and Farah Sheikh. 'Patient-specific induced pluripotent stem cell models: Generation and characterization of cardiac cells'. In: *Methods in Molecular Biology* (2014), pp. 147–162.

[142] Davi M. Lyra-Leite, Óscar Gutiérrez-Gutiérrez, Meimei Wang, Yang Zhou, Lukas Cyganek and Paul W. Burridge. 'A review of protocols for human iPSC culture, cardiac differentiation, subtype-specification, maturation, and direct reprogramming'. In: *STAR Protocols* 3.3 (2022), p. 101560.

[143] Dries A Feyen, Wesley L McKeithan, Arne A Bruyneel, Sean Spiering, Larissa Hörmann, Bärbel Ulmer, Hui Zhang, Francesca Briganti, Michaela Schweizer, Bence Hegyi, Zhandi Liao, Risto-Pekka Pölönen, Kenneth S Ginsburg, Chi Keung Lam, Ricardo Serrano, Christine Wahlquist, Alexander Kreymerman, Michelle Vu, Prashila L Amatya, Charlotta S Behrens, Sara Ranjbarvaziri, Renee G Maas, Matthew Greenhaw, Daniel Bernstein, Joseph C Wu, Donald M Bers, Thomas Eschenhagen, Christian M Metallo and Mark Mercola. 'Metabolic Maturation Media Improve Physiological Function of Human iPSC-Derived Cardiomyocytes'. In: *Cell Reports* 32.3 (2020), p. 107925.

[144] Walter E. Knight, Yingqiong Cao, Ying-Hsi Lin, Congwu Chi, Betty Bai, Genevieve C. Sparagna, Yuanbiao Zhao, Yanmei Du, Pilar Londono, Julie A. Reisz, Benjamin C. Brown, Matthew R.G. Taylor, Amrut V. Ambardekar, Joseph C. Cleveland, Timothy A. McKinsey, Mark Y. Jeong, Lori A. Walker, Kathleen C. Woulfe, Angelo D'Alessandro, Kathryn C. Chatfield, Hongyan Xu, Michael R. Bristow, Peter M. Buttrick and Kunhua Song. 'Maturation of Pluripotent Stem Cell-Derived Cardiomyocytes Enables Modeling of Human Hypertrophic Cardiomyopathy'. In: *Stem Cell Reports* 16.3 (2021), pp. 519–533.

[145] Ingra Mannhardt, Alexandra Eder, Berengere Dumotier, Maksymilian Prondzynski, Elisabeth Krämer, Martin Traebert, Klaus-Dieter Söhren, Frederik Flenner, Konstantina Stathopoulou, Marc D. Lemoine, Lucie Carrier, Torsten Christ, Thomas Eschenhagen and Arne Hansen. 'Blinded Contractility Analysis in hiPSC-Cardiomyocytes in Engineered Heart Tissue Format: Comparison With Human Atrial Trabeculae'. In: *Toxicological Sciences* 158.1 (2017), pp. 164–175.

[146] Bärbel M Ulmer, Andrea Stoehr, Mirja L Schulze, Sajni Patel, Marjan Gucek, Ingra Mannhardt, Sandra Funcke, Elizabeth Murphy, Thomas Eschenhagen and Arne Hansen. 'Contractile Work Contributes to Maturation of Energy Metabolism in hiPSC-Derived Cardiomyocytes'. In: *Stem Cell Reports* 10.3 (2018), pp. 834–847.

[147] Malte Tiburcy, Tim Meyer, Norman Y Liaw and Wolfram-Hubertus Zimmermann. 'Generation of Engineered Human Myocardium in a Multi-well Format'. In: *STAR Protocols* 1.1 (2020), p. 100032.

[148] Matthew E Hartman, Dao-Fu Dai and Michael A Laflamme. 'Human pluripotent stem cells: Prospects and challenges as a source of cardiomyocytes for in vitro modeling and cell-based cardiac repair'. en. In: *Advanced Drug Delivery Reviews* 96 (2016), pp. 3–17.

[149] Tsukasa Kamakura, Takeru Makiyama, Kenichi Sasaki, Yoshinori Yoshida, Yimin Wuriyanghai, Jiarong Chen, Tetsuhisa Hattori, Seiko Ohno, Toru Kita, Minoru Horie, Shinya Yamanaka and Takeshi Kimura. 'Ultrastructural maturation of human-induced pluripotent stem cell-derived cardiomyocytes in a long-term culture'. en. In: *Circulation Journal* 77.5 (2013), pp. 1307–1314.

[150] Josè Manuel Pioner, Alice W Racca, Jordan M Klaiman, Kai-Chun Yang, Xuan Guan, Lil Pabon, Veronica Muskheli, Rebecca Zaunbrecher, Jesse Macadangdang, Mark Y Jeong, David L Mack, Martin K Childers, Deok-Ho Kim, Chiara Tesi, Corrado Poggesi, Charles E Murry and Michael Regnier. 'Isolation and mechanical measurements of myofibrils from human induced pluripotent stem cell-derived cardiomyocytes'. en. In: *Stem Cell Reports* 6.6 (2016), pp. 885–896.

[151] Razan Elfadil Ahmed, Tatsuya Anzai, Nawin Chanthra and Hideki Uosaki. 'A brief review of current maturation methods for human induced pluripotent stem cells-derived cardiomyocytes'. en. In: *Frontiers in Cell and Developmental Biology* 8 (2020), p. 178.

[152] Alejandro Lopez-Perez, Rafael Sebastian and Jose M Ferrero. 'Three-dimensional cardiac computational modelling: methods, features and applications'. In: *BioMedical Engineering OnLine* 14.1 (2015).

[153] Peter M. Kekenes-Huskey, Tao Liao, Andrew K. Gillette, Johan E. Hake, Yongjie Zhang, Anushka P. Michailova, Andrew D. McCulloch and J. Andrew McCammon. 'Molecular and Subcellular-Scale Modeling of Nucleotide Diffusion in the Cardiac Myofilament Lattice'. In: *Biophysical Journal* 105.9 (2013), pp. 2130–2140.

[154] Elisa Passini, Oliver J Britton, Hua Rong Lu, Jutta Rohrbacher, An N. Hermans, David J Gallacher, Robert J H Greig, Alfonso Bueno-Orovio and Blanca Rodriguez. 'Human In Silico Drug Trials Demonstrate Higher Accuracy than Animal Models in Predicting Clinical Pro-Arrhythmic Cardiotoxicity'. In: *Frontiers in Physiology* 8 (2017).

[155] Jason H Yang and Jeffrey J Saucerman. 'Computational Models Reduce Complexity and Accelerate Insight Into Cardiac Signaling Networks'. In: *Circulation Research* 108.1 (2011), pp. 85–97.

[156] Francesca Margara, Zhinuo J Wang, Francesc Levrero-Florencio, Alfonso Santiago, Mariano Vázquez, Alfonso Bueno-Orovio and Blanca Rodriguez. 'In-silico human electro-mechanical ventricular modelling and simulation for drug-induced pro-arrhythmia and inotropic risk assessment'. In: *Progress in Biophysics and Molecular Biology* 159 (2021), pp. 58–74.

[157] Denis Noble. 'Cardiac Action and Pacemaker Potentials based on the Hodgkin-Huxley Equations'. In: *Nature* 188.4749 (1960), pp. 495–497.

[158] Cong-Hui Luo and Yoram Rudy. 'A model of the ventricular cardiac action potential. Depolarization, repolarization, and their interaction.' In: *Circulation Research* 68.6 (1991), pp. 1501–1526.

[159] Christopher S Oehman, Wayne R Giles and Semahat S Demir. 'Mathematical Model of the Rapidly Activating Delayed Rectifier Potassium Current IKr in Rabbit Sinoatrial Node'. In: *Journal of Cardiovascular Electrophysiology* 13.11 (2002), pp. 1131–1140.

[160] Michelangelo Paci, Elisa Passini, Aleksandra Klimas, Stefano Severi, Jari Hyttinen, Blanca Rodriguez and Emilia Entcheva. 'All-Optical Electrophysiology Refines Populations of In Silico Human iPSC-CMs for Drug Evaluation'. In: *Biophysical Journal* 118.10 (2020), pp. 2596–2611.

[161] Jussi T Koivumäki, Nikolay Naumenko, Tomi Tuomainen, Jouni Takalo, Minna Oksanen, Katja A Puttonen, Šárka Lehtonen, Johanna Kuusisto, Markku Laakso, Jari Koistinaho and Pasi Tavi. 'Structural Immaturity of Human iPSC-Derived Cardiomyocytes: In Silico Investigation of Effects on Function and Disease Modeling'. In: *Frontiers in Physiology* 9 (2018).

[162] Divya C Kernik, Stefano Morotti, HaoDi Wu, Priyanka Garg, Henry J Duff, Junko Kurokawa, José Jalife, Joseph C Wu, Eleonora Grandi and Colleen E Clancy. 'A computational model of induced pluripotent stem-cell derived cardiomyocytes incorporating experimental variability from multiple data sources'. In: *The Journal of Physiology* 597.17 (2019), pp. 4533–4564.

[163] Michelangelo Paci, Jussi T Koivumäki, Hua Rong Lu, David J Gallacher, Elisa Passini and Blanca Rodriguez. 'Comparison of the Simulated Response of Three in Silico Human Stem Cell-Derived Cardiomyocytes Models and in Vitro Data Under 15 Drug Actions'. In: *Frontiers in Pharmacology* 12 (2021).

[164] Juliana Rengifo, Rafael Rosales, Adom González, Heping Cheng, Michael D. Stern and Eduardo Ríos. 'Intracellular Ca2+ Release as Irreversible Markov Process'. In: *Biophysical Journal* 83.5 (2002), pp. 2511–2521.

[165] Archibald Vivian Hill. 'The heat of shortening and the dynamic constants of muscle'. In: *Proceedings of the Royal Society of London. Series B - Biological Sciences* 126.843 (1938), pp. 136–195.

[166] Andrew F Huxley. 'Muscle Structure and Theories of Contraction'. In: *Progress in Biophysics and Biophysical Chemistry* 7 (1957), pp. 255–318.

[167] Kenneth S Campbell, Paul M L Janssen and Stuart G Campbell. 'Force-Dependent Recruitment from the Myosin Off State Contributes to Length-Dependent Activation'. In: *Biophysical Journal* 115.3 (2018), pp. 543–553.

[168] Sander Land, So-Jin Park-Holohan, Nicolas P Smith, Cristobal G dos Remedios, Jonathan C Kentish and Steven A Niederer. 'A model of cardiac contraction based on novel measurements of tension development in human cardiomyocytes'. In: *Journal of Molecular and Cellular Cardiology* 106 (2017), pp. 68–83.

[169] Mohamadamin Forouzandehmehr, Jussi T. Koivumäki, Jari Hyttinen and Michelangelo Paci. 'A mathematical model of hiPSC cardiomyocytes electromechanics'. In: *Physiological Reports* 9.22 (2021).

[170] Rahul R Rajendran, Sathyanand Kumaran, Arindam Banerjee and Ariel Berlinski. 'A hybrid in vitro in silico framework for albuterol delivery through an adult ventilator circuit to a patient-specific lung airway model'. In: *Journal of Aerosol Science* 158 (2021), p. 105844.

[171] Lukas Kovar, Lena Wien, Dominik Selzer, Yvonne Kohl, Robert Bals and Thorsten Lehr. 'In Vitro–In Silico Modeling of Caffeine and Diclofenac Permeation in Static and Fluidic Systems with a 16HBE Lung Cell Barrier'. In: *Pharmaceuticals* 15.2 (2022), p. 250.

[172] John J Rice, Fei Wang, Donald M Bers and Pieter P de Tombe. 'Approximate Model of Cooperative Activation and Crossbridge Cycling in Cardiac Muscle Using Ordinary Differential Equations'. In: *Biophysical Journal* 95.5 (2008), pp. 2368–2390.

[173] Stuart G Campbell, Fred V Lionetti, Kenneth S Campbell and Andrew D McCulloch. 'Coupling of Adjacent Tropomyosins Enhances Cross-Bridge-Mediated Cooperative Activation in a Markov Model of the Cardiac Thin Filament'. In: *Biophysical Journal* 98.10 (2010), pp. 2254–2264.

[174] Sander Land, Steven A Niederer, Jan Magnus Aronsen, Emil K S Espe, Lili Zhang, William E Louch, Ivar Sjaastad, Ole M Sejersted and Nicolas P Smith. 'An analysis of deformation-dependent electromechanical coupling in the mouse heart'. In: *The Journal of Physiology* 590.18 (2012), pp. 4553–4569.

[175] Clinton Wang, Jonas Schwan and Stuart G Campbell. 'Slowing of contractile kinetics by myosin-binding protein C can be explained by its cooperative binding to the thin filament'. In: *Journal of Molecular and Cellular Cardiology* 96 (2016), pp. 2–10.

[176] Srbolujub M Mijailovich, Djordje Nedic, Marina Svicevic, Boban Stojanovic, Jonathan Walklate, Zoltan Ujfalusi and Michael A Geeves. 'Modeling the Actin.myosin ATPase Cross-Bridge Cycle for Skeletal and Cardiac Muscle Myosin Isoforms'. In: *Biophysical Journal* 112.5 (2017), pp. 984–996.

[177] Nathalie A Balakina-Vikulova, Alexander Panfilov, Olga Solovyova and Leonid B Katsnelson. 'Mechano-calcium and mechano-electric feedbacks in the human cardiomyocyte analyzed in a mathematical model'. In: *The Journal of Physiological Sciences* 70.1 (2020).

[178] Aurore Lyon, Lauren J Dupuis, Theo Arts, Harry J G M Crijns, Frits W Prinzen, Tammo Delhaas, Jordi Heijman and Joost Lumens. 'Differentiating the effects of -adrenergic stimulation and stretch on calcium and force dynamics using a novel electromechanical cardiomyocyte model'. In: *American Journal of Physiology-Heart and Circulatory Physiology* 319.3 (2020), H519–H530.

[179] Lauren J Dupuis, Joost Lumens, Theo Arts and Tammo Delhaas. 'High tension in sarcomeres hinders myocardial relaxation: A computational study'. In: *PLOS ONE* 13.10 (2018), e0204642.

[180] Srboljub M. Mijailovich, Momcilo Prodanovic, Corrado Poggesi, Michael A. Geeves and Michael Regnier. 'Multiscale modeling of twitch contractions in cardiac trabeculae'. In: *Journal of General Physiology* 153.3 (2021).

[181] Gianluigi Savarese and Lars H Lund. 'Global Public Health Burden of Heart Failure'. In: *Cardiac Failure Review* 03.01 (2017), p. 7.

[182] Hariharan Subramanian and Viacheslav O Nikolaev. 'A-Kinase Anchoring Proteins in Cardiac Myocytes and Their Roles in Regulating Calcium Cycling'. In: *Cells* 12.3 (2023), p. 436.

[183] John M Cruickshank. 'Phosphodiesterase III inhibitors: Long-term risks and short-term benefits'. In: *Cardiovascular Drugs and Therapy* 7.4 (1993), pp. 655–660.

[184] Emmanuelle Massouridès, Jérôme Polentes, Philippe-Emmanuel Mangeot, Virginie Mournetas, Juliette Nectoux, Nathalie Deburgrave, Patrick Nusbaum, France Leturcq, Linda Popplewell, George Dickson, Nicolas Wein, Kevin M. Flanigan, Marc Peschanski, Jamel Chelly and Christian Pinset. 'Dp412e: a novel human embryonic dystrophin isoform induced by BMP4 in early differentiated cells'. In: *Skeletal Muscle* 5.1 (2015).

[185] Andreas Koschinski and Manuela Zaccolo. 'Micro-2D Cell Culture for cAMP Measurements Using FRET Reporters in Human iPSC-Derived Cardiomyocytes'. In: *Methods in Molecular Biology*. Springer US, 2022, pp. 141–165.

[186] Manuela Zaccolo and Tullio Pozzan. 'Discrete microdomains with high concentration of cAMP in stimulated rat neonatal cardiac myocytes'. en. In: *Science* 295.5560 (2002), pp. 1711–1715.

[187] J Russel Grove, Paul J Deutsch, Daniel J Price, Joel F Habener and Joseph Avruch. 'Plasmids encoding PKI(1–31), a specific inhibitor of cAMP-stimulated gene expression, inhibit the basal transcriptional activity of some but not all cAMP-regulated DNA response elements in JEG-3 cells'. In: *Journal of Biological Chemistry* 264.33 (1989), pp. 19506–19513.

[188] Amy J Tibbo, Delphine Mika, Sara Dobi, Jiayue Ling, Aisling McFall, Gonzalo S Tejeda, Connor Blair, Ruth MacLeod, Niall MacQuaide, Caglar Gök, William Fuller, Brian O Smith, Godfrey L Smith, Grégoire Vandecasteele, Thomas Brand and George S Baillie. 'Phosphodiesterase type 4 anchoring regulates cAMP signaling to Popeye domain-containing proteins'. In: *Journal of Molecular and Cellular Cardiology* 165 (2022), pp. 86–102.

[189] Bracy Andrea Fertig. 'Characterising the phosphorylation and SUMOylation of cardiac troponin I in heart failure'. In: (2019).

[190] Robert Terry, York-Fong Cheung, Morten Praestegaard, George S Baillie, Elaine Huston, Irene Gall, David R Adams and Miles D Houslay. 'Occupancy of the catalytic site of the PDE4A4 cyclic AMP phosphodiesterase by rolipram triggers the dynamic redistribution of this specific isoform in living cells through a cyclic AMP independent process'. In: *Cellular Signalling* 15.10 (2003), pp. 955–971.

[191] Jeffrey Klarenbeek, Joachim Goedhart, Aernoud van Batenburg, Daniella Groenewald and Kees Jalink. 'Fourth-Generation Epac-Based FRET Sensors for cAMP Feature Exceptional Brightness, Photostability and Dynamic Range: Characterization of Dedicated Sensors for FLIM, for Ratiometry and with High Affinity'. In: *PLOS ONE* 10.4 (2015), e0122513.

[192] Michael J Previs, Benjamin L Prosser, Ji Young Mun, Samantha Beck Previs, James Gulick, Kyounghwan Lee, Jeffrey Robbins, Roger Craig, W Jonathan Lederer and David M Warshaw. 'Myosin-binding protein C corrects an intrinsic non-uniformity in cardiac excitation-contraction coupling'. In: *Biophysical Journal* 108.2 (2015), 362a.

[193] C Amelia Sumandea, Mary L Garcia-Cazarin, Catherine H Bozio, Gail A Sievert, C William Balke and Marius P Sumandea. 'Cardiac Troponin T, a Sarcomeric AKAP, Tethers Protein Kinase A at the Myofilaments'. In: *Journal of Biological Chemistry* 286.1 (2011), pp. 530–541.

[194] Richard L Moss, Daniel P Fitzsimons and J Carter Ralphe. 'Cardiac MyBP-C Regulates the Rate and Force of Contraction in Mammalian Myocardium'. In: *Circulation Research* 116.1 (2015), pp. 183–192.

[195] Nazha Hamdani, Kalkidan G Bishu, Marion von Frieling-Salewsky, Margaret M Redfield and Wolfgang A Linke. 'Deranged myofilament phosphorylation and function in experimental heart failure with preserved ejection fraction'. In: *Cardiovascular Research* 97.3 (2012), pp. 464–471.

[196] Carsten Tschöpe, Christoph Birner, Michael Böhm, Oliver Bruder, Stefan Frantz, Andreas Luchner, Lars Maier, Stefan Störk, Behrouz Kherad and Ulrich Laufs. 'Heart failure with preserved ejection fraction: current management and future strategies: Expert opinion on the behalf of the Nucleus of the "Heart Failure Working Group" of the German Society of Cardiology (DKG)'. In: *Clinical Research in Cardiology* 107.1 (2017), pp. 1–19.

[197] Paul W Tillberg, Fei Chen, Kiryl D Piatkevich, Yongxin Zhao, Chih-Chieh Yu, Brian P English, Linyi Gao, Anthony Martorell, Ho-Jun Suk, Fumiaki Yoshida, Ellen M DeGennaro, Douglas H Roossien, Guanyu Gong, Uthpala Seneviratne, Steven R Tannenbaum, Robert Desimone, Dawen Cai and Edward S Boyden. 'Protein-retention expansion microscopy of cells and tissues labeled using standard fluorescent proteins and antibodies'. en. In: *Nature Biotechnology* 34.9 (2016), pp. 987–992.

[198] Thomas M D Sheard and Izzy Jayasinghe. 'Enhanced expansion microscopy to measure nanoscale structural and biochemical remodeling in single cells'. In: *Methods in Cell Biology*. Methods in cell biology (2021), pp. 147–180.

[199] Joshua Deal, Donald J Pleshinger, Santina C Johnson, Silas J Leavesley and Thomas C Rich. 'Milestones in the development and implementation of FRET-based sensors of intracellular signals: A biological perspective of the history of FRET'. In: *Cellular Signalling* 75 (2020), p. 109769.

[200] Delphine Mika, Pierre Bobin, Marta Lindner, Angele Boet, Amir Hodzic, Florence Lefebvre, Patrick Lechène, Malha Sadoune, Jane-Lise Samuel, Vincent Algalarrondo, Catherine Rucker-Martin, Virginie Lambert, Rodolphe Fischmeister, Grégoire Vandecasteele and Jérôme Leroy. 'Synergic PDE3 and PDE4 control intracellular cAMP and cardiac excitation-contraction coupling in a porcine model'. In: *Journal of Molecular and Cellular Cardiology* 133 (2019), pp. 57–66.

[201] Takashi Chijiwa, Atsushi Mishima, Masatoshi Hagiwara, Mamoru Sano, Kyozo Hayashi, Tsutomu Inoue, Kenji Naito, Tadashi Toshioka and Hiroyoshi Hidaka. 'Inhibition of forskolin-induced neurite outgrowth and protein phosphorylation by a newly synthesized selective inhibitor of cyclic AMP-dependent protein kinase, N-[2-(p-bromocinnamylamino)ethyl] -5-isoquinolinesulfonamide (H-89), of PC12D pheochromocytoma cells.' In: *Journal of Biological Chemistry* 265.9 (1990), pp. 5267–5272.

[202] Nikoleta Pavlaki, Kirstie A. De Jong, Birgit Geertz, Viacheslav O. Nikolaev and Alexander Froese. 'Cardiac Hypertrophy Changes Compartmentation of cAMP in Non-Raft Membrane Microdomains'. In: *Cells* 10.3 (2021), p. 535.

[203] Jia X Shen and Dermot M F Cooper. 'AKAP79, PKC, PKA and PDE4 participate in a Gq-linked muscarinic receptor and adenylate cyclase 2 cAMP signalling complex'. In: *Biochemical Journal* 455.1 (2013), pp. 47–56.

[204] Karnam S Murthy, Huiping Zhou and Gabriel M Makhlouf. 'PKA-dependent activation of PDE3A and PDE4 and inhibition of adenylyl cyclase V/VI in smooth muscle'. en. In: *American Journal of Physiology-Cell Physiology* 282.3 (2002), pp. C508–17.

[205] Kavee Limbutara, Andrew Kelleher, Chin-Rang Yang, Viswanathan Raghuram and Mark A. Knepper. 'Phosphorylation Changes in Response to Kinase Inhibitor H89 in PKA-Null Cells'. In: *Scientific Reports* 9.1 (2019).

[206] Rinzhin T Sherpa, Karni S Moshal, Shailesh R Agarwal, Rennolds S Ostrom and Robert D Harvey. 'Role of protein kinase A and A kinase anchoring proteins in buffering and compartmentation of cAMP signalling in human airway smooth muscle cells'. In: *British Journal of Pharmacology* 181.15 (2024), pp. 2622–2635.

[207] Simon Alberti, Amy Gladfelter and Tanja Mittag. 'Considerations and Challenges in Studying Liquid-Liquid Phase Separation and Biomolecular Condensates'. In: *Cell* 176.3 (2019), pp. 419–434.

[208] Nitin K Pandey, Jobin Varkey, Anakha Ajayan, Gincy George, Jeannie Chen and Ralf Langen. 'Fluorescent protein tagging promotes phase separation and alters the aggregation pathway of huntingtin exon-1'. In: *Journal of Biological Chemistry* 300.1 (2024), p. 105585.

[209] Robert Düster, Ines H Kaltheuner, Maximilian Schmitz and Matthias Geyer. '1, 6-Hexanediol, commonly used to dissolve liquid–liquid phase separated condensates, directly impairs kinase and phosphatase activities'. In: *Journal of Biological Chemistry* 296 (2021), p. 100260.

[210] Julia C Hardy, Emily H Pool, Jessica G H Bruystens, Xin Zhou, Qingrong Li, Daojia R Zhou, Max Palay, Gerald Tan, Lisa Chen, Jaclyn L C Choi, Ha Neul Lee, Stefan Strack, Dong Wang, Susan S Taylor, Sohum Mehta and Jin Zhang. 'Molecular determinants and signaling effects of PKA RI phase separation'. In: *Molecular Cell* 84.8 (2024), 1570–1584.e7.

[211] Anastasios Lymperopoulos. 'Clinical pharmacology of cardiac cyclic AMP in human heart failure: too much or too little?' In: *Expert Review of Clinical Pharmacology* 16.7 (2023), pp. 623–630.

[212] Manuel D Leonetti, Sayaka Sekine, Daichi Kamiyama, Jonathan S Weissman and Bo Huang. 'A scalable strategy for high-throughput GFP tagging of endogenous human proteins'. In: *Proceedings of the National Academy of Sciences* 113.25 (2016).

[213] Sergey V Ulianov, Artem K Velichko, Mikhail D Magnitov, Artem V Luzhin, Arkadiy K Golov, Natalia Ovsyannikova, Igor I Kireev, Alexey S Gavrikov, Alexander S Mishin, Azat K Garaev, Alexander V Tyakht, Alexey A Gavrilov, Omar L Kantidze and Sergey V Razin. 'Suppression of liquid–liquid phase separation by 1, 6-hexanediol partially compromises the 3D genome organization in living cells'. In: *Nucleic Acids Research* 49.18 (2021), pp. 10524–10541.

[214] Xinyi Liu, Shaoshuai Jiang, Lin Ma, Jiale Qu, Longying Zhao, Xing Zhu and Junjun Ding. 'Time-dependent effect of 1,6-hexanediol on biomolecular condensates and 3D chromatin organization'. In: *Genome Biology* 22.1 (2021).

[215] Theodora Myrto Perdikari, Anastasia C Murthy and Nicolas L Fawzi. 'Molecular insights into the effect of alkanediols on FUS liquid-liquid phase separation'. In: *bioRxiv preprint* (2022).

[216] Can Balaban, Martin Sztacho, Michaela Blažíková and Pavel Hozák. 'The F-Actin-Binding MPRIP Forms Phase-Separated Condensates and Associates with PI(4, 5)P2 and Active RNA Polymerase II in the Cell Nucleus'. In: *Cells* 10.4 (2021), p. 848.

[217] Alex Bateman et al. 'UniProt: the Universal Protein Knowledgebase in 2023'. In: *Nucleic Acids Research* 51.D1 (2022), pp. D523–D531.

[218] Nathan H Cho, Keith C Cheveralls, Andreas-David Brunner, Kibeom Kim, André C Michaelis, Preethi Raghavan, Hirofumi Kobayashi, Laura Savy, Jason Y Li, Hera Canaj, James Y S Kim, Edna M Stewart, Christian Gnann, Frank McCarthy, Joana P Cabrera, Rachel M Brunetti, Bryant B Chhun, Greg Dingle, Marco Y Hein, Bo Huang, Shalin B Mehta, Jonathan S Weissman, Rafael Gómez-Sjöberg, Daniel N Itzhak, Loïc A Royer, Matthias Mann and Manuel D Leonetti. 'OpenCell: Endogenous tagging for the cartography of human cellular organization'. In: *Science* 375.6585 (2022).

[219] Shawn Irgen-Gioro, Shawn Yoshida, Victoria Walling and Shasha Chong. 'Fixation can change the appearance of phase separation in living cells'. In: *eLife* 11 (2022).

[220] David T. McSwiggen, Mustafa Mir, Xavier Darzacq and Robert Tjian. 'Evaluating phase separation in live cells: diagnosis, caveats, and functional consequences'. In: *Genes amp; Development* 33.23–24 (2019), pp. 1619–1634.

[221] Manisha Poudyal, Komal Patel, Laxmikant Gadhe, Ajay Singh Sawner, Pradeep Kadu, Debalina Datta, Semanti Mukherjee, Soumik Ray, Ambuja Navalkar, Siddhartha Maiti, Debdeep Chatterjee, Jyoti Devi, Riya Bera, Nitisha Gahlot, Jennifer Joseph, Ranjith Padinhateeri and Samir K. Maji. 'Intermolecular interactions underlie protein/peptide phase separation irrespective of sequence and structure at crowded milieu'. In: *Nature Communications* 14.1 (2023).

[222] Wei Li and Hao Jiang. 'Nuclear Protein Condensates and Their Properties in Regulation of Gene Expression'. In: *Journal of Molecular Biology* 434.1 (2022), p. 167151.

[223] Zhengyu Xu, Wei Wang, Yi Cao and Bin Xue. 'Liquid-liquid phase separation: Fundamental physical principles, biological implications, and applications in supramolecular materials engineering'. In: *Supramolecular Materials* 2 (2023), p. 100049.

[224] Timothy B Johnstone, Kaitlyn H Smith, Cynthia J Koziol-White, Fengying Li, Austin G Kazarian, Maia L Corpuz, Maya Shumyatcher, Frederick J Ehlert, Blanca E Himes, Reynold A Panettieri and Rennolds S Ostrom. 'PDE8 Is Expressed in Human Airway Smooth Muscle and Selectively Regulates cAMP Signaling by 2-Adrenergic Receptors and Adenylyl Cyclase 6'. In: *American Journal of Respiratory Cell and Molecular Biology* 58.4 (2018), pp. 530–541.

[225] Nefeli Grammatika Pavlidou, Shokoufeh Dobrev, Kira Beneke, Franziska Reinhardt, Simon Pecha, Eric Jacquet, Issam H Abu-Taha, Constanze Schmidt, Niels Voigt, Markus Kamler, Renate B Schnabel, Istvan Baczkó, Anne Garnier, Hermann Reichenspurner, Viacheslav O Nikolaev, Dobromir Dobrev and Cristina E Molina. 'Phosphodiesterase 8 governs cAMP/PKA-dependent reduction of L-type calcium current in human atrial fibrillation: a novel arrhythmogenic mechanism'. In: *European Heart Journal* 44.27 (2023), pp. 2483–2494.

[226] Amel Lounas, Nathalie Vernoux, Marc Germain, Marie-Eve Tremblay and François J. Richard. 'Mitochondrial sub-cellular localization of cAMP-specific phosphodiesterase 8A in ovarian follicular cells'. In: *Scientific Reports* 9.1 (2019).

[227] Saiyang Xie, Mengya Chen, Wenxi Fang, Shiqiang Liu, Qingqing Wu, Chen Liu, Yun Xing, Wenke Shi, Man Xu, Min Zhang, Si Chen, Xiaofeng Zeng, Shasha Wang, Wei Deng and Qizhu Tang. 'Diminished arachidonate 5-lipoxygenase perturbs phase separation and transcriptional response of Runx2 to reverse pathological ventricular remodeling'. In: *eBioMedicine* 86 (2022), p. 104359.

[228] Aidan M Fenix, Yuichiro Miyaoka, Alessandro Bertero, Steven M Blue, Matthew J Spindler, Kenneth K B Tan, Juan A Perez-Bermejo, Amanda H Chan, Steven J Mayerl, Trieu D Nguyen, Caitlin R Russell, Paweena P Lizarraga, Annie Truong, Po-Lin So, Aishwarya Kulkarni, Kashish Chetal, Shashank Sathe, Nathan J Sniadecki, Gene W Yeo, Charles E Murry, Bruce R Conklin and Nathan Salomonis. 'Gain-of-function cardiomyopathic mutations in RBM20 rewire splicing regulation and re-distribute ribonucleoprotein granules within processing bodies'. In: *Nature Communications* 12.1 (2021).

[229] Yuanxi Mo, Yuliang Feng, Wei Huang, Ning Tan, Xinyi Li, Minwen Jie, Tong Feng, Hao Jiang and Lei Jiang. 'Liquid–Liquid Phase Separation in Cardiovascular Diseases'. In: *Cells* 11.19 (2022), p. 3040.

[230] Michele E Day, Guido M Gaietta, Mira Sastri, Antonius Koller, Mason R Mackey, John D Scott, Guy A Perkins, Mark H Ellisman and Susan S Taylor. 'Isoform-specific targeting of PKA to multivesicular bodies'. In: *Journal of Cell Biology* 193.2 (2011), pp. 347–363.

[231] Ibrahim Bedioune, Marine Gandon-Renard, Matthieu Dessillons, Aurélien Barthou, Audrey Varin, Delphine Mika, Saïd Bichali, Joffrey Cellier, Patrick Lechène, Sarah Karam, Maya Dia, Susana Gomez, Walma Pereira de Vasconcelos, Françoise Mercier-Nomé, Philippe Mateo, Audrey Dubourg, Constantine A Stratakis, Jean-Jacques Mercadier, Jean-Pierre Benitah, Vincent Algalarrondo, Jérôme Leroy, Rodolphe Fischmeister, Ana-Maria Gomez and Grégoire Vandecasteele. 'Essential Role of the RI Subunit of cAMP-Dependent Protein Kinase in Regulating Cardiac Contractility and Heart Failure Development'. In: *Circulation* (2024).

[232] Jonas Schwan, Andrea T Kwaczala, Thomas J Ryan, Oscar Bartulos, Yongming Ren, Lorenzo R Sewanan, Aaron H Morris, Daniel L Jacoby, Yibing Qyang and Stuart G Campbell. 'Anisotropic engineered heart tissue made from laser-cut decellularized myocardium'. In: *Scientific Reports* 6.1 (2016).

[233] Lorenzo R Sewanan, Jonas Schwan, Jonathan Kluger, Jinkyu Park, Daniel L Jacoby, Yibing Qyang and Stuart G Campbell. 'Extracellular Matrix From Hypertrophic Myocardium Provokes Impaired Twitch Dynamics in Healthy Cardiomyocytes'. In: *JACC: Basic to Translational Science* 4.4 (2019), pp. 495–505.

[234] Milda Folkmanaite, Xin Zhou, Francesca Margara, Manuela Zaccolo and Blanca Rodriguez. 'In Silico Human Induced Pluripotent Stem Cell Derived Cardiomyocyte Electro-Mechanical Modelling and Simulation'. In: *2021 Computing in Cardiology (CinC)*. Vol. 10. IEEE, 2021, pp. 1–4.

[235] Nimer Ballan, Naim Shaheen, Gordon M. Keller and Lior Gepstein. 'Single-Cell Mechanical Analysis of Human Pluripotent Stem Cell-Derived Cardiomyocytes for Drug Testing and Pathophysiological Studies'. In: *Stem Cell Reports* 15.3 (2020), pp. 587–596.

[236] George Kensah, Angelica Roa Lara, Julia Dahlmann, Robert Zweigerdt, Kristin Schwanke, Jan Hegermann, David Skvorc, Anke Gawol, Azadeh Azizian, Stefan Wagner, Lars S. Maier, Andreas Krause, Gerald Dräger, Matthias Ochs, Axel Haverich, Ina Gruh and Ulrich Martin. 'Murine and human pluripotent stem cell-derived cardiac bodies form contractile myocardial tissue in vitro'. In: *European Heart Journal* 34.15 (2012), pp. 1134–1146.

[237] Jia-Ling Ruan, Nathaniel L Tulloch, Maria V Razumova, Mark Saiget, Veronica Muskheli, Lil Pabon, Hans Reinecke, Michael Regnier and Charles E Murry. 'Mechanical Stress Conditioning and Electrical Stimulation Promote Contractility and Force Maturation of Induced Pluripotent Stem Cell-Derived Human Cardiac Tissue'. In: *Circulation* 134.20 (2016), pp. 1557–1567.

[238] Priyanka Garg, Angelos Oikonomopoulos, Haodong Chen, Yingxin Li, Chi Keung Lam, Karim Sallam, Marco Perez, Robert L Lux, Michael C Sanguinetti and Joseph C Wu. 'Genome Editing of Induced Pluripotent Stem Cells to Decipher Cardiac Channelopathy Variant'. In: *Journal of the American College of Cardiology* 72.1 (2018), pp. 62–75.

[239] Christopher Rao, Themistoklis Prodromakis, Ljudmila Kolker, Umar A R Chaudhry, Tatiana Trantidou, Arun Sridhar, Claire Weekes, Patrizia Camelliti, Sian E Harding, Ara Darzi, Magdi H Yacoub, Thanos Athanasiou and Cesare M Terracciano. 'The effect of microgrooved culture substrates on calcium cycling of cardiac myocytes derived from human induced pluripotent stem cells'. In: *Biomaterials* 34.10 (2013), pp. 2399–2411.

[240] Azra Fatima, Guoxing Xu, Kaifeng Shao, Symeon Papadopoulos, Martin Lehmann, Juan J Arnáiz-Cot, Angelo O Rosa, Filomain Nguemo, Matthias Matzkies, Sven Dittmann, Susannah L Stone, Matthias Linke, Ulrich Zechner, Vera Beyer, Hans Christian Hennies, Stephan Rosenkranz, Baerbel Klauke, Abdul S Parwani, Wilhelm Haverkamp, Gabriele Pfitzer, Martin Farr, Lars Cleemann, Martin Morad, Hendrik Milting, Juergen Hescheler and Tomo Šaric. 'lt;igt;In vitrolt;/igt; Modeling of Ryanodine Receptor 2 Dysfunction Using Human Induced Pluripotent Stem Cells'. In: *Cellular Physiology and Biochemistry* 28.4 (2011), pp. 579–592.

[241] Masaki Honda, Jumpei Kiyokawa, Mitsuyasu Tabo and Tomoaki Inoue. 'Electrophysiological Characterization of Cardiomyocytes Derived From Human Induced Pluripotent Stem Cells'. In: *Journal of Pharmacological Sciences* 117.3 (2011), pp. 149–159.

[242] Junyi Ma, Liang Guo, Steve J Fiene, Blake D Anson, James A Thomson, Timothy J Kamp, Kyle L Kolaja, Bradley J Swanson and Craig T January. 'High purity human-induced pluripotent stem cell-derived cardiomyocytes: electrophysiological properties of action potentials and ionic currents'. In: *American Journal of Physiology-Heart and Circulatory Physiology* 301.5 (2011), H2006–H2017.

[243] Thomas Colatsky, Bernard Fermini, Gary Gintant, Jennifer B Pierson, Philip Sager, Yuko Sekino, David G Strauss and Norman Stockbridge. 'The Comprehensive in Vitro Proarrhythmia Assay (CiPA) initiative — Update on progress'. In: *Journal of Pharmacological and Toxicological Methods* 81 (2016), pp. 15–20.

[244] Jakub Tomek, Alfonso Bueno-Orovio, Elisa Passini, Xin Zhou, Ana Minchole, Oliver Britton, Chiara Bartolucci, Stefano Severi, Alvin Shrier, Laszlo Virag, Andras Varro and Blanca Rodriguez. 'Development, calibration, and validation of a novel human ventricular myocyte model in health, disease, and drug block'. In: *eLife* 8 (2019).

[245] Jia-Ling Ruan, Nathaniel L Tulloch, Maria V Razumova, Mark Saiget, Veronica Muskheli, Lil Pabon, Hans Reinecke, Michael Regnier and Charles E Murry. 'Mechanical Stress Conditioning and Electrical Stimulation Promote Contractility and Force Maturation of Induced Pluripotent Stem Cell-Derived Human Cardiac Tissue'. In: *Circulation* 134.20 (2016), pp. 1557–1567.

[246] Jennifer D Cohen, Joshua E Babiarz, Rory M Abrams, Liang Guo, Sei Kameoka, Eric Chiao, Jack Taunton and Kyle L Kolaja. 'Use of human stem cell derived cardiomyocytes to examine sunitinib mediated cardiotoxicity and electrophysiological alterations'. In: *Toxicology and Applied Pharmacology* 257.1 (2011), pp. 74–83.

[247] Wendy Keung, Patrick K W Chan, Peter C Backeris, Eugene K Lee, Nicodemus Wong, Andy O T Wong, Gabriel K Y Wong, Camie W Y Chan, Bernard Fermini, Kevin D Costa and Ronald A Li. 'Human Cardiac Ventricular-Like Organoid Chambers and Tissue Strips From Pluripotent Stem Cells as a Two-Tiered Assay for Inotropic Responses'. In: *Clinical Pharmacology amp; Therapeutics* 106.2 (2019), pp. 402–414.

[248] Ksenia Blinova, Qianyu Dang, Daniel Millard, Godfrey Smith, Jennifer Pierson, Liang Guo, Mathew Brock, Hua Rong Lu, Udo Kraushaar, Haoyu Zeng, Hong Shi, Xiaoyu Zhang, Kohei Sawada, Tomoharu Osada, Yasunari Kanda, Yuko Sekino, Li Pang, Tromondae K Feaster, Ralf Kettenhofen, Norman Stockbridge, David G Strauss and Gary Gintant. 'International Multisite Study of Human-Induced Pluripotent Stem Cell-Derived Cardiomyocytes for Drug Proarrhythmic Potential Assessment'. In: *Cell Reports* 24.13 (2018), pp. 3582–3592.

[249] Ingra Mannhardt, Umber Saleem, Diogo Mosqueira, Malte F Loos, Bärbel M Ulmer, Marc D Lemoine, Camilla Larsson, Caroline Améen, Tessa de Korte, Maria L H Vlaming, Kate Harris, Peter Clements, Chris Denning, Arne Hansen and Thomas Eschenhagen. 'Comparison of 10 Control hPSC Lines for Drug Screening in an Engineered Heart Tissue Format'. In: *Stem Cell Reports* 15.4 (2020), pp. 983–998.

[250] Z Wang, B Fermini and S Nattel. 'Mechanism of flecainide's rate-dependent actions on action potential duration in canine atrial tissue.' In: *Journal of Pharmacology and Experimental Therapeutics* 267.2 (1993), pp. 575–581.

[251] Nicoletta Biglia, Valentina E Bounous, Tommaso Susini, Silvia Pecchio, Luca G Sgro, Valentina Tuninetti and Riccardo Torta. 'Duloxetine and escitalopram for hot flushes: efficacy and compliance in breast cancer survivors'. In: *European Journal of Cancer Care* 27.1 (2016), e12484.

[252] Hadine Joffe, Claudio N Soares, Laura F Petrillo, Adele C Viguera, Brittny L Somley, Jennifer K Koch and Lee S Cohen. 'Treatment of Depression and Menopause-Related Symptoms With the Serotonin-Norepinephrine Reuptake Inhibitor Duloxetine'. In: *The Journal of Clinical Psychiatry* 68.06 (2007), pp. 943–950.

[253] Junjun Li, Ying Hua, Shigeru Miyagawa, Jingbo Zhang, Lingjun Li, Li Liu and Yoshiki Sawa. 'hiPSC-Derived Cardiac Tissue for Disease Modeling and Drug Discovery'. In: *International Journal of Molecular Sciences* 21.23 (2020), p. 8893.

[254] Paz Ovics, Danielle Regev, Polina Baskin, Mor Davidor, Yuval Shemer, Shunit Neeman, Yael Ben-Haim and Ofer Binah. 'Drug Development and the Use of Induced Pluripotent Stem Cell-Derived Cardiomyocytes for Disease Modeling and Drug Toxicity Screening'. In: *International Journal of Molecular Sciences* 21.19 (2020), p. 7320.

[255] Stephan Lange, Nikos Pinotsis, Irina Agarkova and Elisabeth Ehler. 'The M-band: The underestimated part of the sarcomere'. In: *Biochimica et Biophysica Acta (BBA) - Molecular Cell Research* 1867.3 (2020), p. 118440.